CHARLES UNIVERSITY

Faculty of Science

Department of Physical and Macromolecular Chemistry

INTERACTION DYNAMICS OF CYTOSKELETAL POLYMERS

STUDIUM DYNAMIKY CYTOSKELETÁLNÍCH POLYMERÚ

M.Sc. Jochen Krattenmacher

Doctoral thesis

Supervisor: RNDr. Zdeněk Lánský, PhD.

Prague 2024

Declaration

I declare that I wrote this thesis independently and cited all the information sources and literature used. I also declare that I indicated the contributions of co-authors appropriately. In particular, certain parts of data acquisition of the Tau-related experiments were performed by Valerie Siahaan (a member of the Laboratory of Structural Proteins), as described in the "Publications" section of this thesis. No substantial part of this work has been submitted for the award of any other or the same academic degree, though a small share of the results presented in this thesis was also presented in the doctoral thesis by Valerie Siahaan, which was difficult to avoid given our tight collaboration during some of the time of my work in the Laboratory of Structural Proteins and us consequently sharing first-authorship in our publication "Kinetically distinct phases of Tau on microtubules regulate kinesin motors and severing enzymes." The figure panels which have also been presented in Valerie's thesis (Siahaan 2024) are marked as such in the respective figure captions.

In Berlin, 14th of October 2024 Jochen Krattenmacher

Acknowledgements

I first and foremost want to thank my two supervisors Zdenek Lansky and Marcus Braun for the opportunity to work on the projects presented in this thesis, their continued support, and not least their patience throughout my sometimes rather zigzaggy journey! I also want to thank Valerie Siahaan for the productive collaboration on the Tau story and the beautiful experimental data she produced. Similarly, I want to thank all the other co-authors of my publications for the fruitful collaboration, in particular Manuel-Lera Ramirez, Stefan Diez, Alexandre Beber, Amayra Hernandez-Vega, Lenka Grycova, and Francois Nedelec. Special thanks also to Ilia Zhernov and Jan Sabo for having been super-helpful colleagues, as well as the members of the BIOCEV imaging facility!

Abstract

The cytoskeleton is a complex network of interlinking protein filaments which fulfills a diverse range of functions for the cell. One of the key type of protein filaments are microtubules, which themselves are present in a diverse set of cellular contexts. In axons, long, stable microtubule arrays within the microtubule shaft form highways for molecular motors, enabling them to efficiently transport cargo across the cell. *In vitro* experiments, i.e., experiments where cellular components of interest are investigated outside of their cellular context, can help shed light on potential microscopic mechanisms underlying and giving rise to observed macroscopic phenomena. The results of the *in vitro* experiments conducted for this thesis contribute to our understanding how these arrays could potentially be stabilized and protected against microtubule-severing enzymes while other microtubule regions within the neuron can remain dynamic. In particular, the results presented here show how the microtubule-associated protein Tau, which preferentially locates to axonal shafts, cooperatively binds to microtubules, forming islands which are highly effective at protecting microtubules against severing. We also show that these Tau islands regulate the activity of the molecular motor kinesin-8, and that this motor in turn is also capable of disassembling Tau islands. In the second *in vitro* case study presented in this thesis, we show that the microtubule-crosslinking protein Ase1 can selectively stabilize antiparallel microtubule arrays, as they are found during mitosis, against depolymerization from the microtubule ends. This case study also shows that Ase1 is being herded by depolymerizing microtubule ends, and that this phenomenon likely is related to the propensity of Ase1 to oppose microtubule depolymerization. Overall, this the results in this thesis contribute to our understanding of how distinct interaction patterns between microtubules and microtubule-associated proteins can give rise to macroscopic structures within the cell.

Abstrakt

Cytoskelet je složitá síť vzájemně propojených proteinových filament, která plní v buňce celou řadu funkcí. Jedním z klíčových typů proteinových filament jsou mikrotubuly. Mikrotubuly v axonech tvoří dlouhé, stabilní struktury podél nichž se pohybují molekulární motory, které umožňují transport buněčného nákladu, jako jsou například organely, napříč buňkou. Experimenty in vitro, tj. experimenty, při nichž jsou zkoumány buněčné složky mimo jejich buněčný kontext, mohou pomoci objasnit potenciální molekulární mechanismy, které jsou základem a příčinou pozorovaných makroskopických jevů. Výsledky první in vitro studie provedené v rámci této práce přispívají k pochopení toho, jak mohou být mikrotubuly stabilizovány a chráněny v určité části buňky, zatímco mikrotubuly v jiné oblasti mohou zůstat dynamické. Předkládané výsledky ukazují, jak se mikrotubulární protein Tau, který se lokalizuje zejména na axonální mikrotubuly, kooperativně váže na tyto mikrotubuly a vytváří ostrůvky, které ochraňují a stabilizují mikrotubuly. Ukázali jsme také, že tyto Tau ostrůvky regulují aktivitu molekulárního motoru kinesinu-8 a že tento motor je také schopen tyto ostrůvky rozkládat. Ve druhé in vitro studii, kterou předkládáme v této práci, ukazujeme, že mikrotubulární spojovací protein Ase1 selektivně stabilizuje antiparalelní mikrotubulární struktury, které jsou například v centru mitotického vřeténka. Naše výsledky ukazují, že molekuly Ase1 jsou během depolymerace mikrotubulu shromážděné pomocí depolymerujícího konce mikrotubulu, což má za následek zpomalení depolymerace. V souhrnu, výsledky prezentované v této práci ukazují jak interakce mezi mikrotubuly a mikrotubulárními proteiny mohou ovlivňovat mikrotubulární dynamiku a tím buněčné pochody.

Contents

List of Figures

List of Tables

Background

The biologist Carl Woese suggested that "Organisms are resilient patterns in a turbulent flow — patterns in an energy flow" (Woese 2004). If this somewhat captures life, then the formation and maintenance of patterns are essential. On the sub-cellular level, an important component conferring structure and organization is the cytoskeleton. The cytoskeleton is a complex, dynamic network of protein filaments which can be found in the cytoplasm of all cells, including bacteria and archaea. Eukaryotes employ three different types of filaments: microtubules, actin filaments and intermediate filaments. These filaments interact interact with a plethora of other biopolymers in the cell, allowing the cytoskeleton to fulfill vital functions in a diverse set of domains, such as locomotion of the cell, maintaining structural integrity, chromosome segregation and cytokinesis during mitosis and the transport of cargoes within the cell. The cytoskeleton confers structure to the cell, but what confers structure to the cytoskeleton itself? While some of the patterning stems from interactions with other large entities, such as the cell membrane, the organization of the cytoskeleton partly emerges from the collective behavior of the involved cytoskeletal polymers. In other words, the cytoskeleton and its associates are known to display self-organization (Karsenti 2008). This work aims to expand our understanding of how, and to which extent, cytoskeletal polymers interact to give rise to supramolecular patterning.

To minimize the number of factors which could possibly give rise to patterns such to reveal underlying molecular mechanisms, we followed a bottom-up approach, where we sought to reconstitute cytoskeletal features *in-vitro* with a minimum number of components. We focused on microtubules, where we were interested in two cytoskeletal systems of which they are prominent members: (1) Axonal microtubule arrays and (2) the mitotic spindle. These two systems are very different, which is reflected in the different behavior of microtubules within them. This different behavior is also the consequence of differences in the cellular context, including the proteins interacting, or associating with microtubules. Thus, this thesis contains two parts, each dedicated to one of these systems, or more accurately, the microtubule-associated proteins we focused on in each series of respective experiments. Each of these systems and the respective microtubule-associated proteins are introduced below (see subsection 1.2.1 for axonal microtubule arrays and subsection 1.2.2 for the mitotic spindle). As in both systems, microtubules are an integral part of the experimental setup, I

in subsection 1.1.2 offer an introduction to them. I also give a brief primer on the biological, chemical and physical characteristics of proteins in general (subsection 1.1.1), as well as on the most prominent methods used in the course of this work (subsection 1.1.3).

1.1 Foundations

1.1.1 Proteins

Proteins are biological macromolecules composed of amino acid residues. A protein may simply be one long linear chain of amino acid residues, a so-called polypeptide, or it may be a polypeptide multimer, i.e., consisting of several polypeptides tightly bound to each other. Each peptide has a C-terminal and an N-terminal, named after the group at the respective end of the polymer chain (either a carboxyl or an amine group). There are 20 common amino acids (Frauenfelder 2010), which differ in their chemical and physical properties, enabling the vast functional and structural diversity among proteins. For instance, some amino acids are more hydrophilic in nature while others, are more hydrophobic (Kessel et al. 2018).

Cells synthesize a given protein by first transcribing the DNA sequence(s) which encode this protein into RNA(s) and then translating this/these RNA(s) into the corresponding sequence of amino acid residues (Kessel et al. 2018). The whole process of protein production is termed protein expression. Protein expression also involves additional steps which may occur after translation, i.e., post-translational modifications. This includes chemical modifications of single amino acid residues, for example phosphorylation, where a phosphate group is reversibly added to the residue. Post-translational modification also typically includes the process of protein folding, where a linear polypeptide folds into a three-dimensional structure, as illustrated in Figure 1.1. Some proteins are homo- or heteromers consisting of several polypeptides, where *homo* denotes that the polypeptide subunits are identical in sequence, while *hetero* denotes that the subunits are different. Such multimers form by association of their fully-folded subunits (Kessel et al. 2018). Notably, not all amino acid residue sequences fold into threedimensional structures, and indeed, some proteins do not feature any stable threedimensional structure. These proteins are termed intrinsically disordered proteins.

1.1.2 Microtubules

Microbules are long hollow tubes present in all eukariotic cells. They play important roles in a number of processes, including in cell division, intracellular transport, and cell motility (Akhmanova and Kapitein 2022).

1.1.2.1 Subunits

Microtubules are comprised of heterodimers of the protein *tubulin*. In cells, tubulin exists almost exclusively as the $\alpha\beta$-tubulin heterodimer (Figure 1.1). α- and β-tubulin are conserved throughout eukaryotes, sharing over 40% sequence identity with nearly the same secondary

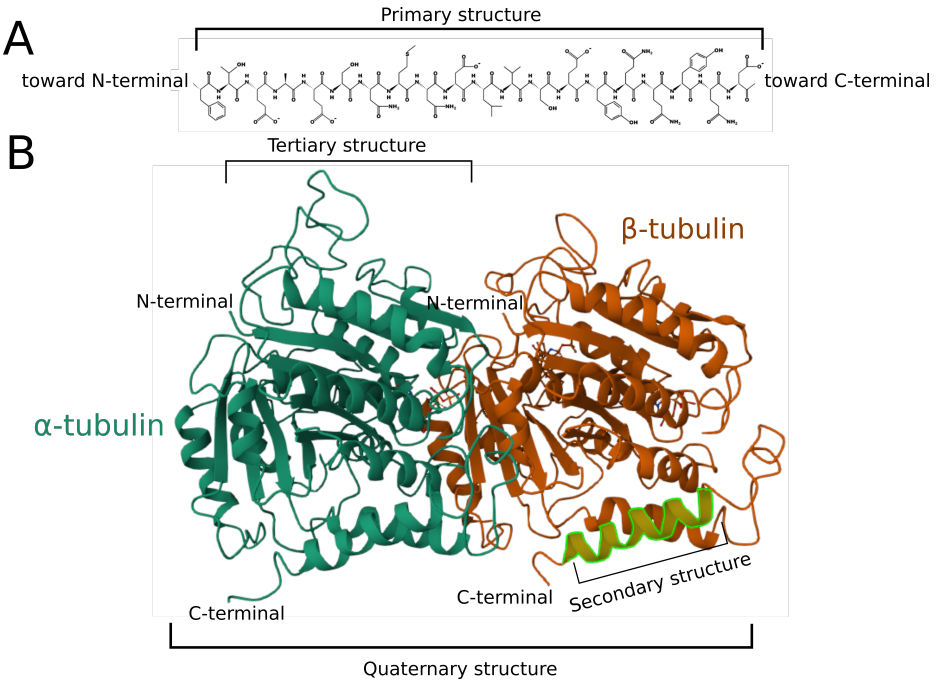

Figure 1.1: **Introduction to proteins.** (A) The threedimensional structure of proteins arises from the folding of linear chains of amino acid residues, the so-called primary structure. (B) Local three-dimensional arrenagements such as helices or the sheets are classified as secondary structures, while the folding of such local arrenagements into a complex whole results in the tertiary structure (Kessel et al. 2018). Some proteins, as the $\alpha\beta$-tubulin heterodimer shown here, consist of multiple polypeptides, the complex of which results in a so-called quaternary structure. In this case, the protein tubulin is used as an example, which assembles into a heterodimer subsubsection 1.1.2.1. The residue sequence shown in A corresponds to the residues of the helix highlighted in B (which is part of the β-tubulin polypeptide). The C-terminal of each tubulin subunit is indicated. Source: Own work (using rcsb.org/3d-sequence/1TUB and pepdraw.com).

and tertiary structures (Downing et al. 1998). Each tubulin monomer is a globular protein and consists of three closely interacting domains: an N-terminal nucleotide-binding domain, an intermediate domain, and a carboxy-terminal (C-terminal) helical region (Gregory M Alushin et al. 2014a). The disordered, negatively charged C-terminal tails of tubulin protrude outwards from the microtubule surface.

As is the case with many other proteins, tubulins express in different isoforms, arising from the expression of alternative tubulin-encoding genes. In humans, α- and β-tubulin are encoded in 9 genes each (Carsten Janke et al. 2020). Many, but not all, of these subtypes are highly conserved across species (Carsten Janke et al. 2020), in other words, they are almost identical. Tubulins further can be modulated by post-translational modifications, thus providing an additional level of microtubule regulation (C. Janke 2014). Modification of the C-terminal region in particular has been found to affect microtubule properties and their interactions with other proteins (Carsten Janke et al. 2020).

1.1.2.2 Structure

The microtubule lattice can be described as a lateral association of so-called protofilaments, which are linear strands of α- and β-tubulin heterodimers (Figure 1.3A). Their arrangement

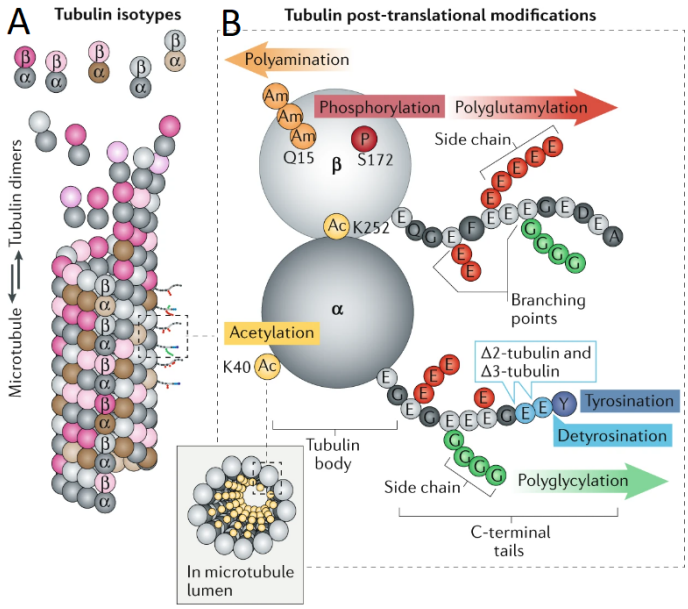

Figure 1.2: **Introduction to tubulin.** (A) Microtubules are constituted by α- and β-tubulin, which in humans are expressed in different isoforms. (B) α- and β-tubulin can undergo various types of post-translational modifications. This includes additions of groups, mainly to the C-terminal of either tubulin, but also other sites, e.g., the acetylation of a α-tubulin residue pointing toward the inside of the microtubule (the lumen). It also includes detyrosination, which is the removal of a tyrosine from the α-tubulin C-terminal. Adapted from Carsten Janke et al. 2020.

in a ring leads to the cylindrical structure of microtubules with an outer diameter of approximately 25 nm and an inner diameter of 17 nm (Figure 1.3B, (Hawkins et al. 2010)). The hollow tube architecture of microtubules allows for the high persistence length of microtubules, which is in the low millimeter range (Hawkins et al. 2010). This high persistence length allows microtubules to stretch over distances comparable to the size of a whole cell. Owing to the uniform orientation of the tubulin dimers, microtubules are directional polymers, with the β-subunits pointing to one end (called 'plus end') and the α-subunits pointing to the opposite end (called 'minus end'). Microtubules overall are negatively charged, and apart some positively charged regions, their surface is mostly negatively charged, even when not accounting for the negatively charged C-terminals of the tubulin subunits (Baker et al. 2001).

In spite of their high persistence length, microtubules are not static. Indeed, the microtubule lattice is increasingly understood to be rather responsive to external factors (Cross 2019). For instance, upon binding by kinesin-1, a motor protein (see subsubsection 1.2.1.3), the microtubule lattice expands (Peet et al. 2018). In another example illustrating the plasticity of the microtubule lattice, it has been shown that microtubules soften under mechanical strain (Memet et al. 2018).

In cells, microtubules usually have 13 protofilaments, however, in some cell types, microtubules with a different number of protofilaments have been observed, with observed numbers ranging from 11 to 15. For example, the nerve cords of nematodes harbour microtubules with 11 protofilaments, and 15-protofilament microtubules have been found

in various animal cells implicated in mechanosensation (Chaaban et al. 2017). Meanwhile, microtubules polymerized *in vitro* feature between 9 and 16 protofilaments (Chaaban et al. 2017). The number of protofilaments appears to be partially determined by the isotype of the involved tubulin dimers (Ti et al. 2018). *In vitro*, the number of protofilaments also depends on whether and how the microtubules have been stabilized subsubsection 1.1.3.1. This flexibility in terms of protofilament number allows for lattice defects to occur where the number of protofilaments may differ in different parts of a given microtubule (Chretien et al. 2000). It is also worth noting that depending on the number of protofilaments, the protofilaments in a given microtubule align differently: In the 13-protofilament variant, microtubules have a helical pitch of 1.5 dimers, i.e., their structure repeats every 1.5 dimers. Here, protofilaments are in an arrangement where tubulin subunits laterally associate with the opposite type (i.e., α- with β-tubulin), except at the seam, where tubulins of the same type associate (Figure 1.3B). A different number of protofilaments typically results in a different pitch, and in some instances in microtubules without a seam (Hawkins et al. 2010). Finally, a different number of protofilaments typically results in a structure where protofilaments no longer are straight but curl around the microtubule in what amounts to a superhelical twist of the microtubule's tubulin subunits (Chaaban et al. 2017).

1.1.2.3 Polymerization

Microtubules grow in every eukaryotic cell and can also be polymerized *in vitro*, i.e., in assays outside of cells given an adequate experimental buffer. Notably, the spontaneous assembly of microtubules, i.e., spontaneous *microtubule nucleation*, is kinetically unfavorable because the intermediate tubulin structures required for forming a full ring are not very stable (Akhmanova and Kapitein 2022). Spontaneous nucleation thus can occur only at high concentrations of free tubulin (Fygenson et al. 1994). In a more kinetically favorable mechanism, the *de novo* assembly of microtubules is partly directed by designated γ-tubulin nucleation complexes, which provide templates for the outgrowth of new microtubules (Akhmanova and Kapitein 2022). These nucleation complexes can be found in microtubule-organizing centers such as the centrosome of the spindle (subsection 1.2.2), and in some cases also along pre-existing microtubules (Janson et al. 2007; Akhmanova and Kapitein 2022). Another means by which the cell can multiply the number of microtubules is by severing existing microtubules (Vemu et al. 2018, see subsubsection 1.2.1.2). Notably, the fact that spontaneous nucleation is kinetically unfavorable gives the cell a high degree of control over the number and distribution of microtubules over time and space.

The most conspicuous feature of microtubule polymerization dynamics is that their plus ends are stochastically switching between phases of growth and shrinkage (Jánosi et al. 2002). This property is termed *dynamic instability*. According to the widely accepted and GTP cap model of microtubule instability (Gudimchuk et al. 2021), microtubule dynamic instability stems from the existence of two conformationally distinct populations of tubulin dimers: GTP-tubulin and GDP-tubulin, having GTP respectively GDP bound to their β-tubulin.

Mostly, it is free GTP-tubulin that adds to the lattice of a polymerizing microtubule. Shortly after polymerization, the β-tubulin hydrolyzes its GTP, resulting in conformational changes which result in mechanical tension. GTP-hydrolysis of a lattice-incorporated tubulin has no immediate consequences for the microtubule as a whole. However, if GTP-hydrolysis occurs at a microtubule end, the higher degree of freedom allows for conformational relaxation and eventual removal of the resulting GDP-tubulin from the microtubule end. This conformational relaxation typically takes the form of a curving of the protofilament, breaking lateral bonds with neighbouring protofilaments and thereby further destabilizing the microtubule end. Thus, if a microtubule loses too many GTP-tubulins at its plus end, i.e., if it loses its GTP cap, it switches to a regime of quick depolymerization where most protofilaments are curved outwards, giving the microtubule end the appearance of a "ram's horn" (Figure 1.3C). This outward-curling of protofilaments, due to the relaxation of the involved tubulin dimers, involves force-generation (Molodtsov et al. 2005).

While the GTP cap model of dynamic instability is experimentally strongly supported, there is less clarity on why exactly GTP-tubulin lattices are more stable than GDP-lattices, and multiple, non-mutually-exclusive models exist (Gudimchuk et al. 2021). In one model, GTP tubulin dimers are straighter than GDP tubulin dimers already in their relaxed state, facilitating their lattice incorporation. In another model, GTP tubulin might more readily change into a straight conformation than GDP tubulin, and in this model the microtubule lattice thus acts as an allosteric effector which straightens newly-incorporated tubulin dimers (Cross 2019). A third model proposes that GTP hydrolysis introduces relevant conformational changes at the interface between the adjacent dimers of a given protofilament. The latter is supported evidence that GTP hydrolysis introduces changes at these interfaces (Gregory M. Alushin et al. 2014b), however, this does not seem to be the case for all species (Cross 2019).

A change from continued polymerization to rapid depolymerization is called a *catastrophe* event. A reversal from depolymerization to polymerization can also occur and is called a *rescue* event. In the absence of rescue-promoting microtubule-associated proteins (sub-subsection 1.1.2.4), rescues are currently hypothesized to occur mainly at positions where GTP islands have formed within the otherwise GDP-dominated microtubule lattice. This hypotehsis is supported by *in vitro* experiments showing rescues to coincide with GTP islands (Aumeier et al. 2016). These islands had further been shown to be the result of microtubule self-repair, i.e., instances where free GTP-tubulin was incorporated into a damaged part of the microtubule (Aumeier et al. 2016). Recently, microtubule self-repair and GTP islands have also been observed *in vivo* (Gazzola et al. 2023).

As a final note, microtubule minus ends *in vivo* have not been observed to elongate, i.e., microtubule polymerization happens exclusively at the plus end (Dammermann et al. 2003). *In vitro*, minus ends can also exhibit polymerization, yet the plus end nonetheless polymerizes more quickly and is generally more dynamic (Howard et al. 2003).

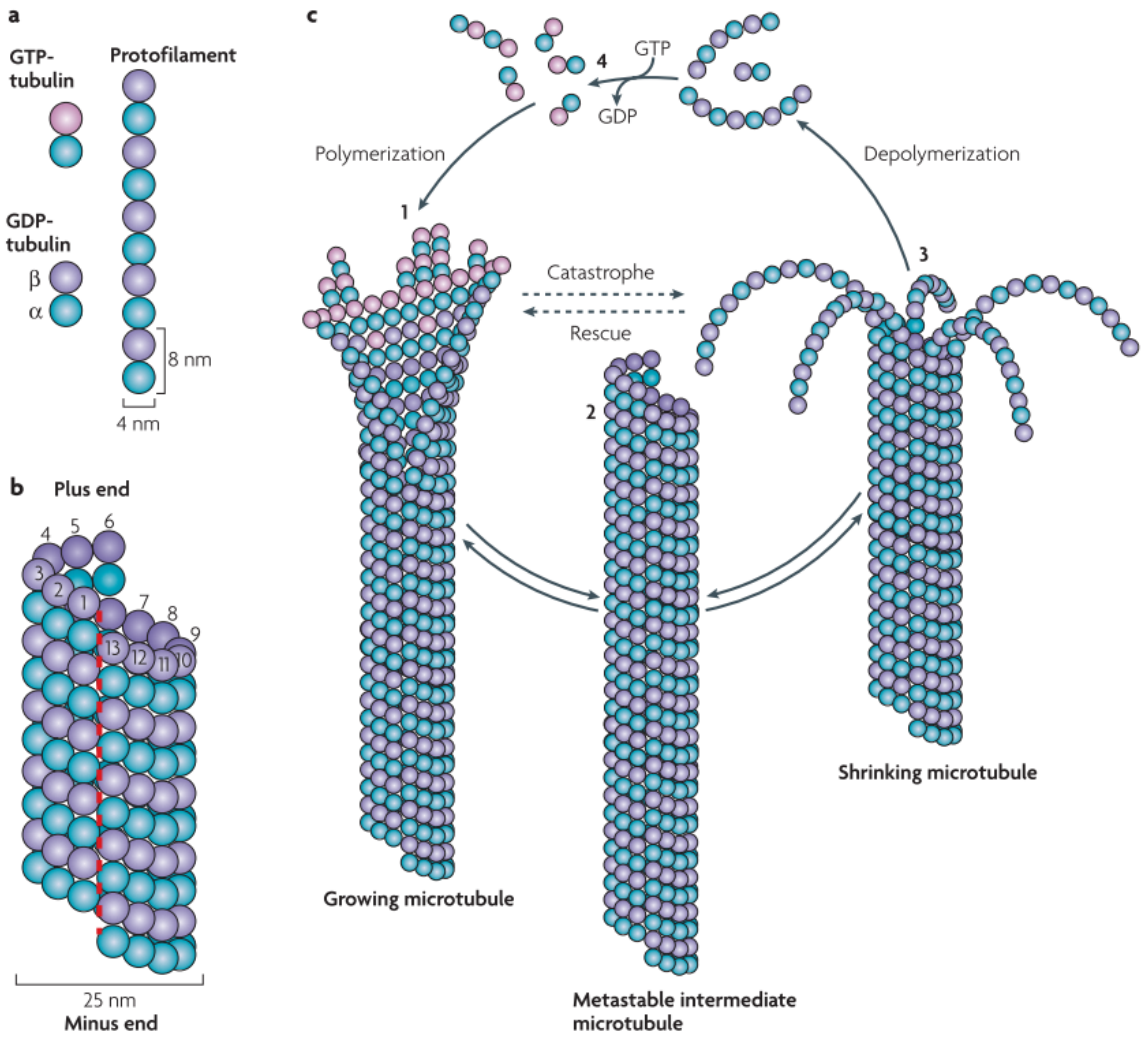

Figure 1.3: **Introduction to microtubules.** (A) Microtubules consist of $\alpha\beta$ heterodimers. While α-tubulin normally retains its GTP, the GTP molecule of β-tubulin can be both hydrolyzed and exchanged for ADP. (B) *In vivo*, microtubules are composed of 13 protofilaments. Since the 12 nm helical pitch does not equal the dimer length, a lattice seam occurs. (C) Due to the GTP-hydrolysis of incorporated β-tubulin, microtubule ends undergo a permanent cycle of growth (1) and shrinkage (3), closed by the exchange of GDP for GTP for the disassembly products (4). This cycle can briefly come to a halt during a less prevalent metastable state (2), from which microtubules can switch either to growth or to shrinkage. All sketches adapted from Akhmanova and Steinmetz 2008.

1.1.2.4 Microtubule-associated proteins

The vast functional diversity of microtubules is enabled by their interactions with microtubule-associated proteins (MAPs). Typically, MAPs bind either to the intradimer contact between the α- and the β-tubulin of a given dimer, or to the longitudinal contact between two dimers (the interdimer surface) (Nogales et al. 2016). Because the nucleotide of the β-tubulin is close to the interdimer site, binding to the interdimer surface is sensitive to nucleotide state (i.e., whether GTP or GDP is bound), which e.g. allows certain MAPs to preferentially locate to the growing tip of microtubules (Nogales et al. 2016). Bodakuntla et al. 2019 categorize MAPs into different groups depending on their mode of action, namely i) molecular motors

generating movement along microtubules, ii) enzymes destabilizing the microtubule lattice, iii) MAPs promoting microtubule nucleation, iv) microtubule-end binding proteins and v) structural MAPs controlling microtubule polymerization, stabilization and assembly into microtubule bundles. One MAP may belong to several of these groups, for instance, the molecular motor Kip3 is known to also cause microtubule polymerization (Gardner et al. 2011). In the course of my work, I have worked with four different MAPs as introduced further below, namely Tau (subsubsection 1.2.1.1), Katanin (subsubsection 1.2.1.2), Kip3 (subsubsection 1.2.1.3), and Ase1 (subsubsection 1.2.2.1).

1.1.3 Employed technologies

Below a primer on some of the main technologies which enabled the work performed for this thesis.

1.1.3.1 In-vitro stabilization of microtubules

For in-vitro experiments, it often is desirable to stabilize microtubules such that they remain polymerized even in the absence of GTP and/or free tubulin, in other words, to prevent microtubule instability. I had employed two common stabilization methods:

- **Stabilization via GMPCPP.** GMPCPP is a non-hydrolyzable analog of GTP that binds to the GTP-binding site of tubulin. By mimicking GTP, GMPCPP stabilizes the microtubule lattice, without any hydrolysis occurring which would normally induce lattice instability. This stabilization allows microtubules to remain polymerized even in the absence of free tubulin, GTP, or GMPCPP (A. A. Hyman et al. 1992). GMPCPP-tubulin lattices are thought to closely resemble GTP-tubulin lattices as one might observe at the tip of growing microtubules (Kellogg, N. M. Hejab, et al. 2017).

- **Stabilization via paclitaxel**. Paclitaxel, also known as taxol, does not directly interfere with the GTP cycle of tubulin but rather binds along the microtubule. This binding enhances microtubule stability, even under conditions that would normally induce shrinkage, such as low tubulin concentrations (Schiff et al. 1979). Notably, paclitaxel is not tightly bound to microtubules (Díaz et al. 1998), and thus paclitaxel-stabilized microtubules need to be stored in buffer solutions containing paclitaxel.

It is worth noting that the choice of stabilization impacts the mechanical properties of microtubules. For example, paclitaxel-stabilized microtubules tend to feature a wide variability in their protofilament number while GMPCPP-stabilized microtubules typically feature 14 protofilaments (Andreu et al. 1992; Meurer-Grob et al. 2001). In another example, GMPCPP-stabilized microtubules have been measured to have twice the flexural rigidity of paclitaxel-stabilized microtubules (Mickey et al. 1995). Interestingly, the effect of paclitaxel on the microtubule lattice appears to be dependent on whether paclitaxel is added to microtubules already before or only after microtubule polymerization: While adding it before

polymerization results in an axial repeat of 8.23 nm, adding it only after polymerization results in an axial repeat of 8.18 nm (Kellogg, N. M. Hejab, et al. 2017). This is compared to an axial repeat of 8.32 nm in the case of GMPCPP-stabilized microtubules, and an axial repeat of 8.15 nm for GDP lattices (Kellogg, N. M. Hejab, et al. 2017).

1.1.3.2 Labelling with fluorescent proteins

The first discovered fluorescent protein is green fluorescent protein (GFP), which was discovered around 60 years ago in the jellyfish Aequorea victoria (Shimomura 2005). Today, due to the discovery of new fluorescent proteins in other species as well as genetic engineering, a range of fluorescent proteins with different characteristics are available for use in laboratory work (Kremers et al. 2011). A common use case of fluorescent proteins, as made use of in this work, is labeling a protein of interest, thereby allowing for determining the location of the protein of interest via fluorescence microscopy techniques (see below). To achieve this labeling, the gene encoding the protein of interest is joined with the gene encoding a given fluorescent protein via recombinant DNA technology. Expressing this DNA construct then yields the protein of interest fused to the fluorescent protein. Notably, despite the relatively large size of fluorescent proteins (they all have a size around 27 kDa, compare e.g. to tubulin with a size of approximately 50 kDa), fusing them either to the C- or the N-terminal of a given protein usually does not significantly impair its function (Kremers et al. 2011).

1.1.3.3 Total internal reflection (TIRF) microscopy

The main experimental method employed during the course of this work was total internal reflection fluorescence (TIRF) microscopy. TIRF microscopy takes advantage of the physical phenomenon of total internal reflection, whereas light is fully reflected from a surface, yet a so-called evanescent field emanates beyond the surface of reflection, decaying exponentially in intensity. Because the evanescent field does not propagate, this phenomenon allows to selectively illuminate fluorophores near the glass/water surface, in our case the immobilized microtubules and their associated MAPs. By avoiding to excite fluorophores further away from the immobilized microtubules, background fluorescence can be reduced, as mainly the fluorophores of interest are excited. This is crucial for assays with a large number of labeled proteins in solution.

The main experimental method employed during the course of this work was total internal reflection fluorescence (TIRF) microscopy. TIRF microscopy is a specialized technique derived from fluorescence microscopy, which itself is a powerful tool used to study the distribution of fluorophore-labeled molecules within cells and other biological samples. Fluorescence microscopy relies on the excitation of fluorophores by specific wavelengths of light, leading to the emission of light at a longer wavelength. This process enables the visualization of structures and molecules with high specificity due to the different spectral signatures of different dyes or proteins (Lichtman et al. 2005). A higher specificity can be achieved by employing optical filters, which for instance is useful when working with multiple fluorophores

in the same sample. Optical filters can be employed to minimize "bleeding" of the signal of one fluorophore when aiming to detect the signal of the other.

TIRF microscopy, in particular, takes advantage of the physical phenomenon of total internal reflection, where light is fully reflected at the interface between two media with different refractive indices, such as glass and water. Although the light is fully reflected, a so-called evanescent field extends beyond the surface of reflection, decaying exponentially in intensity. This non-propagating field allows for the selective excitation of fluorophores located within approximately 100 nm of the glass/water interface, making it ideal for visualizing surface-bound molecules (Mattheyses et al. 2010). In our experiments, TIRF microscopy was used to illuminate fluorophores associated with immobilized microtubules and their associated microtubule-associated proteins (MAPs). By restricting the excitation to fluorophores near the surface, background fluorescence from molecules further away from the surface is significantly reduced, improving the signal-to-noise ratio. This selective excitation is crucial in assays involving a large number of labeled proteins in solution, as it ensures that only the fluorophores of interest contribute significantly to the observed fluorescence signal (Mattheyses et al. 2010).

1.1.3.4 Interference reflection microscopy (IRM)

For a few experiments (as indicated in methods section) we had employed interference reflection microscopy (IRM). In contrast to fluorescence-based microscopy methods, IRM allows for label-free imaging of biological samples. In the IRM setup, light from the light source passes through the aperture diaphragm and the field diaphragm, which regulate the amount of light reaching the camera. The 50/50 mirror then divides the light into two beams: one transmitted and one reflected, each with half the intensity of the original beam. The reflected beam is directed toward the objective, reflects off the sample, and then travels back through another 50/50 mirror and the tube lens to the camera. The resulting image is determined by the interference of reflections at the glass/water and water/sample interfaces. These reflections are influenced by differences in refractive indices — greater differences result in higher intensity of the reflected light beam (Barr et al. 2009). IRM thus requires particles large enough to generate noticable shifts in the phase of the reflected light. Due to the relatively large size of microtubules, IRM can be used to visualize them, with the advantage of requiring relatively few changes to typical microscope setups compared to more advanced techniques such as interferometric scattering (iSCAT) microscopy (Mahamdeh et al. 2018).

1.1.3.5 Fluorescence recovery after photobleaching (FRAP)

We for a few experiments also employed fluorescence recovery after photobleaching (FRAP) to investigate the binding kinetics of microtubule-associated proteins (MAPs). In the FRAP setup, a focused laser, in our case using the TIRF setup, is used to photobleach fluorescently-labelled molecules within a given region, creating a dark spot. The recovery of fluorescence in

this region is then monitored over time as unbleached molecules diffuse into or associate with the bleached microtubule area, while bleached molecules dissociate or move away (Axelrod et al. 1976). FRAP was a relevant for us due to its ability to provide insights into the unbinding rate k_{off} of a given microtubule-associated protein. If the binding sites on a microtubule for a given MAP are covered such that an equilibrium exists (i.e. no net binding or unbinding of MAPs occurs), after bleaching all of the MAPs on that microtubule, the rate of recovery depends only on k_{off}, assuming that the fluorescent MAPs in solution were not significantly depleted by the photobleaching (Bulinski et al. 2001), which in our case is true due to our employment of TIRF. Specifically, to determine k_{off}, one can fit the following function to the signal $I(t)$ measured experimentally by imaging the region over time (taking care to not signficantly bleach the sample due to this imaging): $I(t) = 1 - e^{-k_{off}t}$ (Bulinski et al. 2001).

1.2 Microtubule systems

Microtubules behave differently and fulfill different functions depending on the cellular context they are in. The two systems where I with this thesis aim to contribute understanding to are axonal microtubule systems (with a focus on Tau, Katanin, and kinesin-8) and the mitotic spindle (with a focus on Ase1).

1.2.1 Axonal microtubule arrays

The complex development and functionality of the nervous system rely heavily on microtubule-related processes, as microtubules play key roles in guiding cellular organization and intracellular transport (Kapitein and Hoogenraad 2015). Prominently, neurons develop two types of cytoplasmic protrusions: (i) Axons (also called nerve fibers) and (ii) dendrites. A typical neuron has one axon, which can reach to distant parts within the animal's body, and multiple dendrites, which are shorter, and connected to axons via synapses. While axons primarily contain long, stable microtubules, dendrites harbor shorter, more dynamic microtubules (Tas et al. 2017). To understand their cellular context, it is instructive to introduce axonal microtubule arrays vis-a-vis dendritic microtubule arrays.

Regarding intracellular transport, microtubules prominently serve as highways for molecular motors, most prominently kinesins, but also dyneins which are minus-end directed motors (Kapitein and Hoogenraad 2015). Efficient directional transport is especially crucial in neurons, given that dendrites and especially axons grow to macroscopic lengths. It is thus not surprising that within axons, microtubules bundle and point toward the same direction, namely with their plus ends away from the cell body (the soma) toward the distal end of the axon (Tas et al. 2017). Such an alignment lends itself to efficient transport of cargo between these distant parts of the cell, as a given motor cannot accidentally switch to an antiparallely aligned microtubule and travel in the opposite direction than previously. At the same time, within mammalian dendrites, there are both inward- and outwardpointing micro-

tubules in equal parts (Tas et al. 2017). Here, sufficiently effective transport is achieved by bundling microtubules such that a given bundle in a given dendrite predominantly comprises microtubules of the same orientation (Tas et al. 2017). Notably, and puzzingly, despite the existence of plus-end-outward microtubules in dendrites, many plus-end directed motors, including kinesin-8, only enter the axon (Lipka et al. 2016).

Regarding the guiding of cellular organization, the remodeling of microtubule arrays plays a central role in cell migration as well as the development of axons, dendrites, and synaptic connections (Kapitein and Hoogenraad 2015). For example, some molecular motors transport signaling factors or can even have non-motor signaling functions themselves, and as such the positioning of the microtubules becomes a determinant of developments within the cell (Hirokawa et al. 2010). Microtubules and microtubule motors are also involved in generating mechanical forces that drive cellular processes. For instance, dynein motors, by sliding axonal microtubules against each other, can push microtubules into growth regions of the axon, thereby in their interplay with opposing kinesin motors co-determining the direction of axonal growth (Kahn et al. 2016). Notably, post-translational modifications of tubulin (see subsubsection 1.1.2.1) play an essential role in fine-tuning microtubule dynamics and stability. Tubulin acetylation, for example, is associated with stable microtubules, which can be found e.g. in the axonal shaft but also in dendrites (Tas et al. 2017). Dynamic (or "labile") microtubules, which undergo frequent cycles of growth and shrinkage, comprise less acetylated tubulin, and can be found in dendrites and at the tips of growing axons, where active remodeling is necessary (Baas et al. 2016; Tas et al. 2017).

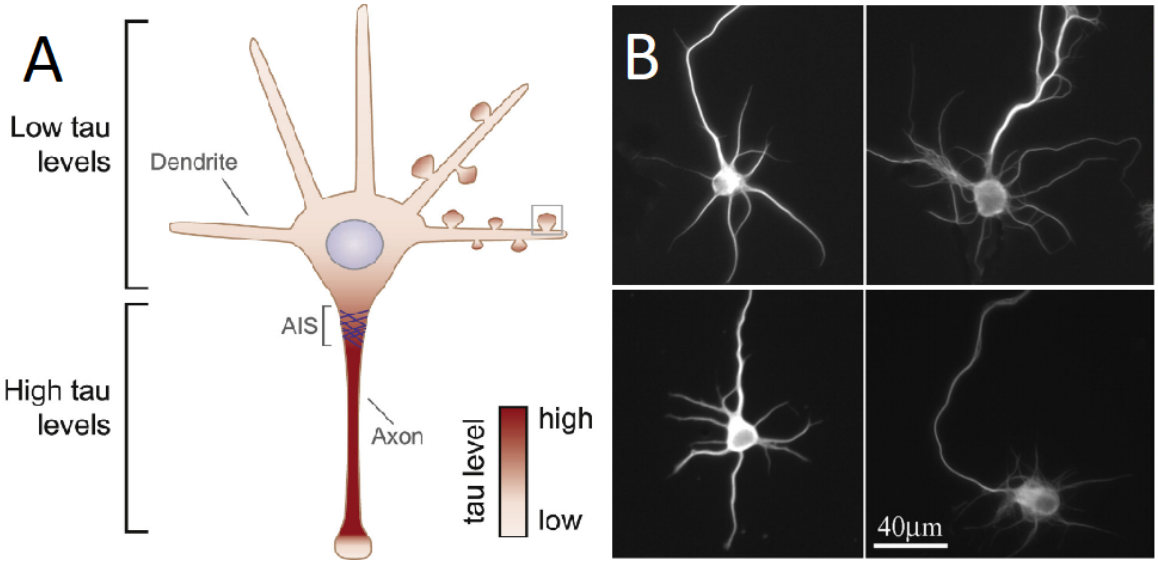

Figure 1.4: **Tau in the neuronal context.** (A) Tau distribution in the neuron (adapted from Ittner et al. 2018). Tau enrichment in the axon is facilitated by the axon initial segment (AIS) which acts as a diffusion barrier for Tau. (B) Microtubule immunostains of cultured rat hippocampal neurons, adapted from Qiang et al. 2006. Upper left: Control condition. Lower left: Depletion of Tau. The panels on the right side show cells where the Katanin p60 subunit was overexpressed (with no change in Tau levels in the upper panel and depletion of Tau in the lower panel).

1.2.1.1 Tau

Tau is an intrinsically disordered protein (see subsection 1.1.1) belonging to the MAP2/MAP4/Tau family. While MAP4 is found in other cells of the body, MAP2 and Tau are found within neurons (Dehmelt et al. 2005). Within the neuron, MAP2 is primarily found in dendrites, while Tau is mostly found in the axonal shaft, i.e. the most stable part of the neuronal microtubule architecture (Dehmelt et al. 2005, Figure 1.4A). An important function of Tau is to enhance the stability of microtubules. Tau binding for instance promotes microtubule polymerization, not only by enhancing microtubule growth rates but also by reducing the rate of catastrophes as well as depolymerization speed (Drechsel et al. 1992). Tau binding also has been found to increase the flexural rigidity of microtubules (Mickey et al. 1995). Tau can also stabilize microtubules via its capability to regulate the interaction of other MAPs with the microtubule surface (Morris et al. 2011). In particular, Tau mislocalization has *in vivo* been shown to protect axonal microtubules against microtubule-severing enzymes such as Katanin, and its mislocalization thus leads to microtubule destabilization and the eventual degeneration of the axon (Figure 1.4B) (Qiang et al. 2006). Given the importance of microtubules, and given that Tau protects microtubules, it is not surprising that malfunctions related to Tau have been implicated in a number of neurodegenerative diseases (Morris et al. 2011; Iqbal et al. 2016; Gao et al. 2018). For example, displacement of Tau from the axon is one of the hallmark events during the onset of the Alzheimer's disease (Zempel et al. 2015). Conspicuously, when Tau is hyperphosphorylated, i.e., contains more phosphate than normally, it aggregates into neurofibrillary tangles rather than binding to microtubules (Wang et al. 2012). There are six isoforms of Tau in humans, of which the longest form, "full-length" Tau, is the most studied and the one we worked with (Buchholz et al. 2024).

As depicted in Figure 1.5A, full-length Tau is intrinsically disordered and includes a negatively charged projection domain (its N-terminal domain), a proline-rich domain, a positively charged microtubule-binding region of four imperfect sequence repeats (R1-4), and a positively charged C-terminal domain (Himmler et al. 1989). Several different observations and explanations for how Tau interacts with microtubules can be found in the literature:

- Tau has been found to engage with microtubules in a mode where it diffuses along the microtubule, likely due to an attraction of the positively-charged parts of Tau with the negatively-charged C-terminals of tubulin on the microtubule surface (Hinrichs et al. 2012).
- In addition, Tau has been found to also bind to the microtubule stationarily, often in tandem with one or two Tau molecules with which they seem to form a static complex on the microtubule. This binding mode was observed on taxol-stabilized microtubules but not on GMPCPP-stabilized microtubules (Mcvicker et al. 2014). Moreover, Tau molecules were observed to switch between this mode and a diffusive mode (Mcvicker et al. 2014).
- Recently, it was found that the Tau microtubule binding repeats can bind to micro-

tubules in a consistent, orderly fashion, enough so to allow for an insightful cryo-EM study (Kellogg, N. M. A. Hejab, et al. 2018). In this study, Tau, through its multiple conserved tubulin-binding domains, was observed to bind longitudinally along the crest of a given protofilament via electrostatic as well as hydrophobic interactions, thereby tethering together several tubulin dimers (Figure 1.5B-C). This tethering, the authors suggested, stabilizes (longitudinal) inter-dimer interfaces and can explain the stabilization of microtubules by Tau. Notably, this study found the major microtubule binding site of Tau to correspond to an 'anchor point' which had previously been discovered (Zhang et al. 2015) at the inter-dimer interface that is virtually unaltered during the structural changes accompanying GTP hydrolysis (structural changes as mentioned in subsubsection 1.1.2.3). This would explain why Tau can bind to both bent and straight protofilaments (Kellogg, N. M. A. Hejab, et al. 2018).

- A recent NMR study drew attention to a pseudorepeat region R' located within the C-terminal region of Tau, between R1-R4 and residue 400 (R' is not explicitly indicated in Figure 1.5A) (Mammeri et al. 2022). The authors from their data inferred that full-length Tau binds to the microtubule primarily via R' and R4 (the repeat next to R'), likely due to the highly positively charged nature of R' (Mammeri et al. 2022). The authors argue that the study by Kellogg, N. M. A. Hejab, et al. 2018 had major limitations, as Kellogg, N. M. A. Hejab, et al. 2018 for their high-resolution reconstructions could not use full-length, wildtype Tau, but had to use recombinant Tau where the R1-4 pseudorepeats were replaced by four copies of either R1 or R2 (Kellogg, N. M. A. Hejab, et al. 2018). They claim that the density maps obtained by Kellogg, N. M. A. Hejab, et al. 2018 obtained for full-length Tau can also be explained by their model in which R' and R1 are the most tightly bound domains of Tau, and where the other domains are less stably bound to microtubules.

Further, it recently has been shown that Tau protein, can undergo liquid-liquid phase separation, as had previously already been observed for some other intrinsically disordered proteins (Hernández-Vega, Braun, Scharrel, Jahnel, Wegmann, Bradley T. Hyman, et al. 2017b). Furthermore, tubulin was observed to partition into these "Tau drops," and to assemble into microtubule bundles within these drops, offering another potential mechanism for microtubule nucleation in axons. Finally, another notable characteristic of Tau is that the projection domain of Tau appears to determine and cause the spacing between the microtubules within axonal microtubule arrays (Chen et al. 1992). Previously it had been suggested that Tau decoration of the microtubule might act as a "polymer brush," where the projection domains of each Tau molecule cause repulsion between microtubules, thereby counteracting attraction between microtubules and causing spaces between them (Mukhopadhyay et al. 2004). However, recent research questioned this model, arguing that the Tau-tubulin ratio in cells was too low for this model, such that Tau molecules could simply diffuse to other locations on the microtubule and thereby allow a given microtubule pair to align (Mephon-Gaspard et al. 2016). Instead, it was proposed that Tau molecules

associated with one microtubule bind to Tau molecules associated with another microtubule (with their projection domains), forming "bridges" which thus cannot simply diffuse away (Mephon-Gaspard et al. 2016).

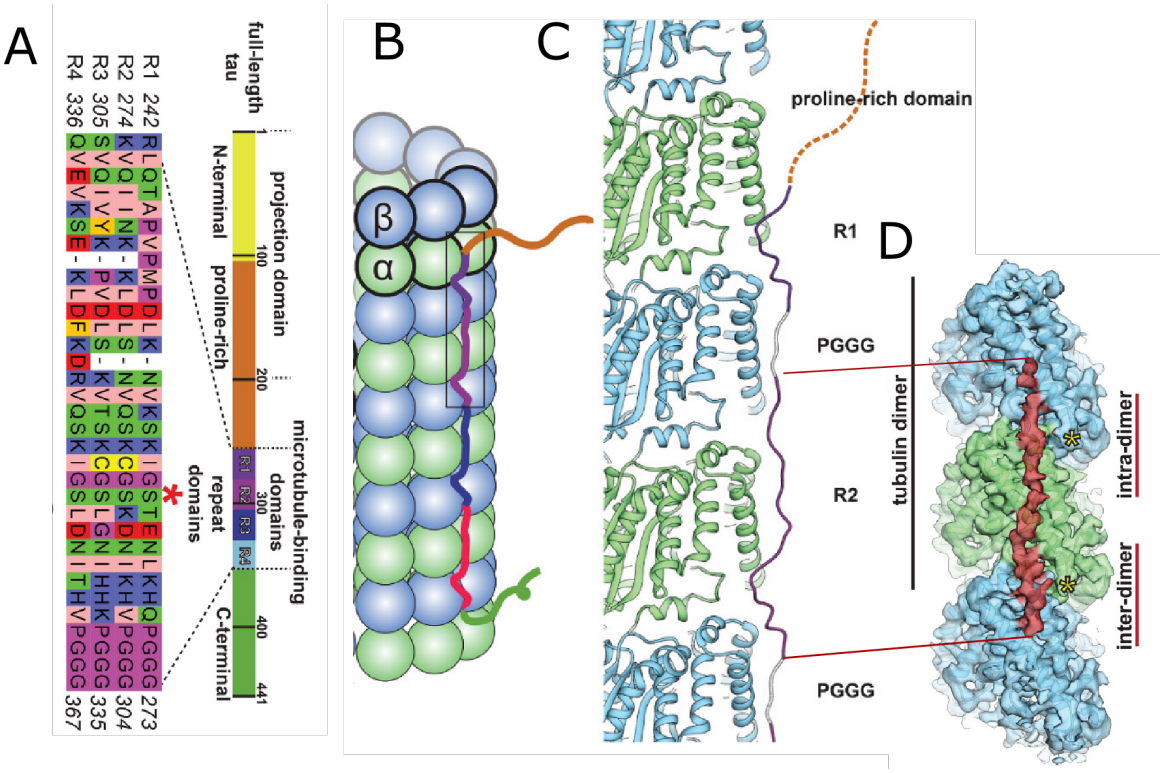

Figure 1.5: **Introduction to Tau.** (A) Schematic of the domains of full-length Tau protein. Inset shows the sequence alignment of the four microtubule binding repeat sequences, R1-4, that make up the repeat domain. (B) Model of full-length Tau binding to microtubules and tubulin oligomers proposed by a recent cryo-EM study (Kellogg, N. M. A. Hejab, et al. 2018). (C) Detailed representation of that model. (D) Cryo-EM density map of a part of the microtubule surface under the presence of Tau, as observed by Kellogg, N. M. A. Hejab, et al. 2018 (top view, looking onto the surface of the microtubule). The additional density (in addition to tubulin) is colored in red and likely due to Tau binding to the microtubule with its microtubule binding repeats. The PGGG sequences between the repeats were not visible on the density map, indicating that they did not bind to the microtubules in an orderly fashion. The positions of the C-terminals of tubulin are indicated with asterisks. Adapted from Kellogg, N. M. A. Hejab, et al. 2018.

1.2.1.2 Katanin

Katanin is a microtubule-severing enzyme that plays a critical role in the remodeling of the microtubule cytoskeleton by generating internal breaks in microtubules. This severing function modulates microtubule dynamics and organization, contributing to essential processes such as cell division, migration, and neuronal development (Roll-Mecak et al. 2010; Lombino et al. 2019). Indeed, Katanin levels in neurons are highest during developmental stages where a high dynamicity is required, and both depleting and overexpressing the p60 subunit have been shown to result in impaired neuronal development (Karabay et al. 2004). Katanin is a heterodimer composed of two subunits: a catalytic p60 subunit and a regulatory p80 subunit. The p60 subunit belongs to the AAA+ (ATPases Associated with various cellular

Activities) protein family, containing the ATPase motor domain responsible for generating mechanical force required for microtubule severing (K. McNally et al. 2014; Johjima et al. 2015). While the p60 subunit has been shown to on its own exhibit microtubule-severing activity (K. McNally et al. 2014), the p80 subunit has been shown to regulate the spatial distribution of Katanin by targeting Katanin to the centrosome (Hartman et al. 1998). This spatial regulation is vital, as indiscriminate severing of microtubules can lead to deleterious effects on cell function. In addition to its centrosomal localization, the p80 subunit plays a role in regulating the overall activity of the catalytic p60 subunit (K. P. McNally et al. 2000).

Katanin's severing activity appears to at least partially depend on ATP hydrolysis. ATP binding and subsequent hydrolysis stimulated by the microtubule provide the energy required for conformational changes in the p60 subunit, enabling it to exert mechanical force on the microtubule lattice (Zehr et al. 2017). Specifically, Katanin is thought to pull on the C-terminal tails of tubulin subunits, destabilizing the lateral interactions between protofilaments in a step-wise manner, leading to local lattice destabilization and often microtubule breakage (Figure 1.6). After the microtubule breakage, whether the newly created microtubule plus end polymerizes or depolymerizes depends on the presence of free tubulin (Vemu et al. 2018; Y.-W. Kuo et al. 2021). At a low free tubulin concentration, the newly-created plus end will shrink. However, if there is sufficient free tubulin present, the microtubule has a high chance of entering a growth regime, because the likelyhood is high that at the site of breakage, a sufficient number of GTP-tubulin has been incorporated, establishing a protective cap (see subsubsection 1.1.2.3). Similarly, it should be noted that incorporation of GTP-tublin also occurs at microtubule sites where severing is not fully completed, which can lead to the emergence of GTP islands in the lattice with higher resistance against depolymerization (Vemu et al. 2018). These mechanisms can explain the perhaps counterintuitive phenomenon that the loss of Katanin has been found to cause a decrease in microtubule mass (Vemu et al. 2018).

In addition to it's severing activity, Katanin also promotes depolymerization of microtubules from their ends, in a manner which is independent from ATP hydrolysis and the C-terminal tails of tubulin (Belonogov et al. 2019).

1.2.1.3 Kinesin-8/Kip3

Molecular motors convert chemical energy in form of ATP into mechanical energy. One of the three large superfamilies of molecular motors are kinesins. To date more than 600 kinesin sequences with 45 kinesin genes in the human- 17 -genome (Endow et al. 2010) have been identified. Kinesins are divided into 14 kinesin sub-families based on their structure and function. I worked with Kip3, a kinesin-8 family found in budding yeast. We chose budding yeast kinesin instead of neuronal kinesin such to minimize the chance of chemical interactions with Tau or Katanin, allowing us to focus on physical effects. Like the first discovered kinesin kinesin-1 (Endow et al. 2010), Kip3 is a homodimeric complex that moves toward the

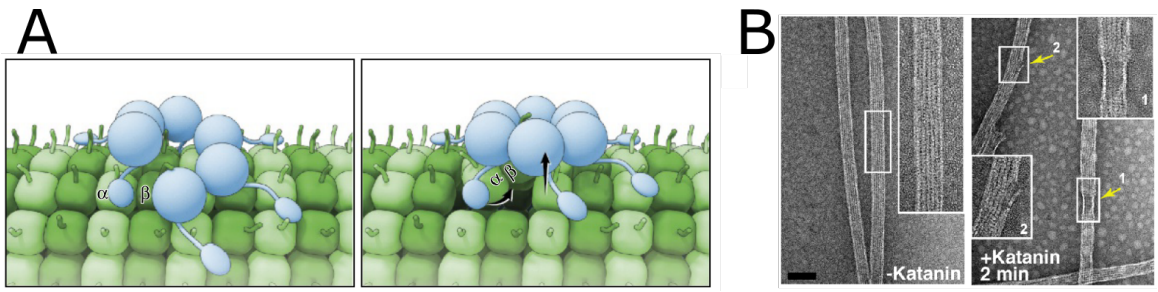

Figure 1.6: **Introduction to Katanin.** (A) Cartoon illustrating how the p60 subunit of Katanin is hypothesized to extract tubulin dimers. Left, Katanin p60 (blue) assembles as a hexamer with each monomer's N-terminal domain emanating from the motor core and making multivalent interactions with the microtubule (green). The flexible tubulin C-terminal is engaged in the axial pore of the p60 hexamer. Right, ATP hydrolysis leads to closure of the ring that drags with it the bound C-terminal tail of a tubulin monomer. The cycle is repeated until lattice contacts unravel and the microtubule severs. Adapted from Zehr et al. 2017. (B) GMPCPP-microtubules incubated with buffer or 100 nM Katanin and visualized by transmission electron microscopy. Arrows indicate damage in the microtubule lattice. Adapted from Grigorieff et al. 2018.

microtubule plus-end along protofilaments, propelled by its two motor domains connected by a neck linker which is essential for dimerization (Lin et al. 2020). As in the case of kinesin-1, these two motor domains proceed along a given protofilament in a hand-over-hand manner, where the motor domains alternately bind to the microtubule with each step being 8 nm long, the same as the inter-tubulin-dimer distance (Xie 2021). This directed movement is achieved via cycles of ADP release, ATP binding, and ATP hydrolysis in each of the motor domains (Xie 2021). However, while kinesin-1 typically detaches from microtubules after a few hundred steps, Kip3 is much more processive, to a point where it usually reaches the plus end of the microtubule (Varga et al. 2009). This processivity is attributed to the tail domain of Kip3, which can bind to microtubules (Su et al. 2011).

Due to the additional affinity for the microtubule caused by its tail domain, whenever the binding of its motor domains to the microtubule gets interrupted, Kip3 has a much higher chance to diffuse along the microtubule rather than away from the microtubule (Xie 2021). If there is no available binding site within reach, Kip3 pauses for extended periods of time (Varga et al. 2009), resulting in the formation of traffic jams at the end of microtubules (Leduc et al. 2012). Moreover, Kip3 has the conspicuous characteristics of being able to switch protofilaments with a leftwards bias (Bormuth et al. 2012), and promoting microtubule depolymerization at the microtubule plus end (Lin et al. 2020). The latter enables the cell to differentially regulate microtubule length via Kip3, as more Kip3 molecules land on longer microtubules, which therefore experience more Kip3 residence at their plus ends than short microtubules and thus a higher depolymerization activity (Varga et al. 2009). The above points are illustrated in Figure 1.7.

Finally, while kinesin-8 binding to the microtubule is centered on intradimer interfaces (Locke et al. 2017), the microtubule interaction sites of kinesin motor domains and the microtubule binding repeats of Tau partially overlap (Kellogg, N. M. A. Hejab, et al. 2018). Tau has been shown to regulate the microtubule interactions of the molecular motors kinesin-1 and dynein (Ebneth et al. 1998; Trinczek et al. 1999; Seitz et al. 2002; Vershinin et al. 2007;

Dixit et al. 2008; Chaudhary et al. 2018). However, before our study, it was unknown how Tau might interact with kinesin-8. Our knowledge about kinesin-8 in neurons generally is scarce. It certainly does play an important role: A study has found that depleting Kif18A, a kinesin-8 member, increases mirotubule catastrophe frequency and reduce axon length (Kevenaar et al. 2016).

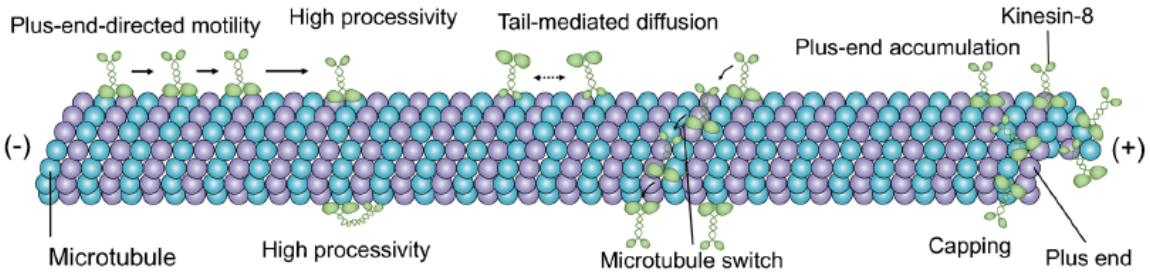

Figure 1.7: **Introduction to Kinesin-8/Kip3.** An illustration of the typical characteristics of members of the Kinesin-8 family, including Kip3. Adapted from Lin et al. 2020.

1.2.2 The mitotic spindle

The fission yeast Schizosaccharomyces pombe (S. pombe) is a popular eukaryotic model organism for studying the cell cycle including the mitotic spindle (Uzsoy et al. 2021; Vyas et al. 2021), in part due to its relatively low complexity, as evidenced by its small number of protein-coding genes (Wood et al. 2002). Other than in animal cells, where the mitotic spindle is established in the cytoplasm, the mitotic spindle of S. pombe forms inside the nucleus (Kilmartin 2014). As in animals cells, the mitotic spindle allows the cell to separate its two chromosome sets (each containing the DNA for each forthcoming dauther cell) (Figure 1.8A).

1.2.2.1 Ase1

We were interested in the (potential) role of microtubule crosslinkers in building and maintaining the mitotic spindle, where we worked with the S. pombe protein Ase1. Ase1 is a conserved microtubule-bundling protein with orthologues e.g. in plants (MAP65) and mammals (PRC1). During mitosis, Ase1 proteins (or its orthologues in other organisms) are found preferentially at the spindle midzone (Figure 1.8B), and are involved in spindle integrity and regulation of spindle elongation (Löiodice 2005; Yamashita 2005; She et al. 2019). S. pombe Ase1 deletion mutants, although viable, exhibit interphase microtubules with reduced bundling and mitotic spindles that often fall apart as they elongate in anaphase (Löiodice 2005; Yamashita 2005).

Microtubule bundles crosslinked by Ase1 feature microtubules spaced 30nm apart from each other (Khmelinskii et al. 2009). Characteristically, the geometry of Ase1 favors antiparallel microtubule arrays, which results in increased Ase1/MAP65/PRC1 affinities for antiparallel microtubule overlaps and preferential antiparallel crosslinking activity (Janson et al. 2007; Gaillard et al. 2008; Bieling et al. 2010; Subramanian et al. 2010; Kellogg, Howes,

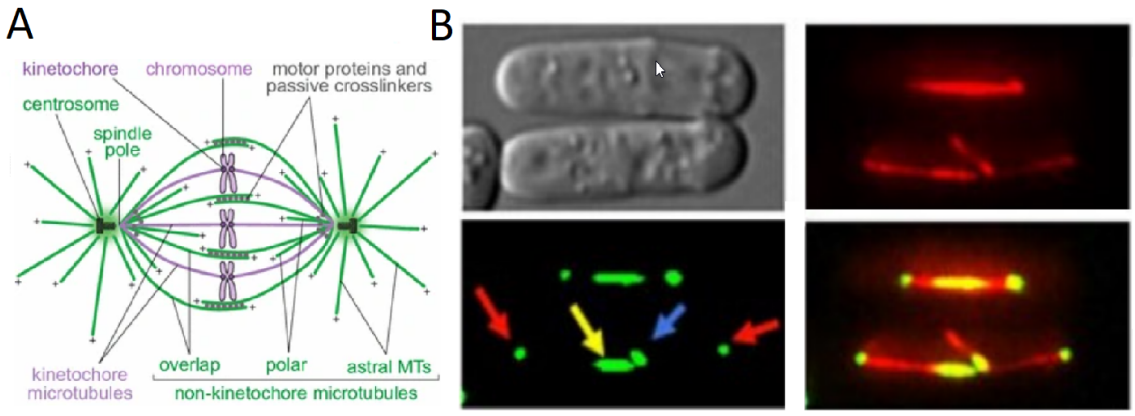

Figure 1.8: **Microtubule crosslinkers in the context of the mitotic spindle.** (A) An illustration of the mitotic spindle in animal cells (S. pombe features spindle pole bodies instead of centrosomes, and therefore no astral microtubules (Kilmartin 2014)). The polar microtubules grow from the centrosome, overlapping in an antiparallel fashion in the middle of the nucleus. There, they are crosslinked by passive crosslinkers such as Ase1, but also motor proteins which together with passive crosslinkers contribute to a proper positioning of the mitotic spindle (Janson et al. 2007; Braun, Lansky, et al. 2011). Adapted from Tolić 2018. The kinetochore microtubules separate the chromosomes from each other and pull them toward the centrosomes (in the next phase of mitosis not shown here). (B) 3D projection images of wild-type S. pombe cells taken during mitosis, with tubulin (CFP-tub1p) in red and Ase1 (Ase1-GFP) in green. Top-left picture taken with differential interference contrast (DIC) microscopy. Yellow arrow: The spindle midzone, where Ase1 is binding in between antiparallel microtubule overlaps. Blue and red arrows: Microtubule organizing centers where microtubules are nucleated (the red arrows indicating the centers located at the spindle poles). Adapted from Löiodice 2005.the SPBs (red arrows) and the eMTOCs (blue arrow) and with the spindle midzone (yellow arrow) during mitosis.

et al. 2016; She et al. 2019). The preferred binding of Ase1/MAP65/PRC1 family proteins to antiparallel microtubules leads to the recruitment of other proteins that can locally alter microtubule dynamics, such as CLASP (Bratman et al. 2007; Liu et al. 2009; Kitazawa et al. 2014) or kinesin-4 (Bieling et al. 2010; Mani et al. 2021). By recruiting these additional factors, Ase1 family proteins can differentially regulate the dynamics of bundled microtubules, specifically affecting the dynamics of antiparallel bundles (Bratman et al. 2007; Bieling et al. 2010; Thomas et al. 2020; Mani et al. 2021). The recruitment of these additional factors moreover itself may often be tunable by posttranslational modification of Ase1, for instance, phosphorlyation of Ase1 has been shown to impact the recruitment of klp9p, a kinesin-6 motor (Fu et al. 2009).

Ase1 family members themselves are also known to have direct effects on microtubule dynamics. In vitro experiments have shown that MAP65-1, upon crosslinking microtubules, promotes rescues (Stoppin-Mellet et al. 2013). Based on the modeling of their observed overlap dynamics, Stoppin-Mellet et al. 2013 predicted MAP65-1 to have more effect on antiparallel microtubules compared to parallel ones. However, this prediction has not yet been directly experimentally validated.

Ase1 possesses a structured N-terminal domain, a central spectrin domain, and an intrinsically disordered C-terminal domain (Kapitein, Janson, et al. 2008; Kellogg, Howes, et al. 2016). Ase1 molecules self-associate into homodimers. The N-terminal domain supports this homodimerization and is necessary for microtubule crosslinking activity (Janson et al.

2007). The spectrin domain and the unstructured C-terminal interact with the microtubule, both of which feature positively-charged residues positioned to interact with the negatively-charged microtubule surface (Kellogg, Howes, et al. 2016). While the spectrin domain binds to a single tubulin dimer (at the intradimer interface), the C-terminal region is positioned such that it can interact with the laterally adjacent tubulin dimer (a dimer from a neighbouring protofilament) (Kellogg, Howes, et al. 2016). The C-terminal region also has been reported to recruit the microtubule-rescue factor CLASP to the microtubule Bratman et al. 2007. The C-terminal region directly adjacent to the spectrin domain furthermore have been found to be crucial for localization of Ase1 to the nucleus (Thomas et al. 2020).

Ase1 interacts with microtubules diffusively by exhibiting a one-dimensional random walk along the microtubule lattice. It does so in a "leaping" fashion, where each leap closely matches the tubulin-dimer periodicity, with an approximately twofold higher probability of Ase1 stepping along a given protofilament rather than stepping laterally to an adjacent tubulin dimer of the neighbouring protofilament (Bujak et al. 2021). When diffusing on a single microtubule, the free microtubule-binding domain samples a large space, allowing for "catching" of another microtubule which subsequently is crosslinked to the first microtubule, preferably in antiparallel fashion (Janson et al. 2007, Figure 1.9). Within the resulting antiparallel microtubule bundle, Ase1 does still diffuse, albeit with an approximately eight-times lower diffusion coefficient than on single microtubules (Lansky et al. 2015). Notably, because Ase1 molecules have a higher affinity for antiparallel overlaps, microtubules which are not yet fully overlapping with each other experience an expansive force directed at increasing the overlap region. This is because the confinement of the Ase1 molecules within the overlap is comparable to the confinement of gas particles within a piston, and thus gives rise to an entropic force (Lansky et al. 2015).

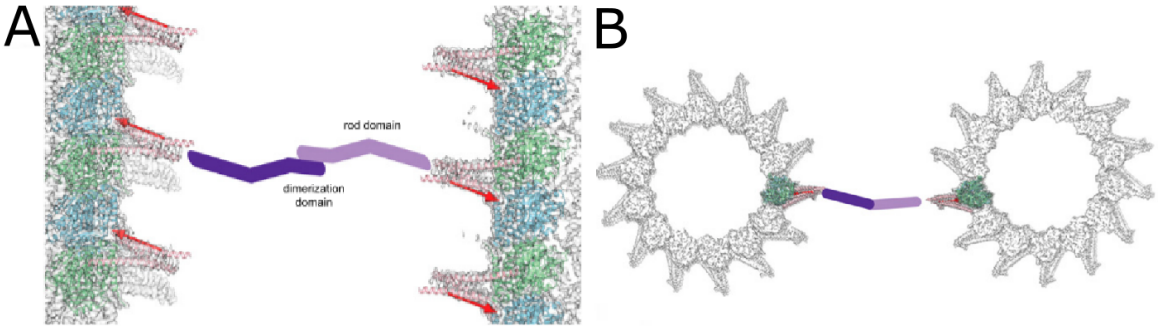

Figure 1.9: **Introduction to Ase1.** A model of how PRC1, a Ase1 homologue, binds to two antiparallely aligned microtubules, based on cryo-EM data. The cryo-EM reconstruction is overlayed with shades of green and blue (α and β-tubulin) and pink (the spectrin domain, the microtubule-binding domain of PRC1 and Ase1). The dimerization domains of PRC1 are shown as cartoons in shades of purple (the cryo-EM study was conducted with a PRC1 construct without the dimerization domain). Adopted from Kellogg, Howes, et al. 2016. (A) View from side. (B) Cross section view (from bottom of what panel A shows).

Aim

The aim of this thesis and the work underlying it is to further our understanding of the ways in which cytoskeletal polymers, in particular microtubules and microtubule-associated proteins (MAPs) interact to give rise to emergent phenomena. To achieve this, we sought to reconstitute microtubule-based cytoskeletal systems *in vitro* (i.e., outside of biological cells) with a minimal variety of components. This approach can help elucidate which components are needed at a minimum for a given phenomenon to emerge. Moreover, given the low number of confounding factors in such relatively simple assays, it often is possible to gain insights into biophysical mechanisms underlying a given observation.

We focused on two different MAPs, aiming to elucidate and potentially recreate phenomena which others had previously observed in the case of *in vivo* cytoskeletal systems in which these MAPs are prominently featured. In both cases, we have a strong focus on the distribution of these MAPs on microtubules and the effects of this distribution, aiming to contribute to our understanding of how these MAPs may interact with their environment to help spatially organize microtubules within cells. Importantly however, these two MAPs, namely Ase1 and Tau (see subsubsection 1.1.2.4), are found in distinct cellular contexts. While Ase1 and its orthologues are primarily involved in mitotic spindle dynamics and cytokinesis, Tau is predominantly functioning in the stabilization of axonal microtubules in neurons. Given that they operate under different cellular environments, we have studied these MAPs separately. This separation also reflects the structure of the research publications that form the basis of this thesis, one of which focusing on Tau, the other on Ase1 (see chapter 3). To facilitate a clear presentation of the findings presented in these two publications, I have structured the results and the discussion of this thesis accordingly, i.e., these sections each feature two separate subsections.

Publications related to this thesis

Two publications are related to this thesis, according to which the results part of this thesis is structured. Unless indicated otherwise, all figure panels have been reproduced from the respective publications.

3.1 Publication 1: Kinetically distinct phases of Tau on microtubules regulate kinesin motors and severing enzymes

In this publication in Nature Cell Biology (Siahaan, Krattenmacher, et al. 2019) (Appendix A), we share our discovery that there exist two distinct modes of Tau-microtubule interaction which result in distinct phases of Tau on microtubules. We furthermore show that these phases differ in their interaction with microtubule-associated motor proteins and the microtubule severing enzyme Katanin. This research thus has contributed to our understanding of how Tau may perform its manifold different regulatory functions (see subsubsection 1.2.1.1; Morris et al. 2011 in particular have emphasized the astonishing versatility of Tau).

As mentioned in the declaration at the beginning of this thesis, many of the Tau-related experiments were performed by Valerie Siahaan (a member of the Laboratory of Structural Proteins), with whom I shared first-authorship: Valerie conducted the experiments related to Tau only and experiments with Katanin, while I analyzed the data which Valerie had generated from these experiments. In the case of the experiments with Kinesin-8, experiments were both conducted and analyzed by me.

In this thesis, the results of this work, as well as some additional Tau-related data which Valerie had generated and I had analyzed and which was not presented in the mentioned publication or any other (shown in Figure 5.6), are presented in section 5.1.

3.2 Publication 2: Ase1 selectively increases the lifetime of antiparallel microtubule overlaps

With this publication in Current Biology (Krattenmacher et al. 2024) (Appendix B), we add to our understanding of how Ase1 and potentially other diffusive microtubule crosslinkers

affect microtubule dynamic instability (see subsubsection 1.1.2.3). In particular, our research shows that Ase1, without the help of any other MAP, can, at least *in vitro*, give rise to long-lasting antiparallel microtubule overlaps, which are structurally critical features of mitotic spindles. Notably, earlier in-vitro experiments had already shown that MAP65-1 (a Ase1 analogue in plants), when bundling microtubules, promotes microtubule rescues (Stoppin-Mellet et al. 2013). However, it was still unclear whether, and in how far, microtubules bundled in parallel fashion are affected differently than microtubules bundled in antiparallel fashion (subsubsection 1.2.2.1), a question which our publication provides answers for. We also observed Ase1 to directly have an impact on the depolymerization of single microtubules by reducing the speed of depolymerization of microtubules. Via mathematical modeling, we in our article show that this effect may well be related to another phenomenon we report, namely the herding of Ase1 by depolymerizing microtubule ends.

As mentioned in the declaration at the beginning of this thesis, most of the experimental work and data analysis related to this publication was done by me. The major exception to this is the experimental work done by Alexandre Beber, who for the revision of the manuscript had performed the experiments where 10nM Ase1 was present in solution, and 2 of each of the experiments where 42 and 420 nM Ase1 were in solution (the majority of experiments at 42 and 420nM were performed by me). As a more minor point, it is also worth noting that our collaborator Manuel Lera Ramirez provided an intial algorithm for fitting Ase1 densities at the ends of depolymerizing microtubules (which I then adjusted). Also, again as noted in the declaration, Manuel did most of the modeling-related work. To be more accurate, my contribution was, building on Manuel's single protofilament model, the ideation and implementation of the multi-protofilament model.

In this thesis, the results of this work are presented in section 5.2.

Methods

4.1 Microtubule preparation

4.1.1 Tubulin preparation

Tubulin was extracted from pig brains and labeled following previously described methods (Castoldi et al. 2003). Fresh pig brains were cleaned and homogenized in a blender using an ice-cold depolymerization buffer, then centrifuged at 29,000 x g for 60 minutes at 4 ºC. The supernatant was then mixed with an equal volume of high-molarity PIPES, supplemented with 1.5 mM ATP and 0.5 mM GTP, and warmed glycerol at 37 ºC to induce microtubule polymerization. This mixture was incubated for 60 minutes at 37 ºC, followed by centrifugation at 150,000 x g for 30 minutes at 37 ºC. The resulting microtubule pellet was depolymerized by resuspension in ice-cold depolymerization buffer, dounced on ice for 10 minutes, and then incubated for an additional 60 minutes on ice before centrifuging at 70,000 x g for 30 minutes at 4 ºC. Subsequently, the supernatant containing depolymerized tubulin was diluted with equal volumes of prewarmed high-molarity PIPES and glycerol, supplemented with 1.5 mM ATP and 0.5 mM GTP, incubated at 37 ºC for 30 minutes to promote microtubule polymerization, and centrifuged again at 150,000 x g for 30 minutes at 37 ºC. Finally, the microtubule pellet was depolymerized by resuspension in ice-cold BRB80 and dounced on ice for 10 minutes. After an additional 10-minute incubation on ice, the solution was centrifuged at 100,000 x g for 30 minutes at 4 ºC (SW 41Ti rotor). Tubulin was aliquoted, flash-frozen in liquid nitrogen, and stored at -80 ºC for later use. Some tubulin was aliquoted at high concentrations for subsequent labeling (performed by a laboratory assistant), as described by A. Hyman et al. 1991. Briefly, tubulin labeling involved polymerizing microtubules, incubating them with fluorescent dye, and then depolymerizing the microtubules to obtain labeled tubulin.

4.1.2 Microtubule polymerization

For preparation of biotinylated microtubules, isolated tubulin was mixed with biotinylated tubulin (Cytoskeleton Inc., T333P) at 50:1 mass ratio. For preparation of labeled microtubules, isolated tubulin was mixed with labeled tubulin. We employed two microtubule

stabilization techniques (subsubsection 1.1.3.1): i) Polymerizing microtubules under the presence of GMPCPP. ii) Stabilization of microtubules by having paclitaxel present in the buffer (Schiff et al. 1979). GMPCPP-stabilized microtubules were grown using a mixture of 2 μM tubulin, 1 mM GMPCPP and 4 mM $MgCl_2$ in BRB80 and incubated for 3 hours at 37°C. Paclitaxel-stabilized microtubules were polymerized using a mixture of 1 mM GTP, 4 mM $MgCl_2$ and 5 % DMSO in BRB80 for 30 minutes and subsequently stabilized by diluting the mixture in BRB80 + 10 µM paclitaxel. In both the GMPCPP and the paclitaxel procedure, the resulting mixture was then spun at 12000 g in a tabletop centrifuge. Finally, the supernatant was discarded, and the pellet was resuspended in 50 μl BRB80, respectively BRB80 + 10 µM paclitaxel. The paclitaxel-stabilized microtubules were not used for assays with dynamic microtubules, as the paclitaxel would cause uninterrupted growth and inhibit catastrophes.

4.2 Sample Preparation

To conduct our microscopy, we implemented a procedure which has already been described earlier (Gell et al. 2010). We manufactured microfluidic channels as depicted in Figure 4.1A and after some further preparation steps as described below mounted these channels on the microscope, e.g., for TIRF microscopy as shown in Figure 4.1B. The coverslips used in the process, after a cleaning procedure, were functionalized with dichlorodimethylsilane (DDS) to allow for antibody binding to the surface.

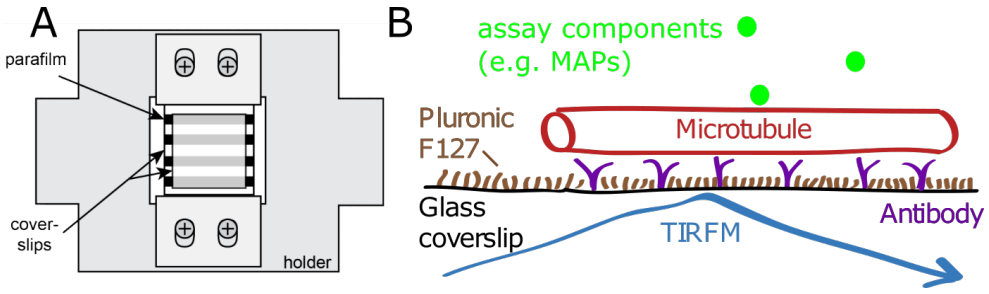

Figure 4.1: (A) A sketch of the flow cell layout and handling. The four depicted Parafilm stripes were put as spacers in between two DDS-coated glass slides to form three channels. To seal the channels, this construct was then heated up for about 30 seconds while gently pressing the upper slide onto the lower. Next, it was clamped into a brass sample holder. To fill the initially dry channels with liquid, vacuum was employed. Further perfusion steps were conducted by simply utilizing a filter paper as is illustrated. Adapted from Gell et al. 2010. (B) Schematic of our our experimental setup. The labeling of our microtubules and the included assay components varied from experiment to experiment. Adapted from Siahaan, Krattenmacher, et al. 2019.

After manufacturing, flow channels were incubated with antibodies in PBS for 1 to 5 minutes (to immobilize biotinylated microtubules, we used anti-biotin antibodies, to immobilize microtubules without biotin, we used anti-β-tubulin antibodies), followed by incubation for at least 30 min with 1% pluronic F-127 in PBS to prevent unspecific protein binding. The flow channel was then washed with BRB80 prior to addition of microtubules for antibodyspecific binding ("template microtubules"). Unbound microtubules were then removed in another wash step.

After these preparatory steps (and in some cases additional steps, see below sections), the assay buffer was added, the flow chambers were sealed in the case of longer experiments to prevent changes in concentrations due to evaporation, and the coverslip holder was mounted onto the microscope stage (setup shown in Figure 4.1).

4.3 Imaging

Atto647-labeled microtubules, mCherry- and mEGFP-labeled proteins were visualized sequentially by switching between the Cy5, TRITC and GFP channels (Chroma filter-cubes) using Nikon-Ti E microscope equipped with 100x Nikon TIRF objective and either Hamamatsu Orca Flash 4.0 sCMOS or Andor iXon EMCCD cameras. In the case of Tau experiments, the acquisition rate varied between 1 frame per 30 ms to 1 frame per 30 seconds depending on the particular experiment and is indicated in the corresponding figure. In the case of one set of Ase1 experiments (Set A, see subsection 4.7.2), the GFP channel was visualized or the IRM channel (or both with sequential switching), at a framerate of 5s. For the other set of Ase1 experiments (Set B), channels were sequentially switched at a framerate of 2.6 seconds (with a 633x Zeiss oil immersion TIRF objective in combination with a Andor iXon DV 897 (Andor Technology) EMCCD camera). Imaging conditions in experiments used for quantitative estimation of kinetic parameters were set such that photo-bleaching effects were negligible (< 2 % fluorescent intensity loss during the experiment). Finally, for Ase1 Set A experiments, the Alexa647-labeled microtubule seeds were imaged before the start of the time lapse, and only the Ase1-mNeonGreen channel was imaged during the time lapse. For Set B experiments, the rhodamine (tubulin) and the GFP (Ase1-GFP) channel where imaged sequentially, whereas every 40th frame the Alexa647 channel was imaged in place of the GFP channel, in order to track the location of the GMPCPP-stabilized seeds (which we with this data determined to not move significantly during experiment time).

4.4 Image analysis

Data was analyzed using FIJI (Schindelin et al. 2012) and custom written Matlab (Mathworks) routines.

4.4.1 Density estimation

Kymographs (KymographBuilder plugin, custom-modified to compute integrated intensity instead of finding the maximum intensity, see Zenodo: doi.org/10.5281/zenodo.3270572) along the microtubule length were used to read out the fluorescent signal and to estimate the integrated signal intensity of fluorescent proteins bound to the microtubule (if necessary, time series were drift-corrected with FIESTA (Ruhnow et al. 2011)). The recorded signal in regions directly adjacent to the microtubule was subtracted as background signal. Kymograph pixels were then manually categorized according to the type of microtubule region they covered

(island, curved microtubule, regions surrounding the islands in case of Tau, overlapping microtubules or single microtubules in the case of Ase1). The integrated intensity averaged along the microtubule length for each region type was then computed by taking the mean of the categorized kymograph pixels (in the case the Ase1 assays, only regions with dynamic extensions present were measured). The density of labeled MAPs bound to the microtubule was then estimated by dividing the averaged integrated intensity by estimated intensity per single molecule times unit length. Conversion to the number of MAP molecules per tubulin dimer was performed assuming 13 available protofilaments and 8 nm length of a tubulin dimer.

4.4.2 Diffusion coefficient estimation

Single Tau molecule tracking for the estimation of diffusion coefficients was performed using FIESTA (Ruhnow et al. 2011) software. For reconnecting tracks, a threshold velocity of 12000 nm/s had been chosen, and tracks were allowed to have at most 3 missing frames between two data points. To minimize false-positive connecting of separate molecules, the tracks obtained by FIESTA were cut into pieces such that the maximum distance between two data points was never above 360 nm.

4.4.3 Fluorescent signal of a single fluorescent molecule

In our assays, we often were interested in the absolute number of labeled proteins bound to microtubules. To estimate this number, it was necessary to know the contribution of single fluorophores to the measured signal. The fluorescent signal of a single fluorescent molecule was determined by generating intensity time-traces of single fluorophore-labeled kinesin-1 molecules tightly bound to the microtubule in presence of AMP-PNP (in the absence of ATP) and estimating the height of the occurring bleaching steps. The number of steps was first estimated by eye, and this number was used as input for the *findchangepoints* function of Matlab to determine the position of the steps (see Figure 4.2). To yield the intensity per single molecule, the heights of these steps were averaged (and in the case of Ase1, multiplied by two, given that Ase1 forms homodimers).

4.5 Data representation

In all boxplots presented in the figures, horizontal midline indicates the median; bottom and top box edges indicate the 25th and 75th percentiles, respectively; the whiskers extend to the most extreme data points not considered as outliers (the function Alternative box plot from the IoSR Matlab Toolbox has been used); the numbers indicate the sample size; the notches are centered on the median and extend to ±1.58*IQR/sqrt(sample size). Where single, colored data points are presented, points from the same experiment are indicated by the same color (unless otherwise stated).

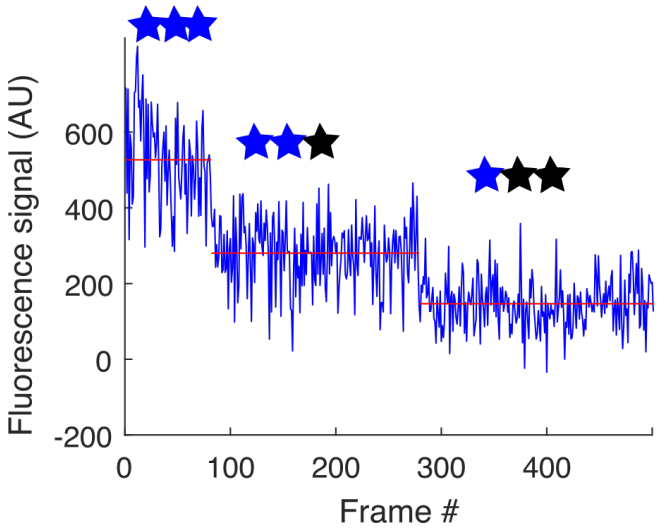

Figure 4.2: **An illustration explaining our estimation of the fluorescent signal of a single fluorophore.** The signal recorded on a particular spot on a microtubule decorated with immobilized fluorophore-labeled kinesin-1 molecules. The signal shows a step-wise decay due to photobleaching of the fluorophores. The bleaching steps were detected detection of significant changes of the mean values.

4.6 Procedures specific to Tau experiments

4.6.1 Protein expression and purification

mEGFP or mCherry tagged Tau and TauΔN, Kinesin-1, Kip3 and Katanin (M. musculus Katanin p60/p80C, Jiang et al. 2017) were expressed and purified as described previously (Nitzsche et al. 2010; Hernández-Vega, Braun, Scharrel, Jahnel, Wegmann, Bradley T Hyman, et al. 2017a; Herrmann et al. 2018; Mitra et al. 2018). In particular, all Tau variants (Figure 4.3) were purified from insect cells using the baculovirus expression system. Recombinant baculovirus for each construct was produced as described by Woodruff et al. 2015. Sf9 insect cells in log phase (1 million cells/ml, Expression system) were infected with 5 ml of P2 baculovirus stock, incubated at 27°C with moderate shaking, and harvested 72 hours post-infection. The cells were collected by centrifugation at 700g for 8 minutes and then resuspended in resuspension buffer [25 mM HEPES, 150 mM KCl, 20 mM imidazole (pH 7.4) with 1 mM DTT, 1 mM PMSF (Sigma), and 1x Protease Inhibitors Cocktail (Calbiochem, Type III)]. Cell lysis was performed using an Emulsiflex (Emulsiflex-C5, Avestin). The lysate was centrifuged at 35,000 rpm for 45 minutes, and the supernatant was collected. The supernatant was filtered through a 0.45 µm filter and incubated with Ni-NTA agarose resin (QIAGEN) HiTrap for 1 hour. The beads were collected and washed using disposable gravity columns (20 mL, Biorad). The columns were washed four times with 20 ml of wash buffer (25 mM HEPES, 150 mM KCl, 30 mM imidazole, 1 mM DTT, pH 7.4) and eluted with an elution buffer (same buffer containing 250 mM imidazole). The 6xHis tag was removed by treatment with PreScission protease (3C HRV protease, 1:100, 1 µg enzyme/100 µg of protein) overnight at 4°C. Imidazole was removed by dialysis (slide-a-lyzer with a 20 KDa cut-off) overnight at 4°C, with His tag cleavage occurring simultaneously with dialysis.

The protein was further purified by size-exclusion chromatography using a HiLoad 16/60 Superdex 200 column with an ÄKTA Pure Chromatography system (GE Healthcare) in 25 mM HEPES, 150 mM KCl, 1 mM DTT (pH 7.4). Collected peak fractions were concentrated to 100 µM or 200 µM using Amicon Ultra 30K (Millipore). Protein concentration was measured using a NanoDrop ND-1000 spectrophotometer (Thermo Scientific) at 280 nm absorbance. Proteins were flash-frozen in liquid nitrogen and stored at -80°C. All steps in the purification were performed at 4°C.

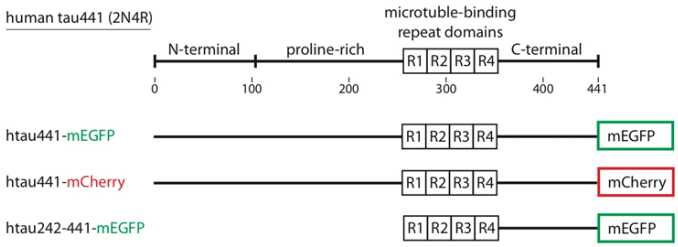

Figure 4.3: **Schematics showing the Tau constructs used in this study.**

4.6.2 In vitro Tau-microtubule binding assay

Biotinylated, paclitaxel-stabilized, Atto647-labeled microtubules in BRB80T (80 mM Pipes pH 6.9 adjusted with KOH, 1 mM MgCl2, 1 mM EGTA, 10 µM paclitaxel) were immobilized in a flow chamber using biotin antibodies (section 4.2). Subsequently, assay buffer was flushed into the flow cell (20 mM HEPES pH 7.2, 1 mM EGTA, 75 mM KCl (unless stated otherwise in the main text), 2 mM MgCl2, 1 mM ATP (+Mg), 10 mM dithiothreitol, 0.02 mg/ml casein, 10 µM paclitaxel, 20 mM d-glucose, 0.22 mg/ml glucose oxidase and 20 µg/ml catalase). Then, Tau in assay buffer was flushed in at the final assay concentration stated in the main text. In experiments involving multiple successive Tau additions, the flow cell was rinsed between each Tau addition with a high ionic strength buffer (200 mM KCl in addition to the assay buffer). To remove Tau from the solution, the chamber was perfused with approximately four times the chamber volume using assay buffer without Tau. For high Tau concentrations (>200 nM), larger volumes (up to ten times the chamber volume) were used to ensure complete removal of Tau. In experiments with kinesin-8, Katanin, or kinesin-1, islands were preformed before introducing the respective protein into the solution, while maintaining a constant Tau concentration. In the Katanin experiment with elevated Tau concentration (see Figure 5.7), microtubules were first incubated with 0.8 µM Tau-mCherry for 5 minutes. Tau-mCherry was then temporarily removed from the measurement chamber for less than 1 minute to identify the position of the islands, which were obscured by the high Tau-mCherry density in the surrounding areas. Tau-mCherry was then reintroduced at 0.8 µM, and after 5 minutes, 215 nM Katanin-GFP was added to the solution, while maintaining the Tau concentration at 0.8 µM. All experiments were conducted at room temperature.

4.6.3 Coverage by Tau islands

The proportion of microtubule length occupied by Tau islands was determined by representing both islands and microtubules as segmented lines, measuring their respective lengths, and then calculating the ratio of the total island length on a given microtubule (or within a field of view) to the length of that microtubule (or the combined length of all microtubules in the field of view).

4.6.4 Estimation of velocities

The rates of assembly and disassembly of island boundaries (in the absence or presence of Katanin or Kip3) were determined by fitting straight lines to the advancing or retreating edges of Tau islands in kymographs. The velocity provided in the text represents a duration-weighted average of these segments. To convert this velocity to the number of Tau molecules per second, it was multiplied by the estimated density of Tau within the islands (in molecules per nanometer), assuming Tau binds to 13 protofilaments with a tubulin dimer length of 8 nm. The velocities of Kip3 and kinesin-1 were determined by fitting straight lines to the kymographs of the moving motors, both inside and outside the islands.

4.6.5 Estimation of the Tau unbinding time

To determine the unbinding times of Tau inside and outside the islands, the decay in Tau density over time was analyzed after a buffer exchange either removing Tau from the solution or replacing Tau-mEGFP with Tau-mCherry. Each analyzed region (island or surrounding area) provided a time trace of Tau density decay following the buffer exchange. Time traces from representative experiments were combined, as shown in Figure 5.2E,F, with the thick line representing the median of all traces at each time point and the bounds showing the first and third quartiles. To estimate the mean residence times of Tau inside and outside the islands, individual density time traces were fitted with an exponential decay using the Matlab function fit, excluding data points before the solution exchange. The fits and mean residence times presented were calculated by averaging the coefficients from the individual fits.

4.6.6 Katanin severing rate estimation

Severing rates in regions surrounding the islands were determined by fitting an exponential decay to the number of pixels corresponding to the original microtubule position that exceeded a manually set threshold, which encompassed the microtubule. In island regions, the severing events were counted. In Figure 5.7B, the estimated severing rates include both straight and curved microtubules. In Figure 5.9H, the severing rates are categorized based on the following criteria: straight microtubules were defined as stretches where the orientation did not change by more than 10 degrees, while curved regions were defined as 0.5 µm long stretches centered at the point of greatest curvature with a radius of less than 2.5 µm.

4.7 Procedures specific to Ase1 experiments

4.7.1 Protein expression and purification

Ase1-GFP (Janson et al. 2007) and Ase1-mNeonGreen were expressed in E. coli strain BL21 (DE3) (Altium International). After harvesting the cells, the cell pellet was resuspended in 5 mL ice-cold phosphate buffered saline (PBS) and stored at -80°C for further use. For cell lysis, the cells were homogenized in 30 mL of ice-cold His-Trap buffer (50 mM Na-phosphate buffer, pH 7.5, 5% glycerol, 300 mM KCl, 1 mM MgCl2, 0.1% Tween 20, 10 mM BME, 0.1 mM ATP) supplemented with 30 mM imidazole, Protease Inhibitor Cocktail (cOmplete, EDTA free, Roche), and benzonase (Novagen) at a final concentration of 25 units/mL. The mixture was then sonicated and subsequently centrifuged at 45,000 x g for 60 minutes at 4°C using an Avanti J-26S ultracentrifuge (JA-30.50Ti rotor, Beckman Coulter). The clarified cell lysate was incubated with Ni-NTA resin (HisPur Ni-NTA Superflow Agarose, Thermo Scientific) pre-equilibrated with lysis buffer for 2 hours at 4°C. The resin was then sequentially washed with wash buffer I (His-Trap buffer with 60 mM imidazole) and wash buffer II (His-Trap buffer with 60 mM imidazole and 700 mM NaCl). Ase1-GFP was eluted using His-Trap buffer supplemented with 300 mM imidazole. For Ase1-mNeonGreen, after the second wash with buffer II, the resin was further washed with wash buffer I containing 3C PreScission protease (Merck Millipore), which cleaved Ase1-mNeonGreen from the column at the 3C protease cleavage site between mNeonGreen and the 6xHis-tag (the Ase1-mNeonGreen construct had been created by Lenka Grycova). The mixture was incubated overnight at 4°C. The following day, the beads were removed, and the cleaved protein was collected. Both Ase1-GFP and Ase1-mNeonGreen were concentrated by centrifugation at 3500 RPM at 4°C using a 100 kDa centrifugal filter tube (Amicon Ultra-15, Merck). Ase1-mNeonGreen underwent a second purification step through size exclusion chromatography using a Superdex 200 10/300 column. The size exclusion buffer consisted of 100 mM Tris, 150 mM NaCl, 1 mM MgCl2, 1 mM DTT, 0.05% Tween, 0.1 mM ATP, and 10% glycerol. Fractions containing the protein were collected and concentrated. The final protein concentrations were measured with a NanoDrop ND-1000 spectrophotometer (Thermo Scientific) at absorbances of 280 and 506 nm. The protein was flash-frozen in liquid nitrogen and stored at -80°C. All purification steps were performed at 4°C.

4.7.2 In vitro Ase1-microtubule binding assay

Biotinylated, GMPCPP-stabilized, fluorescence-labeled microtubules in BRB80 (80 mM Pipes/KOH pH 6.9, 1 mM MgCl2, 1 mM EGTA) were flushed into the prepared channels, were given time to bind to biotin antibodies, and were removed from solution, as described in section 4.2. In the case of Ase1 Set B experiments, additional preparatory steps occured: First, a buffered solution with a low concentration of Ase1 was flushed in, Ase1 was allowed to sparsely bind to the template microtubules, removed from solution, and subsequently non-biotinylated GMPCPP-stabilized microtubules were flushed into the flow cell which

got crosslinked to the template microtubules by the Ase1 on these microtubules. These microtubules were labelled with both rhodamine and Alexa647 (represented in sketches in dark blue), while the templates in these assays were only very weakly labelled with Alexa646 (represented in sketches in light blue). Then, the "transport" microtubules were removed from solution so that only transports which formed overlaps with templates would remain in the channel.

The buffer in the flow cell was then exchanged for assay buffer. Finally, Ase1 in assay buffer was flushed into the flow cell at the final assay concentration stated in the main text, together with tubulin, and the channels were sealed. Set A experiments (shown in Figures 5.10, 5.11, 5.12A-E, 5.13 and 5.15) were performed at room temperature and with 32μM unlabeled tubulin present in solution. Set B experiments (shown in Figures 5.14, 5.16, 5.17C,D and 5.21) were performed at 29°C and with 14μM tubulin, 7% of which was labeled with rhodamine. The following buffer components common to all used buffers in experiments involving Ase1: 20mM PIPES pH 6.9, 10mM HEPES pH 7.2, 0.5mM EGTA, 1mM MgCl2, 0.5mM Mg-ATP, 0.67mM GTP, 0.67% Tween20, 6.7mM DTT, 0.3 mg/ml Casein, 13.5mM D-Glucose, 0.3mg/ml glucose oxidase and 0.03mg/ml catalase. The buffer for Set A experiments, in addition to these components, contained 70mM KCl, and 0.1% Methylcellulose, 0.1% Glycerol, 1mM sodium phosphate and 1µM ATP. The buffer for Figure Set B experiments, in addition to the components common to all buffers, contained 116mM KCl and 0.065% Methylcellulose. Experiments shown in Figures 5.12F and 5.17A,B were performed at the same experimental conditions as Set A experiments (with small differences dependent on the particular experiment as stated in the main text/figure captions).

4.7.3 Estimating Overlap Lifetime

The lifespan of microtubule overlap regions was determined for two distinct microtubule configurations: Antiparallel "midzones," where two dynamic extensions converged to form a dynamic midzone (as depicted in Figure 5.10 left panel), and parallel bundles composed of two dynamic extensions (as shown in Figure 5.10 right panel). In both cases, whether antiparallel midzones or parallel bundles, the lifetime was considered to begin when the dynamic (GDP) lattices of each participating microtubule were crosslinked (for antiparallel configurations, an additional condition was that both plus ends had to be within 3 microns of each other at the event's start) and ended when one of the microtubules depolymerized back to its GMPCPP-stabilized segment. For antiparallel bundles, the lifetime also concluded when the midzone was no longer present. If an overlap region persisted until the time-lapse movie concluded, the event was classified as censored. Figure 5.10A and Figure 5.12B were created using the Matlab function ecdf with the “survival” option enabled.

4.7.4 Adjustment for Ase1 Signal Measurement

To measure the equilibrium density of Ase1, the signal per unit length (S) detected on isolated microtubules was used to adjust for the reduced illumination intensity in the outer

regions of the field of view (when a region of interest (ROI) was located in those regions). Explicitly, $S_{\text{corrected}}(ROI)$ was computed by multiplying the original signal density $S(ROI)$ by $\frac{S(\text{isolated microtubule in center of field of view})}{S(\text{isolated microtubule near ROI})}$.

4.7.5 Determining Microtubule Dynamic Instability Parameters

The parameters of microtubule dynamics for Set A experiments were estimated by generating kymographs and fitting straight lines to track the position of microtubule plus ends over time and space (using the Ase1-mNeonGreen signal to visually track microtubule ends, as microtubules were not directly imaged). For Set B experiments, the FIESTA software was employed to pinpoint the locations of microtubules (Ruhnow et al. 2011). Both methods provided measurements of polymerization and depolymerization velocities. Rescues were identified as instances where a microtubule transitioned from depolymerization to polymerization before reaching the GMPCPP-stabilized seed, while catastrophes were noted when polymerization switched to depolymerization. The frequencies of rescues and catastrophes were calculated by dividing the number of rescues and catastrophes by the total distance depolymerized and polymerized by all plus ends, respectively. In the case of Set A experiments, we tested 10nM during the revision phase, a time when room temperatures were less stable. Consequently, microtubule velocities at all Ase1 concentrations differed from our initial experiments. To allow pooling these results with our initial data, we adjusted the velocities from these experiments by multiplying them by a factor calculated as follows: The mean polymerization and depolymerization velocity of isolated microtubules at 42nM from the initial experiments was divided by the mean respective velocity of isolated microtubules at 42nM from the revision-phase experiments (these mean velocities were weighted by the duration of each polymerization or depolymerization event). The resulting adjustment factors were 0.4 for polymerization and 0.39 for depolymerization.

4.7.6 Estimation of amount of Ase1 being swept

To estimate the number of swept Ase1 molecules for corresponding panels in Figure 5.16 (Set B experiments), we first obtained density traces for each frame during a microtubule depolymerization period. These traces were obtained by summing the pixel intensities perpendicular to the microtubule, i.e., by generating kymograph where each pixel represents such a sum (doi.org/10.5281/zenodo.3270572). For each frame f we analyzed the corresponding density trace D_f as follows. (1) We computed D_s by subtracting the density trace $D_{before\_catastrophe}$ of the microtubule before the catastrophe had occurred from D_f ($D_s = D_f - D_{before_catastrophe}$) (2) We obtained $x = 0 = X_{Dsmax}$, the location of the local maximum of D_s in vicinity of the microtubule plus end. (3) We obtained $X_{Dsright}$ by finding the first local minimum of D_s to the right of $X_{Dsright}$ (to reduce the effect of noise, we smoothed D_s for this computation). "Right" of D_s, in the here-chosen coordinate system, means toward the microtubule seed ($x > 0$). (4) $X_{Dsleft} = X_{Dsmax} -$ 471nm (471 nm = 3 pixels). (5) We computed D_A. D_A is equal to D_f to the left of X_{Dsmax}, and equal to

$D_s + Df(X_{Dsmax}) - D_s(X_{Dsmax})$ to the right of X_{Dsmax}. (6) We fitted a distribution Y_F (shape see below) plus an error function Y_E to D_A between XDsleft and $X_{Dsright}$. We required both Y_F and the error function to not have any x-offset: Y_F was a right-sided decaying exponential $exp^{-x/\sigma}$ ($Y_F = 0$ where $x < 0$, and with λ bounded between 1 and 1000 nm) convolved with a gaussian $exp^{-x2/2\sigma 2}$ (with σ bounded between 180 to 190 nm to account for the point spread function of our setup; this same σ had been used as input for Y_E). Instead of a blurred right-sided decaying exponential, we for some fits (shown in Figure 5.21) used a gaussian $exp^{-x2/2\sigma_G 2}$ for Y_F (with a σ_G between 180 nm and 450 nm, which was independent of the σ used for blurring Y_F). We also fixed $G + E$ (plus a constant value) to approach the minimum of D_A to the left of the end, and the average of D_A to the right of $X_{Dsright}$ (the average of D_A within 5 microns from $X_{Dsright}$, giving more weight to values close to $X_{Dsright}$). (6) We then summed the Ase1 density below Y_F (as discretized in x by the pixel size), which we took as a proxy for the number of swept Ase1-GFP molecules after dividing by the intensity per Ase1 dimer (obtained as described above).

4.7.7 Fluorescence recovery after photobleaching (FRAP)

Biotinylated GMPCPP-stabilized microtubules were immobilized on the coverslip. We then flushed in the same assay buffer as for Set A experiments, incubated until the Ase1 density on microtubules reached a steady-state, and subsequently bleached Ase1-mNeonGreen molecules and recorded the recovering Ase1-mNeonGreen signal. We fitted the resulting recovery curve to the expression $D_s - cexp(-bt)$, where D_s is the steady state density, and c and b are fitting parameters (see subsubsection 1.1.3.5). Results for fitting parameter b are shown in Figure S4D.

4.7.8 Mathematical modelling

The scripts to reproduce the modelling, and to plot experimental and theoretical results from Figure 5.18 and Figure 5.20 can be found in Zenodo: doi.org/10.5281/zenodo.12169420.

4.7.8.1 Assumptions

The model of Ase1 accumulation on depolymerizing microtubules, and its effect on depolymerization velocity (Figure 5.18A) is built on the following assumptions:

1. We neglect interactions between protofilaments and only consider a one-dimensional lattice, where lattice of size $a = 8$nm start at index $i = 1$ at the plus end, extending to $i = 400$.

2. Only bound Ase1 molecules are considered by recording the presence or absence (0 or 1) of Ase1 in each lattice site. Bound Ase1 molecules exchange with solution with two constant rates (k_{on}, k_{off}). Binding is only allowed if the lattice site is empty (Figure 5.18A). k_{off} was directly measured, and k_{on} was adjusted to match the Ase1 equilibrium density on microtubules (Table 5.1).

3. Ase1 particles on the lattice undergo unbiased diffusion characterized by a constant hopping rate (k_h). Hopping is only allowed to an empty site (Figure 5.18A). The rate k_h is calculated from the experimentally measured diffusion coefficient of Ase1 (Table 5.1), as $k_h = D/a^2$.

4. The Ase1 particle in the terminal site ($i = 1$), cannot hop past the microtubule end (red arrow on the left of Figure 5.18A), but can detach with rate k_{off}.

5. The terminal lattice site may dissociate from the microtubule, with rate k_d which depends on the presence of Ase1, according to each model:

   (a) In Model 1, it occurs with rate k_d^0 if the terminal lattice site is not occupied (Figure 5.18B, top), and with rate $(1 - \Omega)k_d^0$ if it is occupied (Figure 5.18B, bottom). Ω is a parameter between zero and one. If $\Omega = 0$, the presence of Ase1 has no effect, and if $\Omega = 1$, the first tubulin subunit cannot unbind if it is bound to Ase1.

   (b) In Model 2, the rate of tubulin subunits loss at the plus end is reduced by a factor $(1 - \Omega)$ if any of the N terminal sites is occupied. At steady state, this rate is $k_d = k_0^d[1 - \Omega(1 - \prod_{i=1}^{i=N}(1 - P_i))]$, where P_i is the probability of site i being occupied by Ase1.

   k_d^0 is derived from the depolymerization rate of microtubules in the absence of Ase1 (v_0), measured experimentally (Table 5.1), such that $k_d^0 = v_0/a$.

6. If the terminal lattice site dissociates when a molecule of Ase1 is bound to it, this Ase1 is lost as well (Figure 5.18B, bottom).

4.7.8.2 Simplification to a system of constant size

Since terminal subunits are more likely to be lost when they are without Ase1 than when they are with Ase1, any dissociation event increases the density of Ase1 remaining on the microtubule. This effect is only present at the microtubule end, and away from the end, the probability of a binding site being occupied is only determined by the binding and unbinding constants: $\alpha = k_{on}/(k_{on} + k_{off})$. Therefore, we can restrict the model to a section of the microtubule with L lattice sites, as long as the probability of finding a molecule at position L is close to α. When a depolymerisation event happens, we shift the lattice indexes such that site $i + 1$ becomes site i, and set $P_{i=L} = \alpha$.

4.7.8.3 Mean field theory

The system can be solved using a mean-field approximation, by just considering the ensemble of P_i, the average probability of a site i being occupied and neglecting higher-order correlations between neighbouring sites. We can then write a set of discrete differential equations to

represent the dynamics of the system:

$$\frac{dP_i}{dt} = (P_{i+1} + P_{i-1} - 2P_i)k_h + (1 - P_i)k_{on} - P_i k_{off} + (P_{i+1} - P_i)k_d \tag{4.1}$$

Specific equations apply at the boundaries $i = 1$ and L:

$$\frac{dP_1}{dt} = k_h(P_2 - P_1) - P_1 k_{off} + (1 - P_1)k_{on} + k_d P_2 - k_d^0 P_1(1 - \Omega) \tag{4.2}$$

$$dP_L/dt = 0 \tag{4.3}$$

The terms of the equation are associated with the rates of diffusion, binding, unbinding $(k_h, k_(on), k_{off})$ which are constant, and the depolymerization rate (k_d), which is affected by lattice occupancy in a different way in each model (see Assumptions).
For Model 1, $k_d = k_d^0(1 - \Omega P_1)$.
For Model 2, $k_d = k_d^0[1 - \Omega + \Omega \prod_{i=1}^{i=N}(1 - P_i)]$.
This dynamical system can be evolved from any initial conditions, converging to the unique steady-state solution for a set of given parameters. Assuming that the microtubule is at binding equilibrium when it starts depolymerizing, we initially set $P_i = \alpha$ for all sites. From those initial conditions, we integrate the equations numerically using Python's *odeint* function (see source code).

4.7.8.4 Modelling of overlaps

To model microtubule overlaps (Figure 5.18E,G), we assume that the Ase1 measured in the overlaps (see Image Analysis above) is evenly distributed among 3 protofilaments that are involved in crosslinking the microtubules. We neglect the other protofilaments. We had also modelled 2 protofilaments instead of 3, which did not fit the experimental data as well as 3 protofilaments.

4.7.9 Comparison of experimental data and model

To compare the predicted and observed timescale of Ase1 accumulation (τ) and Ase1 accumulation at steady state (A_{end}), the accumulated Ase1 as a function of time was fitted to $A_{end}(1 - exp^{-t/\tau})$ in experiments and model predictions (e.g., Figure 5.18F for isolated microtubules at 6nM of Ase1). In the model, the accumulation of Ase1 at any given timepoint is defined as $(\sum_{i=0}^{i=L} Pi) - \alpha L$. As a proxy of velocity of depolymerization at steady state, we used the average velocity of depolymerization observed after 20 seconds of depolymerization in experiments and compared it to the depolymerization velocity at the last simulated timepoint (Figure 5.18F). The 95% confidence intervals of these magnitudes were estimated using the bootstrap method. For each experimental condition with N depolymerization events, a thousand sets of N depolymerization events were drawn through sample with replacement. For each of those sets, τ and A_{end} were calculated by fitting all observations in the set, and the average velocity after 20 seconds was calculated. Then, the distribution of

each magnitude across all sets was used to calculate the 95% confidence intervals (see source code).

Results

5.1 Interactions of distinct phases of Tau with other MAPs

5.1.1 Tau has one diffusive and one cooperative microtubule binding mode

To study the interaction of Tau with microtubules, we immobilized Atto-647-labeled microtubules on a coverslip, added full-length Tau (fluorescently-labeled with the proteins mEGFP or mCherry) and performed time-lapse imaging using TIRF microscopy (Methods). Conspicuously, after the addition of 20 nM Tau, we observed a formation of high-density Tau islands, surrounded by regions with low Tau density (Figure 5.1A-C).

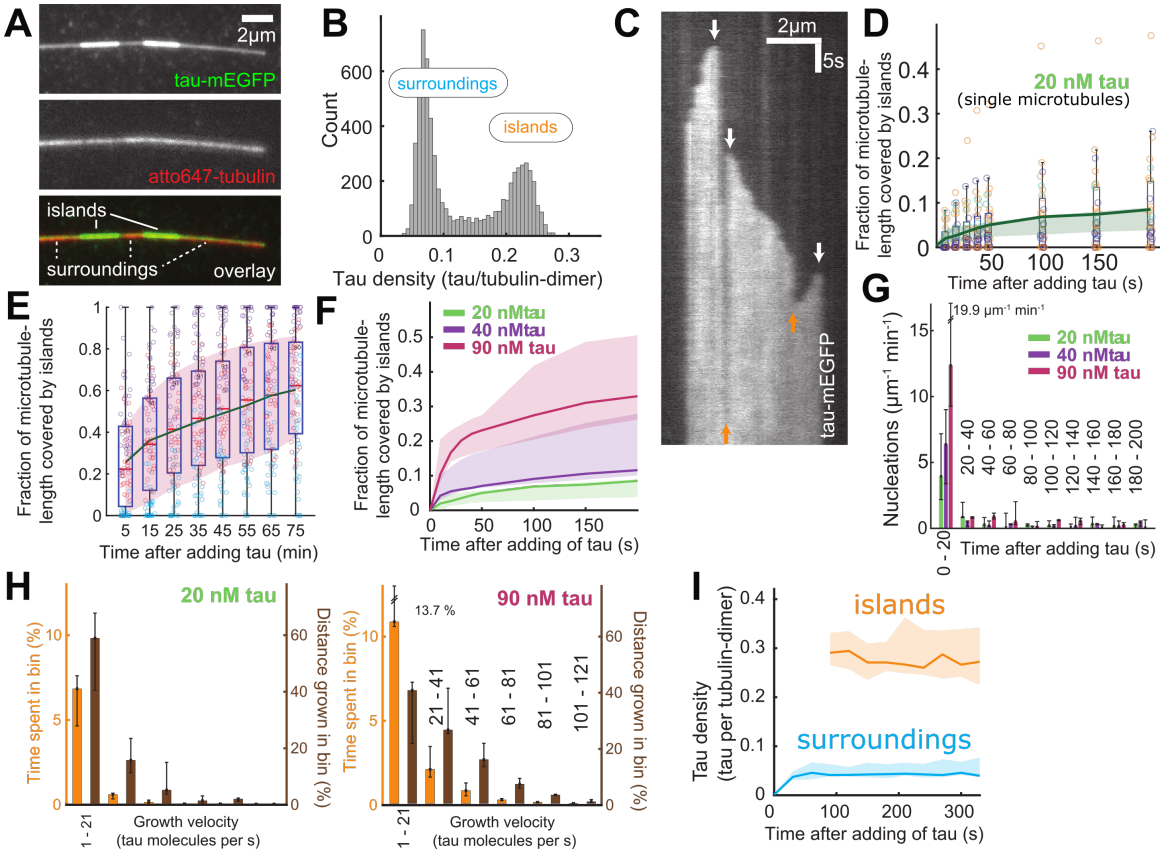

Figure 5.1: **Tau assembles into Tau islands on microtubules.** (A) Multichannel fluorescence micrograph showing areas of high-density Tau (bright green) surrounded by regions of low-density Tau (dim green) on an Atto-647-labeled microtubule (red). Images taken 5 minutes after adding 20 nM Tau. (B) Distribution of fluorescence intensity of Tau along the microtubules such as shown in A showing two distinct populations. (C) Kymograph showing the fluorescence signal of Tau on a microtubule after the addition 20 nM Tau. Initially the microtubule is covered by low Tau density. Over time, high-density regions ("islands") start to assemble. White arrows indicate the nucleation points; orange arrows indicate the merging of two neighboring islands growing towards each other. (D) Fraction of microtubule length covered by Tau islands at different concentrations after adding Tau at time = 0 (n = 3 experiments, shaded area is drawn between the experiment with least coverage and experiment with most coverage, line shows coverage in remaining experiment). Boxplots represent the coverage statistics of individual microtubules. (E) The same data representation as in D, only showing a longer time horizon on the x-axis. (F) Fraction of microtubule length covered by Tau islands over time under different Tau concentrations (3 experiments per condition). The green line is also shown in D. (G) Tau island nucleation frequency over time (3 experiments per condition, n = 610 nucleation events). Bars show the median; error bars show the minimum and the maximum value. (H) Histograms of island growth velocities at different Tau concentrations in solution (n = 2131 velocity traces). The fractions of all bins, together with the fraction of time where growth halted (not shown), add up to 100%. (I) Exemplary time-trace of the Tau density in the islands and their surroundings (Methods) after adding Tau (n = 5 microtubules; thick lines and shaded areas indicate median and first and third quartiles, respectively). This experiment was performed with lower frame rate than in C to minimize photo-bleaching. Panels from Siahaan, Krattenmacher, et al. 2019. Panels A and C are also shown in Siahaan 2024.

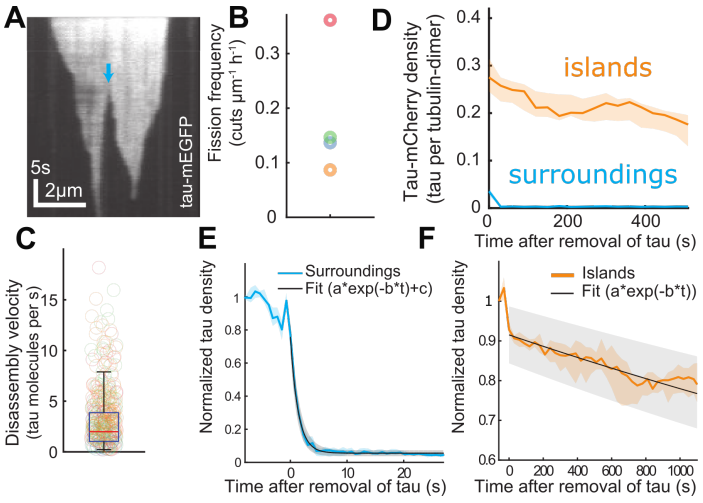

Figure 5.2: **Tau islands disassemble slowly upon the removal of Tau from solution.** (A) Kymograph showing the fluorescence signal of Tau on the microtubule after the removal of Tau from solution. The blue arrow indicates a fission event that here occurred during island disassembly. (B) Frequency of fissions occurring within islands upon removing Tau from solution. Colors encode different experiments. (C) Distribution of island disassembly velocities upon removing Tau from solution. Colors encode experiments (same as in B), circles represent deassembly traces. (D) Exemplary time-trace of the Tau density inside and outside the islands after removing (20nM) Tau from solution (n = 9 microtubules). (E,F) Exemplary time-trace of Tau density inside and Tau density outside the islands after removing (20nM) Tau from solution, analogous to the results presented in E (n = 6 microtubules). Single exponential fits are indicated by solid lines. Panels from Siahaan, Krattenmacher, et al. 2019. Panel A is also shown in Siahaan 2024.

These islands, after nucleating from diffraction-limited spots, grew along along a given microtubule to cover more and more of its length (Figure 5.1C,D). After 75 minutes, most of the microtubule length in a given field of view was covered with islands, with islands still continuing to grow (Figure 5.1E). When repeating this experiment with higher Tau concentrations of 40 and 90nM, microtubules were covered more quickly (Figure 5.1F), due to a higher nucleation rate of islands (Figure 5.1G) as well as due to faster and more consistent growth at island boundaries (Figure 5.1H).

Generally, the islands did not grow monotonously at their boundaries, but with variable velocities in the order of 25 nm/s, corresponding to about 10 molecules added per second (Figure 5.1H). Importantly, the Tau density in the is-

lands stayed constant during the period of growth (Figure 5.1I), suggesting that the islands grow by the addition of Tau molecules at their boundaries, reminiscent of epitaxial growth of thin films. As another indication that islands are formed by a well-defined Tau layer occupying the entire accessible surface of the microtubule, we never observed an increase in the Tau density when the boundaries of neighboring growing islands came into contact (Figure 5.1C).

When Tau was removed from solution, the islands disassembled slowly from their boundaries, occassionally fissioning inside (Figure 5.2A-B). In contrast to island growth, this island shrinkage rarely halted (Figure 5.2B), and proceeded with a median velocity of approximately 2 Tau molecules unbinding per second at a given island boundary (Figure 5.2C). Importantly, the Tau density within islands only declined very slowly after removing Tau from solution compared to the decline in Tau density on all regions outside of islands (the "island surroundings") (Figure 5.2D). Indeed, while in the surroundings Tau unbound with a time constant of about 2 seconds as inferred from the decay of the fluorescence signal (Figure 5.2E), within the islands Tau molecules unbound on the timescale of tens of minutes (Figure 5.2F). This extremely low unbinding rate explains the preservation of the islands in absence of Tau in solution and suggests that the occasional island fissions observed during disassembly occur after rare events of Tau molecules unbinding from inside the island. The large difference in the Tau unbinding rates within islands compared to island surroundings, together with the assembly and disassembly kinetics at the island boundaries, indicate that Tau molecules in the islands bind to microtubules cooperatively.

To more thoroughly explore whether and how the phenomena we observed were dependent on concentration, we conducted additional experiments, increasing the range of tested Tau concentrations. Our observations revealed that island formation did not occur below a critical Tau concentration of approximately 5 nM (n = 245 microtubules in 5 experiments; these experiments were performed by my colleague Valerie Siahaan). Above this threshold, we noted that the Tau density both within and outside the islands increased with the Tau concentration in solution (Figure 5.3A). We had noticed this previously already with our experiments at 20, 40 and 90nM Tau, yet with much larger concentrations it in addition became apparent that Tau binding to microtubules in our buffer condition reaches a saturation point at around 1000nM (Figure 5.3A). Moreover,under such saturated binding conditions, the density on the microtubule appears to be uniform (Figure 5.3A), i.e., a distinction between islands and surroundings based on Tau density can no longer be made. However, upon removing Tau from solution, in areas surrounding the islands, the Tau density rapidly returned to background levels within seconds (Figure 5.3B-E), consistent with our previous surrounding-related findings when removing 20nM Ase1 (Figure 5.2E). Meanwhile, the islands persisted (Figure 5.3B-C) as observed previously (Figure 5.2A). However, at higher Ase1 concentrations it became apparent that the Tau density within the islands exhibits a two-phase decay upon removal of Tau: an initial rapid, uniform decrease along the entire island length, followed by a slower density reduction (Figure 5.3E). Importantly, the Tau

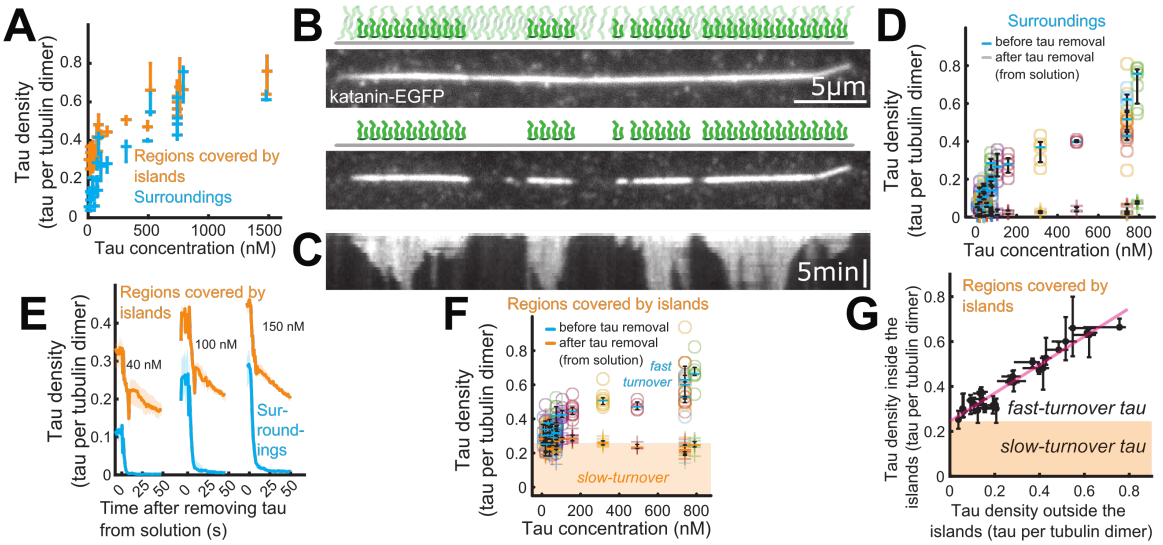

Figure 5.3: **Tau islands are distinguished by cooperative Tau binding** (A) The (equilibrium) density of Tau on microtubules plotted against concentration of Tau in solution. Horizontal lines indicate the three quartiles. (B) Fluorescence micrographs showing the coverage of a microtubule by Tau. Upper panel: 5 minutes after the addition of 0.8 µM Tau. Lower panel: 30 seconds after the removal of Tau from solution. (C) Kymograph of the experiment presented in B showing the disassembly of the islands after removing Tau from solution. (D) Tau densities in microtubule regions surrounding islands, before and after removing Tau from solution. (E) Exemplary time-traces of Tau density outside and inside the islands during subsequent cycles of adding increasing concentrations of Tau followed by removing Tau from solution. Experiment such as presented in D and F. (F) Tau densities in microtubule regions with islands, before and after removing Tau from solution. (G) The (equilibrium) density of Tau on microtubules inside island regions plotted against the density of Tau in the surroundings, using the data presented in A. The red line visualizes a linear fit. Points are color-coded by experiment, horizontal lines indicate the three quartiles of each experiment (in some panels the median is indicated by circle). In C and G, the characteristic island density (Main text, Methods) is indicated by the height of the shaded area. Panels from Siahaan, Krattenmacher, et al. 2019.

density within the islands, following the rapid density drop, consistently measured 0.26 ± 0.05 Tau molecules per tubulin dimer (average ± SD, n = 101 microtubules, 14 experiments, Methods). This value remained constant regardless of the initial Tau concentration in solution (Figure 5.3F).

Combining these results with our findings from Figure 5.1 and Figure 5.2, we conclude that cohesive islands on microtubules form through the cooperative binding of Tau molecules, resulting in their slow unbinding. At physiological Tau concentrations (Wegmann et al. 2018), ranging from 0.5 to 1.5 µM, we observed the co-localization of rapidly turning over Tau molecules with the islands. The density of these co-localized Tau molecules, which appears to correlate with the Tau concentration in solution similarly to the Tau density outside the islands (Figure 5.3G), does not seem to be part of the cooperative island formation process.

To further explore the dynamics of Tau molecules in the islands, we formed islands using 20 nM Tau-mCherry and, after 15 minutes, replaced the assay buffer by a solution containing 20 nM Tau-mEGFP. Outside the islands, Tau-mCherry was replaced quickly by Tau-mEGFP (Figure 5.4A). This included the growth of new islands, which now proceeded by addition of Tau-mEGFP (Figure 5.4A). However, within the islands, Tau-mCherry visibly remained bound to microtubules for longer (Figure 5.4A,B). We quantified this effect by fitting the

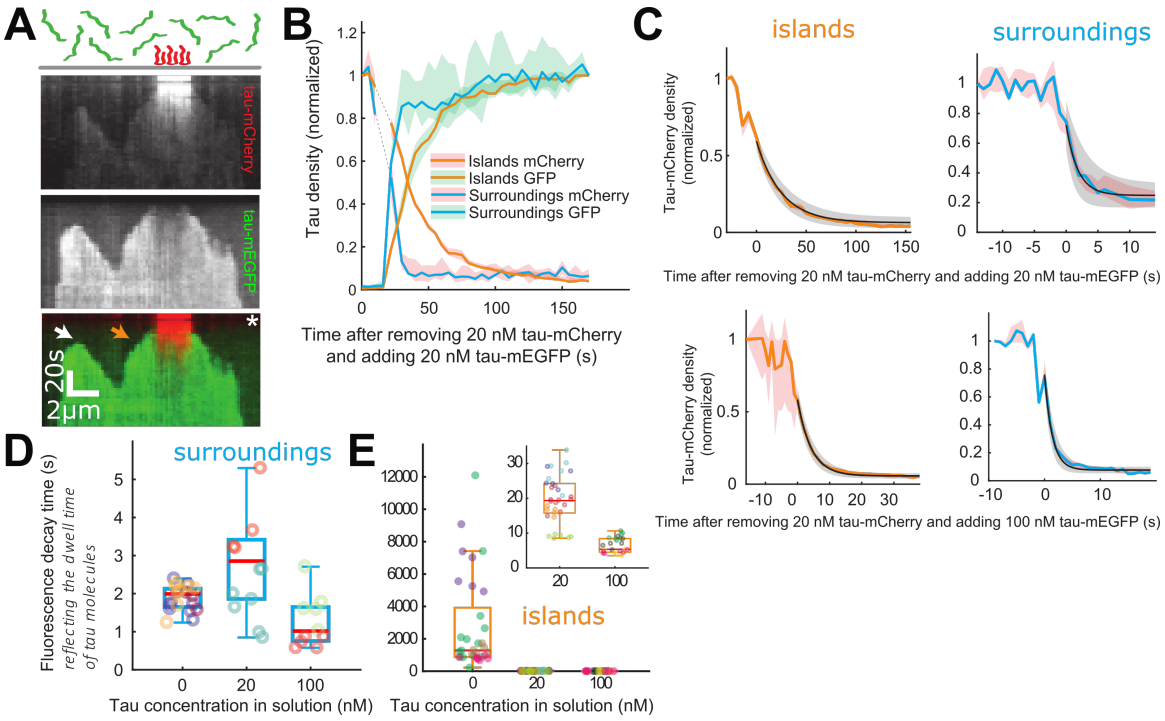

Figure 5.4: **Tau molecules in the islands exchange with Tau in solution.** (A) Multichannel kymograph showing an island pre-formed in presence of 20 nM Tau-mCherry (red). After the addition (time marked by white asterisk) of 20 nM Tau-mEGFP (green), removing most of the Tau-mCherry from solution, Tau-mEGFP replaces Tau-mCherry inside and outside of the islands. An example of an island resuming its growth by the addition of Tau-mEGFP is marked by an orange arrow, a nucleation event is marked by a white arrow. (B) Exemplary time-trace of normalized Tau-mCherry and Tau-mEGFP density inside and outside the islands after exchange of 20 nM Tau-mCherry for 20 nM Tau-mEGFP. Photo-bleaching during this experiment was negligible (Methods); the dotted line indicates that the sample was out of focus at the time. (D) Dwell times of Tau-mCherry derived from fitting exponential decay functions to Tau densities over time in the surroundings of islands. (E) Same representation as D, for island regions. The inset displays the 20 nM and 100 nM boxes on a magnified y-scale. Data points are color-coded by experiments. Panels from Siahaan, Krattenmacher, et al. 2019. Panels A and E are also shown in Siahaan 2024.

Tau density in a given region at different time points to an exponential decay function (Figure 5.4C): In the low-density regions, surrounding the islands, Tau-mCherry dissociated from the microtubules with an average residence time of about 3 seconds (Figure 5.4D), a value comparable to the residence time where Tau was completely removed from solution without replacement (Figure 5.2E). By contrast, within the islands Tau-mCherry dissociated markedly slower, with an average residence time of 20 ± 7 s (average ± SD) seconds (Figure 5.4E). This value is, however, substantially faster than in the situation when Tau was completely removed from solution, in which case the dwell time was 45 ± 46 min (compare to Figure 5.2F). Thus, we observed that Tau unbinding from the islands depends on the Tau concentration in solution. As another piece of evidence confirming this dependence, we observed that Tau-mCherry unbound form islands even faster when adding 100nM Tau-mEGFP as compared to the addition of 20nM Tau-mEGFP (in this case, the dwell time was 6.4 ± 2.1 s) (Figure 5.4E).

To further study the spatio-temporal interaction dynamics of Tau and microtubules, we

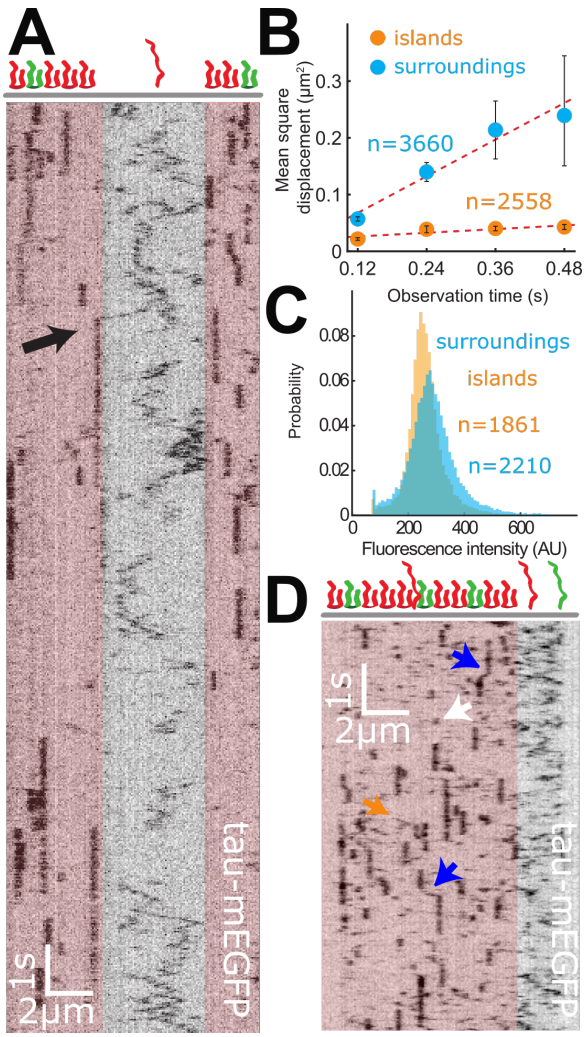

Figure 5.5: **Tau molecules are stationary within the islands.** (A) Intensity-inverted kymograph showing single Tau-mEGFP molecules interacting with a microtubule covered by two Tau-mCherry islands (light red regions) at 20nM Tau-mCherry in solution. Black arrow: An event where a diffusing Tau-mEGFP molecule gets associated with an island. (B) Mean square displacement over time of single Tau-EGFP molecules inside and outside Tau-mCherry islands. (C) Histograms of fluorescence intensities of single Tau-mEGFP particles bound to microtubules in experiments as presented in A. (D) Same as A, however, with 100nM Tau-mCherry in solution instead of 20nM. Orange arrow: A brief and diffusive interaction of a Tau molecules inside the island. Blue arrows: Island-bound Tau molecules switche to a (more) diffusive binding mode. White arrow: A brief Tau interaction within islands. Panels from Siahaan, Krattenmacher, et al. 2019, except for panel D, which is published only in this thesis (experiment conducted by Valerie Siahaan, data analyzed and interpreted by me). Panel A is also shown in Siahaan 2024.

formed islands using a mixture of 20 nM Tau-mCherry and 1 nM Tau-mEGFP. This strategy allowed us to observe the motion of individual Tau-mEGFP molecules even within Tau islands, as these islands were mainly comprised of Tau-mCherry molecules. In the low-density regions, single Tau-mEGFP molecules diffused rapidly (Figure 5.5A). By contrast, in the islands the Tau-mEGFP molecules did not display any noticable movement (Figure 5.5A). Quantifying these phenomena (Methods), we measured that outside the islands, Tau molecules diffused with a diffusion constant of 0.27 ± 0.15 $\mu m^2 s^{-1}$ (95% confidence bounds) (Figure 5.5B), comparable to values reported before by Hinrichs et al. 2012. Within the islands, we measured Tau-mEGFP molecules to have a diffusion constant of 0.027 ± 0.016 $\mu m^2 s^{-1}$ (Figure 5.5B). To test whether we indeed observed single Tau molecules rather than conglomerates which had formed in solution, we generated fluorescence intensity histogram of individual Tau-mEGFP particles (Figure 5.5C). These exhibited a single Gaussian profile in the islands just as in their surroundings, indicating that Tau-Tau interactions indeed occurred only on the microtubule lattice. We also formed islands using a mixture of 100 nM Tau-mCherry and 1 nM Tau-mEGFP. Consistent with the results shown in Figure 5.3, we observed diffusive and/or brief interactions of Tau molecules inside islands (Figure 5.5D). It also beas noting that occasionally, single Tau-mEGFP molecules initially diffusing outside an island became stationary when associating with an island boundary (Figure 5.5A), hinting at growth of the islands from the boundary.

Finally, we were interested in exploring

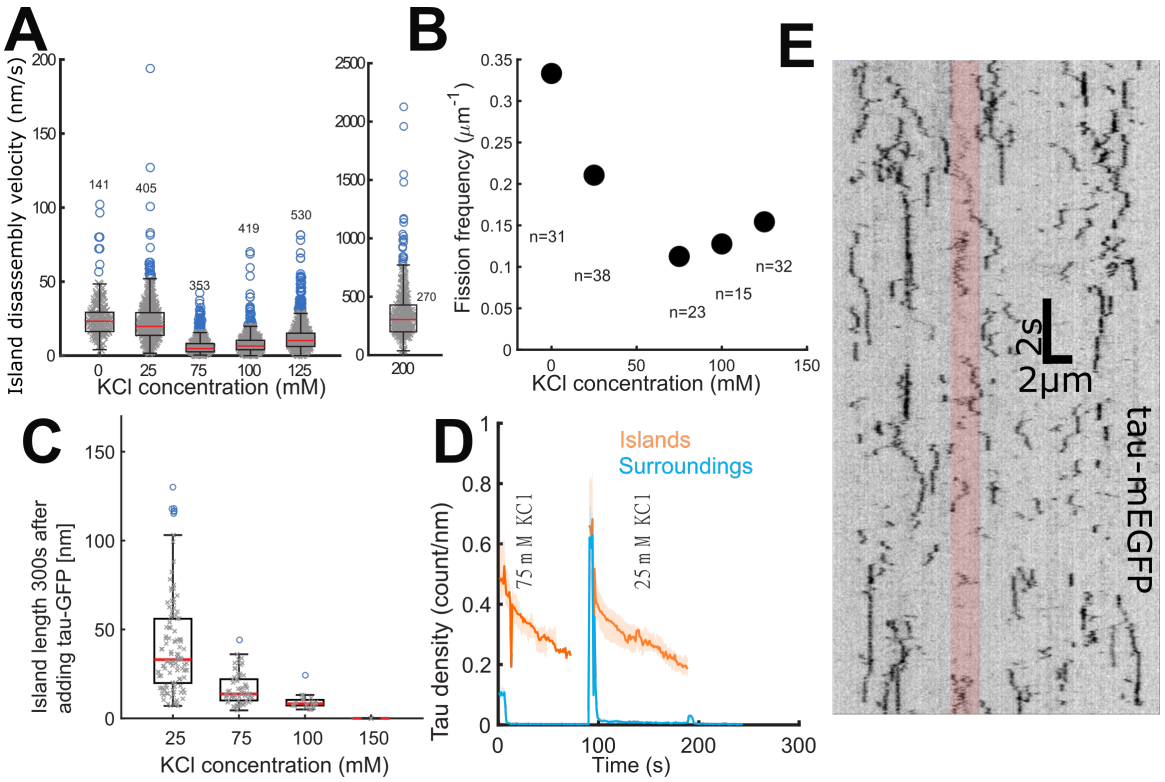

Figure 5.6: **The preferred binding mode of Tau varies with ionic strength.** (A,B) Island disassembly velocities and fission frequencies at different concentrations of KCl (after Tau had been removed from solution; islands had been grown at 75mM KCl). Numbers show the number of measured disassembly periods (panel A) or observed fissions (panel B). (C) Lengths of islands measured 300s after adding 40nM Tau at varying concentrations of KCl. (D) Cycles of adding and removing 100nM Tau to/from solution (additions at t=-100s and t=100s, removals roughly at t=10s and t=110s). In the second cycle, the solution contained only 25mM KCl rather than 75mM, which was used in all previously shown experiments. Bleaching was not negligible in this experiment. (E) Intensity-inverted kymograph showing single Tau-mEGFP molecules interacting with a microtubule covered by a Tau-mCherry island (highlighted by the red area) at 25mM KCl. Findings shown in this figure have not been published yet.

some plausible determinants of island assembly beside Tau concentration. First, because the N-terminus of Tau mediates Tau-Tau interactions (Gamblin et al. 2003), we attempted to grow Tau islands with a truncated Tau construct comprising the four-repeat microtubule-binding domain and the C-terminus but lacking the N-terminus (TauΔN-mEGFP, Figure 4.3). Although TauΔN-mEGFP did interact with the microtubules, we did not observe any island formation even at 0.5 µM TauΔN-mEGFP (these experiments were performed by my colleague Valerie Siahaan). Second, we varied the ionic strength of our buffer solution by varying the concentration of KCl (these experiments were largely performed by me; for reasons of space we did not include these findings in Siahaan, Krattenmacher, et al. 2019). We noticed that increasing as well as decreasing the concentration of KCl from the level we had used for the experiments we have reported on so far, namely 75mM, both tended to decrease the stability of Tau islands: 0, 25, 100, and 125nM KCl islands disassembled quicker once Tau was removed from solution than at 75mM KCl (Figure 5.6A,B). Disassembly speed was drastically higher at 200mM KCl (Figure 5.6A right panel). Generally, Tau binding to

the microtubule was less pronounced at higher KCl concentrations, both in terms of island formation and binding to surrounding regions (data not shown). However, interestingly, at 0 and 25mM KCl, island assembly was more pronounced than at 75mM KCl (Figure 5.6C). At the same time, at these low KCl concentrations, more Tau bound to the microtubule via the diffusive binding mode, visible from the high Tau densities in the surrounding regions (Figure 5.6D). Consistent with the observation that islands at lower ionic strengths were less stable, when looking at single Tau-mEGFP molecules in a Tau-mCherry-dominated environment, we observed that the distinction between binding within the islands versus binding outside the islands was less clear-cut than at 75mM KCl (Figure 5.6E). Tau molecules appeared to switch regularly between diffusive and stationary interactions within islands, though the diffusive interactions appeared more tightly bound to the microtubule than outside the islands (Figure 5.6E). We had observed such switches already at 75mM KCl, though at that condition these switches were much less prevalent (Figure 5.5D).

Combined, our results show that Tau molecules bind to microtubules in two distinct binding modes. The diffusive binding mode had already been described before (Hinrichs et al. 2012). However, we together with R. Tan et al. 2019 discovered another, cooperative, binding mode, which results in the formation of what we termed Tau islands (in more recent publications on the topic the term "envelopes" is used, see e.g. Siahaan, R. Tan, et al. 2022). This cooperative binding mode, unlike the diffusive mode, is dependent on the N-terminus region of Tau. The strength of this cooperative binding mode moreover varies differently with ionic strength than the strength of the diffusive binding mode.

5.1.2 Cooperatively bound Tau uniquely interacts with MAPs

To investigate how Tau islands interact with other microtubule-associated proteins (MAPs), we formed Tau islands and tested the interaction of other axonal MAPs with such Tau-decorated microtubules. Among others, we tested the microtubule-transport motor kinesin-1, where we found that while these motors could move freely through surrounding regions, they were totally blocked from accessing island-decorated microtubule regions. However, these experiments were exclusively performed and analzed by my colleague Valerie Siahaan, thus the results for these experiments (see Siahaan, Krattenmacher, et al. 2019) are not shown in this thesis. As mentioned in chapter 3, I contributed to our results regarding the cutting enzyme Katanin and was exclusively conducting and analyzing experiments regarding the motor protein kinesin-8.

After the addition of 100nM (GFP-labeled) Katanin to microtubules in the presence of 20nM (mCherry-labeled) Tau, we observed Katanin binding almost exclusively to the low-density Tau regions surrounding the islands (Figure 5.7A, 15s panel). As one may expect from this observation, we then subsequently observed microtubule disassembly predominantly in these regions (Figure 5.7A, 30s panel). Only on longer time scales, the island-covered regions of the microtubules started to disassemble from their boundaries, with occassional cuts occuring inside Tau islands (Figure 5.7A-C). Combined, these results show that Tau

islands constitute a protective envelope around the microtubule surface, which can hinder the activity of microtubule-severing factors and block kinesin-1-based transport.

As shown in the previous section, higher Tau concentrations, the Tau densities inside and outside Tau islands are comparable (Figure 5.3A). We thus wondered if the discretely binding Tau molecules in the island surroundings, at these concentrations, are sufficient for shielding the microtubule against microtubule severing. We thus formed Tau islands at saturating conditions (0.8 µM). After 5 minutes of incubation we briefly removed Tau from solution to note the position of the islands, and then again re-introduced 0.8 µM Tau in the assay. We then exposed such Tau decorated microtubules to 0.2 µM Katanin analogously to the experiment presented in Figure 5.7A. Strikingly, we observed qualitatively identical results as in Figure 5.7A. Namely, regions surrounding the islands and occupied by the diffusible Tau phase were severed and rapidly disassembled, while microtubule regions shielded by the islands persisted (Figure 5.7D). This demonstrates that the density of Tau on the microtubule surface is not the factor determining the shielding function of Tau. Rather it is the unique nature of the cooperative Tau binding mode which protects the microtubules. This conclusion is supported by our observation that increasing the Tau concentration in solution did not substantially increase shielding against Tau, neither in the island regions (Figure 5.7B,C) nor in their surroundings (Figure 5.7E).

Kinesin-8, in contrast to kinesin-1, is a super-processive motor (subsubsection 1.2.1.3), which led us to hypothesize that its interaction with Tau islands might differ from the behavior by kinesin-1. For our experiments, we used S. cerevisiae Kip3, the best described member of the kinesin-8 family (subsubsection 1.2.1.3). After the addition of 45nM (GFP-labeled) Kip3 to microtubules in the presence of 20nM or 100nM (mCherry-labeled) Tau, we observed that Kip3 molecules could move in the low-density Tau regions, like kinesin-1 (Figure 5.8A,B). However, in contrast to kinesin-1, and presumably related to its characteristic of super-processivity, Kip3 could also traverse Tau islands, albeit at a decreased velocity (Figure 5.8A-C). Similarly, we also observed Kip3 to be less prevalent in regions covered by Tau islands, indicating a lower affinity for these regions (Figure 5.8A,D). We also observed the previously described (subsubsection 1.2.1.3) traffic jams at the end of microtubules (Figure 5.8A,B). Interestingly however, we also observed that Kip3 accumulated, in the direction of its movement, at the boundaries of Tau islands (Figure 5.8A,B). Such Kip3 traffic jams evidently caused enhanced unbinding of Tau at these positions, eventually leading to a disassembly of the islands from their boundaries with a velocity slightly lower than the velocity of Kip3 within islands (Figure 5.8B,C,E,F). Notably, Tau islands which had been removed in this way typically regrew after the Kip3 accumulates had passed (Figure 5.8E). The island displacement by Kip3 shows that not only do Tau islands regulate the interaction of other MAPs with the microtubule surface but that, vice versa, the activity of other MAPs, such as super-processive motors proteins, can regulate the dynamics of the islands themselves.

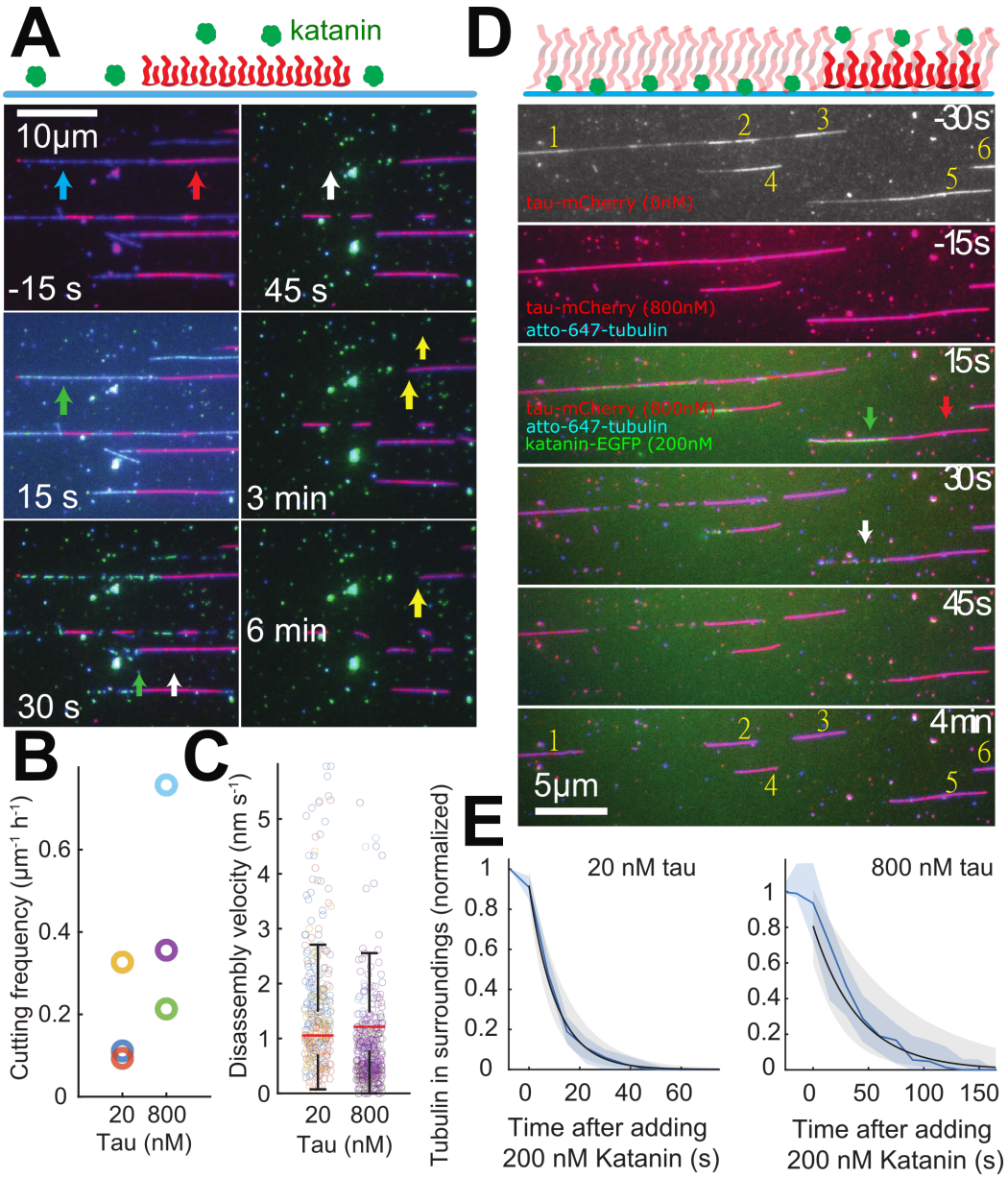

Figure 5.7: **Tau islands constitute a protective envelope around microtubules.** (A) Fluorescence micrographs showing Katanin-driven (green, example indicated by green arrow) disassembly of Atto-647-microtubules (blue) decorated with Tau islands (red, example indicated by red arrow) interspersed by regions of low Tau-mEGFP density (indicated by blue arrow). An example region outside an island is indicated by white arrow. An example of an island-covered region being slowly shortened by Katanin is indicated by a yellow arrow. (B,C) Boxplots of the velocities of Katanin-driven disassembly of stretches of microtubules covered by Tau islands (evaluated per island boundary) and the rate of Katanin-generated cuts occurring within them, at the two different tested Tau concentrations. (E) Exemplary time-traces of normalized tubulin signal outside the island-covered microtubule regions (blue line) decaying during its Katanin-driven disassembly. Single exponential fits to the data (black lines) yield a tubulin residence time of 17 ± 6.4 s (average ± S.D., n = 17 microtubules in 2 experiments) in presence of 20 nM Tau and 34 ± 23 s (n = 18 microtubules in 2 experiments) in presence of 800 nM Tau. Photo-bleaching during this experiment was negligible (Methods). (D) Fluorescence micrographs showing Katanin-driven (green) disassembly of Atto-647-microtubules (blue) decorated with Tau islands (red) formed at 0.8 µM Tau concentration. The island positions (indicated by numbers) were determined via a brief removal of Tau from solution. Green arrow: A region outside of islands and its decoration with Katanin. Red arrow: Island-covered region (Katanin was absent from such regions). White arrow: Rapid disassembly of surrounding regions. Compare to A. Panels from Siahaan, Krattenmacher, et al. 2019. Panel A is also shown in Siahaan 2024.

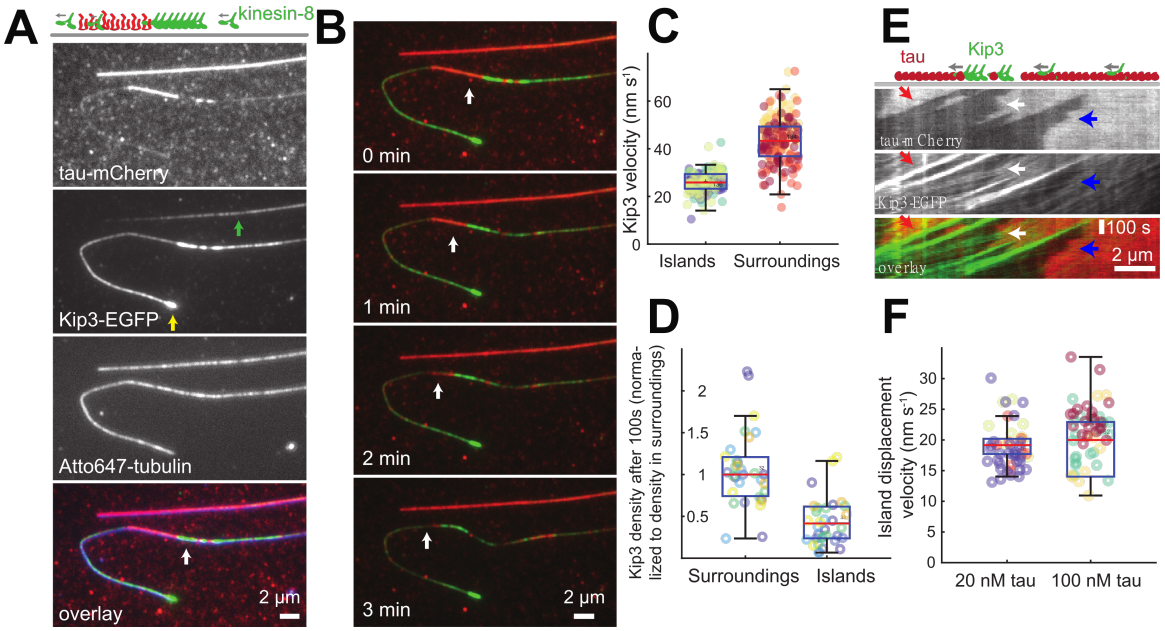

Figure 5.8: **Tau islands can be regulated by super-processive kinesin motors.** (A) Multichannel fluorescence micrographs showing Kip3 (kinesin-8, green) localizing outside and within the Tau (red) islands (biggest island indicated by green arrow) on Atto-647-labeled microtubules (blue). An accumulation of Kip3 at an microtubule end is highlighted by an yellow arrow, an accumulation in front of an island by a white arrow. (B) Multicolor timelapse micrographs of the event shown in A documenting the removal of a Tau island by Kip3 accumulating in front of it, where the receding of the island boundary is indicated by white arrow. (C) The measured velocities of single Kip3 motors moving inside and outside the islands at 10 nM Tau in solution (3 experiments). (D) The measured Kip3 density inside and outside the islands 100 seconds after the addition of Kip3 (6 experiments). (E) Multichannel fluorescence kymograph showing a different event than A and B. The red arrows indicate an accumulation of Kip3 in front of an island, disassembling it. The white arrows indicate an instance where Kip3 molecules can clearly been observed to speed up as they leave the island. The blue arrows (added for this thesis) show a region of Tau island "growing back" after having been disassembled. (F) Velocities of Kip3-GFP-driven disassembly of Tau islands established at two different Tau concentrations (3 experiments). Panels from Siahaan, Krattenmacher, et al. 2019.

5.1.3 Highly curved microtubule regions displayed unique MAP interaction patterns

In our assays, we noticed that at low Tau concentrations, Tau preferentially localized to highly-curved microtubules compared to regions outside of islands (Figure 5.9A-C), as had previously been reported (Samsonov 2004). To be more precise, we observed that regions of highly curved microtubules (radius < 2.5 µm) exhibited a Tau density that was higher than in the surroundings, but lower than in Tau islands (Figure 5.9D). In contrast to the islands, there was no growth from boundaries. Instead, in the high-curvature regions the Tau density increased immediately after the addition of Tau in solution, similar to the behavior in the regions surrounding the islands (Figure 5.9C). Indeed, we observed very similar timescales of binding till saturation (6 ± 2 s for high-curvature regions, 8 ± 6 s for surroundings, weighted average $\pm$ S.D., 5 experiments). Moreover, the Tau bound to highly curved microtubule regions also did not unbind as quickly as in the surroundings (Figure 5.9E,G upper panel). Not only were these highly curved regions different from islands, we also never observed islands to form in such regions. This was the case even at 800nM Tau in solution, where the regions adjacent to highly curved regions were (interestingly) always covered with islands (Figure 5.9F). Taken together, these findings indicate that Tau cannot bind in a cooperative manner to highly curved microtubule regions. We thus hypothesized that highly curved microtubule regions would never be protected from Katanin severing. This was indeed the case (Figure 5.9G,H).

In summary, we have shown that on microtubules, the neuronal protein Tau can bind cooperatively to the microtubule to form islands, thereby giving rise to emergent phenomena such as protection of the microtubule against severing by Katanin. I now turn to the results of our experiments focused on the microtubule-crosslinking protein Ase1 aimed at furthering our understanding of the structural integrity of the mitotic spindle.

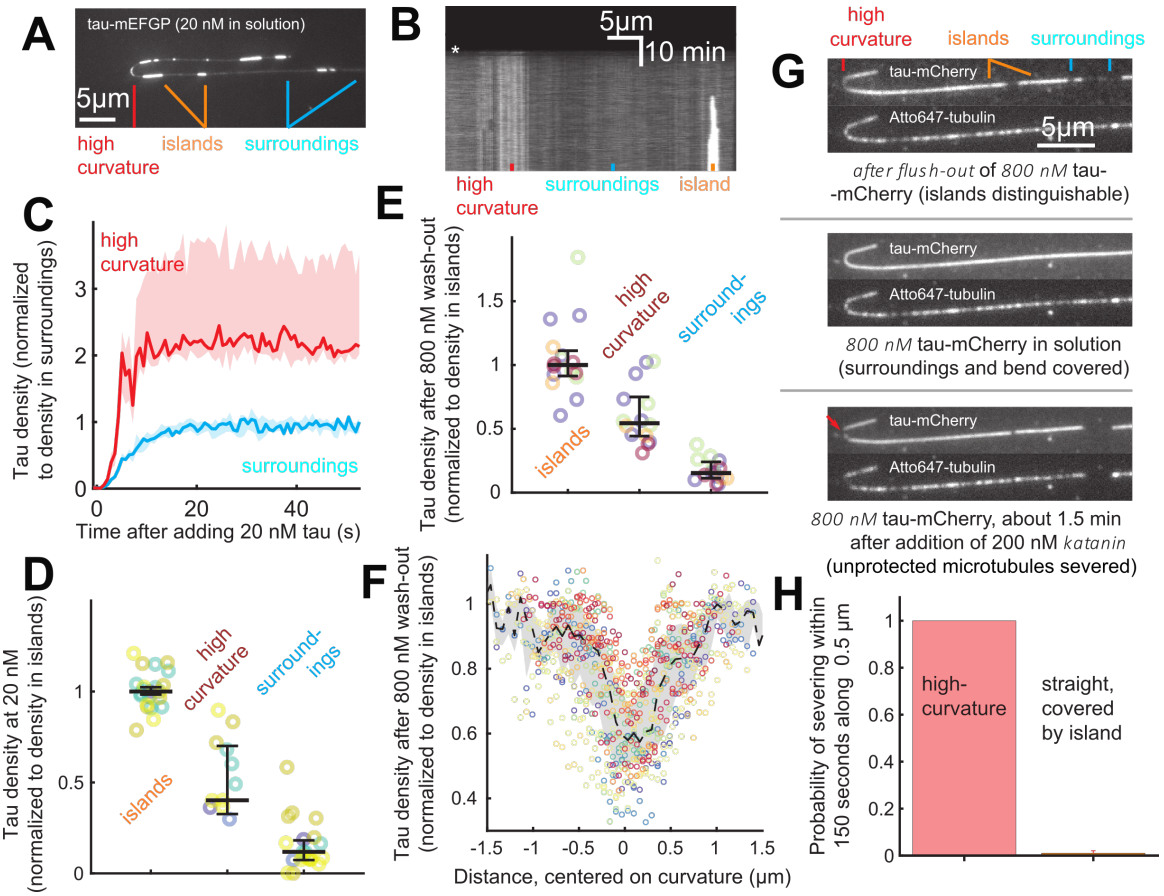

Figure 5.9: **Tau islands do not form at microtubule regions with high curvature.** (A) Fluorescence micrograph showing the Tau distribution on a highly curved microtubule at 20 nM Tau in solution. (B) Kymograph showing the change in Tau density along a highly curved region of a microtubule as well as the assembly of an island upon the addition of Tau in solution. (C) Exemplary time-trace of the three different types of regions as shown in A and B after addition of 20 nM Tau-mEGFP in solution (n = 5 microtubules). (D) Normalized steady-state densities measured in these three region types at 20 nM Tau in solution (n = 11 high-curvature regions in 5 experiments). Points are color-coded by experiments, weighted such that each experiment has equal weight. (E) Normalized densities measured in the three region types around 1 minute after the removal of 0.8 µM Tau from solution. Points are color-coded by experiments (n = 15 high-curvature regions in 4 experiments), weighted such that each experiment has equal weight. (F) Tau density profiles along highly curved microtubule regions around 1 minute after removing 800 nM Tau from solution. X-axis is centered on the point of highest curvature. Data are color-coded by microtubule and the density is normalized to the 90th percentile of the density-values of the respective microtubule. The red line represents the median of n = 30 microtubules (7 experiments). At 800 nM Tau, there always were islands adjacent to microtubule bends, which is why the Tau density to the left and right of the curved microtubule region is high even though Tau has been removed from solution. A clear decrease in the Tau density is apparent at the point of highest curvature. (G) Tau on microtubules after removing 800 nM Tau from solution (upper panel); the same microtubule when having reintroduced 800 nM Tau in solution (middle panel); the same microtubule shortly after 200 nM Katanin have been added to the solution. The red arrow highlights cut in the high curvature region. (H) Probability of severing of highly curved microtubule regions and adjacent straight island-covered microtubule regions, within 150 s after adding Katanin. The bars represent the probability averaged over n = 4 experiments (29 bends and 82 straight microtubules), error bars represent the S.D. Curved microtubule regions were always severed. In panels C-F, horizontal lines/lines/shaded areas represent the three quartiles. Panels from Siahaan, Krattenmacher, et al. 2019.

5.2 Interactions Between Ase1 and Dynamic Microtubules

5.2.1 The presence of Ase1 stabilizes microtubules, mainly antiparallel microtubules

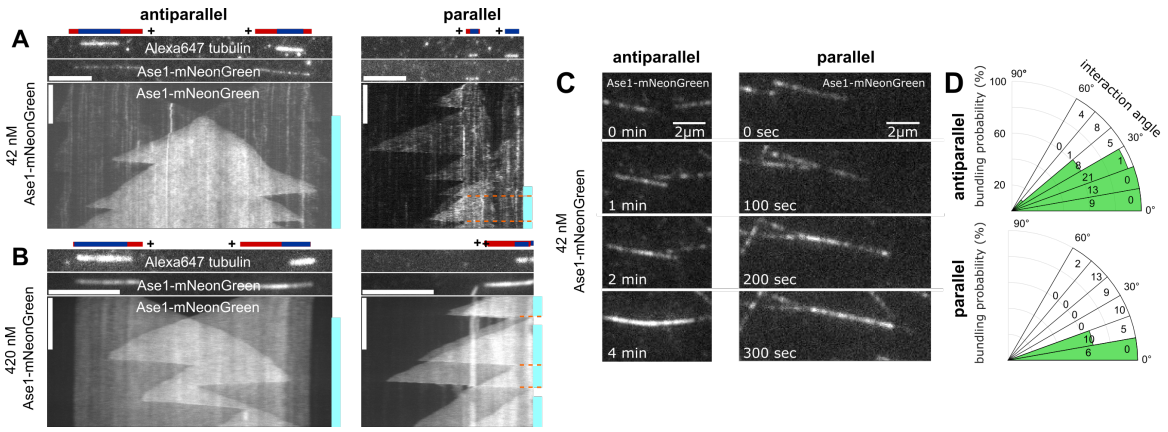

Figure 5.10: **With dynamic microtubule extensions and Ase1, we observed microtubule bundling as previously reported.**(A) Kymographs of an antiparallel (left panel) and a parallel microtubule overlap forming due to the microtubules polymerizing such to enable bundling by Ase1, which is present in solution (42nM). The scale bars are 5 micron and 10 minutes. In sketches, dynamic extensions with GDP lattices are red, and stabilized GMPCPP seeds are blue. The teal bars next to kymographs indicate the presence of regions of overlap (we only counted regions where the two partaking microtubule regions are constituted by GDP-tubulin, i.e., a seed stabilized by GMPCPP did not count). The orange lines indicate a termination of the overlapping period, as evaluated for Figure 5.11A. (B) Same representation as A showing events from experiments performed at 420nM Ase1. (C) Snapshots of different events than shown in A and B, illustrating microtubule bundling (at 42nM). (D) Bundling probability for instances where microtubule plus ends encountered other microtubules, in either parallel or antiparallel orientation, versus the initial angle of interaction (results pooled for all Ase1 concentrations). The outer numbers denote the numbers of recorded crossings at the respective angle, while the inner denote the numbers of bundling events (the sum of both numbers is the total number of observed events). Panels taken from Krattenmacher et al. 2024.

To investigate the interaction dynamics between diffusible microtubule crosslinkers and microtubules, we employed total internal reflection fluorescence (TIRF) and interference reflection microscopy (IRM) (subsection 1.1.3) time-lapse imaging of immobilized, GMPCPP-stabilized microtubule seeds in the presence of 30 µM free tubulin and varying concentrations of Ase1 (Methods). At concentrations of 42 nM and 420 nM Ase1, we observed dynamic, Ase1-decorated microtubule extensions polymerizing from the microtubule seeds (Figure 5.10A,B). When two microtubule plus ends, emanating from different seeds and polymerizing towards each other, encountered each other, the microtubules either bundled or crossed, depending on the angle of incidence. Typically, at high angles, the microtubules crossed and only interacted at the crossing point, while at small angles, either parallel or antiparallel associations could be formed (Figure 5.10C). As previously reported (Janson et al. 2007), antiparallel bundles formed even at large initial angles of incidence (up to 40°), while parallel bundles only formed at initial angles below 20° (Figure 5.10D).

Quantitative analysis revealed increased lifetimes of antiparallel overlaps compared to parallel ones (Figure 5.11A) Notably, at 42 nM Ase1 in solution, the Ase1 density on

antiparallel overlaps was an order of magnitude higher than on parallel ones (Figure 5.11B) consistent with the previously reported differential affinities (Janson et al. 2007). At 420 nM Ase1, we observed the density of Ase1 to be similar on antiparallel and parallel bundles, roughly twice the density found on isolated microtubules (Figure 5.11B). This possibly indicated that, at this high concentration, a similar number of Ase1 molecules was present within parallel and antiparallel overlaps. Note, however, that this value represents the total density of Ase1 at the bundle, which might differ from the density of Ase1 molecules directly engaged in microtubule crosslinking by being bound simultaneously to both microtubules. Despite similar decoration levels by Ase1, antiparallel overlaps were still significantly more stable than parallel ones (Figure 5.11A) Given the low polymerization velocity of minus ends, we very rarely observed antiparallel overlaps formed by two minus ends encountering each other, and we thus could not meaningfully quantify the associated lifetime. Generally, we chose to not analyze minus ends given that they are not dynamic *in vivo* (Dammermann et al. 2003).

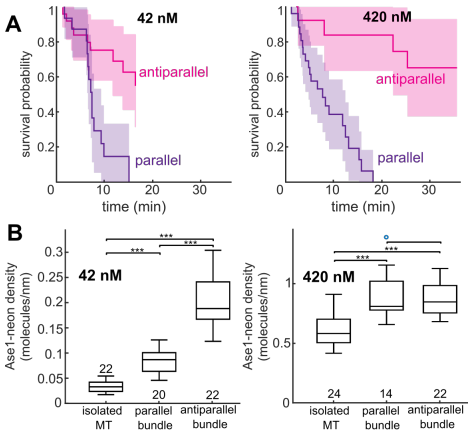

Figure 5.11: **Ase1 selectively stabilizes antiparallel overlaps.** (A) Survival probability of antiparallel and parallel overlaps, showing the probability that an overlap formed by two dynamic microtubule extensions still persists at a given time after its formation (Methods). Semitransparent regions indicate 95% lower and upper confidence bounds. (B) Quantification of the density of Ase1 on isolated microtubules and (anti)parallel bundles (Methods). The numbers below the boxes indicate the number of analyzed microtubule bundles. Panels show data for microtubule plus ends (minus ends generally were not analyzed). Panels taken from Krattenmacher et al. 2024.

To test whether the relative stability of antiparallel overlaps was caused by Ase1 crosslinking or the bundling itself (as was requested by a reviewer), we also conducted experiments at 10nM Ase1. At this concentration, we observed significantly less Ase1 within antiparallel bundles (Figure 5.12A), and indeed, antiparallel bundles were no more stable than parallel bundles (Figure 5.12B). Also, at 10nM Ase1 we observed antiparallel microtubules to no longer bundle as readily as at higher Ase1 concentrations (Figure 5.12C). While we could detect an Ase1 signal at antiparallel overlaps, we did observe events where Ase1 crosslinking apparently was not strong enough to keep a microtubule plus end bundled to the microtubule along which it was growing in an antiparallel orientation (Figure 5.12D,E left panel). Finally, to test whether microtubule bundling in our assays was partially a result of molecular crowding (and not Ase1), we performed an assay at 0nM Ase1. In absence of Ase1, microtubules never bundled, even when very close to each other over extended periods of time, indicating that molecular crowding did not play a role in the microtubule bundling we observed (Figure 5.12F).

The relative stability of antiparallel overlaps at high Ase1 concentrations may at least partly owe to the fact that antiparallel overlaps grow with twice the speed of parallel overlaps

(since both microtubules polymerize in opposite directions, however it should be noted that once a minus end has been surpassed the antiparallel overlaps does no longer grow as quickly on the side in question); hence, there is more opportunities for rescues to occur during depolymerization. However, our kymographs suggested that antiparallel overlaps may be additionally stabilized by an increase in rescue frequency (Figure 5.13A), and we set out to quantify this issue next.

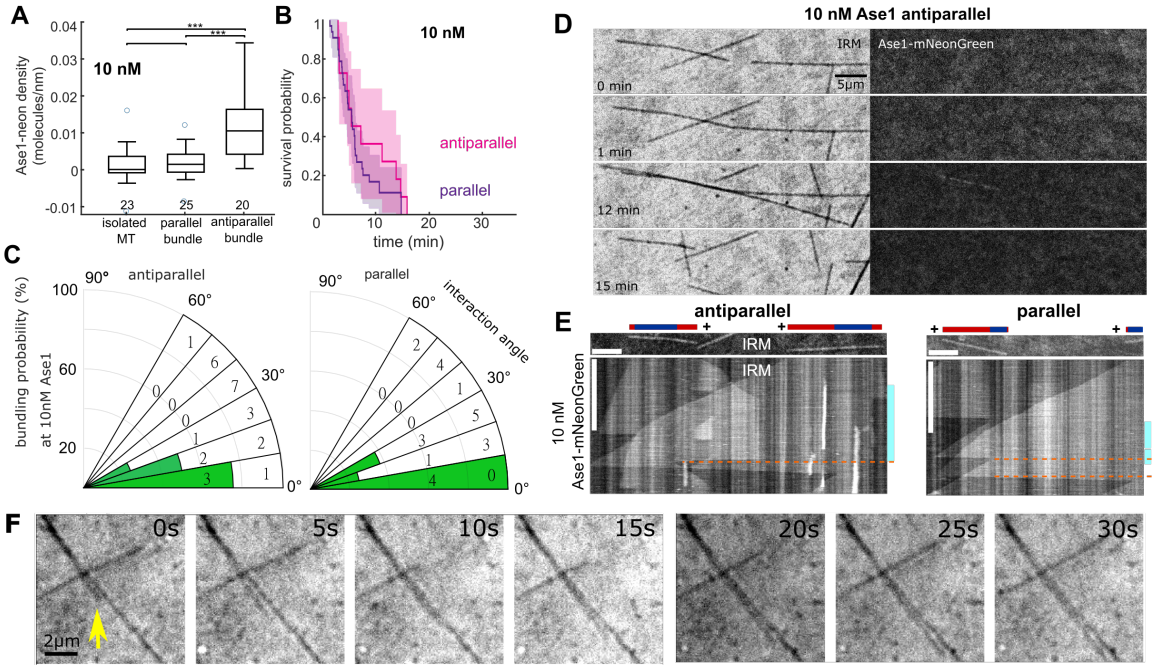

Figure 5.12: **Antiparallel overlaps are not significantly stabilized at low Ase1 concentrations.** (A,B) Quantifications of Ase1 densities and lifetimes for the 10nM Ase1 condition analogous to panels in Figure 5.11. (C) Quantifications of bundling probabilities for the 10nM Ase1 condition analogous to Figure 5.10D. (D) Snapshots of an antiparallel overlap at 10nM Ase1. (E) Kymographs for the 10nM Ase1 condition, representation analogous to Figure 5.10A. The left panel shows the same event as D. (F) A microtubule polymerizing close to another, parallel microtubule at 0nM Ase1 (imaged with IRM). The tip of microtubule in question is indicated by a yellow arrow. As can be seen, no bundling is occurring in spite of the fact that the microtubules are very close to each other. Panels taken from Krattenmacher et al. 2024.

Indeed, as indicated by the kymographs shown in (Figure 5.13A), we found rescue frequencies to be increased for antiparallelly crosslinked microtubules at the Ase1 concentrations where we had observed increased lifetimes of these overlaps (Figure 5.13B). To test whether Ase1 crosslinking might have other significant effects on microtubule polymerization, we next quantified the other three parameters of microtubule dynamic instability. We found that catastrophe frequencies were similar across the tested conditions, with no statistically significant difference between the different populations (Figure 5.13C). Polymerization velocities were similar for all microtubule types, either isolated or bundled, across all tested Ase1 concentrations as well (Figure 5.13D). However, at 420nM Ase1, microtubules depolymerized markedly slower than at lower Ase1 concentrations. Further, at 42nM and 420nM Ase1, antiparallel microtubules displayed a marked decrease in depolymerization velocity compared to isolated and parallel microtubules (Figure 5.13E). Thus, we observed Ase1 to only have a

measurable effect on microtubule depolymerization, by reducing the rate of depolymerization and increasing chances for rescue, with no effect on polymerization.

If one only considers our results at 42nM, one could speculate that the particularly pronounced stabilization of antiparallel microtubules was due to the increased number of Ase1 molecules on antiparallel microtubules as compared to parallel and isolated microtubules. However, at 420nM, the number of Ase1 molecules per microtubule was similar across all types of microtubules, while the antiparallel microtubules still were more stable, despite indistinguishable Ase1 densities on antiparallel versus parallel microtubule overlaps (Figure 5.13F,G). Thus, Ase1 engaged in antiparallel crosslinking seems to have a stronger effect on microtubule depolymerization than Ase1 engaged in parallel crosslinking or Ase1 not engaged in crosslinking. This deduction is supported by the fact that the number of Ase1 molecules engaged in Ase1 crosslinking was the only factor we could identify as influencing the frequency of rescues (note, however, that the number of molecules directly participating in the crosslinking process, i.e. simultaneously bound to both crosslinked microtubules, is not measurable in this assay). Showing the robustness of our finding, we with altered buffer conditions (I call this set of experiments "Set B experiments," see Methods) found the same result Figure 5.14: At these conditions, we observed antiparallely linked microtubules to exhibit rescues, at a density of around 0.2 molecules per nm which we at these buffer conditions had established with 1nM Ase1 (Figure 5.14B,C) (as a side note, the Ase1 used in these experiments had a different fluorescence label, GFP instead of mNeonGreen). At these buffer conditions, isolated microtubules did not exhibit any rescues at all, even when we increased the Ase1 concentration from 1 to 6nM such that the Ase1 density on isolated microtubules was comparable to the Ase1 density on antiparallel bundles at 1nM Ase1 (Figure 5.14B,C). The depolymerization velocity similarly decreased with increasing Ase1 concentration (Figure 5.14D). Altogether, these results show that Ase1 can stabilize antiparallel microtubules while only having minor stabilization effects on microtubules outside of such overlaps.

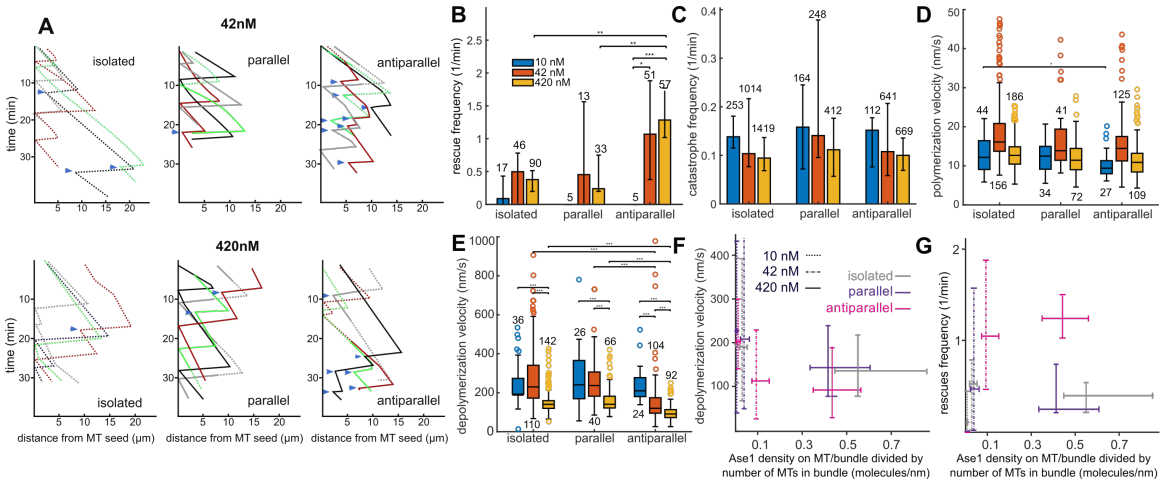

Figure 5.13: **Ase1 obstructs microtubule depolymerization.** (A) Representative kymograph traces of the types of events we observed in our dataset which we present in Figure 5.10, Figure 5.11 and Figure 5.12A-E. Blue arrows indicate rescue events. Dotted lines indicate stretches where the microtubule was isolated. (B) Rescue frequency, (C) catastrophe frequency, (D) polymerization velocity, and (E) depolymerization velocity of dynamic microtubule plus ends in different configurations and in the presence of varying concentrations of Ase1-mNeonGreen. (F) Depolymerization velocity (see E) versus Ase1-mNeonGreen density on a given microtubule or bundle divided by number of microtubules in that bundle (i.e., the density as shown in Figure 5.11B is divided by 2 in the case of parallel and antiparallel microtubules). (G) Rescue frequency (see B) versus Ase1-mNeonGreen density (see Figure 5.11B). All plots show results for the same experiments as shown in Figure 5.10 and Figure 5.11. * $p<0.05$, ** $p<0.01$, *** $p<0.001$ (Tukey's test; only significance levels are visualized that share either the same microtubule type or the same concentration. No visual link between two populations sharing one such characteristic signifies $p>0.05$. In B and C a given population comprises the frequencies recorded for the respective experiments, in D and E the velocities recorded for respective sampled periods). Boxplots are weighted by the length of a sampled period of polymerization or depolymerization. In boxplots, the numbers indicate the number of recorded events; in bar plots, the numbers indicate the sum of the length of all sampled periods of polymerization or depolymerization (in minutes). In bar plots, the height of the bar show the catastrophe/rescue frequency as determined from all time lapses (number of total events divided by total duration of depolymerization), while the error bars show the lowest and highest rates as determined from each isolated time lapse; velocities are normalized to the median velocity of isolated microtubules (Methods). Panels taken from Krattenmacher et al. 2024.

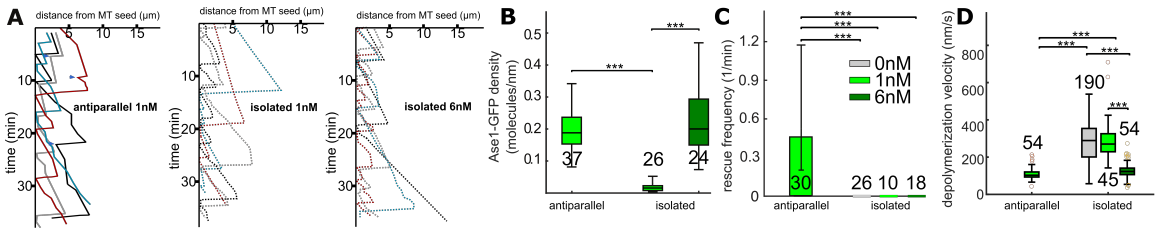

Figure 5.14: **Microtubule dynamics under altered buffer conditions.** Data obtained from a second set of experiments ("Set B experiments", see Methods) with different experimental parameters than the data from the set of experiments shown thus far ("Set A experiments," e.g. as shown in Figure 5.13). (A) Representative kymograph traces, representation analogous to Figure 5.13A. (B) Quantification of the density of Ase1-GFP(Methods). The numbers below the boxes show the number of analyzed microtubule bundles. (C) Rescue frequency and (D) depolymerization velocity, representations analogous to Figure 5.13B,E. Legend for B-D in C, showing the concentration of Ase1-GFP in each set of experiments. Panels taken from Krattenmacher et al. 2024, except panels C and D, which I created only for this thesis.

5.2.2 Ase1 herding by the depolymerizing microtubule end correlates with microtubule stabilization

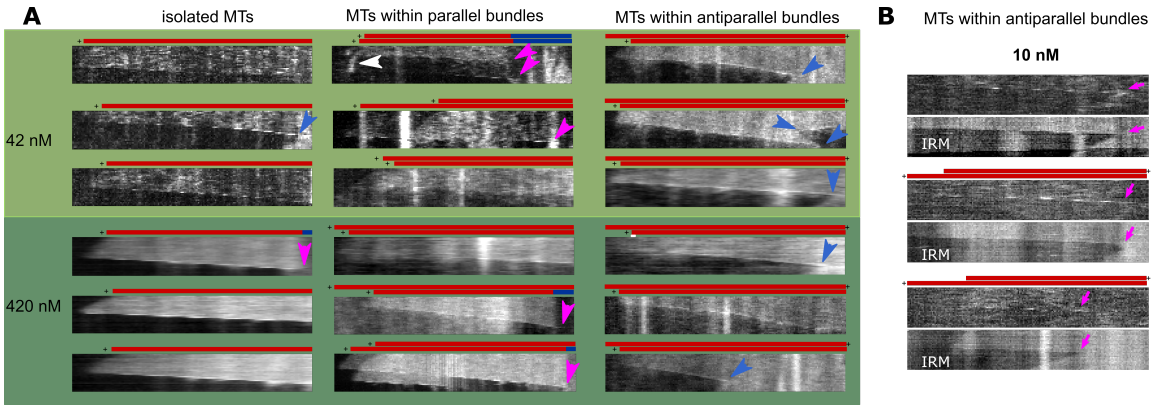

Figure 5.15: **Ase1 accumulates at the ends of depolymerizing microtubules.** Kymographs of depolymerization events (same experiments as shown in Figure 5.13). (A) Kymographs of all examined microtubule configurations at 42nM and 420nM Ase1. (B) Kymographs of events observed at 10nM Ase1 (antiparallel overlaps only, since at this concentration there was no Ase1-mNeonGreen signal at the ends of parallel overlaps and isolated microtubules). Each kymograph is 12 µm in width and 150 seconds in height; contrast and balance varies from panel to panel (each kymograph shows a different microtubule). To facilitate understanding of the kymographs, rescues are indicated with blue arrows. Pink arrows indicate microtubule tips reaching their GMPCPP seeds. The white arrow indicates an instance where one of the parallel microtubules, before catastrophing, had briefly engaged in antiparallel crosslinking with another isolated microtubule. Where no arrows are shown, the microtubules continue to depolymerize toward the right. Panels taken from Krattenmacher et al. 2024.

Given that we had shown that Ase1 can stabilize depolymerizing microtubules, we suspected that Ase1 molecules very likely interact directly with depolymerizing microtubule ends. This is indeed what we found when examining the distribution of Ase1. The kymographs which we had generated showed that Ase1 accumulated at depolymerizing microtubule ends, for Set A experiments (Figure 5.15A,B) as well as Set B experiments (Figure 5.16A). At the same time, it can be noted that Ase1 did show no preference for binding to polymerizing microtubule ends, as well as a preference for the GDP-lattice dynamic extensions of our microtubules rather than the GMPCPP-stabilized part, indicating a preference for compacted microtubule lattices (subsubsection 1.1.3.1). We now set out to quantify the accumulation of Ase1 at depolymerizing microtubule ends.

Because the data for Set B experiments allowed for a more fine-grained analysis due to a higher framerate and a more pronounced accumulation effect, we in the following limited our analysis to the Set B experimental data. Given that isolated and parallel microtubules behaved very similarly in our assays (though only in Set A experiments we observed a sufficiently high number of parallel overlaps for a thorough analysis), we also chose to focus on comparing isolated and antiparallel microtubules. Our quantitative analysis of Ase1 accumulation at depolymerizing microtubule ends confirmed the visual impression given by the kymographs — Ase1 was indeed accumulating at depolymerizing microtubule ends, for both isolated and antiparallel microtubules (Figure 5.16B). In addition, the quantitative analysis also revealed that the Ase1 accumulates were growing the quickest during the

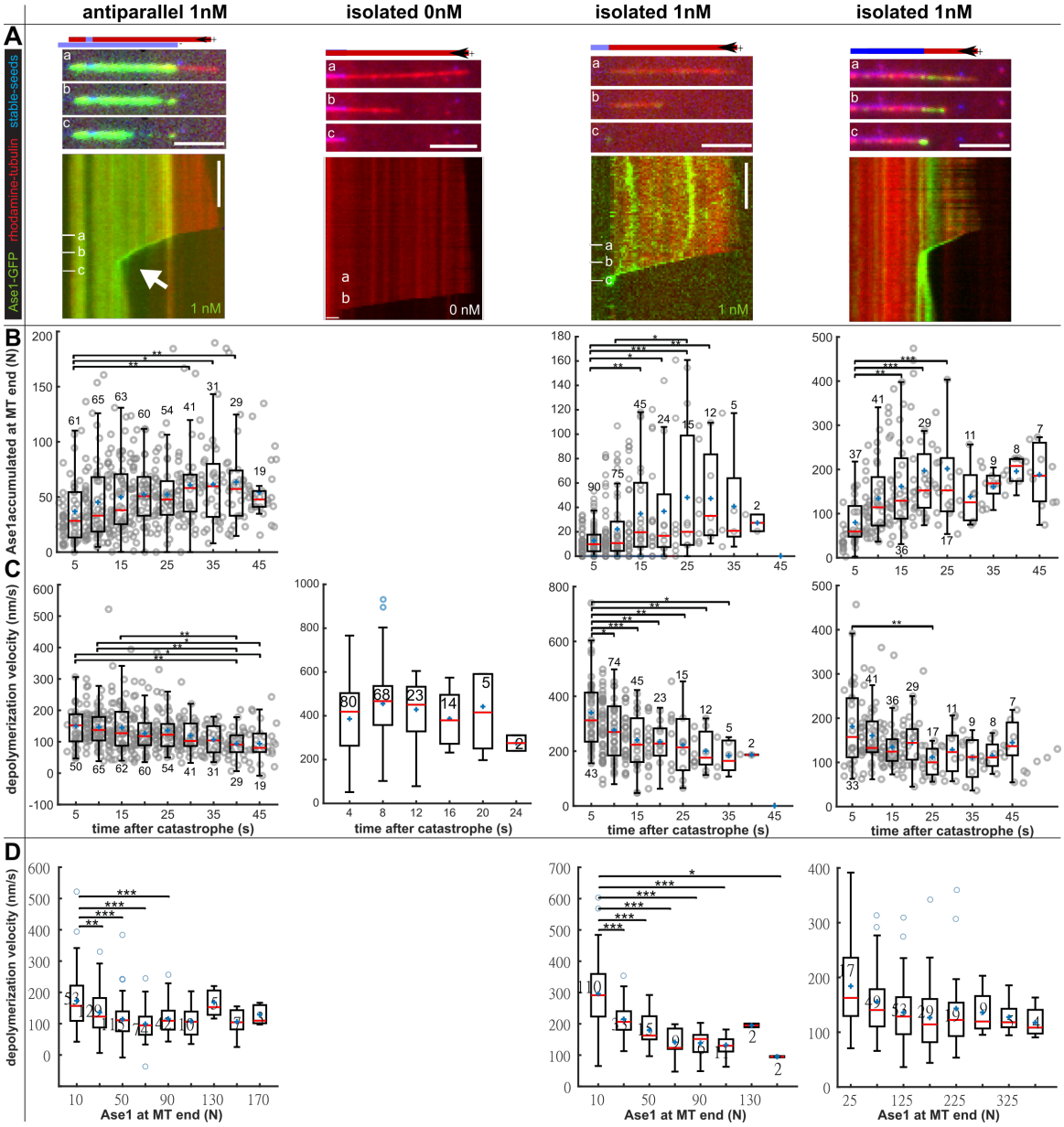

Figure 5.16: **Microtubule depolymerization slows down while Ase1 accumulates.** Experimental data on herding of Ase1 (same experiments as shown in Figure 5.14). (A) Kymographs of depolymerizing microtubules. The stabilized GMPCPP-microtubule seeds were labelled with 15% rhodamine and 15% Alexa647 (or, alternatively, with 2% Alexa647), with the free tubulin in solution being labelled with 7% rhodamine. In sketches, dynamic extensions with GDP lattices are colored red, and stabilized GMPCPP seeds are colored blue or light blue (in case of the weakly-labelled seeds). The scale bars are 5 micron and 1 minute, contrast and balance vary from panel to panel (each kymograph shows a different microtubule). White arrows highlight rescue events. We observed a clear preference of Ase1 molecules for binding to the dynamic extensions rather than the GMPCPP-stabilized parts of microtubules, as can be seen here (not explicitly pointed out in Krattenmacher et al. 2024). (B) The number of additional Ase1 molecules observed at the end of depolymerizing microtubules, plotted over the time passed since the catastrophe. Each data point represents data extracted from one line scan. (C) The frame-to-frame depolymerization velocity of microtubules over time (analogous to B) (because the exact time of catastrophe is unknown due to limits in temporal resolution, the velocity measurement right after catastrophe underestimates the actual velocity). (D) Instantaneous depolymerization velocity plotted over number of additional Ase1 molecules at the microtubule end. Panels taken from Krattenmacher et al. 2024.

early stages of depolymerization (Figure 5.16B). Intuitively, one may expect that this accumulation is related to the stabilization of microtubules during depolymerization. Indeed, Ase1 accumulation correlated with a decrease in depolymerization speed (Figure 5.16B-D). While this correlation does not imply a causal relationship, it does lend support to the existence of such a relationship. An alternative explanation could be a possible hidden third factor, most notably the natural slowdown of depolymerization velocity after catastrophe which has been observed by others (Luchniak et al. 2023). In other words, it is conceivable that depolymerizing microtubules accumulate Ase1 and slow down over time, and that these two phenomena are not causally related. However, in the absence of Ase1 we had not observed any slowdown in microtubule depolymerization comparable to what we observed in the presence of Ase1 (Figure 5.16C).

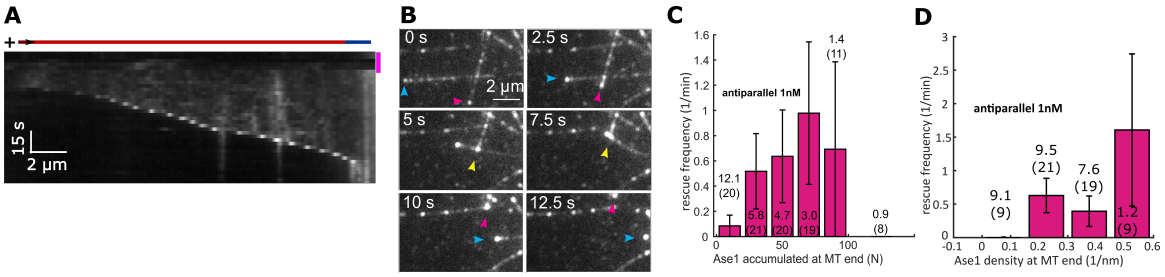

Figure 5.17: **Ase1 is herded by depolymerizing microtubules.** (A) Kymograph (Ase1-mNeonGreen channel) of depolymerizing microtubule. In this experiment, Ase1 and tubulin had been removed from the assay buffer. This removal (performed during the time frame indicated by the pink bar next to the kymograph) prompted subsequent microtubule depolymerization and concomitant Ase1 accumulation at the end. (B) Time series of micrographs (Ase1-GFP channel) showing an event where the herded Ase1 at one depolymerizing microtubule end (indicated by red arrows) causes the end to "drag" a microtubule it crosses with it, thereby bending it (yellow arrows). The blue arrows indicate the (depolymerizing) end of the microtubule before and after it got bent. (C) Rescue frequency plotted over number of herded Ase1 molecules at the microtubule end. The duration depolymerized at a respective x-value was added to the respective bin. The number of rescues observed in the same bin (N) was divided by the sum of depolymerization durations (shown in min, the number in parentheses refers to the number of microtubules) to estimate the rescue frequency. The correlation coefficient (weighted (Pelletier 2024) by sums of depolymerization durations) is 0.67. The total length of a given error bar equals two times the square root of the number of the rescues in the corresponding bin divided by the sum of the time microtubules spent depolymerizing in the corresponding bin. (D) Rescue frequency plotted versus the height of the peak of the Ase1 density at the microtubule end (the weighted correlation coefficient is 0.76). Representation analogous to C. C and D show data from same experiments as Figure 5.14. Panels taken from Krattenmacher et al. 2024.

Our findings so far suggested that we observed "herding" (Al-Hiyasat et al. 2023) of Ase1 by the depolymerizing microtubule end, a phenomenon which has recently been reported for a synthetic microtubule crosslinker (Drechsler et al. 2019) and the microtubule-severing enzyme spastin (Y. W. Kuo et al. 2019). To confirm this, we needed to exclude the possibility that Ase1 specifically tracks depolymerizing microtubule ends by having a higher affinity for depolymerizing microtubule regions. We thus performed an experiment where we removed both Ase1 and tubulin from solution after first having polymerized Ase1-decorated microtubules. We found Ase1 to still accumulate at the ends of depolymerizing microtubule (Figure 5.17A), indicating that the accumulates are indeed comprised of Ase1 molecules that were already bound to the microtubule lattice before catastrophe had occurred. As

reported for the synthetic polymer (Drechsler et al. 2019), we also observed instances of depolymerizing microtubule ends which herded Ase1 molecules pulling on other microtubules (Figure 5.17B). This indicates that substantial forces can be transmitted via Ase1 herding.

What is the impact of Ase1 herding on the depolymerization of antiparallel microtubules in particular? Similarly to what we found in subsection 5.2.1, we found that the impact of single Ase1 molecules on the depolymerization of antiparallel microtubules is stronger than in the case of isolated microtubules: While isolated microtubules at 6nM Ase1 herded more Ase1 than antiparallel microtubules at 1nM Ase1, they did not depolymerize more slowly than antiparallel microtubules (Figure 5.16B,C). For antiparallel microtubules, we also observed the number of herded Ase1 molecules to positively correlate with the probability of a rescue occuring (Figure 5.12C). Moreover, the Ase1 density at the microtubule end, which is a measure for not only accumulated Ase1 but the total number of Ase1 molecules present at the end, also shows a positive correlation with rescue frequency (Figure 5.12D).

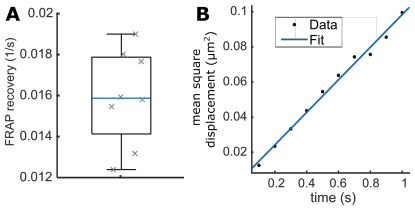

Figure 5.19: **Experimental determination of the diffusion coefficient and off-rate of Ase1.** (A) Observed FRAP recovery times on isolated microtubules (see Methods); the median value was used as k_{off} for modelling. (B) Mean square displacement of single Ase1 molecules diffusing on isolated microtubules during the first second of their interaction with the microtubule (see Methods) and fitted line; the slope of the fitted line D was used for modeling ($kh = Da^2$, with a being the tubulin dimer length) (number of molecules = 2008). Panels taken from Krattenmacher et al. 2024.

Our experiments thus demonstrate that lattice-bound Ase1 molecules are herded by the depolymerizing microtubule ends and that the number of swept Ase1 molecules correlates with reduced depolymerization. Yet how do these effects relate to each other? We set out to tackle this question by mathematically modeling Ase1 herding, focusing on the relation between depolymerization velocity and Ase1 accumulation. We thus developed a simple mathematical model that considers a one-dimensional microtubule made of lattice sites corresponding to tubulin heterodimers, starting at the plus end (see Methods). The model neglects the interaction between protofilaments, and for simplicity focuses on the effect of Ase1 on the depolymerization velocity of isolated microtubules. Events such as Ase1 binding, unbinding, and hopping to neighboring sites are stochastic with constant rates k_{on}, k_{off}, k_h (Figure 5.13A). These rates were determined experimentally, via velocity measurements of depolymerizing microtubules under the absence of Ase1 (Figure 5.16C, mid panel), fluorescence recovery after photobleaching (FRAP) experiments (Figure 5.19A) and tracking of single Ase1 molecules diffusing on isolated microtubules (Figure 5.19B). Importantly, in the model, only one Ase1 molecule can be attached to any one tubulin heterodimer, and Ase1 can thus only hop to unoccupied neighboring sites. We also assume that Ase1 does not fall off from the microtubule by hopping at its plus ends, as shown experimentally (Braun, Lansky, et al. 2011). Microtubule depolymerization is modelled stochastically by detachment of the terminal subunit, at a rate that is affected by Ase1 (Figure 5.13B). Specifically, this rate is k_d^0 when the first tubulin subunit is free of Ase1, and $k_d = (1 - \Omega)k_d^0$, if Ase1 is bound at the terminal

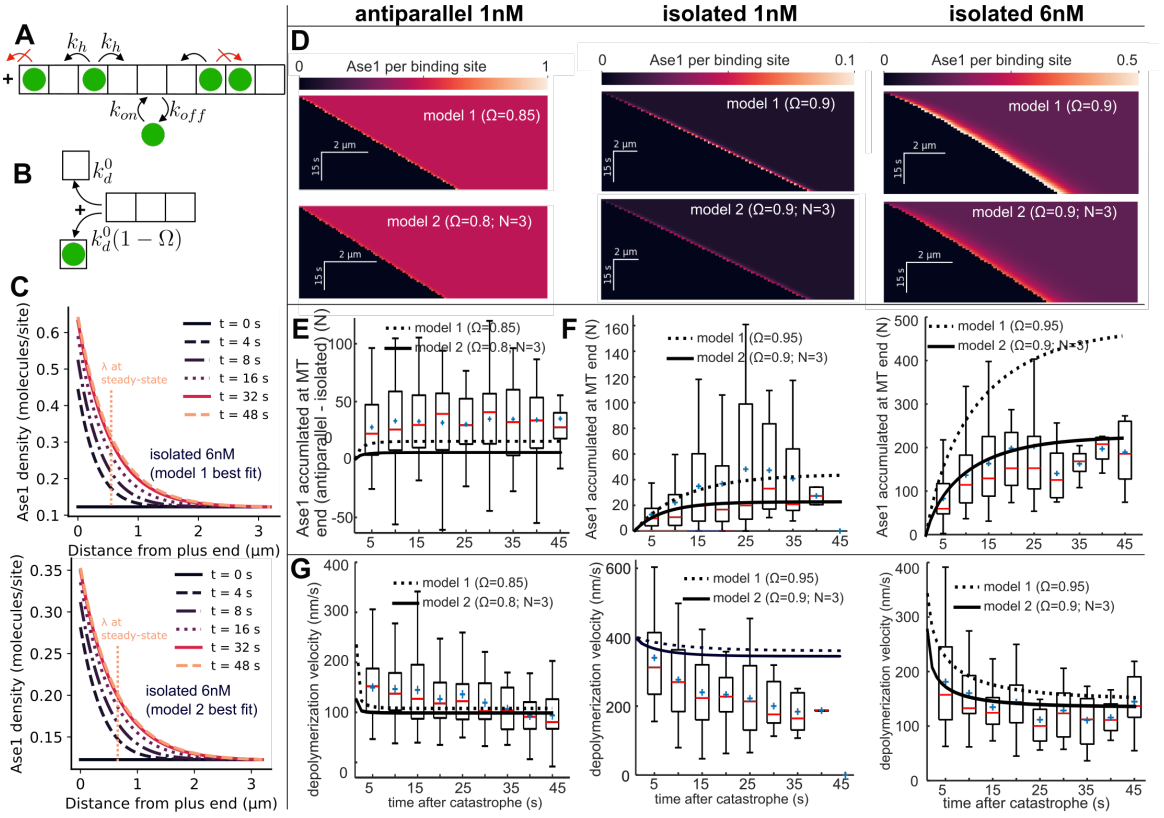

Figure 5.18: **Modeling of Ase1 herding — results.** (A,B) Cartoons representing model assumptions (see Methods): (A) Ase1 binding, unbinding, and hopping to neighboring sites are modeled as stochastic events with constant rates k_{on}, k_{off}, k_h. Maximally one Ase1 molecule can be attached to any one tubulin heterodimer, so moving or binding to an occupied binding site is not allowed (red crossed arrow on the right). Moreover, Ase1 does not fall off from the microtubule by hopping at its plus ends (red crossed arrow on the left). (B) In the case of Model 1, we assume that the detachment rate of the tubulin terminal subunit is k_d^0 when the first tubulin subunit is free of Ase1, and $k_d = (1-\Omega)k_d^0$ if Ase1 is bound at the terminal site (for Model 2, see Main Text and Methods). (C) Spatial distribution of Ase1 density on terminal sites for the indicated timepoints (see legend) as predicted by Model 1 and 2 with model parameters as in F (right panel). λ, a characteristic x-axis location (see Methods), is visualized for the steady-state curve. (D-G) Modelling results for Model 1 and Model 2 with N=3 (for both models; 3 PFs had been assumed to be engaged in crosslinking in the case of antiparallel microtubules, see Methods). Experimental data is presented in the form of boxplots. (D) Distribution of Ase1 density in time represented as simulated kymographs (see scalebars; in the case of antiparallel microtubules, values are for the PFs engaged in crosslinking, the other PFs are assumed to have 0 coverage). (E) Number of crosslinked Ase1 molecules plotted over time after catastrophe. As an estimate of the number of crosslinked Ase1 molecules, the following is represented by the y-axis position: The number of additional Ase1 molecules at the end of a depolymerizing antiparallel microtubule at a given time (Figure 5.16B, left panel) minus the median number of additional Ase1 molecules at the ends of isolated microtubules in the same experiment as a given antiparallel microtubule (at the same time after catastrophe) (Figure 5.16B, mid panel). (F,G) Values of Ase1 accumulation and depolymerization velocity as derived from experiments (boxplots) or as predicted by Model 1 and 2 (lines). The boxplots in F and G are the same as in the corresponding plots in Figure 5.16. Panels taken or slightly adapted from Krattenmacher et al. 2024.

site. The value of k_d^0 is set by the microtubule depolymerization velocity in the absence of Ase1, measured experimentally (Table 5.1). The parameter $\Omega \in [0,1]$ specifies the effect of Ase1 on depolymerization. If $\Omega = 0$, Ase1 has no effect, while if $\Omega = 1$, the terminal subunit cannot unbind if Ase1 is bound. For any value $\Omega > 0$, this simple model leads to an exponentially-declining accumulation of Ase1 near the depolymerizing end (Figure 5.18C).

The accumulation occurs because subunits without Ase1 are more likely to be lost at the plus end, so depolymerization increases the density of Ase1 at the depolymerizing end. At steady state, the system can be characterized by the probability P_1 of the terminal site to be occupied, and the rate of subunits loss is $k_d = k_d^0(1 - \Omega P_1)$.

Parameter	Value(s)		Source
MT depolymerization rate at 0 Ase1	rate equivalent of 400 nm/s		Figure 5.16C, mid panel
Ase1 off-rate (k_{off})	0.016 s^{-1}		Figure 5.19A
Ase1 diffusion coefficient, isolated MTs	0.09 $\mu m^2/s$		Figure 5.19B
Ase1 diffusion coefficient, antiparallel MTs	0.011 $\mu m^2/s$		8 times lower than isolated MTs (Lansky et al. 2015)
Ase1 on-rate (k_{on})	Isolated 1nM	0.00012 s^{-1}	Calculated from experimentally measured k_{off} and equilibrium density on MT (Figure 5.14B)
	Isolated 6nM	0.00224 s^{-1}	
	Antiparallel (3 PFs)	0.01369 s^{-1}	
Tubulin dimer/binding site length (a)	8nm		Song et al. 1995

Table 5.1: **Model parameters that are experimentally constrained.** MT = microtubule. PF = protofilament.

Measurement	Value and 95% confidence interval		Source
Timescale of accumulation (τ)	Isolated 1nM	6.1 [3.5, 11.4] s	Fit of data shown in Figure 5.18E,F to $A_{end}(1 - e^{-t/\tau})$
	Isolated 6nM	7.2 [5.5, 11.4] s	
	Antiparallel	2.4 [1.2, 4.9] s	
Molecules accumulated at steady state, per MT (A_{end})	Isolated 1nM	22 [17, 29]	
	Isolated 6nM	185 [160, 247]	
	Antiparallel	31 [24, 41]	
Depolymerization velocity at steady state	Isolated 1nM	226 [194, 254] nm/s	Average value after 20 seconds of depolymerization
	Isolated 6nM	137 [122, 151] nm/s	
	Antiparallel	117 [108, 125] nm/s	

Table 5.2: **Experimental measurements that are compared with model predictions.** Confidence intervals (95%) are calculated with the bootstrap method (see Methods). MT = microtubule.

All parameters of this model (Model 1) were set from experimental measurements except for Ω. Therefore, we tested whether any value of Ω could quantitatively recapitulate the experimental behavior of isolated microtubules. We chose to focus on the 6nM Ase1 condition, as the case of antiparallel microtubules is structurally more complex (see Discussion), and as our mean field approach may not be suitable for the low Ase1 densities we observed for isolated microtubules at the 1nM Ase1 condition. Specifically, we aimed to reproduce the timescale of accumulation of Ase1, and the total amount of Ase1 accumulated and depolymerizing velocity reached at steady state (Table 5.2). For $\Omega = 0.95$, the model predicted depolymerization

velocities comparable to the ones observed experimentally (Figure 5.13G, right panel), but the timescale and number of Ase1 molecules accumulated at steady state were respectively two and three times higher than experimentally observed (Figure 5.13F, right panel). Therefore, despite recapitulating the experimental phenomenology qualitatively (Figure 5.13D, right panel), this first model was insufficient to quantitatively reproduce our experimental results.

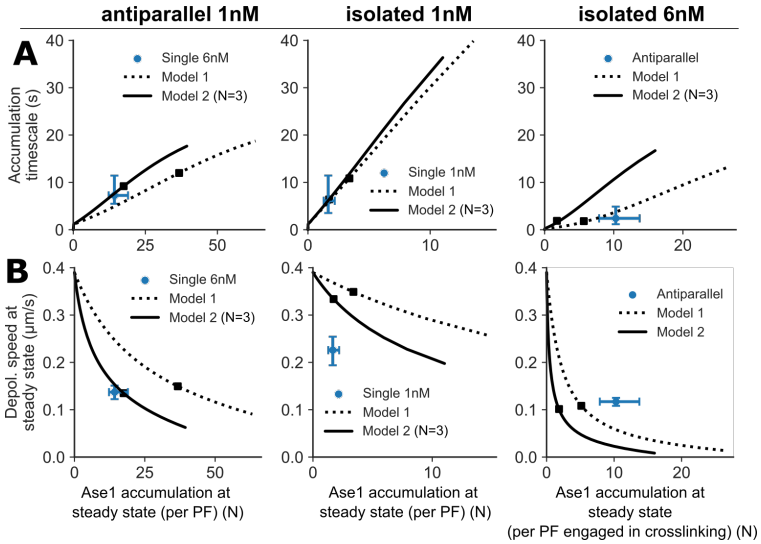

Figure 5.20: **Steady-state analysis of the mathematical models.** (A) Values of depolymerization velocity and Ase1 accumulation at steady state derived from experiments (blue dot) or predicted by Model 1 and 2 (lines). Experimental values were derived from the depolymerization events shown in Figure 3, and the error bars represent 95% confidence intervals calculated using the bootstrap method (see Table 5.2 and Methods). The lines represent all the solutions of each model from $\Omega = 0$ to $\Omega = 1$, with $N = 3$ for Model 2. Black squares mark the parameter values of Ω that best fit the experimental data: Model 1 with $\Omega = 0.95$ and Model 2 with $\Omega = 0.9$ for isolated microtubules (assuming 13 PFs), and Model 1 with $\Omega = 0.85$ and Model 2 with $\Omega = 0.8$ for antiparallel overlaps (assuming 3 crosslinking PFs). PF = Protofilament. (B) Same as A, with accumulation timescale in the x axis.

The failure of Model 1 indicated that Ase1 should affect microtubule depolymerization at lower density. We thus hypothesized that Ase1 molecules located at lattice sites other than the terminal one could affect depolymerization. Therefore, we tested the possibility that the rate of tubulin subunits loss at the plus end would be reduced by a factor $(1 - \Omega)$ if any of the N terminal sites were occupied. This rate at steady state would then be $k_d = k_0^d[1 - \Omega 1 - \prod_{i=1}^{i=N}(1 - P_i)]$, where P_i is the probability of site i being occupied by Ase1. N is not experimentally constrained, but the range of possible values is small, since it is unlikely that distant tubulin subunits could affect the detachment of the terminal subunit. For $N = 3$ and $\Omega = 0.9$ this model (Model 2) recapitulated the dynamics of the system (Figure 5.18F,G, right panels) and reproduced microtubule depolymerization velocity and Ase1 accumulation at steady state and Ase1 accumulation timescale (Figure 5.20). The model predicts that at steady state Ase1 density should decay exponentially from the plus end with a length scale of around 600nm (Figure 5.18C). Experimentally, we observed a decay of Ase1 signal from the plus end with length scale of around 200 nm (Figure 5.21A).

Using Model 2 with the same value of $\Omega = 0.9$, we could recapitulate the Ase1 accumulation timescale and steady state accumulation in isolated microtubules with 1nM of Ase1 (Figure 5.18F), but the model predicted a 15% decrease with respect to the maximum velocity while the experimentally observed decrease was between 35% and 50% (Figure 5.18G, Table 5.2). The reason for this disagreement is likely the low density of Ase1 molecules at 1nM

concentration (<1% of tubulin dimers bound to Ase1 in the body of isolated microtubules vs. 12% at 6nM of Ase1). At this very low density, the stochasticity of the system may not be well captured by our mean field approach (see Methods). The model also fails to reproduce the behavior of antiparallel overlaps (Figure 5.18E,G left panel, Figure 5.20 left panels). In the discussion, I bring forward potential explanations for the discrepancies we observed.

In summary, we have shown that Ase1 hampers the depolymerization of microtubules, particularly for antiparallel overlaps. It does so by slowing down depolymerization, and in the case of antiparallel overlaps also by increasing the rescue frequency. We moreover showed that Ase1 is herded by depolymerizing microtubules, and that this effect can likely be explained simply by a putative tendency of Ase1 to block the dissociation of terminal tublin subunits it is bound to or neighbours.

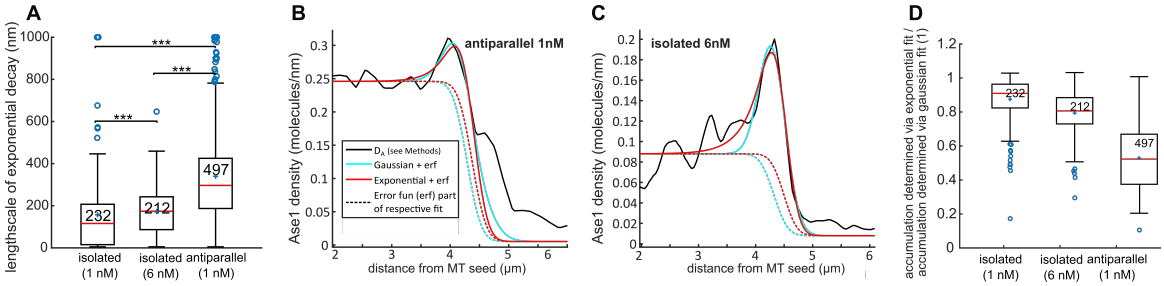

Figure 5.21: **Difference between the distribution of Ase1 on antiparallel and isolated microtubules.** (A) Fitting results for the lengthscale of the exponential decay λ for all fitted density profiles D_A(as described in the methods). *** p<0.001 (Tukey's test). (B) An example Ase1 density profile D_A and visualized fitting results for an antiparallel overlap midway during depolymerization. The microtubule seed is on the left, and depolymerization proceeds toward the left. The yellow region shows the fitted region between X_{Dsleft} and $X_{Dsright}$ (Methods). (C) An example Ase1 density profile D_A visualized fitting results for an isolated microtubule midway during depolymerization (representation analogous to B). (D) The number of accumulated Ase1 molecules as determined by the exponential (plus error function) fit divided by the number of accumulated Ase1 molecules as determined by the gaussian (plus error function) fit (numbers as determined for each respective density profile). Panel A taken from Krattenmacher et al. 2024, the others I created only for this thesis. Data from same experiments as shown in Figure 5.14.

Discussion

6.1 Tau

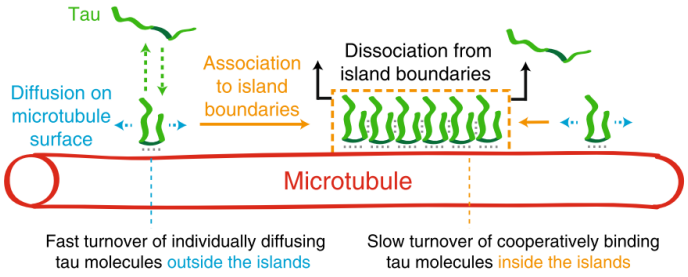

Figure 6.1: **Schematic representation of island formation.** Tau molecules bind and unbind with high rates to microtubules, on which they diffuse (fast turnover). When encountering an island (dashed orange box), Tau molecules cooperatively associate with the island at its boundaries, rendering the Tau molecules stationary, decreasing their unbinding rate (slow turnover), and causing the island to grow in size laterally. Tau molecules from solution can only bind to the inside of an island via displacement of an island-associated Tau molecule, resulting in the observed concentration-dependent turnover of Tau inside islands. After removal of Tau from solution, Tau molecules dissociate from the island boundaries, making the island shrink in size laterally.

In our investigation of Tau interactions with microtubules, we have contributed to our understanding of the distinct binding modes of Tau to the microtubule, thereby contributing to our understanding of potential molecular mechanisms governing axonal microtubule arrays. While the diffusive binding mode of Tau to microtubules was already well-described, our key contribution is that Tau can cooperatively bind to form cohesive islands on the microtubule. Our findings, coupled with complementary work by R. Tan et al. 2019, paint a detailed picture of Tau's multifaceted behavior on microtubules.

The cooperative binding mode results in a population of stationary Tau molecules characterized by remarkably low turnover rates. This is in contrast to the diffusive mode, where Tau molecules exhibit high turnover rates. At physiological concentrations, these two distinct populations coexist on the microtubule surface. It is possible that these islands have not yet been described is because the rapidly turning over Tau has the potential to mask the underlying island structures, adding a layer of complexity to the visualization and study of these formations Figure 6.1. It is also possible that Mcvicker et al. 2014 had already

observed the cooperative binding mode underlying the formation of Tau islands, given that they describe the association of a small number of Tau molecules and a concomitant marked reduction of the diffusion coefficient of Tau. This view is supported by their observation that these small Tau complexes only formed on paclitaxel-stabilized microtubules, but not on GMPCPP-stabilized microtubules, which aligns with the same observations by R. Tan et al. 2019 regarding the formation of Tau islands. That Mcvicker et al. 2014 did not observe "fully formed" islands could potentially be explained by different assay conditions, e.g., the use of a different buffer. Also, Mcvicker et al. 2014 used a lower Tau concentration (5nM). In case of the condition at which they did use a high concentration (300nM), most of the Tau was not labeled, hence it is possible that islands were present in the assay but not visible.

We measured a characteristic density within Tau islands of approximately 0.26 Tau molecules per tubulin dimer. This value would indicate the formation of an ordered monolayer, likely involving all four microtubule-binding repeats of Tau, as suggested by the cryo-EM study by Kellogg, N. M. A. Hejab, et al. 2018 (see subsubsection 1.2.1.1). It bears noting that the diffusive, rapidly turning over Tau population likely is too elusive to detect in these structural studies due to its transient and fast-moving nature. In addition, this type of binding may reflect the intrinsically disordered nature of Tau, and thus not result in any favored binding conformations where an averaging of multiple binding events would lead to an increase in resolution.

The integrity of Tau islands appears to hinge on cooperative interactions between the constituent molecules. This cooperativity could stem from direct Tau-Tau interactions, a hypothesis supported by previous studies demonstrating Tau's propensity for liquid-liquid phase separation (Hernández-Vega, Braun, Scharrel, Jahnel, Wegmann, Bradley T Hyman, et al. 2017a) and its ability to form neurofibrillary tangles when hyperphosphorylated (Iqbal et al. 2016). Alternatively, or perhaps additionally, this cooperativity might arise from local Tau-induced impacts on the microtubule lattice. Such modifications could conceivably translate along the microtubule lattice to adjacent binding sites, thereby enhancing the affinity for incoming Tau molecules. This possibility is supported by two observations:

1. Within regions of high microtubule curvature, in contrast to surrounding regions, we observed Tau binding to persist after Tau had been removed from solution, a characteristic it shared with Tau molecules within Tau islands.

2. R. Tan et al. 2019 had reported that islands did not grow on GMPCPP-stabilized microtubules. GMPCPP lattices feature a higher axial repeat, in other words, an expanded lattice when compared to paclitaxel-stabilized microtubules (subsubsection 1.1.3.1).

I had thus hypothesized that Tau islands may require a specific spacing of tubulin dimers to accommodate a proper binding of all microtubule binding repeats. This spacing, I hypothesized, was given both in the case of high-curvature regions as well as within island regions (on paclitaxel-stabilized microtubules).

- In the case of islands, a favorable microtubule region would at first allow for island

nucleation, upon which these initial Tau molecules would change the spacing of tubulin dimers in their vicinity, allowing for additional Tau molecules to bind, leading to island growth.

- In the case of high-curvature regions, it is clear that the tubulin dimers are spaced differently than on straightd microtubule regions. In the inside of the curved region, tubulin dimers are closer to each other, while on the outside, dimers are further apart from each other. Thus, if the stationary Tau binding mode indeed possesses a preference for a different lattice spacing than given on a (undecorated) straight microtubule, it appears likely that this binding mode does occur on some parts of curved microtubules (likely on the inside, given that the non-binding to GMPCPP lattices indicates a preferences for compacted lattices). Importantly, this type of stationary binding would not require any cooperative behavior, and would even preclude such cooperative binding and its concomitant shielding of the microtubule from Katanin severing, as we had observed, see e.g. Figure 5.9F-H (given mechanical constraints set by the microtubule and the antibodies it is bound to, though we did frequently observe Tau islands to straighten curved microtubule regions).

Indeed, this hypothesis was confirmed in a follow-up study by my former colleague Valerie Siahaan and collaborators: They found that the cooperative Tau binding mode of Tau depends on and stabilizes a compacted microtubule lattice (Siahaan, R. Tan, et al. 2022). As a small deviation from my initial reasoning above, while the slightly lower axial repeat of paclitaxel-stabilized microtubules as compared to GMPCPP-stabilized microtubules may facilitate initial binding, the main reason for why islands can form on paclitaxel-stabilized microtubules appears to be that cooperative Tau binding displaces paclitaxel from its binding site, further compacting the lattice to an axial repeat similar to that of unstabilized GDP lattices (Siahaan, R. Tan, et al. 2022). Indeed, Siahaan, R. Tan, et al. 2022 found Tau to readily bind cooperatively to unstabilized GDP lattices, and the introduction of paclitaxel to cause the destabilization of Tau islands and Tau unbinding.

Given that some MAPs are known to affect the spacing of tubulin dimers, one is tempted to ask whether regulation of the microtubule axial repeat is a common feature of MAP regulation. For example, kinesin-1 is known to expand the microtubule lattice (Peet et al. 2018), which could explain why it does not bind to island regions as shown by Valerie's work for our article showed cannot enter Tau islands (and the associated compacted microtubule lattice) (Siahaan, Krattenmacher, et al. 2019). Thus, Siahaan, R. Tan, et al. 2022 have also investigated whether the other members of the Tau/MAP2/MAP4 family bind cooperatively to the lattice. They found that while MAP4 does not form islands, MAP2 does, and that MAP2 can form islands together with Tau (while MAP4 does not partition into these islands). The indirect interplay of different MAPs on microtubules via changes of the microtubule lattice could add another dimension to MAP sorting and regulation. For example, MAP7 and Tau exclude each other when binding to the microtubule, and, oppositely to Tau, MAP7 recruits kinesin-1 binding to the microtubule Monroy et al. 2018, which could point to

such an indirect lattice-based interplay. It is conceivable that the displacement of Tau by kinesin-8/Kip3 could also constitute an instance of such an interplay: Given that kinesin-1 has been found to expand the microtubule lattice, it appears possible that kinesin-8 may also cause lattice expansion, thereby causing the disassembly of Tau islands. However, a point against such a hypothesis is the fact that Kip3 has been observed to have a higher affinity for taxol-stabilized microtubules than for GMPCPP-stabilized microtubules (Arellano-Santoyo et al. 2017), which is the opposite of what has been observed for kinesin-1 (Nakata et al. 2011). Importantly, this could explain our finding that Kip3 can penetrate Tau islands while kinesin-1 cannot.

It also is tempting to speculate that the absence of Tau from highly curved microtubules *in vivo* may fulfill a regulatory purpose by allowing for a Katanin-mediated removal of ill-positioned microtubules. In this respect, it should be noted that another MAP, doublecortin, has already been shown to both bind to microtubules cooperatively and bind to curved microtubule regions as well (Bechstedt and Brouhard 2012; Bechstedt, Lu, et al. 2014). Bechstedt and Brouhard 2012 had also found doublecortin to be sensitive to the number of protofilaments of a given microtubule, in particular, it appeared to stabilize 13-protofilament microtubules. Interestingly, in a different study, Tau had also been found to be sensitive to protofilament number, apparently stabilizing 14-protofilament microtubules (Choi et al. 2009). Indeed, 14-protofilament-microtubules were the most common microtubule population in the study by Kellogg, N. M. A. Hejab, et al. 2018. These similarities of Tau are particularly notable as doublecortin does not share any sequence homology with Tau, and in particular it appears to be more ordered, with its two repeat domains forming globular structures (Moores et al. 2004). A better comparative understanding of the features of Tau and doublecortin may be insightful for exploring the mechanisms underlying these features. Moreover, both doublecortin and Tau are located in neurons, and in contrast to MAP2, doublecortin does not share a binding site with Tau (Moores et al. 2004). Thus, it would be interesting to explore the potential interplay of these MAPs on the microtubule surface *in vitro*, which to my knowledge has not yet been done.

It is also interesting to note that the protection of microtubules from severing by Katanin could also serve to indirectly decrease the nucleation of new microtubules along the axonal shaft, given that Katanin activity can result in more microtubules (subsubsection 1.2.1.2). As a final point regarding Katanin, the fact that islands under the presence of Katanin depolymerized from their ends appears to reflect the microtubule-depolymerizing activity of Katanin which has been found to be distinct from its severing activity (Belonogov et al. 2019).

Another intriguing observation from our study was that Tau unbinding from islands increases with rising Tau concentration in solution. Importantly, this phenomenon cannot be attributed solely to the rapidly turning over Tau pool that co-localizes with islands at elevated concentrations. At 20 nM and 100 nM Tau, this pool accounts for only approximately 20% and 40% of the total Tau in the islands, respectively, while the average unbinding time drops

by two orders of magnitude. We propose that this concentration-dependent unbinding results from the multivalent attachment of island-incorporated Tau, mediated by its four microtubule-binding repeats and potential Tau-Tau interaction sites. Such concentration-dependent unbinding mechanism has been previously reported for other multivalently interacting macromolecules, in the case of microtubules as well as DNA (Sing et al. 2014; Lansky et al. 2015). Specifically, our model suggests that the multiple interaction sites undergo transient cycles of unbinding and rebinding. At low Tau concentrations, transiently released bonds are likely reestablished as partially-bound Tau molecules remain anchored to the microtubule by their persisting binding sites. However, with increasing Tau concentration in solution, it becomes increasingly probable that a binding site of a solution-phase Tau molecule establishes a bond to a temporarily-vacated binding site on the microtubule. This process could sequentially replace an island-incorporated Tau molecule, one bond at a time. Similarly, a step-by-step displacement mechanism could also be at play in the case of kinesin-8-driven island disassembly.

Beside probing the mechanisms behind the displacement of Tau islands by Kip3, our results further suggest an intriguing avenue for further research in this respect. For example, one can envision cycles of island growth, kinesin-8 traffic jam formation at island boundaries, eventual overwhelming and disassembly of the island by Kip3, propagation of the traffic jam as a high-density "pulse" along the microtubule, followed by island regrowth and repetition of the process. This dynamic interplay could potentially result in pulsatile kinesin-8 movement along axonal microtubules, adding another layer of complexity to cellular transport regulation.

All of the above points, the consistent density of islands, of 0.26 Tau molecules per tubulin dimer, the (now-confirmed) dependence of the cooperative binding mode on a specific lattice constant (Siahaan, R. Tan, et al. 2022) as well as the concentration-dependence of Tau unbinding from island regions hint at an integral role of the microtubule binding repeats in the cooperative binding mode. Our (not-yet-published) findings regarding the ionic strength dependence of island stability (Figure 5.6) provide further support for the involvement of microtubule binding repeats in cooperative binding. We observed optimal stability at 75mM KCl, suggesting a delicate balance between hydrophobic interactions, likely mediated by the repeats, and ionic interactions, potentially mediated by the more positively-charged C-terminal domain of Tau (subsubsection 1.2.1.1). The stronger diffusive mode at 0mM KCl indeed implies a predominance of ionic bonds in this binding mode and is consistent with the findings of Hinrichs et al. 2012 who found the Tau diffusion coefficient to decrease with decreasing ionic strength. These ionic strength dependencies could also explain the varying stationarity of Tau molecules within islands at different KCl concentrations. At lower KCl concentrations, single Tau molecules within islands were less stationarily bound, potentially switching binding modes more frequently and often having only a subset of their microtubule binding repeats engaged.

Our findings can also be interpreted as supporting the feasibility of the polymer brush model of microtubule spacing in axonal microtubule arrays. As mentioned in section 5.1,

the N-terminal domain of Tau determines the spacing between axonal microtubules. The argument by Mephon-Gaspard et al. 2016 against the polymer brush model was that the stoichiometry of Tau:tubulin in the axon is likely too low for Tau-decorated microtubules to be repelled from each other, as Tau molecules can simply diffuse away from the inter-microtubule space, is weakened due to points:

1. Our study supports the model that one (full-length) Tau molecules binds 4 tubulin dimers, which reduces the required number of Tau molecules to fully cover the microtubule compared to models where Tau binds to e.g. only 1 tubulin dimer.

2. Moreover, within Tau islands, diffusion is greatly reduced, thus it is thinkable that Tau islands interspersed on a given microtubule would be sufficient to keep microtubules apart, i.e. full coverage of the microtubule would not be possible. Curiously, a recent study employing super-resolution fluorescence imaging combined with antibody-based fluorescent labeling of all Tau isoforms reported that within rat neurons, Tau forms complexes interspersed on the microtubule (Gyparaki et al. 2021). These complexes in my view could potentially be Tau islands.

It bears noting that the model of 4-repeat binding of full-length Tau to the microtubule as supported by Kellogg, N. M. A. Hejab, et al. 2018 and our findings is in conflict with the model proposed by Mammeri et al. 2022. This is chiefly because the model proposed by Mammeri et al. 2022 would suggest each Tau molecule to bind only one tubulin dimer tightly. This binding is proposed to take place via the highly positively charged pseudorepeat R' and repeat R4, while the remaining repeats to progressively detach from the microtubule. It is important to note that this proposed binding mode would also constitute longitudinal binding to protofilaments and feature interactions with multiple tubulin dimers. Thus, it would not be incompatible with our proposed mechanism for concentration-dependent unbinding. Furthermore, the finding by Mammeri et al. 2022 that Tau binding is more unstable on GMPCPP-stabilized microtubules than on paclitaxel-stabilized microtubules appears consistent with our findings. However, the fact that the NMR spectra observed by Mammeri et al. 2022 did not differ significantly when cutting off the N-terminal domain of Tau (which we observed to be necessary for island formation) raises the possibility that their experimental conditions did not precipitate Tau island formation.

Finally, the comparatively high Tau island nucleation rate right after flushing in Tau (Figure 5.1G) implies that some microtubule regions are more suitable for the nucleation of Tau islands than others. This could be due to mechanical constraints related for instance to where a given microtubule is tied to the coverslip surface via an antibody. Another determinant of island growth could be post-translational tubulin modifications. Indeed, recent *in vitro* experiments have shown that polyglutamylation of tubulin results in a higher affinity of Tau for microtubules and a higher rate of island formation (Genova et al. 2023). Thus, Tau island formation may potentially serve as a readout of such modifications, which would in effect allow to amplify the impact of such modifications given the distinct and

striking interaction patterns of Tau islands with other MAPs. Vice versa, modifications of Tau could impact its ability to form islands. Indeed, the data presented in a recent preprint suggests that hyperphosphorylation of Tau negatively affects island integrity, decreasing their protection against severing by Katanin (Siahaan, Weissova, et al. 2024). One may wonder about the significance of these findings for the neuronal context, which is why it is notable that Siahaan, R. Tan, et al. 2022 had cultured cells with Tau fused to GFP, and upon introducing paclitaxel, had observed an unbinding of Tau conspicuously similar to the disassembly of Tau islands as we had reported in Figure 5.2. This strongly indicates that Tau islands indeed are a biologically relevant phenomenon. The implications of the findings presented in this thesis and in the work building on it thus extend to neurodegenerative diseases, where alterations in Tau's ability to form islands could trigger various downstream pathophysiological effects.

6.2 Ase1

In this study, we examined how the diffusible crosslinker Ase1 affects microtubule depolymerization, both when connecting microtubules and on individual microtubules. Our findings indicate that Ase1 reduces microtubule depolymerizing speeds and selectively enhances rescue frequencies of microtubules in antiparallel configurations, thereby stabilizing antiparallel overlaps while having minimal impact on parallel overlaps or isolated microtubules. In bipolar microtubule arrays like the mitotic spindle, this attribute of Ase1 could enable a selective stabilization of the array's central regions, while keeping the rest of the array dynamic and pliable.

How does Ase1 binding oppose microtubule depolymerization?

- It is possible that the binding of Ase1 induces changes in the microtubule lattice which stabilize it against depolymerization. Indeed, it has been found that microtubules decorated with Ase1 have a lower flexural rigidity than undecorated microtubules (Portran et al. 2013). Portran et al. 2013 had speculated that this may indicate that Ase1 may introduce structural changes to the microtubule lattice. However, no such changes were reported in the cryo-EM study by Kellogg, Howes, et al. 2016, though such potential changes seemingly were not the focus of that study. It bears noting that it appears unlikely that Ase1 stabilizes the (GDP) microtubule lattice in a similar manner as Kinesin-1, which expands the lattice, thereby bringing it into a more GTP-like state (Peet et al. 2018). This is because we observed Ase1 to preferably bind to GDP-lattices (Figure 5.16A), indicating that it prefers a compacted lattice.

- The putative protofilament-bridging characteristic of Ase1 (subsubsection 1.2.2.1) could plausibly cause the microtubule-stabilizing character of Ase1 as reported here. Namely, bridging protofilaments could oppose depolymerization by tethering protofilaments together, thereby preventing them from curling outward (subsubsection 1.2.2.1). Such

a potential stabilization due to the bridging of protofilaments could thus be understood as supporting the role of the microtubule lattice in straightening protofilaments.

Microtubule growth likely proceeds by incorporating slightly outward-bent protofilaments into the lattice while straightening them (Cross 2019). Thus, one may expect Ase1 to also increase microtubule polymerization rates if either of the above explanations is correct, as the stabilization of lateral tubulin bonds is hypothesized to be the mechanism by which the EB protein accelerates microtubules growth (Gudimchuk et al. 2021). The fact that we did not observe such an increase can be explained by our observation that Ase1 prefers to bind to GDP-lattices, i.e., not the GTP-dominated lattice at the tip of growing microtubules (contrary to what is the case for EB proteins).

What causes the markedly-pronounced stabilization of antiparallel microtubules in particular? Four potential mechanisms appear plausible.

- Within antiparallel overlaps, Ase1 diffusion constant and unbinding rates are greatly reduced (Kapitein, Janson, et al. 2008; Lansky et al. 2015), partly due to protein avidity resulting from the multivalent interactions of Ase1 with the microtubules (Braun, Diez, et al. 2020; Erlendsson et al. 2021). In other words, Ase1 molecules within antiparallel overlaps are less likely to unbind from a given binding site, and hence they can counteract microtubule depolymerization (via one or both of the mechanisms proposed above) for a prolonged timeframe when bound to a terminal tubulin dimer.

- Depolymerizing involves a bending of the tubulin subunits at the microtubule tip (subsubsection 1.1.2.3.) However, precisely this bending might be opposed by the other microtubule, as an outward-bending protofilament has to push against it. Under the absence of Ase1 in solution, this is not an issue (as we had shown in Figure 5.12), likely because the other microtubule can easily move away from the tip of the depolymerizing microtubule. However, it seems likely that such a movement would require more energy in the case of a crosslinked microtubule. Not only does it appear likely that the terminal Ase1 would oppose such a separation, but also all the other crosslinking Ase1 molecules in the vicinity of the tip, potentially resulting in a more stable microtubule tip structure allowing for regaining a GTP cap. One may expect this mechanism to apply to parallel overlaps as well. However, given the low affinity of Ase1 molecules to parallel overlaps, it appears plausible that Ase1 binds microtubules in a parallel conformation too weakly to make microtubule unzipping costly enough for it to noticably hamper microtubule depolymerization.

- Another potential mechanism increasing the stabilizing effect of Ase1 in the case of antiparallel overlaps could be the multimerization of Ase1 within antiparallel overlaps as reported by Kapitein, Janson, et al. 2008, a feature recently shown to play a crucial role in slowing motor-driven microtubule sliding (Alfieri et al. 2021). Ase1 multimers could enhance the (potential) capability of Ase1 to bridge multiple protofilaments.

- Lastly, crosslinking Ase1 could increase rescue frequency not due to its presence at the depolymerizing tip but by a putative mechanism based on GTP island creation. Here, the (antiparallel) crosslinking activity of Ase1 would increase the likelihood of lattice defects being incorporated into the lattice of a growing microtubule. For example, at the growing tip, a crosslink could potentially ocassionally be established between one of the growing protofilaments and the template microtubule, introducing conformational constraints which might lead to lattice defects. When later repaired by incorporation of free GTP-tubulin, such defects could result in the emergence of GTP islands and hence potential locations where rescues are more likely (subsubsection 1.1.2.3). This mechanism however cannot account for a correlation between increased rescue frequency at the tip and the number of herded Ase1 molecules at the depolymerizing tip.

The latter three of these proposed mechanisms could potentially account for the qualitative difference we observed between antiparallel and isolated microtubules, namely that Ase1 promoted rescues only in the case of antiparallel microtubules.

In addition to having observed a selective stabilization of antiparallelly crosslinked microtubules, we also observed herding of Ase1 by depolymerizing microtubule ends. We produced a simple model based on the assumption that Ase1 reduces the detachment of the terminal tubulin subunit when bound at the tip (only modeling one protofilament, neglecting potential protofilament interactions). This assumption, when allowing for diffusion of Ase1 molecules along the protofilament, leads to both a decrease of microtubule depolymerization velocity and accumulation of Ase1 at the tip of shrinking microtubules. The same had been found in a parallel effort by Al-Hiyasat et al. 2023, who modeled the accumulation of spastin at the depolymerizing microtubule end and the concomitant decrease in depolymerization velocity.

For isolated microtubules, our model's fit with our data increased substantially when we introduced the assumption that an Ase1 molecule bound to a terminal tubulin dimer also prevents the dimers on the two neighbouring protofilaments from depolymerizing. This supports the notion that Ase1 might bridge protofilaments via its C-terminal. Alternatively, or in addition, one can also envision an indirect stabilization through lateral protofilament interactions. This model quantitatively recapitulated the behavior of the system for 6 nM Ase1, and within an order of magnitude for 1 nM Ase1. Given the low density of Ase1 molecules at 1 nM concentration (<1% of tubulin dimers bound to Ase1), the discrepancy may be due to stochasticity of the system. There was one more potential discrepancy between our modeling results and our experimental results for isolated microtubules, namely that the model predicted a characteristic length λ of the exponential decay of Ase1 at the microtubule end of around 600nm, while we measured only around 200nm. However, this signal is hardly comparable with our isolated-protofilament model, not only because it comes from multiple protofilaments that may not be in register, but also because shrinking protofilaments are likely curved outwards (McIntosh et al. 2008).

What could explain the quantitative disagreement with experimental data for antipar-

allelly crosslinked microtubules? In principle, the fact that a disagreement exists is not surprising, given that overlaps are not symmetric, and some protofilaments have almost no Ase1, while others have extremely high Ase1 density (76% tubulin dimers bound to Ase1 in the microtubule body assuming 2 protofilaments crosslinked, 50% assuming 3, see "Mathematical modelling" in Methods). It is for instance conceivable that the crosslinked protofilements lag behind the non-crosslinked protofilements, similar to what had been observed by Peet et al. 2018 when binding depolymerizing microtubules to the coverslip surface via kinesin-1. Hence, a more complex model accounting for protofilament interactions would be needed for overlaps. Such a model would likely need to be informed by experimental measurements of such interactions. However, it is also possible that we simply are overestimating the number of Ase1 molecules herded by antiparallel microtubules, because part of the Ase1 which is lost at the depolymerizing microtubule end presumably remains bound to the template microtubule, an effect which we do not account for in our estimation. A likely expression of this effect is our observation that while at the ends of isolated microtubules, we observed a (blurred) right-sided exponential decay of additional Ase1 density as predicted by our model, the additional Ase1 density at the ends of antiparallel microtubules were more reminiscent of a gaussian (Figure 5.21B-D). In particular, the exponential fits often did not fully capture the additional Ase1 density we observed which "lingered" behind the depolymerizing microtubule end, an additional density which the gaussian fits did capture (notably, because this additional density is likely due to Ase1 molecules still bound to the template microtubule after detaching from the depolymerizing microtubule end, we decided to base our analysis as shown in Figure 5.18 on the results stemming from the exponential fits). Our model did not include microtubule rescues; however, if one assumes that each crosslink reached by a depolymerizing microtubule tip has a chance of inducing rescue, as proposed by Stoppin-Mellet et al. 2013, we expect a positive correlation between Ase1 density and rescue frequency, consistent with our experimental data for antiparallel overlaps. Indeed, the relationship we observed appeared to be a linear one, which would precisely be the relationship proposed by Stoppin-Mellet et al. 2013.

It also bears noting that protein herding at the depolymerizing microtubule tip has been observed for kinetochore-associated Ndc80 and Dam1 complexes, which crosslink chromosomes to depolymerizing microtubule ends (Westermann et al. 2006; Tooley et al. 2011). Herding of these proteins is thus essential for mitosis. As with Ase1, herding of Dam1- and Ndc80- complexes at depolymerizing microtubule ends hampers the dissociation of tubulin subunits from these microtubule ends (Franck et al. 2007; Umbreit et al. 2012; Grishchuk 2017). However, the word "herding" does not suggest itself for these complexes, because the number of "herded" proteins is much lower than in the Ase1 or spastin cases. Another difference is that these complexes rarely dissociate from the depolymerizing microtubule, presumably due to their high multivalency (Volkov et al. 2018) and formation of ring-structures around the microtubule (Westermann et al. 2006). Nonetheless, given the many similarities to our case study, exploring the literature on this phenomenon is instructive.

Grishchuk 2017 use the term "biased diffusion" to describe a potential mechanism for the herding of Dam1/Ndc80 which essentially is the same as the proposed mechanism underlying our model. They contrast this with a second potential mechanism, which is based on protofilament "powerstrokes," i.e., the fact that protofilaments generate forces when bending outward during depolymerization (subsubsection 1.1.2.3). In this model, the biased movement at the depolymerizing tip, i.e., the herding of Dam1/Ndc80, would stem from such forces. Given that Ndc80 and Dam1 are capable of transducing large forces, it is likely that they indeed harvest protofilament powerstrokes (Grishchuk 2017). In this context, it is interesting to note that we found that accumulated Ase1 can transduce forces to other microtubules (Figure 5.17B). Notably, starPEG-(KA7)4, a synthetic microtubule crosslinker with multivalent microtubule-binding interfaces has recently been shown to also drag microtubules when being swept by depolymerizing microtubules (Drechsler et al. 2019), even though it did not hinder microtubule depolymerization of isolated microtubules, pointing toward a potential powerstroke mechanism. It may be interesting to measure the forces which Ase1 sweeping is capable of transducing, which would also shed light on the question on whether protofilament powerstrokes are an important component of Ase1 sweeping (biased diffusion can also generate forces, see Grishchuk 2017, which can be understood as entropic forces Lansky et al. 2015). Interestingly, in the case of Dam1- and Ndc80- complexes, it has been shown that exerting load on the complexes, i.e., pulling them against the direction of microtubule depolymerization, increases their *in vitro* rescue-promoting activity (Franck et al. 2007; Volkov et al. 2018). This indicates that opposing potential protofilament powerstrokes may induce rescues, and hence lends support to the idea that crosslinking Ase1 promotes rescues by potentially opposing the bending of protofilaments.

Our model of the mechanisms behind Ase1 sweeping moreover suggests that any diffusing molecule that prevents tubulin unbinding will "track" depolymerizing ends, even if it may not be propelled by protofilament powerstrokes. For Ase1 specifically, our finding that Ase1 accumulates at the ends of depolymerizing plus ends may imply interesting biological properties, as it may have relevance for the localization of the MAPs which Ase1 recruits to the microtubule (subsubsection 1.2.2.1). For instance, a high density of Ase1 molecules within a largely-shrunk antiparallel overlap might thus imply a larger recruitment activity for the rescue factor CLASP, ensuring that overlaps do not vanish completely.

Our results show that the presence of diffusible microtubule crosslinkers can suffice to establish enduring antiparallel microtubule overlaps. Antiparallel microtubule overlaps are found in the midzone of mitotic spindles, however, as an important caveat, the biological significance of our findings is unclear. Regarding the mitotic spindle of the fission yeast S. pombe in particular, Bratman et al. 2007 had reported that the microtubule rescue factor CLASP was necessary to stabilize the antiparallel overlap regions against disassmbly via microtubule depolymerization. When removing the C-terminal of Ase1, Ase1 no longer recruited CLASP but still partitioned into antiparallel overlaps, yet the mitotic spindles of cells expressing this Ase1δC construct had a similar number of deformed mitotic spindles

as the spindles of cells which did not express Ase1 at all. While this may seem to directly contradict our findings, it can be noted that the C-terminal of Ase1 not only is important for recruiting CLASP, but also has other regulatory functions potentially relevant in the given context (it should be noted that Bratman et al. 2007 did not truncate the whole C-terminal, in particular, their construct retained the residues crucial for nuclear localization). For instance, the C-terminal region has been found to recruit Klp9p, a kinesin-6 motor promoting spindle elongation (Fu et al. 2009). Given that the interplay of Ase1 and motor proteins controls spindle positioning (Braun, Lansky, et al. 2011), it appears possible that the deletion of the C-terminal region may negatively impact spindle structure also via the failure of such positioning mechanisms. Moreover, given that the C-terminal of Ase1 likely bridges protofilaments (Kellogg, Howes, et al. 2016), it may be essential for its microtubule-stabilizing character as reported here. Future experiments could thus investigate whether our findings also hold for an Ase1 construct lacking the C-terminal. Lastly, while CLASP is a stronger and more vital microtubule rescue factor than Ase1 in fission yeast, microtubule stabilization by Ase1 may still play a supporting role, and potentially a more important role in other organisms.

An earlier study on a plant Ase1 analogue, MAP65-1, found increased rescue rates of microtubules within bundles compared to isolated microtubules (Stoppin-Mellet et al. 2013). This study, however, did not experimentally distinguish between parallel and antiparallel bundles. Our methods allowed us to directly distinguish between different bundling orientations, and our findings in fact support the modeling-based findings by (Stoppin-Mellet et al. 2013). However, our results do not rule out that under different experimental conditions, Ase1 may also stabilize parallel bundles to some degree.

As with Tau, it also in the present case is tempting to speculate that the impact of diffusible crosslinkers on microtubule dynamics may be tunable by posttranslational modifications of either the crosslinkers or the microtubule surface. This could give the cell spatial, and more importantly, temporal control of the stability of (mitotic) microtubule arrays, e.g., given that the phosphorylation state of Ase1 changes during mitosis (Khmelinskii et al. 2009).

Beyond the mitotic spindle and other microtubule systems featuring diffusive microtubule crosslinkers of the Ase1/MAP65/PRC1 family, our findings also could hint at a more general principle: For actin filament overlaps, it has been observed that F-actin crosslinkers slow down actin depolymerization (Maul et al. 2003; Schmoller et al. 2011), suggesting that crosslinker-dependent stabilization of filaments may be a fundamental mechanism, widespread across cytoskeletal systems.

Conclusion

The results presented in this thesis and the two associated publications (Siahaan, Krattenmacher, et al. 2019; Krattenmacher et al. 2024) shine further light on how the structure of the cytoskeleton can emerge from the collective behavior of its constitutive parts. In particular, this work highlights potential mechanisms for the stabilization and maintenance of key microtubule structures, namely axonal microtubule arrays and antiparallel microtubule arrays in the mitotic spindle. To probe for these potential mechanisms, we had established experiments with a minimal number of components such to exclude other potential factors, which allows us to establish that the phenomenona we observed truly emerged solely from the interaction patterns of these components rather than third factors.

In the case of axonal microtubule structures, we focused on the intrinsically disordered protein Tau as well as its interaction patterns with the molecular motor kinesin-8 and the microtubule-severing protein Katanin. Our results highlight the existence of two distinct Tau binding modes: Rapid diffusion along the microtubule as well as stationary, cooperative binding to the microtubule. The cooperative mode involves the formation of Tau islands which grow and shrink from their boundaries. Our findings regarding these Tau islands, in particular their characteristic density of 0.26 Tau molecules per tubulin dimer, support a recently-proposed model of Tau binding, where each Tau molecule binds along the crest of a given protofilament, with each microtubule binding repeat of Tau stretching the length of one tubulin dimer. The fact that we did not observe Tau islands within microtubule bends, but yet observed Tau stationarily bound to such bends, suggested that this stationary binding mode of Tau relies on a specific lattice spacing of the tubulin subunits of microtubules, which was confirmed in later experiments. We found that Tau islands are highly effective at shielding microtubules from severing by Katanin, which contributes to our understanding of how axonal microtubule arrays can be stabilized. Finally, our finding that the molecular motor Kip3 is regulated by Tau islands, and can vice versa can regulate Tau islands, hints at the existence of complex interaction dynamics of microtubule-associated proteins within neuronal microtubule arrays, giving rise to complex patterns in time and/or space.

In the case of antiparallel microtubule arrays during mitosis, we focused on the interaction patterns of the microtubule crosslinker Ase1 and dynamic microtubules. Our results demonstrate that Ase1 selectively stabilizes antiparallel microtubule overlaps by both

reducing depolymerization rates and enhancing rescue frequencies, while having minimal effect on isolated or parallel microtubules. This selective stabilization likely stems from multiple mechanisms, including the enhanced affinity of Ase1 for antiparallel overlaps and the crosslinking activity of Ase1 itself, thereby preventing their outward curling during depolymerization. We have also found that Ase1, similarly as the microtubule-severing enzyme spastin, is being herded by depolymerizing microtubule tips, and that this herding correlates with a slow-down in microtubule depolymerization. Our mathematical model suggests that this herding effect can be explained solely by Ase1 hampering the dissociation of terminal tubulin dimers to which it is bound. In other words, Ase1 accumulation at the depolymerizing tip does not rely on any physiochemical preference of Ase1 for tubulin dimers at the tip, nor does it rely on protofilament powerstrokes moving the molecules in the direction of depolymerization. The selective stabilization of antiparallel microtubules of Ase1 could help explain the stability of antiparallel microtubule arrays in the mitotic spindle and other antiparallel microtubule arrays, while Ase1 herding could have implications for the localization of the proteins it recruits to the microtubule.

Overall, our findings highlight further ways in which microtubules, rather than being static tubes, are physically modifiable structures. This, likely plays an important role in enabling microtubules, in their interaction dynamics with other proteins, to fulfill their diverse roles in the establishment and maintenance of biological patterns.

References

Akhmanova, Anna and Lukas C. Kapitein (Aug. 2022). "Mechanisms of microtubule organization in differentiated animal cells". In: *Nature Reviews Molecular Cell Biology* 23 (8), pp. 541–558. ISSN: 14710080. DOI: 10.1038/s41580-022-00473-y (pages 2, 5).

Akhmanova, Anna and Michel O Steinmetz (2008). "Tracking the ends: a dynamic protein network controls the fate of microtubule tips." In: *Nature reviews. Molecular cell biology* 9.4, pp. 309–322. ISSN: 1471-0072. DOI: 10.1038/nrm2369 (page 7).

Alfieri, Angus, Ignas Gaska, and Scott Forth (2021). "Two modes of PRC1-mediated mechanical resistance to kinesin-driven microtubule network disruption". In: *Current Biology* 31.12, pp. 2495–2506 (page 72).

Alushin, Gregory M et al. (2014a). "High-Resolution Microtubule Structures Reveal the Structural Transitions in $\alpha\beta$-Tubulin upon GTP Hydrolysis". In: *Cell* 157.5, pp. 1117–1129. ISSN: 0092-8674. DOI: https://doi.org/10.1016/j.cell.2014.03.053. URL: https://www.sciencedirect.com/science/article/pii/S0092867414004838 (page 3).

— (May 2014b). "High-Resolution microtubule structures reveal the structural transitions in tubulin upon GTP hydrolysis". In: *Cell* 157 (5), pp. 1117–1129. ISSN: 10974172. DOI: 10.1016/j.cell.2014.03.053 (page 6).

Andreu, J. M. et al. (July 1992). "Low resolution structure of microtubules in solution. Synchrotron X-ray scattering and electron microscopy of taxol-induced microtubules assembled from purified tubulin in comparison with glycerol and MAP-induced microtubules". In: *Journal of Molecular Biology* 226 (1), pp. 169–184. ISSN: 00222836. DOI: 10.1016/0022-2836(92)90132-4 (page 8).

Arellano-Santoyo, Hugo et al. (July 2017). "A Tubulin Binding Switch Underlies Kip3/Kinesin-8 Depolymerase Activity". In: *Developmental Cell* 42 (1), 37–51.e8. ISSN: 18781551. DOI: 10.1016/j.devcel.2017.06.011 (page 68).

Aumeier, Charlotte et al. (Sept. 2016). "Self-repair promotes microtubule rescue". In: *Nature Cell Biology* 18 (10), pp. 1054–1064. ISSN: 14764679. DOI: 10.1038/ncb3406 (page 6).

Axelrod, Daniel et al. (1976). "Mobility measurement by analysis of fluorescence photobleaching recovery kinetics". In: *Biophysical journal* 16.9, pp. 1055–1069 (page 11).

Baas, Peter W. et al. (Sept. 2016). "Stability properties of neuronal microtubules". In: *Cytoskeleton* 73 (9), pp. 442–460. ISSN: 19493592. DOI: 10.1002/cm.21286 (page 12).

Baker, Nathan A. et al. (Aug. 2001). "Electrostatics of nanosystems: Application to microtubules and the ribosome". In: *Proceedings of the National Academy of Sciences of the United States of America* 98 (18), pp. 10037–10041. ISSN: 00278424. DOI: 10.1073/pnas.181342398 (page 4).

Barr, Valarie A and Stephen C Bunnell (2009). "Interference reflection microscopy". In: *Current protocols in cell biology* 45.1, pp. 4–23 (page 10).

Bechstedt, Susanne and Gary J. Brouhard (2012). "Doublecortin Recognizes the 13-Protofilament Microtubule Cooperatively and Tracks Microtubule Ends". In: *Developmental Cell* 23.1, pp. 181–192. ISSN: 15345807. DOI: 10.1016/j.devcel.2012.05.006. URL: http://dx.doi.org/10.1016/j.devcel.2012.05.006 (page 68).

Bechstedt, Susanne, Kevan Lu, and Gary J. Brouhard (2014). "Doublecortin recognizes the longitudinal curvature of the microtubule end and lattice". In: *Current Biology* 24.20, pp. 2366–2375. ISSN: 09609822. DOI: 10.1016/j.cub.2014.08.039. URL: http://dx.doi.org/10.1016/j.cub.2014.08.039 (page 68).

Belonogov, Liudmila et al. (2019). "Katanin catalyzes microtubule depolymerization independently of tubulin C-terminal tails". In: *Cytoskeleton* 76 (3), pp. 254–268. DOI: https://doi.org/10.1002/cm.21522. URL: https://onlinelibrary.wiley.com/doi/abs/10.1002/cm.21522 (pages 16, 68).

Bieling, Peter, Ivo a. Telley, and Thomas Surrey (2010). "A minimal midzone protein module controls formation and length of antiparallel microtubule overlaps". In: *Cell* 142.3, pp. 420–432. ISSN: 00928674. DOI: 10.1016/j.cell.2010.06.033. URL: http://dx.doi.org/10.1016/j.cell.2010.06.033 (pages 18, 19).

Bodakuntla, Satish et al. (2019). "Microtubule-Associated Proteins: Structuring the Cytoskeleton". In: *Trends in Cell Biology* 29.10, pp. 804–819. ISSN: 0962-8924. DOI: https://doi.org/10.1016/j.tcb.2019.07.004. URL: https://www.sciencedirect.com/science/article/pii/S0962892419301205 (page 7).

Bormuth, Volker et al. (July 2012). "The Highly Processive Kinesin-8, Kip3, Switches Microtubule Protofilaments with a Bias toward the Left". In: *Biophysical Journal* 103 (1). doi: 10.1016/j.bpj.2012.05.024, pp. L4–L6. ISSN: 0006-3495. DOI: 10.1016/j.bpj.2012.05.024. URL: https://doi.org/10.1016/j.bpj.2012.05.024 (page 17).

Bratman, Scott V. and Fred Chang (Dec. 2007). "Stabilization of Overlapping Microtubules by Fission Yeast CLASP". In: *Developmental Cell* 13.6, pp. 812–827. ISSN: 15345807. DOI: 10.1016/j.devcel.2007.10.015. arXiv: NIHMS150003. URL: https://linkinghub.elsevier.com/retrieve/pii/S1534580707004157 (pages 19, 20, 75, 76).

Braun, Marcus, Stefan Diez, and Zdenek Lansky (2020). "Cytoskeletal organization through multivalent interactions". In: *Journal of cell science* 133.12, jcs234393 (page 72).

Braun, Marcus, Zdenek Lansky, et al. (2011). "Adaptive braking by Ase1 prevents overlapping microtubules from sliding completely apart". In: *Nature Cell Biology* 13.10, pp. 1259–1264. ISSN: 1465-7392. DOI: 10.1038/ncb2323. URL: http://dx.doi.org/10.1038/ncb2323 (pages 19, 60, 76).

Buchholz, Sarah and Hans Zempel (May 2024). "The six brain-specific TAU isoforms and their role in Alzheimer's disease and related neurodegenerative dementia syndromes". In: *Alzheimer's and Dementia* 20 (5), pp. 3606–3628. ISSN: 15525279. DOI: 10.1002/alz.13784 (page 13).

Bujak, Łukasz et al. (Oct. 2021). "Fast Leaps between Millisecond Confinements Govern Ase1 Diffusion along Microtubules". In: *Small Methods* 5 (10). ISSN: 23669608. DOI: 10.1002/smtd.202100370 (page 20).

Bulinski, J Chloë et al. (2001). "Rapid dynamics of the microtubule binding of ensconsin in vivo". In: *Journal of cell science* 114.21, pp. 3885–3897 (page 11).

Castoldi, Mirco and Andrei V Popov (2003). "Purification of brain tubulin through two cycles of polymerization-depolymerization in a high-molarity buffer". In: *Protein Expression and Purification* 32.1, pp. 83–88. ISSN: 1046-5928. DOI: https://doi.org/10.1016/S1046-5928(03)00218-3. URL: https://www.sciencedirect.com/science/article/pii/S1046592803002183 (page 25).

Chaaban, Sami and Gary J. Brouhard (Nov. 2017). "A microtubule bestiary: Structural diversity in tubulin polymers". In: *Molecular Biology of the Cell* 28 (22), pp. 2924–2931. ISSN: 19394586. DOI: 10.1091/mbc.E16-05-0271 (page 5).

Chaudhary, Abdullah R. et al. (2018). "Tau directs intracellular trafficking by regulating the forces exerted by kinesin and dynein teams". In: *Traffic* 19.2, pp. 111–121. ISSN: 16000854. DOI: 10.1111/tra.12537 (page 18).

Chen, J. et al. (1992). "Projection domains of MAP2 and tau determine spacings between microtubules in dendrites and axons". In: *Nature* 360 (6405), pp. 674–677. ISSN: 00280836. DOI: 10.1038/360674a0 (page 14).

Choi, M. C. et al. (2009). "Human microtubule-associated-protein tau regulates the number of protofilaments in microtubules: A synchrotron X-ray scattering study". In: *Biophysical Journal* 97 (2), pp. 519–527. ISSN: 15420086. DOI: 10.1016/j.bpj.2009.04.047 (page 68).

Chretien, Denis and Stephen D. Fuller (May 2000). "Microtubules switch occasionally into unfavorable configurations during elongation". In: *Journal of Molecular Biology* 298 (4), pp. 663–676. ISSN: 00222836. DOI: 10.1006/jmbi.2000.3696 (page 5).

Cross, Robert A. (Feb. 2019). *Microtubule lattice plasticity*. DOI: 10.1016/j.ceb.2018.10.004 (pages 4, 6, 72).

Dammermann, Alexander, Arshad Desai, and Karen Oegema (2003). "The minus end in sight". In: *Current Biology* 13.15, R614–R624. ISSN: 0960-9822. DOI: https://doi.org/10.1016/S0960-9822(03)00530-X. URL: https://www.sciencedirect.com/science/article/pii/S096098220300530X (pages 6, 53).

Dehmelt, Leif and Shelley Halpain (2005). "The MAP2/Tau family of microtubule-associated proteins". In: *Genome Biology* 6 (1). ISSN: 14656906. DOI: 10.1186/gb-2004-6-1-204 (page 13).

Díaz, J. Fernando et al. (Dec. 1998). "Changes in microtubule protofilament number induced by taxol binding to an easily accessible site: Internal microtubule dynamics". In: *Journal of Biological Chemistry* 273 (50), pp. 33803–33810. ISSN: 00219258. DOI: 10.1074/jbc.273.50.33803 (page 8).

Dixit, R. et al. (Feb. 2008). "Differential Regulation of Dynein and Kinesin Motor Proteins by Tau". In: *Science* 319.5866, pp. 1086–1089. ISSN: 0036-8075. DOI: 10.1126/science.1152993. URL: http://www.sciencemag.org/cgi/doi/10.1126/science.1152993 (page 18).

Downing, Kenneth H and Eva Nogales (1998). "Tubulin and microtubule structure". In: *Current Opinion in Cell Biology* 10.1, pp. 16–22. ISSN: 0955-0674. DOI: https://doi.org/10.1016/S0955-0674(98)80082-3. URL: https://www.sciencedirect.com/science/article/pii/S0955067498800823 (page 3).

Drechsel, D N et al. (Oct. 1992). "Modulation of the dynamic instability of tubulin assembly by the microtubule-associated protein tau". eng. In: *Molecular biology of the cell* 3.10, pp. 1141–1154. ISSN: 1059-1524. DOI: 10.1091/mbc.3.10.1141. URL: https://pubmed.ncbi.nlm.nih.gov/1421571%20https://www.ncbi.nlm.nih.gov/pmc/articles/PMC275678/ (page 13).

Drechsler, Hauke et al. (Nov. 2019). "Multivalent electrostatic microtubule interactions of synthetic peptides are sufficient to mimic advanced MAP-like behavior". In: *Molecular Biology of the Cell* 30 (24). Ed. by Thomas Surrey, pp. 2953–2968. ISSN: 1059-1524. DOI: 10.1091/mbc.E19-05-0247. URL: https://www.molbiolcell.org/doi/10.1091/mbc.E19-05-0247 (pages 59, 60, 75).

Ebneth, A et al. (1998). "Overexpression of tau protein inhibits kinesin-dependent trafficking of vesicles, mitochondria, and endoplasmic reticulum: implications for Alzheimer's disease". In: *The Journal of cell biology* 143.3, pp. 777–794 (page 17).

Endow, Sharyn A, F Jon Kull, and Honglei Liu (2010). "Kinesins at a glance". In: *Journal of Cell Science* 123.20, pp. 3420–3424. ISSN: 0021-9533. DOI: 10.1242/jcs.064113. URL: https://jcs.biologists.org/content/123/20/3420 (page 16).

Erlendsson, Simon and Kaare Teilum (2021). "Binding revisited—avidity in cellular function and signaling". In: *Frontiers in molecular biosciences* 7, p. 615565 (page 72).

Franck, Andrew D. et al. (2007). "Tension applied through the Dam1 complex promotes microtubule elongation providing a direct mechanism for length control in mitosis". In: *Nature Cell Biology* 9.7, pp. 832–837. ISSN: 14657392. DOI: 10.1038/ncb1609 (pages 74, 75).

Frauenfelder, Hans (2010). *The physics of proteins: an introduction to biological physics and molecular biophysics*. Springer Science & Business Media (page 2).

Fu, Chuanhai et al. (2009). "Phospho-regulated interaction between kinesin-6 Klp9p and microtubule bundler Ase1p promotes spindle elongation". In: *Developmental cell* 17.2, pp. 257–267 (pages 19, 76).

Fygenson, Deborah Kuchnir, Erez Braun, and Albert Libchaber (1994). "Phase diagram of microtubules". In: *Physical Review E* 50.2, pp. 1579–1588. ISSN: 1063651X. DOI: 10.1103/PhysRevE.50.1579 (page 5).

Gaillard, Jérémie et al. (2008). "Two Microtubule-associated Proteins of Arabidopsis MAP65s Promote Antiparallel Microtubule Bundling". In: *Molecular Biology of the Cell* 19 (10). PMID: 18667529, pp. 4534–4544. DOI: 10.1091/mbc.e08-04-0341. URL: https://doi.org/10.1091/mbc.e08-04-0341 (page 18).

Gamblin, T Chris, Robert W Berry, and Lester I Binder (Feb. 2003). "Tau Polymerization: Role of the Amino Terminus". In: *Biochemistry* 42.7, pp. 2252–2257. ISSN: 0006-2960. DOI: 10.1021/bi0272510. URL: https://doi.org/10.1021/bi0272510 (page 45).

Gao, Yong-Lei et al. (2018). "Tau in neurodegenerative disease". In: *Annals of Translational Medicine* 6.10, pp. 175–175. ISSN: 23055839. DOI: 10.21037/atm.2018.04.23. URL: http://atm.amegroups.com/article/view/19456/19578 (page 13).

Gardner, Melissa K. et al. (2011). "Rapid microtubule self-assembly kinetics". In: *Cell* 146.4, pp. 582–592. ISSN: 00928674. DOI: 10.1016/j.cell.2011.06.053. arXiv: NIHMS150003 (page 8).

Gazzola, Morgan et al. (Jan. 2023). "Microtubules self-repair in living cells". In: *Current Biology* 33 (1), 122–133.e4. ISSN: 18790445. DOI: 10.1016/j.cub.2022.11.060 (page 6).

Gell, Christopher et al. (2010). *Microtubule dynamics reconstituted in vitro and imaged by single-molecule fluorescence microscopy*. First edit. Vol. 95. C. Elsevier, pp. 221–245. ISBN: 9780123748157. DOI: 10.1016/S0091-679X(10)95013-9. URL: http://dx.doi.org/10.1016/S0091-679X(10)95013-9 (page 26).

Genova, Mariya et al. (Mar. 2023). "Tubulin polyglutamylation differentially regulates microtubule-interacting proteins". In: *The EMBO Journal* 42 (5). ISSN: 0261-4189. DOI: 10.15252/embj.2022112101 (page 70).

Grigorieff, Nikolaus et al. (2018). "Severing enzymes amplify microtubule arrays through lattice GTP-tubulin incorporation". In: *Science* 361.6404, eaau1504. ISSN: 0036-8075. DOI: 10.1126/science.aau1504 (page 17).

Grishchuk, Ekaterina L (2017). "Biophysics of microtubule end coupling at the kinetochore". In: *Centromeres and Kinetochores: Discovering the Molecular Mechanisms Underlying Chromosome Inheritance*, pp. 397–428 (pages 74, 75).

Gudimchuk, Nikita B. and J. Richard McIntosh (Dec. 2021). "Regulation of microtubule dynamics, mechanics and function through the growing tip". In: *Nature Reviews Molecular Cell Biology* 22 (12), pp. 777–795. ISSN: 14710080. DOI: 10.1038/s41580-021-00399-x (pages 5, 6, 72).

Gyparaki, Melina Theoni et al. (May 2021). "Tau forms oligomeric complexes on microtubules that are distinct from tau aggregates". In: *Proceedings of the National Academy of Sciences of the United States of America* 118 (19). ISSN: 10916490. DOI: 10.1073/pnas.2021461118 (page 70).

Hartman, James J et al. (Apr. 1998). “Katanin, a Microtubule-Severing Protein, Is a Novel AAA ATPase that Targets to the Centrosome Using a WD40-Containing Subunit”. In: *Cell* 93 (2). doi: 10.1016/S0092-8674(00)81578-0, pp. 277–287. ISSN: 0092-8674. DOI: 10.1016/S0092-8674(00)81578-0. URL: https://doi.org/10.1016/S0092-8674(00)81578-0 (page 16).

Hawkins, Taviare et al. (Jan. 2010). “Mechanics of microtubules”. In: *Journal of Biomechanics* 43 (1), pp. 23–30. ISSN: 00219290. DOI: 10.1016/j.jbiomech.2009.09.005 (pages 4, 5).

Hernández-Vega, Amayra, Marcus Braun, Lara Scharrel, Marcus Jahnel, Susanne Wegmann, Bradley T Hyman, et al. (2017a). “Local Nucleation of Microtubule Bundles through Tubulin Concentration into a Condensed Tau Phase”. In: *Cell Reports* 20.10, pp. 2304–2312. ISSN: 2211-1247. DOI: https://doi.org/10.1016/j.celrep.2017.08.042. URL: https://www.sciencedirect.com/science/article/pii/S221112471731149X (pages 29, 66).

— (Sept. 2017b). “Local Nucleation of Microtubule Bundles through Tubulin Concentration into a Condensed Tau Phase”. In: *Cell Reports* 20 (10), pp. 2304–2312. ISSN: 22111247. DOI: 10.1016/j.celrep.2017.08.042 (page 14).

Herrmann, Arvid et al. (2018). “ Dual localized kinesin-12 POK 2 plays multiple roles during cell division and interacts with MAP 65-3 ”. In: *EMBO reports* 19.9, pp. 1–16. ISSN: 1469-221X. DOI: 10.15252/embr.201846085 (page 29).

Himmler, A et al. (1989). “Tau consists of a set of proteins with repeated C-terminal microtubule-binding domains and variable N-terminal domains.” In: *Molecular and Cellular Biology* 9.4, pp. 1381–1388. ISSN: 0270-7306. DOI: 10.1128/MCB.9.4.1381. URL: https://mcb.asm.org/content/9/4/1381 (page 13).

Hinrichs, Maike H. et al. (2012). “Tau protein diffuses along the microtubule lattice”. In: *Journal of Biological Chemistry* 287.46, pp. 38559–38568. ISSN: 00219258. DOI: 10.1074/jbc.M112.369785 (pages 13, 44, 46, 69).

Hirokawa, Nobutaka, Shinsuke Niwa, and Yosuke Tanaka (Nov. 2010). “Molecular motors in neurons: Transport mechanisms and roles in brain function, development, and disease”. In: *Neuron* 68 (4), pp. 610–638. ISSN: 08966273. DOI: 10.1016/j.neuron.2010.09.039 (page 12).

Al-Hiyasat, Amer et al. (Apr. 2023). “Herding of proteins by the ends of shrinking polymers”. In: *Physical Review E* 107 (4). ISSN: 24700053. DOI: 10.1103/PhysRevE.107.L042601 (pages 59, 73).

Howard, Joe and Anthony A. Hyman (2003). “Dynamics and mechanics of the microtubule plus end”. In: *Nature* 422.6933, pp. 753–758. ISSN: 0028-0836. DOI: 10.1038/nature01600. URL: http://www.ncbi.nlm.nih.gov/pubmed/12700769 (page 6).

Hyman, A A et al. (1992). “Role of GTP hydrolysis in microtubule dynamics: information from a slowly hydrolyzable analogue, GMPCPP.” In: *Molecular biology of the cell* 3.10, pp. 1155–67. ISSN: 1059-1524. DOI: 10.1091/mbc.E12-03-0186. URL: http://www.ncbi.nlm.nih.gov/pubmed/1421572 (page 8).

Hyman, Anthony et al. (1991). "[39] Preparation of modified tubulins". In: *Molecular Motors and the Cytoskeleton*. Vol. 196. Methods in Enzymology. Academic Press, pp. 478–485. DOI: https://doi.org/10.1016/0076-6879(91)96041-O. URL: https://www.sciencedirect.com/science/article/pii/0076687991960410 (page 25).

Iqbal, Khalid, Fei Liu, and Cheng-Xin Gong (2016). "Tau and neurodegenerative disease: the story so far". In: *Nature reviews neurology* 12.1, pp. 15–27 (pages 13, 66).

Ittner, Arne and Lars M. Ittner (July 2018). "Dendritic Tau in Alzheimer's Disease". In: *Neuron* 99 (1), pp. 13–27. ISSN: 10974199. DOI: 10.1016/j.neuron.2018.06.003 (page 12).

Janke, C. (2014). "The tubulin code: Molecular components, readout mechanisms, and functions". In: *The Journal of Cell Biology* 206.4, pp. 461–472. ISSN: 0021-9525. DOI: 10.1083/jcb.201406055. URL: http://www.ncbi.nlm.nih.gov/pubmed/25135932 (page 3).

Janke, Carsten and Maria M Magiera (2020). "The tubulin code and its role in controlling microtubule properties and functions". In: *Nature Reviews Molecular Cell Biology* 21.6, pp. 307–326. ISSN: 1471-0080. DOI: 10.1038/s41580-020-0214-3. URL: https://doi.org/10.1038/s41580-020-0214-3 (pages 3, 4).

Jánosi, Imre M, Denis Chrétien, and Henrik Flyvbjerg (2002). "Structural microtubule cap: stability, catastrophe, rescue, and third state." In: *Biophysical journal* 83.3, pp. 1317–1330. ISSN: 00063495. DOI: 10.1016/S0006-3495(02)73902-7 (page 5).

Janson, Marcel E. et al. (2007). "Crosslinkers and Motors Organize Dynamic Microtubules to Form Stable Bipolar Arrays in Fission Yeast". In: *Cell* 128.2, pp. 357–368. ISSN: 00928674. DOI: 10.1016/j.cell.2006.12.030 (pages 5, 18–20, 32, 52, 53).

Jiang, Kai et al. (2017). "Microtubule minus-end regulation at spindle poles by an ASPM-katanin complex". In: *Nature Cell Biology* 19.5, pp. 480–492. ISSN: 1476-4679. DOI: 10.1038/ncb3511. URL: https://doi.org/10.1038/ncb3511 (page 29).

Johjima, Ai et al. (May 2015). "Microtubule severing by katanin p60 AAA+ATPase requires the C-terminal acidic tails of both alpha-and beta-tubulins and basic amino acid residues in the AAA+ring pore". In: *Journal of Biological Chemistry* 290 (18), pp. 11762–11770. ISSN: 1083351X. DOI: 10.1074/jbc.M114.614768 (page 16).

Kahn, Olga I. and Peter W. Baas (July 2016). "Microtubules and Growth Cones: Motors Drive the Turn". In: *Trends in Neurosciences* 39 (7), pp. 433–440. ISSN: 1878108X. DOI: 10.1016/j.tins.2016.04.009 (page 12).

Kapitein, Lukas C. and Casper C. Hoogenraad (Aug. 2015). "Building the Neuronal Microtubule Cytoskeleton". In: *Neuron* 87 (3). doi: 10.1016/j.neuron.2015.05.046, pp. 492–506. ISSN: 0896-6273. DOI: 10.1016/j.neuron.2015.05.046. URL: https://doi.org/10.1016/j.neuron.2015.05.046 (pages 11, 12).

Kapitein, Lukas C., Marcel E. Janson, et al. (2008). "Microtubule-Driven Multimerization Recruits ase1p onto Overlapping Microtubules". In: *Current Biology* 18.21, pp. 1713–1717.

ISSN: 09609822. DOI: 10.1016/j.cub.2008.09.046. URL: http://dx.doi.org/10.1016/j.cub.2008.09.046 (pages 19, 72).

Karabay, Arzu et al. (2004). "Axonal Growth Is Sensitive to the Levels of Katanin, a Protein That Severs Microtubules". In: *Journal of Neuroscience* 24 (25), pp. 5778–5788. ISSN: 0270-6474. DOI: 10.1523/JNEUROSCI.1382-04.2004. URL: https://www.jneurosci.org/content/24/25/5778 (page 15).

Karsenti, Eric (2008). "Self-organization in cell biology: A brief history". In: *Nature Reviews Molecular Cell Biology* 9.3, pp. 255–262. ISSN: 14710072. DOI: 10.1038/nrm2357 (page 1).

Kellogg, Elizabeth H., Nisreen M.A. Hejab, et al. (Mar. 2017). "Insights into the Distinct Mechanisms of Action of Taxane and Non-Taxane Microtubule Stabilizers from Cryo-EM Structures". In: *Journal of Molecular Biology* 429 (5), pp. 633–646. ISSN: 10898638. DOI: 10.1016/j.jmb.2017.01.001 (pages 8, 9).

Kellogg, Elizabeth H., Nisreen M.A. A. Hejab, et al. (2018). "Near-atomic model of microtubule-tau interactions". In: *Science* 1780.May, pp. 1–8. ISSN: 10959203. DOI: 10.1126/science.aat1780. URL: http://www.sciencemag.org/lookup/doi/10.1126/science.aat1780 (pages 14, 15, 17, 66, 68, 70).

Kellogg, Elizabeth H., Stuart Howes, et al. (2016). "Near-atomic cryo-EM structure of PRC1 bound to the microtubule". In: *Proceedings of the National Academy of Sciences of the United States of America* 113.34, pp. 9430–9439. ISSN: 10916490. DOI: 10.1073/pnas.1609903113 (pages 18–20, 71, 76).

Kessel, Amit and Nir Ben-Tal (2018). *Introduction to proteins: structure, function, and motion*. Chapman and Hall/CRC (pages 2, 3).

Kevenaar, Josta T et al. (2016). "Kinesin-Binding Protein Controls Microtubule Dynamics and Cargo Trafficking by Regulating Kinesin Motor Activity". In: *Current Biology* 26.7, pp. 849–861. ISSN: 0960-9822. DOI: https://doi.org/10.1016/j.cub.2016.01.048. URL: https://www.sciencedirect.com/science/article/pii/S0960982216001305 (page 18).

Khmelinskii, Anton et al. (Aug. 2009). "Phosphorylation-Dependent Protein Interactions at the Spindle Midzone Mediate Cell Cycle Regulation of Spindle Elongation". In: *Developmental Cell* 17 (2), pp. 244–256. ISSN: 15345807. DOI: 10.1016/j.devcel.2009.06.011 (pages 18, 76).

Kilmartin, John V. (2014). "Lessons from yeast: The spindle pole body and the centrosome". In: *Philosophical Transactions of the Royal Society B: Biological Sciences* 369 (1650). ISSN: 14712970. DOI: 10.1098/rstb.2013.0456 (pages 18, 19).

Kitazawa, Daishi et al. (2014). "Orbit/CLASP is required for myosin accumulation at the cleavage furrow in Drosophila male meiosis". In: *PLoS ONE* 9 (5). ISSN: 19326203. DOI: 10.1371/journal.pone.0093669 (page 19).

Krattenmacher, Jochen et al. (2024). "Ase1 selectively increases the lifetime of antiparallel microtubule overlaps". In: *Current Biology*. ISSN: 0960-9822. DOI: https://doi.org/

10.1016/j.cub.2024.07.055. URL: https://www.sciencedirect.com/science/article/pii/S0960982224009941 (pages 23, 52–54, 56–61, 64, 77).

Kremers, Gert Jan et al. (Jan. 2011). "Fluorescent proteins at a glance". In: *Journal of Cell Science* 124 (2), pp. 157–160. ISSN: 00219533. DOI: 10.1242/jcs.072744 (page 9).

Kuo, Yin Wei et al. (2019). "Spastin is a dual-function enzyme that severs microtubules and promotes their regrowth to increase the number and mass of microtubules". In: *Proceedings of the National Academy of Sciences of the United States of America* 116 (12), pp. 5533–5541. ISSN: 10916490. DOI: 10.1073/pnas.1818824116 (page 59).

Kuo, Yin-Wei and Jonathon Howard (Jan. 2021). "Cutting, Amplifying, and Aligning Microtubules with Severing Enzymes". In: *Trends in Cell Biology* 31 (1). doi: 10.1016/j.tcb.2020.10.004, pp. 50–61. ISSN: 0962-8924. DOI: 10.1016/j.tcb.2020.10.004. URL: https://doi.org/10.1016/j.tcb.2020.10.004 (page 16).

Lansky, Zdenek et al. (2015). "Diffusible Crosslinkers Generate Directed Forces in Microtubule Networks". In: *Cell* 160.6, pp. 1–10. ISSN: 00928674. DOI: 10.1016/j.cell.2015.01.051. URL: http://linkinghub.elsevier.com/retrieve/pii/S0092867415001294 (pages 20, 62, 69, 72, 75).

Leduc, Cécile et al. (2012). "Molecular crowding creates traffic jams of kinesin motors on microtubules". In: *Proceedings of the National Academy of Sciences of the United States of America* 109.16, pp. 6100–6105. ISSN: 00278424. DOI: 10.1073/pnas.1107281109 (page 17).

Lichtman, Jeff W. and José Angel Conchello (Dec. 2005). "Fluorescence microscopy". In: *Nature Methods* 2 (12), pp. 910–919. ISSN: 15487091. DOI: 10.1038/nmeth817 (page 9).

Lin, Yang, Ya Lan Wei, and Zhen Yu She (June 2020). "Kinesin-8 motors: regulation of microtubule dynamics and chromosome movements". In: *Chromosoma* 129 (2), pp. 99–110. ISSN: 14320886. DOI: 10.1007/s00412-020-00736-7 (pages 17, 18).

Lipka, Joanna et al. (Feb. 2016). "Microtubule-binding protein doublecortin-like kinase 1 (DCLK1) guides kinesin-3-mediated cargo transport to dendrites". In: *The EMBO Journal* 35 (3), pp. 302–318. ISSN: 0261-4189. DOI: 10.15252/embj.201592929 (page 12).

Liu, Jing et al. (2009). "PRC1 cooperates with CLASP1 to organize central spindle plasticity in mitosis". In: *Journal of Biological Chemistry* 284 (34), pp. 23059–23071. ISSN: 00219258. DOI: 10.1074/jbc.M109.009670. URL: http://dx.doi.org/10.1074/jbc.M109.009670 (page 19).

Locke, Julia et al. (Nov. 2017). "Structural basis of human kinesin-8 function and inhibition". In: *Proceedings of the National Academy of Sciences of the United States of America* 114 (45), E9539–E9548. ISSN: 10916490. DOI: 10.1073/pnas.1712169114 (page 17).

Löiodice, Isabelle (2005). "Ase1p Organizes Antiparallel Microtubule Arrays during Interphase and Mitosis in Fission Yeast". In: *Molecular biology of the cell* 16.1, pp. 1756–1768. ISSN: 1059-1524. DOI: 10.1091/mbc.E04-10-0899. URL: http://www.molbiolcell.org/cgi/doi/10.1091/mbc.E04?10?0899 (pages 18, 19).

Lombino, Franco L et al. (2019). "The Microtubule Severing Protein Katanin Regulates Proliferation of Neuronal Progenitors in Embryonic and Adult Neurogenesis". In: *Scientific Reports* 9 (1), p. 15940. ISSN: 2045-2322. DOI: 10.1038/s41598-019-52367-3. URL: https://doi.org/10.1038/s41598-019-52367-3 (page 15).

Luchniak, Anna et al. (2023). "Dynamic microtubules slow down during their shrinkage phase". In: *Biophysical Journal* 122 (4), pp. 616–623. ISSN: 15420086. DOI: 10.1016/j.bpj.2023.01.020. URL: https://doi.org/10.1016/j.bpj.2023.01.020 (page 59).

Mahamdeh, Mohammed et al. (2018). "Label-free high-speed wide-field imaging of single microtubules using interference reflection microscopy". In: *Journal of Microscopy* 272 (1), pp. 60–66. ISSN: 13652818. DOI: 10.1111/jmi.12744 (page 10).

Mammeri, Nadia El et al. (July 2022). "Microtubule-binding core of the tau protein". In: *Science Advances* 8 (29). ISSN: 23752548. DOI: 10.1126/sciadv.abo4459 (pages 14, 70).

Mani, Nandini, Sithara S. Wijeratne, and Radhika Subramanian (2021). "Micron-scale geometrical features of microtubules as regulators of microtubule organization". In: *eLife* 10, pp. 1–26. ISSN: 2050084X. DOI: 10.7554/eLife.63880 (page 19).

Mattheyses, Alexa L., Sanford M. Simon, and Joshua Z. Rappoport (Nov. 2010). *Imaging with total internal reflection fluorescence microscopy for the cell biologist*. DOI: 10.1242/jcs.056218 (page 10).

Maul, Raymond S et al. (2003). "EPLIN regulates actin dynamics by cross-linking and stabilizing filaments". In: *The Journal of cell biology* 160.3, p. 399 (page 76).

McIntosh, J. Richard et al. (2008). "Fibrils Connect Microtubule Tips with Kinetochores: A Mechanism to Couple Tubulin Dynamics to Chromosome Motion". In: *Cell* 135 (2), pp. 322–333. ISSN: 00928674. DOI: 10.1016/j.cell.2008.08.038. URL: http://dx.doi.org/10.1016/j.cell.2008.08.038 (page 73).

McNally, Karen et al. (Feb. 2014). "Katanin maintains meiotic metaphase chromosome alignment and spindle structure in vivo and has multiple effects on microtubules in vitro". In: *Molecular Biology of the Cell* 25.7, pp. 1037–1049. ISSN: 1059-1524. DOI: 10.1091/mbc.e13-12-0764. URL: https://doi.org/10.1091/mbc.e13-12-0764 (page 16).

McNally, Karen Perry, Omar A Bazirgan, and Francis J McNally (May 2000). "Two domains of p80 katanin regulate microtubule severing and spindle pole targeting by p60 katanin". In: *Journal of Cell Science* 113 (9), pp. 1623–1633. ISSN: 0021-9533. DOI: 10.1242/jcs.113.9.1623. URL: https://doi.org/10.1242/jcs.113.9.1623 (page 16).

Mcvicker, Derrick P. et al. (2014). "Tau interconverts between diffusive and stable populations on the microtubule surface in an isoform and lattice specific manner". In: *Cytoskeleton* 71.3, pp. 184–194. ISSN: 19493592. DOI: 10.1002/cm.21163 (pages 13, 65, 66).

Memet, Edvin et al. (June 2018). "Microtubules soften due to cross-sectional flattening". In: *eLife* 7. ISSN: 2050-084X. DOI: 10.7554/eLife.34695. URL: https://elifesciences.org/articles/34695 (page 4).

Mephon-Gaspard, Alix et al. (Apr. 2016). "Role of tau in the spatial organization of axonal microtubules: keeping parallel microtubules evenly distributed despite macromolecular crowding". In: *Cellular and Molecular Life Sciences* 73 (19), pp. 3745–3760. ISSN: 14209071. DOI: 10.1007/s00018-016-2216-z (pages 14, 15, 70).

Meurer-Grob, Patricia, Jerome Kasparian, and Richard H Wade (July 2001). "Microtubule Structure at Improved Resolution". In: *Biochemistry* 40 (27). doi: 10.1021/bi010343p, pp. 8000–8008. ISSN: 0006-2960. DOI: 10.1021/bi010343p. URL: https://doi.org/10.1021/bi010343p (page 8).

Mickey, Brian and Jonathon Howard (1995). "Rigidity of microtubules is increased by stabilizing agents". In: *Journal of Cell Biology* 130 (4), pp. 909–917. ISSN: 00219525. DOI: 10.1083/jcb.130.4.909 (pages 8, 13).

Mitra, Aniruddha et al. (Aug. 2018). "Directionally biased sidestepping of Kip3/kinesin-8 is regulated by ATP waiting time and motor-microtubule interaction strength". In: *Proceedings of the National Academy of Sciences* 115.34, E7950 LP –E7959. DOI: 10.1073/pnas.1801820115. URL: http://www.pnas.org/content/115/34/E7950.abstract (page 29).

Molodtsov, M. I. et al. (Mar. 2005). "Force production by depolymerizing microtubules: A theoretical study". In: *Proceedings of the National Academy of Sciences of the United States of America* 102 (12), pp. 4353–4358. ISSN: 00278424. DOI: 10.1073/pnas.0501142102 (page 6).

Monroy, Brigette Y. et al. (2018). "Competition between microtubule-associated proteins directs motor transport". In: *Nature Communications* 9.1, pp. 1–12. ISSN: 20411723. DOI: 10.1038/s41467-018-03909-2. URL: http://dx.doi.org/10.1038/s41467-018-03909-2 (page 67).

Moores, Carolyn A. et al. (June 2004). "Mechanism of microtubule stabilization by doublecortin". In: *Molecular Cell* 14 (6), pp. 833–839. ISSN: 10972765. DOI: 10.1016/j.molcel.2004.06.009 (page 68).

Morris, Meaghan et al. (2011). "Review The Many Faces of Tau". In: *Neuron* 70.3, pp. 410–426. ISSN: 1063-6692. DOI: 10.1109/TNET.2008.923716. URL: http://dx.doi.org/10.1016/j.neuron.2011.04.009 (pages 13, 23).

Mukhopadhyay, Rajendrani, Sanjay Kumar, and Jan H. Hoh (Sept. 2004). "Molecular mechanisms for organizing the neuronal cytoskeleton". In: *BioEssays* 26 (9), pp. 1017–1025. ISSN: 02659247. DOI: 10.1002/bies.20088 (page 14).

Nakata, Takao et al. (July 2011). "Preferential binding of a kinesin-1 motor to GTP-tubulin-rich microtubules underlies polarized vesicle transport". In: *Journal of Cell Biology* 194 (2), pp. 245–255. ISSN: 00219525. DOI: 10.1083/jcb.201104034 (page 68).

Nitzsche, Bert et al. (2010). "Chapter 14 - Studying Kinesin Motors by Optical 3D-Nanometry in Gliding Motility Assays". In: *Microtubules, in vitro*. Ed. by Leslie Wilson and John J Correia. Vol. 95. Methods in Cell Biology. Academic Press, pp. 247–271. DOI: https:

//doi.org/10.1016/S0091-679X(10)95014-0. URL: https://www.sciencedirect.com/science/article/pii/S0091679X10950140 (page 29).

Nogales, Eva and Rui Zhang (Apr. 2016). "Visualizing microtubule structural transitions and interactions with associated proteins". In: *Current Opinion in Structural Biology* 37, pp. 90–96. ISSN: 1879033X. DOI: 10.1016/j.sbi.2015.12.009 (page 7).

Peet, Daniel R., Nigel J. Burroughs, and Robert A. Cross (2018). "Kinesin expands and stabilizes the GDP-microtubule lattice". In: *Nature Nanotechnology* 13.5, pp. 386–391. ISSN: 17483395. DOI: 10.1038/s41565-018-0084-4. URL: http://dx.doi.org/10.1038/s41565-018-0084-4 (pages 4, 67, 71, 74).

Pelletier, Gregory (2024). "Weighted correlation and covariance (weightedcorrs)". In: URL: https://github.com/gjpelletier/weightedcorrs (page 59).

Portran, D et al. (2013). "MAP65/Ase1 promote microtubule flexibility." In: *Molecular biology of the cell* 24 (12), pp. 1964–73. ISSN: 1939-4586. DOI: 10.1091/mbc.E13-03-0141. URL: http://www.pubmedcentral.nih.gov/articlerender.fcgi?artid=3681700&tool=pmcentrez&rendertype=abstract (page 71).

Qiang, Liang et al. (2006). "Tau protects microtubules in the axon from severing by katanin". In: *Journal of Neuroscience* 26 (12), pp. 3120–3129. ISSN: 0270-6474 (pages 12, 13).

Roll-Mecak, Antonina and Francis J McNally (2010). "Microtubule-severing enzymes". In: *Current Opinion in Cell Biology* 22.1, pp. 96–103. ISSN: 0955-0674. DOI: https://doi.org/10.1016/j.ceb.2009.11.001. URL: https://www.sciencedirect.com/science/article/pii/S095506740900194X (page 15).

Ruhnow, Felix, David Zwicker, and Stefan Diez (2011). "Tracking Single Particles and Elongated Filaments with Nanometer Precision". In: *Biophysical Journal* 100.11, pp. 2820–2828. ISSN: 0006-3495. DOI: https://doi.org/10.1016/j.bpj.2011.04.023. URL: https://www.sciencedirect.com/science/article/pii/S000634951100467X (pages 27, 28, 34).

Samsonov, A. (2004). "Tau interaction with microtubules in vivo". In: *Journal of Cell Science* 117.25, pp. 6129–6141. ISSN: 0021-9533. DOI: 10.1242/jcs.01531. URL: http://jcs.biologists.org/cgi/doi/10.1242/jcs.01531 (page 50).

Schiff, Peter B, Jane Fant, and Susan B Horwitz (1979). "Promotion of microtubule assembly in vitro by taxol". In: *Nature* 277.5698, pp. 665–667. ISSN: 1476-4687. DOI: 10.1038/277665a0. URL: https://doi.org/10.1038/277665a0 (pages 8, 26).

Schindelin, Johannes et al. (2012). "Fiji: an open-source platform for biological-image analysis". In: *Nature Methods* 9.7, pp. 676–682. ISSN: 1548-7105. DOI: 10.1038/nmeth.2019. URL: https://doi.org/10.1038/nmeth.2019 (page 27).

Schmoller, Kurt M, Christine Semmrich, and Andreas R Bausch (2011). "Slow down of actin depolymerization by cross-linking molecules". In: *Journal of structural biology* 173.2, pp. 350–357 (page 76).

Seitz, Arne et al. (2002). "Single-molecule investigation of the interference between kinesin, tau and MAP2c". In: *The EMBO journal* (page 17).

She, Zhen Yu et al. (2019). "Mechanisms of the Ase1/PRC1/MAP65 family in central spindle assembly". In: *Biological Reviews* 94.6, pp. 2033–2048. ISSN: 1469185X. DOI: 10.1111/brv.12547 (pages 18, 19).

Shimomura, Osamu (2005). "The discovery of aequorin and green fluorescent protein." In: *Journal of microscopy* 217.1 (page 9).

Siahaan, Valerie (2024). "Tau proteins cooperatively assemble into cohesive envelopes that protect microtubules against severing enzymes". In: URL: https://dspace.cuni.cz/handle/20.500.11956/189810 (pages iii, 40, 43, 44, 48).

Siahaan, Valerie, Jochen Krattenmacher, et al. (2019). "Kinetically distinct phases of tau on microtubules regulate kinesin motors and severing enzymes". In: *Nature Cell Biology* 21 (9), pp. 1086–1092. ISSN: 1465-7392. DOI: 10.1038/s41556-019-0374-6 (pages 23, 26, 40, 42–46, 48, 49, 51, 67, 77).

Siahaan, Valerie, Ruensern Tan, et al. (2022). "Microtubule lattice spacing governs cohesive envelope formation of tau family proteins". In: *Nature chemical biology* 18.11, pp. 1224–1235. DOI: https://doi.org/10.1038/s41589-022-01096-2 (pages 46, 67, 69, 71).

Siahaan, Valerie, Romana Weissova, et al. (Jan. 2024). "Tau phosphorylation impedes functionality of protective tau envelopes". In: *bioRxiv*, p. 2024.03.25.586522. DOI: 10.1101/2024.03.25.586522. URL: http://biorxiv.org/content/early/2024/03/28/2024.03.25.586522.abstract (page 71).

Sing, Charles E, Monica Olvera de la Cruz, and John F Marko (2014). "Multiple-binding-site mechanism explains concentration-dependent unbinding rates of DNA-binding proteins". In: *Nucleic acids research* 42.6, pp. 3783–3791 (page 69).

Song, Y H and E Mandelkow (Jan. 1995). "The anatomy of flagellar microtubules: polarity, seam, junctions, and lattice." In: *Journal of Cell Biology* 128 (1), pp. 81–94. ISSN: 0021-9525. DOI: 10.1083/jcb.128.1.81. URL: https://rupress.org/jcb/article/128/1/81/20223/The-anatomy-of-flagellar-microtubules-polarity (page 62).

Stoppin-Mellet, Virginie et al. (2013). "MAP65 Coordinate Microtubule Growth during Bundle Formation". In: *PLoS ONE* 8.2. ISSN: 19326203. DOI: 10.1371/journal.pone.0056808 (pages 19, 24, 74, 76).

Su, Xiaolei et al. (2011). "Mechanisms Underlying the Dual-Mode Regulation of Microtubule Dynamics by Kip3/Kinesin-8". In: *Molecular Cell* 43.5, pp. 751–763. ISSN: 1097-2765. DOI: https://doi.org/10.1016/j.molcel.2011.06.027. URL: https://www.sciencedirect.com/science/article/pii/S1097276511005375 (page 17).

Subramanian, Radhika et al. (2010). "Insights into antiparallel microtubule crosslinking by PRC1, a conserved nonmotor microtubule binding protein". In: *Cell* 142.3, pp. 433–443. ISSN: 00928674. DOI: 10.1016/j.cell.2010.07.012. URL: http://dx.doi.org/10.1016/j.cell.2010.07.012 (page 18).

Tan, Ruensern et al. (2019). "Microtubules gate tau condensation to spatially regulate microtubule functions". In: *Nature cell biology* 21.9, pp. 1078–1085 (pages 46, 65, 66).

Tas, Roderick P. et al. (Dec. 2017). "Differentiation between Oppositely Oriented Microtubules Controls Polarized Neuronal Transport". In: *Neuron* 96 (6), 1264–1271.e5. ISSN: 10974199. DOI: 10.1016/j.neuron.2017.11.018 (pages 11, 12).

Thomas, Ezekiel C., Amber Ismael, and Jeffrey K. Moore (Nov. 2020). "Ase1 domains dynamically slow anaphase spindle elongation and recruit Bim1 to the midzone". In: *Molecular Biology of the Cell* 31 (24), pp. 2733–2747. ISSN: 19394586. DOI: 10.1091/mbc.E20-07-0493-T (pages 19, 20).

Ti, Shih Chieh, Gregory M. Alushin, and Tarun M. Kapoor (Oct. 2018). "Human beta-Tubulin Isotypes Can Regulate Microtubule Protofilament Number and Stability". In: *Developmental Cell* 47 (2), 175–190.e5. ISSN: 18781551. DOI: 10.1016/j.devcel.2018.08.014 (page 5).

Tolić, Iva M. (Apr. 2018). "Mitotic spindle: kinetochore fibers hold on tight to interpolar bundles". In: *European Biophysics Journal* 47 (3), pp. 191–203. ISSN: 14321017. DOI: 10.1007/s00249-017-1244-4 (page 19).

Tooley, John G., Stephanie A. Miller, and P. Todd Stukenberg (Apr. 2011). "The Ndc80 complex uses a tripartite attachment point to couple microtubule depolymerization to chromosome movement". In: *Molecular Biology of the Cell* 22 (8), pp. 1217–1226. ISSN: 10591524. DOI: 10.1091/mbc.E10-07-0626 (page 74).

Trinczek, B et al. (1999). "Tau regulates the attachment/detachment but not the speed of motors in microtubule-dependent transport of single vesicles and organelles". In: *Journal of cell science* 112.14, pp. 2355–2367 (page 17).

Umbreit, Neil T et al. (2012). "The Ndc80 kinetochore complex directly modulates microtubule dynamics". In: *Proceedings of the National Academy of Sciences* 109.40, pp. 16113–16118 (page 74).

Uzsoy, Ana Sofía M. et al. (Oct. 2021). "Automated tracking of S. pombe spindle elongation dynamics". In: *Journal of Microscopy* 284 (1), pp. 83–94. ISSN: 13652818. DOI: 10.1111/jmi.13044 (page 18).

Varga, Vladimir et al. (2009). "Kinesin-8 Motors Act Cooperatively to Mediate Length-Dependent Microtubule Depolymerization". In: *Cell* 138.6, pp. 1174–1183. ISSN: 00928674. DOI: 10.1016/j.cell.2009.07.032. URL: http://dx.doi.org/10.1016/j.cell.2009.07.032 (page 17).

Vemu, Annapurna et al. (2018). "Severing enzymes amplify microtubule arrays through lattice GTP-tubulin incorporation". In: *Science* 361 (6404), eaau1504. DOI: 10.1126/science.aau1504. URL: https://www.science.org/doi/abs/10.1126/science.aau1504 (pages 5, 16).

Vershinin, Michael et al. (2007). "Multiple-motor based transport and its regulation by Tau". In: *Proceedings of the National Academy of Sciences* 104.1, pp. 87–92 (page 17).

Volkov, Vladimir A et al. (2018). "Multivalency of NDC80 in the outer kinetochore is essential to track shortening microtubules and generate forces". In: *Elife* 7, e36764 (pages 74, 75).

Vyas, Aditi et al. (June 2021). "Fission Yeast Schizosaccharomyces pombe: A Unicellular "Micromammal" Model Organism". In: *Current Protocols* 1 (6). ISSN: 26911299. DOI: 10.1002/cpz1.151 (page 18).

Wang, Jian-Zhi et al. (2012). "Abnormal hyperphosphorylation of tau: sites, regulation, and molecular mechanism of neurofibrillary degeneration". In: *Journal of Alzheimer's Disease* 33.s1, S123–S139 (page 13).

Wegmann, Susanne et al. (2018). "Tau protein liquid-liquid phase separation can initiate tau aggregation". In: *The EMBO Journal* 37.7, e98049. DOI: https://doi.org/10.15252/embj.201798049. URL: https://www.embopress.org/doi/abs/10.15252/embj.201798049 (page 42).

Westermann, Stefan et al. (Mar. 2006). "The Dam1 kinetochore ring complex moves processively on depolymerizing microtubule ends". In: *Nature* 440 (7083), pp. 565–569. ISSN: 14764687. DOI: 10.1038/nature04409 (page 74).

Woese, Carl R. (June 2004). "A New Biology for a New Century". In: *Microbiology and Molecular Biology Reviews* 68.2, pp. 173–186. ISSN: 1092-2172. DOI: 10.1128/MMBR.68.2.173-186.2004. URL: http://doi.wiley.com/10.1890/1540-9295-7.9.455%20https://mmbr.asm.org/content/68/2/173 (page 1).

Wood, V. et al. (Feb. 2002). "The genome sequence of Schizosaccharomyces pombe". In: *Nature* 415 (6874), pp. 871–880. ISSN: 00280836. DOI: 10.1038/nature724 (page 18).

Woodruff, Jeffrey B and Anthony A Hyman (2015). "Method: In vitro analysis of pericentriolar material assembly". In: *Methods in cell biology*. Vol. 129. Elsevier, pp. 369–382 (page 29).

Xie, Ping (Dec. 2021). "A model of processive walking and slipping of kinesin-8 molecular motors". In: *Scientific Reports* 11 (1). ISSN: 20452322. DOI: 10.1038/s41598-021-87532-0 (page 17).

Yamashita, A. (Jan. 2005). "The Roles of Fission Yeast Ase1 in Mitotic Cell Division, Meiotic Nuclear Oscillation, and Cytokinesis Checkpoint Signaling". In: *Molecular Biology of the Cell* 16 (3), pp. 1378–1395. ISSN: 1059-1524. DOI: 10.1091/mbc.E04-10-0859. URL: http://www.molbiolcell.org/cgi/doi/10.1091/mbc.E04-10-0859 (page 18).

Zehr, Elena et al. (2017). "Katanin spiral and ring structures shed light on power stroke for microtubule severing". In: *Nature Structural and Molecular Biology* 24.9, pp. 717–725. ISSN: 15459985. DOI: 10.1038/nsmb.3448 (pages 16, 17).

Zempel, Hans and Eva-Maria Mandelkow (2015). "Tau missorting and spastin-induced microtubule disruption in neurodegeneration: Alzheimer Disease and Hereditary Spastic Paraplegia". In: *Molecular neurodegeneration* 10, pp. 1–12 (page 13).

Zhang, Rui et al. (Aug. 2015). "Mechanistic origin of microtubule dynamic instability and its modulation by EB proteins". In: *Cell* 162 (4), pp. 849–859. ISSN: 10974172. DOI: 10.1016/j.cell.2015.07.012 (page 14).

Appendices

Publication 1: Kinetically distinct phases of Tau on microtubules regulate kinesin motors and severing enzymes

LETTERS
https://doi.org/10.1038/s41556-019-0374-6

nature cell biology

Kinetically distinct phases of tau on microtubules regulate kinesin motors and severing enzymes

Valerie Siahaan[1,5], Jochen Krattenmacher[1,5], Anthony A. Hyman[2,3,6], Stefan Diez[2,3,4,6], Amayra Hernández-Vega[2,6*], Zdenek Lansky[1,6*] and Marcus Braun[1,4,6*]

Tau is an intrinsically disordered protein, which diffuses on microtubules[1]. In neurodegenerative diseases, collectively termed tauopathies, malfunction of tau and its detachment from axonal microtubules are correlated with axonal degeneration[2]. Tau can protect microtubules from microtubule-degrading enzymes such as katanin[3]. However, how tau carries out this regulatory function is still unclear. Here, using in vitro reconstitution, we show that tau molecules on microtubules cooperatively form cohesive islands that are kinetically distinct from tau molecules that individually diffuse on microtubules. Dependent on the tau concentration in solution, the islands reversibly grow or shrink by addition or release of tau molecules at their boundaries. Shielding microtubules from kinesin-1 motors and katanin, the islands exhibit regulatory qualities distinct from a comparably dense layer of diffusible tau. Superprocessive kinesin-8 motors penetrate the islands and cause their disassembly. Our results reveal a microtubule-dependent phase of tau that constitutes an adaptable protective layer on the microtubule surface. We anticipate that other intrinsically disordered axonal proteins display a similar cooperative behaviour and potentially compete with tau in regulating access to the microtubule surface.

Tau is an intrinsically disordered microtubule-associated protein (MAP), which localizes preferentially to neuronal axons and is involved in neurodegenerative diseases[4–6]. Tau enhances the stability of microtubules directly by its presence[7], and by regulating the interactions of other MAPs with microtubules[8–13]. Tau mislocalization during the onset of Alzheimer's disease leaves axonal microtubules unprotected against microtubule-severing enzymes such as katanin[3], leading to microtubule destabilization and the eventual degeneration of the axon. The molecular mechanism underlying this regulatory function of tau is unknown. Here we demonstrate how microtubule-associated tau molecules can collectively regulate molecular motors and severing enzymes.

To study microtubule-associated tau molecules, we immobilized Atto 647-labelled microtubules on a coverslip, added full-length, human tau 441 isoform (encoded by 2N4R), fluorescently labelled on the C terminus with either monomeric enhanced green fluorescent protein (tau–meGFP) or mCherry (tau–mCherry) and performed time-lapse imaging using total internal reflection fluorescence (TIRF) microscopy (Fig. 1a and Methods). After the addition of 20 nM tau–meGFP, we observed the formation of high-density tau–meGFP islands on the microtubules, surrounded by regions of low-density tau–meGFP (Fig. 1b–d and Supplementary Video 1). Tau–meGFP islands originated from diffraction-limited spots, appearing within tens of seconds after the addition of tau (Supplementary Fig. 1a). The islands grew intermittently at their boundaries with variable velocities in the order of 25 nm s^{-1}, corresponding to about 10 molecules added per s (Supplementary Fig. 1b) to highly variable lengths (Supplementary Fig. 1c), progressively covering the microtubules (Fig. 1e and Supplementary Fig. 1d). During experimentally accessible time scales (approximately 1 h), island growth did not cease (Supplementary Fig. 1e). Notably, the tau density in the islands stayed constant during the period of growth (Fig. 1f and Supplementary Fig. 1f), suggesting that the islands grow by the addition of tau molecules at their boundaries, reminiscent of epitaxial growth of thin films. When the boundaries of neighbouring growing islands came into contact, the islands merged (Fig. 1c). At these instances, we never observed an increase in the tau density, suggesting that islands are formed by a well-defined tau layer occupying the entire accessible surface of the microtubule. When tau was removed from solution (Fig. 1g and Supplementary Video 2), tau molecules unbound rapidly and uniformly from all regions outside of islands (the 'island surroundings'), with a time constant of about 2 s, as inferred from the decay of the fluorescence signal (Fig. 1h, Supplementary Fig. 1g and Methods). By contrast, islands prevailed over several minutes, without substantial changes in the initial tau density, while slowly disassembling from their boundaries until they fully disappeared (Fig. 1g,h and Supplementary Fig. 1f). The island boundaries receded with an average velocity of approximately two tau molecules unbinding per second (Supplementary Fig. 1h and Methods). During disassembly, the islands occasionally underwent fission (Supplementary Fig. 1i). In contrast to the fast unbinding of tau from outside the islands, tau molecules unbound from the disassembling islands orders of magnitude slower—on the timescale of tens of minutes (Fig. 1h, Supplementary Fig. 1g and Methods). This extremely low unbinding rate explains the preservation of the islands in the absence of tau in solution and suggests that the occasional island fissions observed during disassembly occur after rare events of tau molecules unbinding from inside the island. Islands thus predominantly disassemble at their boundaries. The marked difference in the tau-unbinding rates inside and outside the islands, together with the assembly and disassembly kinetics at the island boundaries, strongly suggest that tau molecules in the islands cooperate, forming a cohesive layer on the microtubule surface. Because the N terminus of tau mediates

[1]Institute of Biotechnology of the Czech Academy of Sciences, BIOCEV, Prague West, Czech Republic. [2]Max Planck Institute of Molecular Cell Biology and Genetics, Dresden, Germany. [3]Cluster of Excellence Physics of Life, Technische Universität Dresden, Dresden, Germany. [4]B CUBE—Center for Molecular Bioengineering, Technische Universität Dresden, Dresden, Germany. [5]These authors contributed equally: Valerie Siahaan, Jochen Krattenmacher. [6]These authors jointly supervised this work: Anthony A. Hyman, Stefan Diez, Amayra Hernández-Vega, Zdenek Lansky, Marcus Braun. *e-mail: hernande@mpicbg.de; zdenek.lansky@ibt.cas.cz; marcus.braun@ibt.cas.cz

tau–tau interactions[14], we repeated the experiments using a tau construct with a truncated N terminus (tau(ΔN)–meGFP; Supplementary Fig. 1j). Although tau(ΔN)–meGFP interacted with the microtubules, we did not observe any island formation even at tau(ΔN)–meGFP concentrations as high as 0.5 µM. Combined, these results show that full-length tau on microtubules can separate into two kinetically distinct phases, islands of high-density tau with slow turnover surrounded by regions of low-density tau with rapid turnover. Similar observations are reported in a complementary study by Tan et al.[15].

To investigate the dynamics of tau molecules in the islands, we incubated microtubules with 20 nM tau–mCherry and, after 15 min of incubation, replaced the assay buffer with a solution containing 20 nM tau–meGFP (Fig. 2a, Supplementary Fig. 2a and Supplementary Video 3). Tau–meGFP molecules exchanging with the leaving tau–mCherry, bound rapidly to the regions surrounding the islands, while binding with a slower time constant into the islands. In both islands and their surroundings, the turnover from tau–mCherry to tau–meGFP occurred without any positional preferences. Outside the islands, tau–mCherry rapidly dissociated from the microtubules with a time constant of about 3 s, comparable to the value estimated above when tau–meGFP was removed from solution (Supplementary Fig. 2b). Inside the islands, tau–mCherry dissociated with a time constant of about 20 s (Fig. 2b and Supplementary Fig. 2b), which, although an order of magnitude slower than outside the islands, was nevertheless substantially faster than the approximately 1,300 s measured in the absence of tau–meGFP in solution (Fig. 2b). At higher tau concentration (100 nM), we observed a further decrease in the time constant of tau–mCherry unbinding from the islands by about twofold, demonstrating that tau unbinding from the islands depends on the tau concentration in solution (Fig. 2b, Supplementary Fig. 2c and Methods). We did not observe such a trend in the low-density regions (Supplementary Fig. 2d).

To study the spatio-temporal dynamics of tau, we formed islands using a mixture of 20 nM tau–mCherry and 1 nM tau–meGFP, enabling us to observe the motion of individual tau–meGFP particles in an environment dominated by tau–mCherry (Fig. 2c). Fluorescence-intensity histograms of individual tau–meGFP particles has a single-Gaussian profile showing that tau–meGFP was incorporated in the islands as single molecules, highlighting that tau–tau interactions occurred only on the microtubule lattice (Supplementary Fig. 2e). Outside the islands, single tau–meGFP molecules diffused rapidly with a diffusion constant of $0.27 \pm 0.15\,\mu m^2 s^{-1}$ (linear fit coefficient ± 95% confidence bounds, Fig. 2c, Supplementary Fig. 2f and Methods), comparable to previously reported values[1]. By contrast, the tau–meGFP molecules in the islands were stationary, with a negligible diffusion constant of $0.027 \pm 0.016\,\mu m^2 s^{-1}$ (linear fit coefficient ± 95% confidence bounds, Fig. 2c and Supplementary Fig. 2f). Occasionally, single tau–meGFP molecules initially diffusing outside an island became

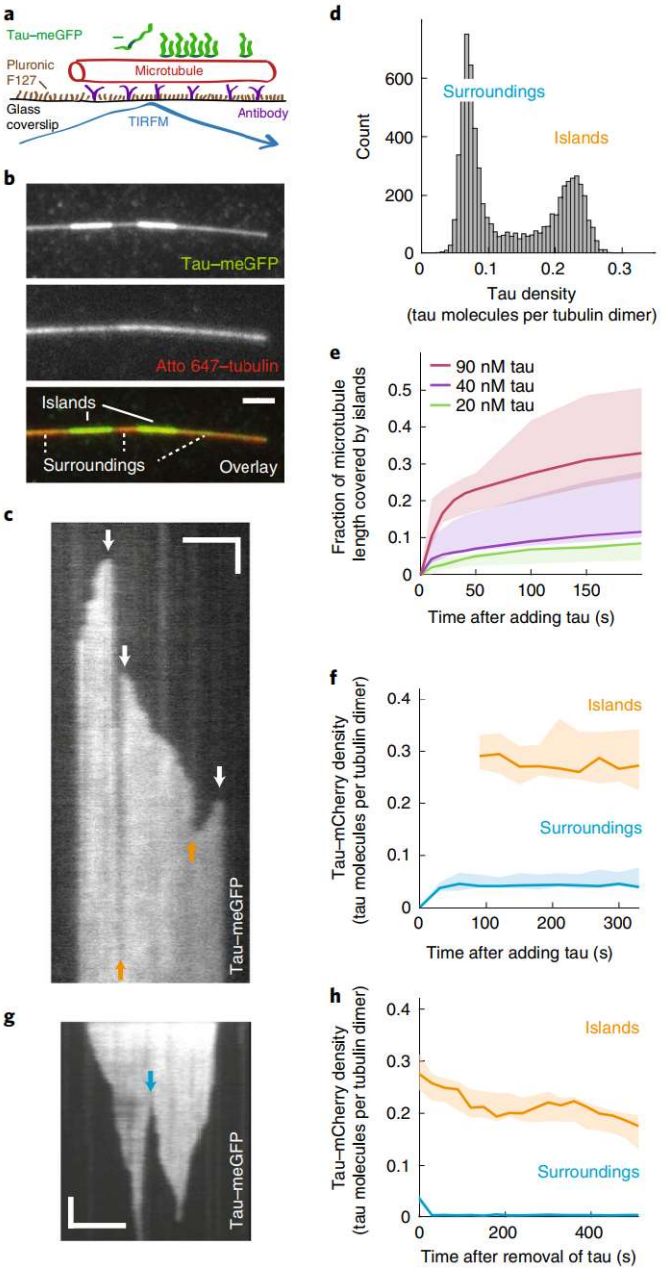

Fig. 1 | Tau on microtubules separates into two kinetically distinct phases. **a**, Schematics depicting the assay geometry. **b**, Multichannel fluorescence micrograph showing islands of high-density tau-meGFP (bright green) surrounded by regions of low-density tau-meGFP (less intense green) on an Atto 647-labelled microtubule (red). Images taken 5 min after the addition of 20 nM tau-meGFP. **c**, Kymograph showing the fluorescence signal of tau-meGFP on a microtubule after the addition 20 nM tau-meGFP. Initially, the microtubule is covered by low tau-meGFP density. Over time, high-density tau-meGFP islands start to assemble. White arrows indicate positions of nucleation. Orange arrows indicate the merging of neighbouring islands growing towards each other. **d**, Distribution of fluorescence intensity of tau-meGFP along microtubules such as the one shown in **c**, showing two distinct populations. **e**, Fraction of microtubule length covered by tau islands after the addition of tau-meGFP ($n = 3$ experiments per condition, 131 microtubules). For statistics calculated over individual microtubules, see Supplementary Fig. 1d. **f**, Example time trace of the tau-mCherry density in the islands and their surroundings (Methods) after the addition of tau-mCherry ($n = 5$ microtubules). The tau-mCherry density within the islands was constant during the experiment. For quantification, see Supplementary Fig. 1f. **g**, Kymograph showing the fluorescence signal of tau-meGFP on the microtubule after the removal of tau-meGFP from solution, visualizing island disassembly. The blue arrow indicates a fission event. **h**, Example time trace of the tau-mCherry density inside and outside the islands after the removal of tau-mCherry from solution ($n = 9$ microtubules). Unbinding rates outside and inside the islands markedly differed and were in the order of seconds and tens of minutes, respectively (for quantification see Fig. 2b and Supplementary Figs. 1g and 2d). Experiments in **g** and **h** were performed with reduced framerate to minimize photobleaching (Methods). Experiments were repeated independently 438 (**b**), 343 (**c**,**d**), 22 (**f**), 115 (**g**) and 16 (**h**) times with similar results. In **e**, thick lines show the median and shaded areas indicate the full range of values; in **f** and **h**, thick lines show the median and shaded areas indicate the range between first and third quartiles. All scale bars, vertical 5 s, horizontal 2 µm.

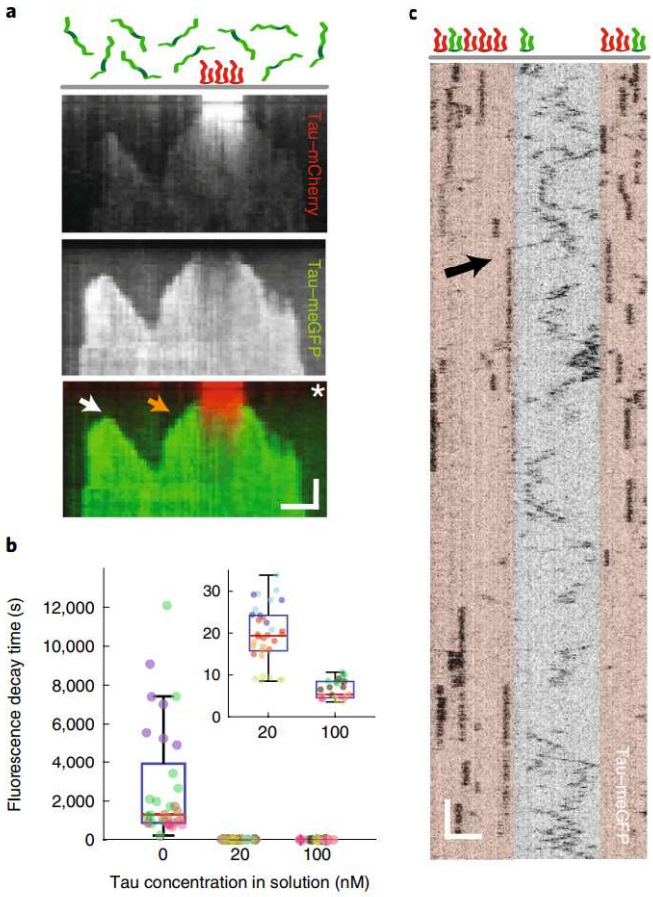

Fig. 2 | Tau molecules in the islands are stationary but exchange with tau in solution. a, Multichannel kymograph showing an island pre-formed in the presence of 20 nM tau–mCherry (red). After removing most of the tau–mCherry from solution by adding of 20 nM tau–meGFP (green; time of addition marked by white asterisk), we observed the exchange of tau–mCherry for tau–meGFP inside and outside of the islands. This exchange occurred along the entire length of the islands. Additionally, islands resumed their growth with the addition of tau–meGFP to their boundaries (an example is marked by an orange arrow). New islands also started to assemble (an example is marked by a white arrow). Scale bars: vertical 20 s, horizontal 2 µm. This experiment was repeated 15 times with similar results. **b**, The dwell time of fluorescently labelled tau in the islands decreases with increasing concentration of tau in solution (0 nM tau: dwell time 45 ± 46 min (mean ± s.d.), $n = 33$ microtubules in 4 experiments; 20 nM tau: dwell time 20 ± 7 s (mean ± s.d., $n = 34$ microtubules in 5 experiments; 100 nM tau: dwell time 6.4 ± 2.1 s (mean ± s.d.), $n = 26$ microtubules in 4 experiments). The inset shows the 20 nM and 100 nM boxes on a magnified *y* scale. The data points are colour-coded by experiments. Typical time traces and corresponding fits underlying these data are shown in Supplementary Figs. 1g, 2b,c. For a description of all box-plot elements see Methods. **c**, Intensity-inverted kymograph showing single tau–meGFP molecules interacting with a microtubule containing two tau–mCherry islands (indicated by beige transparent boxes). Outside the islands, tau–meGFP diffuses rapidly, whereas inside the islands, tau–meGFP is stationary. Occasionally, we observed a diffusing tau–meGFP molecule stopping as it associated with an island (black arrow). Scale bars: vertical 1 s, horizontal 2 µm. This experiment was repeated 65 times with similar results.

stationary when associating with an island boundary (Fig. 2c). We conclude that the tau molecules localizing in the islands are stationary; nevertheless, as demonstrated above in bulk experiments (Fig. 2b) they can exchange with tau in solution.

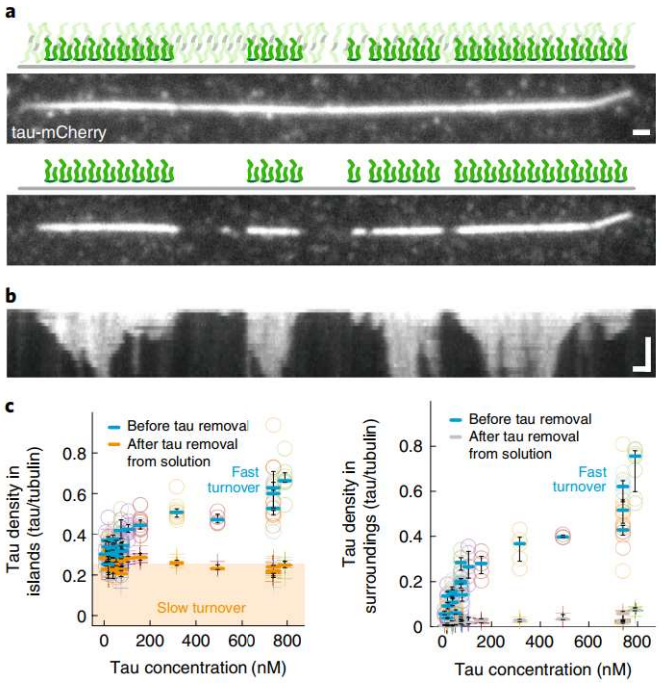

Fig. 3 | Tau islands are characterized by tau cohesion. a, Fluorescence micrographs showing the coverage of a microtubule by tau–mCherry. Top: uniform coverage at high (0.8 µM) concentration 5 min after the addition of tau–mCherry. Bottom: islands, 30 s after the removal of tau–mCherry from solution. This experiment was repeated 17 times with similar results. **b**, Kymograph of the experiment presented in **a**, showing the disassembly of the islands after the removal of tau–mCherry from solution. **c**, Tau densities in regions covered by islands and the surrounding regions established at various tau–meGFP concentrations, before and after the removal of tau–meGFP from solution ($n = 150$ microtubules, 21 experiments). Points are colour-coded by experiment, horizontal lines indicate the three quartiles of each experiment. The characteristic island density (main text, Methods) is indicated by the height of the shaded area (left panel). Scale bars: vertical 5 min, horizontal 1 µm.

To investigate the dependence of island formation on the concentration of tau, we performed experiments with repeated cycles of microtubule incubation with increasing concentrations of tau–meGFP followed by tau–meGFP removal from solution. Below a tau–meGFP concentration of approximately 5 nM, we did not observe any island formation ($n = 245$ microtubules in five experiments). Above this concentration, the tau–meGFP density outside and inside the islands increased with increasing tau–meGFP concentration in solution. After each removal of tau–meGFP, the tau density in the regions surrounding the islands returned to the background level within several seconds (Supplementary Fig. 3a; consistent with the data shown in Fig. 1h). By contrast, after each removal of tau–meGFP, the tau density in the islands decayed in two stages: within a few seconds, a fast density drop occurred uniformly along the whole length of the islands, followed by a slow density decrease, the latter consistent with the data shown in Fig. 1h (Supplementary Fig. 3a). Above a tau–meGFP concentration of approximately 0.5 µM, the tau density on the microtubules reached saturation (Supplementary Fig. 3b), as previously reported[16], suggesting that tau associates with a finite number of interaction sites on the microtubule. In this regime, the islands became apparent only after tau–meGFP was removed from solution, following which tau–meGFP rapidly unbound from the surroundings and islands became discernable (Fig. 3a,b). Of note, in all experiments, the tau–meGFP

density in the islands, after the fast density drop, had the same value of 0.26 ± 0.05 tau molecules per tubulin dimer (mean ± s.d., $n = 101$ microtubules, 14 experiments; Methods), independent of the initial tau concentration in solution (Fig. 3c). Together with the results in Figs. 1 and 2, these experiments show that cohesive islands on microtubules are formed by tau molecules that bind cooperatively and, consequently, turn over slowly. At physiological tau concentrations[17] in the range of 0.5–1.5 µM, tau molecules, which turn over rapidly, co-localize with islands. These tau molecules, whose density depends on the tau concentration in solution in a similar way as the tau density outside the islands (Supplementary Fig. 3c), do not appear to participate in the cooperative island formation.

To investigate how the tau islands may regulate the interaction of other MAPs with microtubules, we formed tau islands using tau–mCherry and tested their effect on GFP-tagged MAPs. First, we tested the molecular motor kinesin-1. After addition of 60 nM kinesin-1–GFP (Methods) to microtubules in the presence of tau–mCherry, we observed processive movement of single motors outside the islands (Fig. 4a and Supplementary Fig. 4a,b). On reaching the island boundaries, the motors dissociated instantaneously from the microtubules (Fig. 4a), similar to previous observations of kinesin-1 encountering static obstacles[18,19]. The kinesin-1 landing rate in the islands was about an order of magnitude lower than in their surroundings (Supplementary Fig. 4c). Notably, at all studied tau concentrations, no kinesin-1 molecules landing inside an island moved processively (total number of 553 molecules in 23 experiments); instead, these transient interactions were static. Second, we tested the microtubule-severing enzyme katanin. After the addition of 200 nM katanin–GFP (subunits p60 and p80[20]) to microtubules in the presence of 20 nM tau–mCherry, we observed katanin–GFP binding and microtubule severing predominantly outside the islands, leading to the disintegration of these microtubule regions (Fig. 4b, Supplementary Fig. 4d and Supplementary Video 4), while island-covered regions prevailed. On longer time scales, the island-covered regions of the microtubules started to disassemble slowly from their boundaries, with only occasional isolated cut observed in the island-covered microtubules (Fig. 4b, Supplementary Fig. 4e and Supplementary Video 4). Whereas non-island microtubule regions disassembled within 1 min, the island-protected microtubule stretches persisted on the timescale of tens of minutes. Third, we tested the effect of the tau islands on superprocessive motors. We used *Saccharomyces cerevisiae* Kip3, the best described member of the kinesin-8 family. Unlike kinesin-1[18,19], Kip3 does not dissociate from the microtubule when the next binding site ahead is occupied, but rather pauses for extended periods of time[21], leading to the formation of 'traffic jams'[22]. As the kinesin- and tau- interaction sites on microtubules overlap[23], we hypothesized that traffic jams might form in front of tau islands. We formed islands using 20 nM or 100 nM tau–mCherry. After the addition of 15 nM Kip3–GFP, we observed Kip3–GFP molecules moving in the low-density tau regions. In contrast to kinesin-1, we also detected Kip3–GFP motility inside the tau islands, albeit at decreased velocity and

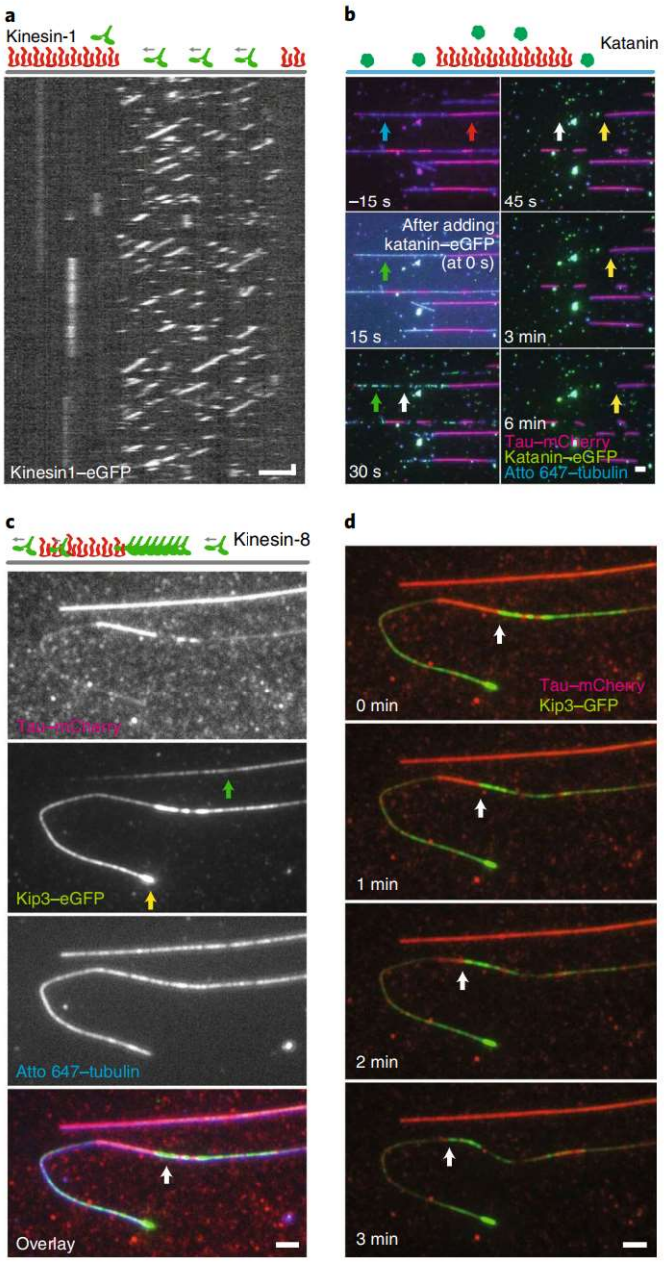

Fig. 4 | Tau islands constitute a protective layer around microtubules. **a**, Fluorescence kymograph showing kinesin-1-GFP molecules moving processively outside the islands and immediately dissociating from the microtubule when reaching the island boundaries (island positions indicated by schematics above the kymograph). No kinesin-1-GFP molecules moved processively inside the islands. This experiment was repeated 124 times with similar results. For quantification of the kinesin-1-GFP landing rates inside and outside the islands, and velocities and dwell times outside the islands at different tau concentrations, see Supplementary Fig. 4a–c. **b**, Multichannel fluorescence micrographs showing katanin-GFP-driven (green, example position indicated by green arrow) severing of Atto 647 microtubules (blue) decorated with tau-mCherry islands (red, example indicated by red arrow) interspersed by regions of low tau-meGFP density (indicated by blue arrow). Katanin-GFP was added at time = 0 s. Initially, microtubule severing and disassembly occurred only in the regions surrounding the islands (example indicated by white arrow). On longer time scales katanin-GFP induced shortening of the island-covered regions of the microtubule (example indicated by yellow arrow). This experiment was repeated 11 times with similar results. **c**, Multichannel fluorescence micrographs showing that Kip3-GFP (kinesin-8, green) localizes both outside and inside the tau-mCherry (red) islands (exemplary localization of Kip3-GFP in the island indicated by green arrow) on Atto 647-labelled microtubules (blue) and accumulates at the microtubule ends (yellow arrow) and in front of the islands (white arrow). This experiment was repeated seven times with similar results. **d**, Multichannel fluorescence micrographs showing that Kip3-GFP (green) accumulating in front of a tau-mCherry island (red) can remove the island by displacing tau-mCherry from the island edge (receding of the island boundary indicated by white arrow). Scale bars: vertical 1 s, horizontal 2 µm.

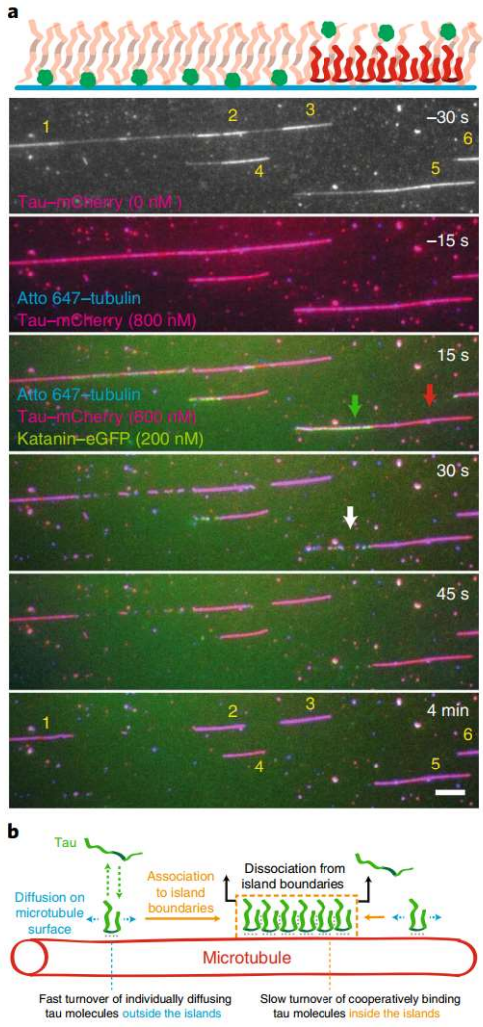

Fig. 5 | Microtubule shielding depends on tau cohesion in the islands. **a**, Multichannel fluorescence micrographs showing katanin–GFP-driven (green) severing of Atto 647-microtubules (blue) decorated with tau–mCherry islands (red) formed at 0.8 µM tau–mCherry. The island positions (indicated by numbers) were determined after a brief removal of tau–mCherry from solution (time = –30 s, Methods). After 0.8 µM tau–mCherry was re-introduced, microtubules became uniformly covered by tau–mCherry (time = –15 s). Katanin–GFP was added at time = 0 s. Katanin–GFP was recruited to regions outside the islands (example indicated by green arrow) and excluded from the islands (example indicated by red arrow). Microtubule severing and disassembly occurred initially only in the regions outside the islands (example indicated by white arrow). Over longer time scales, islands disassembled from their boundaries (compare to Fig. 4b). Scale bar, 2 µm. This experiment was repeated 11 times with similar results. **b**, Schematic representation of island formation. Tau molecules bind and unbind with high rates to microtubules, on which they diffuse (fast turnover). When encountering an island (dashed orange box), tau molecules cooperatively associate with the island at its boundaries, rendering the tau molecules stationary, decreasing their unbinding rate (slow turnover), and causing the island to grow in size laterally. Tau molecules from solution can only bind to the inside of an island via displacement of an island-associated tau molecule, resulting in the observed concentration-dependent turnover of tau inside islands. After removal of tau from solution, tau molecules dissociate from the island boundaries, making the island shrink in size laterally.

density (Fig. 4c,d, Supplementary Fig. 4f–h and Supplementary Video 5). Notably, we observed that Kip3–GFP moving in the low-density tau regions accumulated at the boundaries of the tau islands (Fig. 4c). The resulting high-density traffic jams caused enhanced unbinding of tau–mCherry at these positions, eventually leading to the displacement of the islands (Fig. 4d) at velocities comparable to Kip3–GFP walking within islands (Supplementary Fig. 4g and Supplementary Fig. 4i). These combined results show that tau islands constitute a protective layer on the microtubule surface, which blocks kinesin-1-based transport and obstructs the severing activity of katanin, and that the activity of superprocessive motors can displace existing islands from the microtubule surface.

Because the island and non-island regions exhibited similar tau densities under saturating, physiological tau concentrations (Fig. 3), we considered whether, under these conditions, the diffusible tau molecules in the non-island regions could shield the microtubules against severing. We therefore: (1) formed islands using 0.8 µM tau–mCherry, (2) after 5 min, briefly removed tau–mCherry from solution to note the position of the islands, and (3) re-introduced 0.8 µM tau–mCherry. We then immediately exposed these tau–mCherry fully decorated microtubules to 200 nM katanin–GFP analogously to the experiment presented in Fig. 4b. We observed, similarly to Fig. 4b, that the non-island regions were severed and rapidly disassembled, whereas the island-covered microtubules persisted and only slowly disassembled from their boundaries with an occasional cut in the islands (Fig. 5a, Supplementary Fig. 4d,e and Supplementary Video 6). These experiments show that the density of tau does not determine whether tau forms a protective layer around microtubules. Rather, the microtubule protection is enabled by the cohesion between the cooperatively binding tau molecules that make up the islands (Fig. 5b).

Tau islands displayed a characteristic density of about 0.26 tau molecules per tubulin dimer, suggesting that tau molecules bind to the microtubule in an ordered monolayer, presumably engaging all four microtubule-binding repeats, whose positions at a similar density were shown recently using cryo-electron microscopy[23]. At physiological tau levels (0.5 µM and above), rapidly turning-over tau co-localized with the islands. The transience of these interactions explains why this pool of tau could not be captured by cryo-electron microscopy. Our results suggest that the integrity of the islands depends on cooperativity between the constituent tau molecules. Consistent with this notion, tau molecules on microtubules interact with each other[9,24], in solution can undergo liquid–liquid phase separation[25] or, when hyperphosphorylated, form neurofibrillary tangles[6]. It seems plausible that tau–tau interactions, in addition to the binding of the four tau repeats to the microtubule, underpin the formation of islands. Alternatively, or in addition, cooperativity could depend on the number of microtubule protofilaments, as observed for doublecortin[26], and/or on a local tau-induced modification of the microtubule surface translating along the microtubule lattice into adjacent binding sites and locally increasing the affinity for incoming tau molecules.

Tau unbinding from the islands increases with increasing tau concentration in solution. This observation cannot be attributed to the pool of rapidly turning-over tau, which colocalizes with the island-incorporated tau at high concentrations (Fig. 3). At the concentrations tested (20 nM and 100 nM), this pool accounts for only approximately 20% and 40% of the total number of tau in the islands (Fig. 3c), respectively, whereas the average unbinding time decreases by two orders of magnitude. We interpret this phenomenon as the consequence of a multivalent attachment of island-incorporated tau mediated by the four microtubule-binding repeats of tau and tau–tau interaction sites. These bonds individually undergo transient cycles of unbinding and rebinding. At low tau concentration, transiently released bonds are probably re-established, as a partially bound tau molecule remains anchored to the microtubule via its persisting binding sites, keeping the released binding interfaces in close proximity. With increasing tau concentration in solution however, it becomes increasingly probable that a binding site

of a tau molecule from solution establishes a bond to a temporarily-vacated binding site on the microtubule and thereby, might replace an island-incorporated tau molecule, one bond at a time. Unbinding rates that depend on the concentration of ligands in solution, as previously reported for other multivalently interacting macromolecules[27,28], may also explain the kinesin-8-driven island disassembly. Kinesin-8 does not dissociate when an adjacent binding site on the microtubule is occupied. Instead, the motor pauses in front of a bound tau molecule until, stochastically, this next binding site becomes available by transient unbinding of a microtubule-binding repeat of tau. Kinesin-8 is then favourably positioned to occupy this site on the microtubule and thereby sequentially replace all the microtubule-binding repeats of a tau molecule. In this way, super-processive motors might regulate the localization of tau in neurons. Reciprocally, these motors might be regulated by tau islands, by the formation of traffic jams at their boundaries and reduction of their speed in the island-covered regions.

Highly curved microtubule regions show increased tau binding[29], similar to that of doublecortin[30]. Indeed we observed that tau in regions of highly curved microtubules (radius < 2.5 µm) exhibited higher density than in surrounding regions, but lower than in the islands on straight microtubule regions (Supplementary Fig. 5a (top),b, c). Of note, the highly curved regions were not protected from katanin-mediated severing (Supplementary Fig. 5a,d, Supplementary Video 7), demonstrating that tau molecules in the highly curved regions do not form a cohesive layer. Also, tau–meGFP binding in the curved regions was distinct from island formation on straight microtubules (Supplementary Fig. 5e–h). These results suggest suggest that high microtubule curvatures, though attracting tau, prevent the formation of cohesive tau islands.

In summary, we show that tau on microtubules can coexist in two kinetically distinct phases, resulting in the formation of cohesive tau islands. Complementary work by Tan et al. confirms the existence of these cohesive regions and demonstrate their significance for the regulation of cytoplasmic dynein and spastin[15]. We hypothesize that islands may act as a readout of post-translational tubulin modifications, rendering these regions differentially accessible to other MAPs. Furthermore, other intrinsically disordered proteins, analogously, might also be able to form cohesive islands on microtubules, which could add a further layer of MAP sorting and regulation on microtubules, as suggested recently[31]. It is an intriguing possibility that in neurodegenerative diseases, diminished island assembly—triggered, for example, by hyperphosphorylation of tau—could cause various downstream pathophysiological effects.

Online content

Any methods, additional references, Nature Research reporting summaries, source data, statements of code and data availability and associated accession codes are available at https://doi.org/10.1038/s41556-019-0374-6.

Received: 6 November 2018; Accepted: 18 July 2019;
Published online: 2 September 2019

References

1. Hinrichs, M. H. et al. Tau protein diffuses along the microtubule lattice. *J. Biol. Chem.* **287**, 38559–38568 (2012).
2. Kneynsberg, A., Combs, B., Christensen, K., Morfini, G. & Kanaan, N. M. Axonal degeneration in tauopathies: disease relevance and underlying mechanisms. *Front. Neurosci.* **11**, 572 (2017).
3. Qiang, L. Tau protects microtubules in the axon from severing by katanin. *J. Neurosci.* **26**, 3120–3129 (2006).
4. Morris, M., Maeda, S., Vossel, K. & Mucke, L. The many faces of tau. *Neuron* **70**, 410–426 (2011).
5. Gao, Y.-L. et al. Tau in neurodegenerative disease. *Ann. Transl. Med.* **6**, 175–175 (2018).
6. Iqbal, K., Liu, F. & Gong, C.-X. Tau and neurodegenerative disease: the story so far. *Nat. Rev. Neurol.* **12**, 15–27 (2016).
7. Drechsel, D. N., Hyman, A. A., Cobb, M. H. & Kirschner, M. W. Modulation of the dynamic instability of tubulin assembly by the microtubule-associated protein tau. *Mol. Biol. Cell* **3**, 1141–1154 (1992).
8. Chaudhary, A. R., Berger, F., Berger, C. L. & Hendricks, A. G. Tau directs intracellular trafficking by regulating the forces exerted by kinesin and dynein teams. *Traffic* **19**, 111–121 (2018).
9. Dixit, R., Ross, J. L., Goldman, Y. E. & Holzbaur, E. L. F. Differential regulation of dynein and kinesin motor proteins by Tau. *Science* **319**, 1086–1089 (2008).
10. Vershinin, M., Carter, B. C., Razafsky, D. S., King, S. J. & Gross, S. P. Multiple-motor based transport and its regulation by Tau. *Proc. Natl Acad. Sci. USA* **104**, 87–92 (2007).
11. Seitz, A. et al. Single-molecule investigation of the interference between kinesin, tau and MAP2c. *EMBO J.* **21**, 4896–4905 (2002).
12. Trinczek, B., Ebneth, A., Mandelkow, E. M. & Mandelkow, E. Tau regulates the attachment/detachment but not the speed of motors in microtubule-dependent transport of single vesicles and organelles. *J. Cell Sci.* **112**, 2355–2367 (1999).
13. Ebneth, A. et al. Overexpression of tau protein inhibits kinesin-dependent trafficking of vesicles, mitochondria, and endoplasmic reticulum: implications for Alzheimer's disease. *J. Cell Biol.* **143**, 777–794 (1998).
14. Gamblin, T. C., Berry, R. W. & Binder, L. I. Tau polymerization: role of the amino terminus. *Biochemistry* **42**, 2252–2257 (2003).
15. Tan, R. et al. Microtubules gate tau condensation to spatially regulate microtubule functions. *Nat. Cell Biol.* https://doi.org/10.1038/s41556-019-0375-5 (2019).
16. Makrides, V., Massie, M. R., Feinstein, S. C. & Lew, J. Evidence for two distinct binding sites for tau on microtubules. *Proc. Natl Acad. Sci. USA* **101**, 6746–6751 (2004).
17. Wegmann, S. et al. Tau protein liquid–liquid phase separation can initiate tau aggregation. *EMBO J.* **37**, e98049 (2018).
18. Schneider, R., Korten, T., Walter, W. J. & Diez, S. Kinesin-1 motors can circumvent permanent roadblocks by side-shifting to neighboring protofilaments. *Biophys. J.* **108**, 2249–2257 (2015).
19. Telley, I. A., Bieling, P. & Surrey, T. Obstacles on the microtubule reduce the processivity of Kinesin-1 in a minimal in vitro system and in cell extract. *Biophys. J.* **96**, 3341–3353 (2009).
20. Jiang, K. et al. Microtubule minus-end regulation at spindle poles by an ASPM–katanin complex. *Nat. Cell Biol.* **19**, 480–492 (2017).
21. Varga, V., Leduc, C., Bormuth, V., Diez, S. & Howard, J. Kinesin-8 motors act cooperatively to mediate length-dependent microtubule depolymerization. *Cell* **138**, 1174–1183 (2009).
22. Leduc, C. et al. Molecular crowding creates traffic jams of kinesin motors on microtubules. *Proc. Natl Acad. Sci. USA* **109**, 6100–6105 (2012).
23. Kellogg, E. H. et al. Near-atomic model of microtubule–tau interactions. *Science* **360**, 1242–1246 (2018).
24. McVicker, D. P., Hoeprich, G. J., Thompson, A. R. & Berger, C. L. Tau interconverts between diffusive and stable populations on the microtubule surface in an isoform and lattice specific manner. *Cytoskeleton* **71**, 184–194 (2014).
25. Hernández-Vega, A. et al. Local nucleation of microtubule bundles through tubulin concentration into a condensed Tau phase. *Cell Rep.* **20**, 2304–2312 (2017).
26. Bechstedt, S. & Brouhard, G. J. Doublecortin recognizes the 13-protofilament microtubule cooperatively and tracks microtubule ends. *Dev. Cell* **23**, 181–192 (2012).
27. Sing, C. E., Olvera de la Cruz, M. & Marko, J. F. Multiple-binding-site mechanism explains concentration-dependent unbinding rates of DNA-binding proteins. *Nucleic Acids Res.* **42**, 3783–3791 (2014).
28. Lansky, Z. et al. Diffusible crosslinkers generate directed forces in microtubule networks. *Cell* **160**, 1159–1168 (2015).
29. Samsonov, A., Yu, J.-Z., Rasenick, M. & Popov, S. V. Tau interaction with microtubules in vivo. *J. Cell Sci.* **117**, 6129–6141 (2004).
30. Bechstedt, S., Lu, K. & Brouhard, G. J. Doublecortin recognizes the longitudinal curvature of the microtubule end and lattice. *Curr. Biol.* **24**, 2366–2375 (2014).
31. Monroy, B. Y. et al. Competition between microtubule-associated proteins directs motor transport. *Nat. Commun.* **9**, 1714 (2018).

Acknowledgements

We thank A. Akhmanova and K. Jiang for the generous gift of the katanin plasmid, R. McKenney for feedback and sharing of data, V. Henrichs, I. Zhernov and L. Grycova for help with protein preparation, and Y. Bobrova, S. Dijkstra and C. Bräuer for technical support. We acknowledge the financial support from the Czech Science Foundation (grant no. 18-08304S to Z.L. and 17-12496Y to M.B.), the Introduction of

New Research Methods to BIOCEV (CZ.1.05/2.1.00/19.0390) project from the ERDF, the institutional support from the CAS (RVO: 86652036) and the Imaging Methods Core Facility at BIOCEV, an institution supported by the Czech-BioImaging large RI projects (LM2015062 and CZ.02.1.01/0.0/0.0/16_013/0001775, funded by MEYS CR) for their support in obtaining imaging data presented in this paper.

Author contributions

A.H.-V. and M.B. first observed the islands and initiated the project; A.H.-V., A.A.H., S.D., Z.L. and M.B. conceived the experiments; A.H.-V. generated the tau(ΔN)–meGFP construct; V.S., J.K., A.H.-V. and M.B. generated the proteins, performed and analysed the experiments and V.S., J.K., S.D., Z.L. and M.B. wrote the manuscript. All authors discussed the results and commented on the manuscript.

Competing interests

The authors declare no competing interests.

Additional information

Supplementary information is available for this paper at https://doi.org/10.1038/s41556-019-0374-6.

Reprints and permissions information is available at www.nature.com/reprints.

Correspondence and requests for materials should be addressed to A.H.-V., Z.L. or M.B.

Publisher's note: Springer Nature remains neutral with regard to jurisdictional claims in published maps and institutional affiliations.

Methods

Protein purification. meGFP- or mCherry-tagged tau and tau(ΔN), kinesin-1, Kip3 and katanin were expressed and purified as described previously[20,25,32,33].

In vitro tau–microtubule binding assay. Microtubules and flow chambers were prepared as described previously[33,34]. Biotinylated, paclitaxel-stabilized, Atto 647-labelled microtubules in BRB80T (80 mM PIPES–KOH pH 6.9, 1 mM $MgCl_2$, 1 mM EGTA and 10 μM paclitaxel) were immobilized in a flow chamber using biotin antiboy (Sigma B3640, 20 μg ml^{-1} in PBS). Subsequently, the buffer in the flow chamber was exchanged for assay buffer (20 mM HEPES pH 7.4, 1 mM EGTA, 75 mM KCl, 2 mM $MgCl_2$, 1 mM Mg–ATP, 10 mM dithiothreitol, 0.02 mg ml^{-1} casein, 10 μM paclitaxel, 20 mM D-glucose, 0.22 mg ml^{-1} glucose oxidase and 20 μg ml^{-1} catalase). Tau in assay buffer was then flushed into the flow chamber at the final assay concentration as indicated in the text. To test the robustness of island assembly, we observed island assembly under different conditions of ionic strength (0–125 mM KCl additional to the assay buffer), pH (6.8–7.4) and buffering agent (20 mM HEPES, 50 mM HEPES and 80 mM PIPES). In experiments including multiple subsequent tau additions, the flow chamber was rinsed between each tau addition with high ionic strength buffer (125 mM KCl additional to the assay buffer). To remove tau from solution, the chamber was perfused with approximately four times the chamber volume using assay buffer without tau. For high concentrations of tau (>200 nM), higher volumes (up to ten times the chamber volume) were used to remove tau. In experiments involving kinesin-8, katanin or kinesin-1, islands were first pre-formed before the respective protein was added to the solution (keeping the tau concentration constant). For the katanin experiment at elevated tau concentration (Fig. 5), microtubules were first incubated with 0.8 μM tau–mCherry for 5 min. Tau–mCherry was then briefly removed from the measurement chamber (less than 1 min) for the positions of the islands to be recorded (they were obscured by the high tau–mCherry density in the island surroundings). Tau–mCherry was then added at 0.8 μM. Subsequently, 200 nM katanin–GFP was added to the solution (while maintaining the tau concentration at 0.8 μM). All experiments were performed at room temperature.

Imaging. Atto 647-labelled microtubules and mCherry- and meGFP-labelled proteins were visualized sequentially by switching between the Cy5, TRITC and GFP channels (Chroma filter cubes) on a Nikon-Ti E microscope equipped with a ×100 Nikon TIRFM objective and either Hamamatsu Orca Flash 4.0 sCMOS or Andor iXon EMCCD cameras. The acquisition rate varied between 1 frame per 30 ms to 1 frame per 10 min, depending on the experiment and is indicated in the corresponding figure. Imaging conditions in experiments used for quantitative estimation of kinetic parameters were set such that photobleaching effects were negligible (<2% fluorescent intensity loss during the experiment). Experiments were performed over several months by three researchers. Each experiment was repeated at least on three days. No data was excluded from the study.

Image analysis. Data was analysed using FIJI v.1.52[35] and custom Matlab (Mathworks) routines.

Tau density estimation. Kymographs (using FIJI KymographBuilder plugin, modified to compute integrated intensity instead of finding the maximum intensity) along the microtubule length were used to read out the meGFP or mCherry fluorescent signal and to estimate the integrated signal intensity of meGFP- or mCherry-labelled tau bound to the microtubule (if necessary, time series were drift-corrected with the FIJI plugin 'image stabilizer'). The meGFP signal in regions directly adjacent to the microtubule was estimated in the same way, smoothed with a moving median along the microtubule length and subtracted as background signal. The kymograph pixels were then manually categorized according to the type of microtubule region they covered (islands, regions surrounding the islands, or regions of highly curved microtubules with an increased tau density). The integrated intensity of tau for a region on a microtubule was then computed for each frame by taking the sum of the categorized kymograph pixels. The density of meGFP- or mCherry-labelled tau bound to the microtubule was then estimated by dividing the integrated intensity by the estimated intensity per single fluorescent molecule (either mCherry or meGFP, see below) and the length of the region. Conversion to the number of tau molecules per tubulin dimer was performed assuming tau binding to 13 protofilaments and an 8 nm length of tubulin dimer. The Kip3 densities were estimated analogously: tau–mCherry islands were identified in the corresponding channel (561 nm), and density traces of Kip3–GFP (488 nm) were read out at the corresponding locations.

Single fluorophore quantification. Fluorescent signal of a single fluorescent molecule (meGFP or mCherry) was determined by generating intensity time traces of single meGFP- or mCherry-labelled kinesin-1 molecules tightly bound to the microtubule in presence of adenylyl-imidodiphosphate (in the absence of ATP) and estimating the 'height' of the bleaching steps. The number of steps was first estimated by eye, and this number was used as input for the findchangepoints function of Matlab to determine the position of the steps (by detection of significant changes of the mean value). To yield the intensity per single molecule, the median of the heights of these steps was calculated. The number of averaged steps was at least 15 per estimate. Photobleaching rates (at the given imaging conditions, on the day of the experiment) were determined using the experimental setup described above. Instead of single-molecule intensities, the integrated intensity of all labelled kinesin-1 molecules was measured.

The fraction of microtubule length covered by tau islands. The fraction of microtubule length covered by tau islands was estimated by approximating islands and microtubules with segmented lines, measuring their lengths and dividing the sum of the lengths of the islands on a single microtubule (or in a field of view) by the length of the respective microtubule on which the islands are located (or by the summed length of all microtubules in a field of view).

Estimation of the tau-unbinding time. To estimate the unbinding times of tau inside and outside the islands, we analysed how the tau density in a given region decayed over time after a buffer exchange that either removed tau from solution or replaced tau–meGFP in the solution with tau–mCherry. Every analysed region (island or surrounding) yielded a time trace of tau density decay after a buffer exchange. Time traces from exemplary experiments were combined to be presented in Fig. 1f,h, Supplementary Figs. 1g, 2b,c; the line represents the median value of all traces at the given point in time and the edges of the shaded area represent the first and third quartiles. To estimate the mean residence times of tau inside and outside the islands, individual density time traces as described above were fitted separately by an exponential decay using the Matlab function 'fit' (data points taken before exchange of solution were not taken into account). The presented fits and mean residence times were computed by averaging the coefficients of the individual fits.

Estimation of velocity and diffusion coefficient. Tracking of single tau molecules for the estimation of diffusion coefficient was performed using FIESTA[36] software. To reconnect tracks, a threshold velocity of 12,000 nm s^{-1} was chosen, and tracks were allowed to have at most three missing frames between two data points. To minimize false-positive connections of molecules, the tracks obtained by FIESTA were cut such that the maximum distance between two data points was never more than 360 nm. Island boundary assembly and disassembly velocities (in the absence or presence of katanin or Kip3) were estimated by approximating straight lines onto segments of advancing or receding tau-island edges in kymographs. The value presented in the text is a duration-weighted average of the corresponding segments. This was converted to the number of tau molecules per second by multiplying this velocity by the estimated characteristic tau density within islands (in molecules per nanometre), assuming tau binding to 13 protofilaments and 8 nm length per tubulin dimer. Kip3 and kinesin-1 velocities were estimated by approximating straight lines onto kymographs of moving motors (inside and outside islands).

Katanin severing-rate estimation. Severing rates in the areas surrounding the islands were estimated by fitting exponential decay to the number of pixels in the area of the original microtubule position above a threshold value, which was manually set to encompass the microtubule. In island regions, cuts were counted. In Supplementary Fig. 4e, the estimated severing rates include both straight and curved microtubules. In Supplementary Fig. 5d, the severing rates are sorted according to the following definition: straight microtubules were defined as microtubule stretches in which the microtubule orientation would not change beyond 10°; curved regions were defined as 0.5 μm-long stretches of microtubule centred at the point of highest curvature with radius <2.5 μm.

Data representation. In all box plots presented in the figures, the horizontal midline indicates the median; bottom and top box edges indicate the 25th and 75th percentiles, respectively; the whiskers extend to the most extreme data points not considered as outliers (the function 'Alternative box plot' from the IoSR Matlab Toolbox has been used). Thick lines with shaded areas, unless otherwise indicated, show the median and the 25th and 75th percentiles. Where single data points are presented, points from the same experiment are indicated by the same colour (unless otherwise stated). The individual data points have been weighted such that each experiment carries the same weight for determination of the median and percentile lines. Weighting by experiments has been performed in all data represented in the text or in figures involving averages or quartiles, except for the determination of the diffusion constants of tau, where each experiment was weighted according to how many tau molecules were observed in the respective experiment.

Statistics and reproducibility. Experiments were performed over several months by three researchers; all replication attempts (that were not impeded by unrelated events, such as an image-acquisition-software malfunction) were successful. For each quantified experiment and each exemplary image or kymograph, *N* describes the number of either biologically independent samples (individual tau molecules, islands of tau molecules or microtubules) or the number of independent events (island nucleation, island merging or island fission). In all cases, the number of independent experiments, during which the data were gathered over the course

of several days, refers to the number of independent flow channels, which were assembled, filled with assay components and imaged individually.

Reporting Summary. Further information on research design is available in the Nature Research Reporting Summary linked to this article.

Data availability

Source data for Figs. 1–5 and quantifications given in the main text (island density) have been provided as Supplementary Table 1. Example raw videos are available at BioStudies with accession number S-BSST266. All other data supporting the findings of this study are available from the corresponding authors on reasonable request.

Code availability

Code used to determine single-molecule intensities (GNU General Public License v.3, for further information see repository) is available at https://doi.org/10.5281/zenodo.3270568. Code used to create kymographs (MIT license, for further information see repository) is available at https://doi.org/10.5281/zenodo.3270572. All other custom written code is available from the corresponding authors on request.

References

32. Mitra, A., Ruhnow, F., Girardo, S. & Diez, S. Directionally biased sidestepping of Kip3/kinesin-8 is regulated by ATP waiting time and motor-microtubule interaction strength. *Proc. Natl Acad. Sci. USA* **115**, E7950–E7959 (2018).
33. Nitzsche, B. et al. Studying kinesin motors by optical 3D-nanometry in gliding motility assays. *Methods Cell Biol.* **95**, 247–271 (2010).
34. Braun, M. et al. Adaptive braking by Ase1 prevents overlapping microtubules from sliding completely apart. *Nat. Cell Biol.* **13**, 1259–1264 (2011).
35. Schindelin, J. et al. Fiji: an open-source platform for biological-image analysis. *Nat. Methods* **9**, 676–682 (2012).
36. Ruhnow, F., Zwicker, D. & Diez, S. Tracking single particles and elongated filaments with nanometer precision. *Biophys. J.* **100**, 2820–2828 (2011).

Publication 2: Ase1 selectively increases the lifetime of antiparallel microtubule overlaps

Report

Current Biology

Ase1 selectively increases the lifetime of antiparallel microtubule overlaps

Highlights

- Ase1 can significantly enhance the lifetime of antiparallel microtubule overlaps
- Ase1 selectively promotes rescues for antiparallelly crosslinked microtubules
- Ase1 is herded by depolymerizing microtubule ends
- Ase1 herding correlates with reduced microtubule depolymerization speed

Authors

Jochen Krattenmacher, Manuel Lera-Ramirez, Alexandre Beber, ..., Stefan Diez, Marcus Braun, Zdenek Lansky

Correspondence

marcus.braun@ibt.cas.cz (M.B.), zdenek.lansky@ibt.cas.cz (Z.L.), stefan.diez@tu-dresden.de (S.D.), fjn28@cam.ac.uk (F.N.)

In brief

Krattenmacher et al. demonstrate that the microtubule (MT) crosslinker Ase1 selectively impedes the depolymerization of MTs in antiparallel overlaps, with lesser effects on parallel and isolated MTs. They also show that Ase1 is herded by depolymerizing MT ends, and that this herding correlates with reduced MT depolymerization speed.

Krattenmacher et al., 2024, Current Biology *34*, 4071–4080
September 9, 2024
https://doi.org/10.1016/j.cub.2024.07.055

CellPress

Current Biology

CellPress
OPEN ACCESS

Report

Ase1 selectively increases the lifetime of antiparallel microtubule overlaps

Jochen Krattenmacher,[1,2,3] Manuel Lera-Ramirez,[4] Alexandre Beber,[1] Stepan Herynek,[1] Lenka Grycova,[1] Xiaocheng Liu,[5] Pavel Neuzil,[5] Francois Nedelec,[6,*] Stefan Diez,[2,7,8,*] Marcus Braun,[1,*] and Zdenek Lansky[1,9,*]

[1]Institute of Biotechnology, Czech Academy of Sciences, BIOCEV, 25250 Vestec, Czechia
[2]B CUBE - Center of Molecular Bioengineering, Technische Universität Dresden, 01307 Dresden, Germany
[3]Faculty of Science, Charles University in Prague, 12800 Prague, Czech Republic
[4]Institut Curie, PSL Research University, Sorbonne Université, CNRS UMR144, Paris, France
[5]School of Mechanical Engineering, Department of Microsystem Engineering, Northwestern Polytechnical University, Xi'an, Shaanxi 710072, P.R. China
[6]Sainsbury Laboratory Cambridge, University of Cambridge, CB2 1LR Cambridge, UK
[7]Max Planck Institute of Molecular Cell Biology and Genetics, 01307 Dresden, Germany
[8]Cluster of Excellence Physics of Life, Technische Universität Dresden, 01062 Dresden, Germany
[9]Lead contact
*Correspondence: marcus.braun@ibt.cas.cz (M.B.), zdenek.lansky@ibt.cas.cz (Z.L.), stefan.diez@tu-dresden.de (S.D.), fjn28@cam.ac.uk (F.N.)
https://doi.org/10.1016/j.cub.2024.07.055

SUMMARY

Microtubules (MTs) are dynamically unstable polar biopolymers switching between periods of polymerization and depolymerization, with the switch from the polymerization to the depolymerization phase termed catastrophe and the reverse transition termed rescue.[1] In presence of MT-crosslinking proteins, MTs form parallel or anti-parallel overlaps and self-assemble reversibly into complex networks, such as the mitotic spindle. Differential regulation of MT dynamics in parallel and anti-parallel overlaps is critical for the self-assembly of these networks.[2,3] Diffusible MT crosslinkers of the Ase1/MAP65/PRC1 family associate with different affinities to parallel and antiparallel MT overlaps, providing a basis for this differential regulation.[4–11] Ase1/MAP65/PRC1 family proteins directly affect MT dynamics[12] and recruit other proteins that locally alter MT dynamics, such as CLASP or kinesin-4.[7,13–16] However, how Ase1 differentially regulates MT stability in parallel and antiparallel bundles is unknown. Here, we show that Ase1 selectively promotes antiparallel MT overlap longevity by slowing down the depolymerization velocity and by increasing the rescue frequency, specifically in antiparallelly crosslinked MTs. At the retracting ends of depolymerizing MTs, concomitant with slower depolymerization, we observe retention and accumulation of Ase1 between crosslinked MTs and on isolated MTs. We hypothesize that the ability of Ase1 to reduce the dissociation of tubulin subunits is sufficient to promote its enrichment at MT ends. A mathematical model built on this idea shows good agreement with the experiments. We propose that differential regulation of MT dynamics by Ase1 contributes to mitotic spindle assembly by specifically stabilizing antiparallel overlaps, compared to parallel overlaps or isolated MTs.

RESULTS AND DISCUSSION

Ase1 selectively promotes the persistence of antiparallel microtubule overlaps

To study the interactions of Ase1 and dynamic microtubules (MTs), we employed total internal reflection fluorescence (TIRF) and interference reflection microscopy (IRM) time-lapse imaging of immobilized, GMPCPP-stabilized MT seeds in the presence of free tubulin (30 μM) and fluorescently labeled Ase1 (10, 42, and 420 nM) (STAR Methods). We observed dynamic, Ase1-decorated MT extensions polymerizing from the MT seeds. When a polymerizing MT plus end encountered another MT, it either crossed the other MT or formed a bundle with it (Figures 1A, 1B, and S1A; Videos S1A–S1F), depending on the angle of incidence and Ase1 concentration (Figure S1B). As previously reported,[6] antiparallel bundles formed even at large initial angles of incidence (up to 40° at higher Ase1 concentrations), while parallel bundles mostly formed at initial angles below 20° (Figure S1B). In the absence of Ase1, MTs never bundled, even when very close to each other over extended periods of time (Figure S1C; Video S1G). We then quantified the lifetimes of parallel and antiparallel overlaps in these experiments. Although at 10 nM Ase1 we found that antiparallel overlaps were no more stable than parallel ones (Figure 1C), with increasing Ase1 concentration a difference between the lifetimes increased, with antiparallel overlaps having higher lifetimes (Figure 1C). We

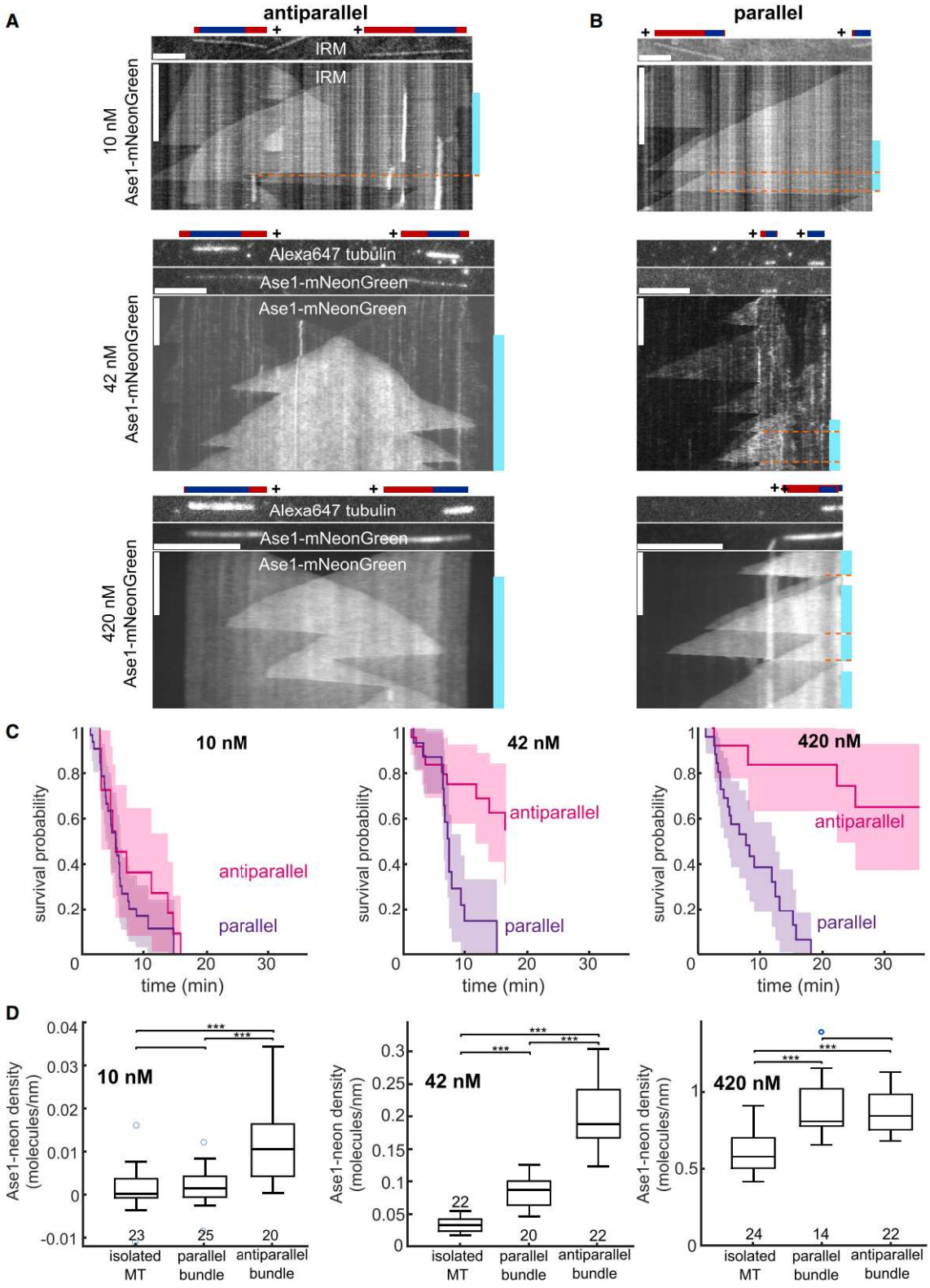

Figure 1. Ase1 selectively promotes the persistence of antiparallel MT overlaps

(A) Kymographs of two MTs polymerizing toward each other in the presence of Ase1-mNeonGreen, subsequently forming a region of antiparallel MT overlap (scale bars, 5 μm and 10 min). In sketches, dynamic extensions with GDP lattices are red and stabilized GMPCPP seeds are blue. The teal bars next to

(legend continued on next page)

hypothesized that this effect could be due to increased densities of Ase1 molecules bound in antiparallel overlaps compared to parallel ones, as reported earlier.[6] Indeed, with 10 and 42 nM Ase1 in solution, the observed Ase1 densities on antiparallel overlaps were much higher than on parallel ones (Figure 1D). At 420 nM Ase1, we observed the density of Ase1 to be similar to Ase1 densities on antiparallel and parallel bundles (Figure 1D). The measured values, however, represent the total density of Ase1 at the position of the overlap, which might differ from the density of Ase1 molecules directly engaged in MT crosslinking by being bound simultaneously to both MTs. Importantly, despite similar decoration levels by Ase1 at 420 nM, antiparallel overlaps nevertheless were significantly more stable than parallel ones (Figure 1C). Combined, these data show that Ase1 selectively promotes the lifetimes of antiparallel overlaps.

Ase1 differentially regulates the dynamics of microtubules in parallel and antiparallel overlaps

The relative stability of antiparallel overlaps at high Ase1 concentrations may, in part, owe to the fact that antiparallel overlaps grow twice as fast as parallel ones, since both MTs polymerize in opposite directions. However, our data suggest that antiparallel overlaps may be additionally stabilized by altered MT dynamics. To investigate this question, we quantified MT dynamics for various Ase1 concentrations (Figures 2 and S2A). We found that polymerization velocities were similar for all MTs, either isolated or bundled, across all tested Ase1 concentrations (Figure 2A). The catastrophe frequencies slightly decreased with Ase1 concentration similarly in isolated or bundled MTs (Figure 2B). Importantly, we found both depolymerization velocities and rescue frequencies to be sensitive to both Ase1 concentration and the MT organization (Figures 2C and 2D). At 420 nM Ase1, MTs depolymerized markedly slower than at lower Ase1 concentrations. Further, at 42 and 420 nM Ase1, antiparallel MTs displayed a marked decrease in depolymerization velocity and a pronounced increase in rescue frequency compared to isolated and parallel MTs (Figures 2C and 2D). Our results at 42 nM Ase1 may indicate that this effect is due to the increased number of Ase1 molecules observed on antiparallel MTs as compared to parallel and isolated MTs. At 420 nM Ase1, however, the decrease in depolymerization velocities and pronounced increase in rescue frequencies persist despite indistinguishable Ase1 densities on antiparallel versus parallel MT overlaps (Figures 2E and 2F). The number of Ase1 molecules localized to the MT overlap was the only factor we could identify as influencing the frequency of rescues (Figures 2D and 2F). Note, however, that the number of molecules directly participating in the crosslinking process, i.e., simultaneously bound to both crosslinked MTs, is not measurable in this assay. Combined, these results demonstrate that Ase1 can differently modulate MT dynamics in parallel and antiparallel overlaps, resulting in stabilization of antiparallel MT overlaps.

Slower MT depolymerization coincides with accumulation of Ase1 at depolymerizing MT ends

To investigate the mechanism underpinning Ase1-dependent MT stabilization, we next examined the localization of Ase1 on MTs. Although on polymerizing MTs Ase1 did not exhibit any specific localization, on depolymerizing MTs, we observed that Ase1 accumulated at MT ends (Figures 1 and S2B). We thus repeated the experiments at a higher frame rate and altered experimental conditions to analyze this process (STAR Methods; Figures S3A and S3B). We had chosen an Ase1 concentration (1 nM) at which we observed very little Ase1 binding to isolated MTs while observing prominent binding to antiparallel overlaps (Figures 3A, 3D, and S3C; Video S2). At the depolymerizing ends of overlaps and isolated MTs, we observed accumulation of Ase1 molecules (Figures 3A, 3B, and S3D). We found that as Ase1 accumulated at the disassembling tip, the velocity of the MT disassembly decreased for both, for overlaps and isolated MTs (Figures 3A–3F and S3E). We next compared Ase1 accumulation at the ends of antiparallel overlaps and isolated MTs, after adjusting the bulk Ase1 concentrations to reach comparable Ase1 densities on the MTs. This was achieved by imaging antiparallel overlaps at 1 nM Ase1 and isolated MTs at 6 nM Ase1 (Figures 3G and S3C). We found that although isolated MTs at 6 nM Ase1 accumulated more Ase1 than antiparallel MTs at 1 nM Ase1, these isolated MTs did not depolymerize slower than the antiparallel MTs at 1 nM (Figures 3B, 3C, 3H, and 3I). While recent results indicate that gradual slowdown of disassembly is an inherent feature of MT depolymerization,[17] in the absence of Ase1 we had not observed any slowdown in MT depolymerization comparable to what we observed in the presence of Ase1 (Figures S3F and S3G). Moreover, we found that with an increasing amount of accumulated Ase1 at the MT tip, as well as with an overall increase in local density of Ase1 molecules at the tip, the probability of rescue increased (Figures 3A–3J and S3H). We repeated the experiment with both Ase1 and tubulin removed from the solution. As MTs started to depolymerize, Ase1 still accumulated at the depolymerizing ends, indicating that the accumulates are composed of Ase1 molecules that were already bound to the MT lattice before catastrophe (Figure S3I; Video S3). As recently reported with a synthetic MT crosslinker,[18] we also observed that a depolymerizing MT end would drag other MTs, indicating that substantial forces could be transmitted by this mechanism (Figure S3J; Video S3). In summary, our experiments demonstrate that lattice-bound Ase1 molecules are swept by the depolymerizing MT ends and that the number of swept Ase1 molecules correlates with reduced depolymerization velocity and increased rescue probability.

kymographs indicate the presence of regions of overlap (we only counted regions where the two partaking MT regions are constituted by GDP-tubulin, i.e., a seed stabilized by GMPCPP did not count). The orange lines indicate a termination of the overlapping period, as evaluated for (C).

(B) Kymographs of two MTs polymerizing in a parallel configuration in the presence of Ase1-mNeonGreen, sometimes forming a region of overlap.

(C) Survival probability of antiparallel and parallel overlaps, showing the probability that an overlap formed by two dynamic MT extensions persists at a given time after its formation (STAR Methods). Semitransparent regions indicate 95% lower and upper confidence bounds.

(D) Quantification of the density of Ase1-mNeonGreen on isolated MTs and (anti)parallel bundles (STAR Methods). The numbers below the boxes denote the number of analyzed MT bundles, $***p < 0.001$ (Tukey's test).

Panels show data for MT plus ends (minus ends generally were not analyzed).

See also Figure S1 and Video S1.

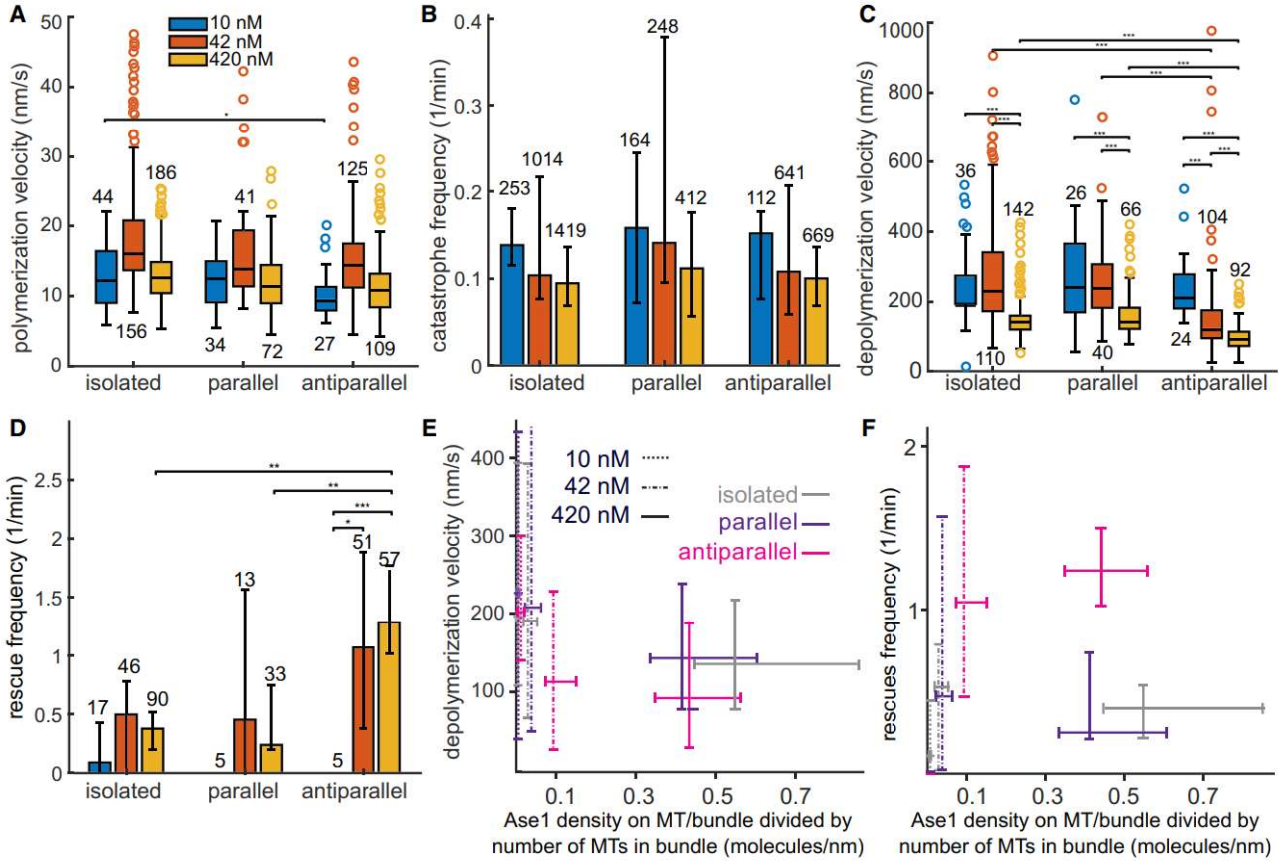

Figure 2. Ase1 differentially regulates the dynamics of microtubules in parallel and antiparallel overlaps

(A–D) Polymerization velocity (A), catastrophe frequency (B), depolymerization velocity (C), and rescue frequency (D) of dynamic MT plus ends in different configurations and in the presence of varying concentrations of Ase1-mNeonGreen.

(E) Depolymerization velocity (see A) versus Ase1-mNeonGreen density on a given MT or bundle divided by number of MTs in that bundle (i.e., the density as shown in Figure 1D is divided by 2 in the case of parallel and antiparallel MTs).

(F) Rescue frequency (see D) versus Ase1-mNeonGreen density (see Figure 1D).

All plots show results for the same experiments as shown in Figure 1. $^{*}p < 0.05$, $^{**}p < 0.01$, $^{***}p < 0.001$ (Tukey's test). Boxplots are weighted by the length of a sampled period of polymerization or depolymerization. In boxplots, the numbers indicate the number of recorded events; in bar plots, the numbers indicate the sum of the length of all sampled periods of polymerization or depolymerization (in minutes). In bar plots, the height of the bar indicates the catastrophe/rescue frequency as determined from all timelapses (number of total events divided by total duration of depolymerization), while the error bars indicate the lowest and highest rates as determined from each isolated timelapse; velocities are normalized to the median velocity of isolated MTs (STAR Methods).

See also Figure S2.

Stabilization of terminal tubulin subunits by Ase1 is sufficient to reproduce Ase1 sweeping and reduced MT depolymerization velocity

To mathematically analyze the molecular mechanism that causes Ase1 to accumulate at depolymerizing MT ends while reducing their depolymerization velocity, we developed a simple model for an isolated MT. This model treats the MT as a 1D lattice of repeating Ase1 binding sites representing tubulin heterodimers of one MT protofilament and neglects its 3D nature and protofilament structure (STAR Methods). Ase1 binding, unbinding, and hopping to adjacent lattice sites are represented as stochastic events. The associated rates, k_{on} , k_{off}, k_h (Figure 4A), are determined experimentally (Table S1). Only one Ase1 molecule can be attached to any one tubulin heterodimer, meaning that Ase1 can hop only to unoccupied neighboring sites. When reaching the end of an MT, Ase1 can either hop away from this end (if the proximal binding site is unoccupied) or unbind with rate k_{off}, as modeled previously.[20] MT depolymerization is modeled discretely with stochastic detachment of the terminal heterodimer. The rate of depolymerization is affected by Ase1 (Figure 4B). Specifically, this rate is k_d^0 when the terminal tubulin is free of Ase1 and $k_d = (1 - \Omega)k_d^0$ otherwise. The value of k_d^0 is calibrated from the MT depolymerization velocity in the absence of Ase1, measured experimentally (Table S1). The parameter $\Omega \in [0, 1]$ specifies the effect of Ase1 on depolymerization. If $\Omega = 0$, Ase1 has no effect, while if $\Omega = 1$, the terminal subunit cannot unbind while Ase1 is bound. For $\Omega > 0$, this model leads to an accumulation of Ase1 near the depolymerizing end accompanied by a decrease of the depolymerization velocity (Figures 4C–4E, S4A, and S4B). The accumulation occurs because subunits without Ase1 are more likely to be lost at the plus end. Selective loss of tubulin without Ase1 thus increases

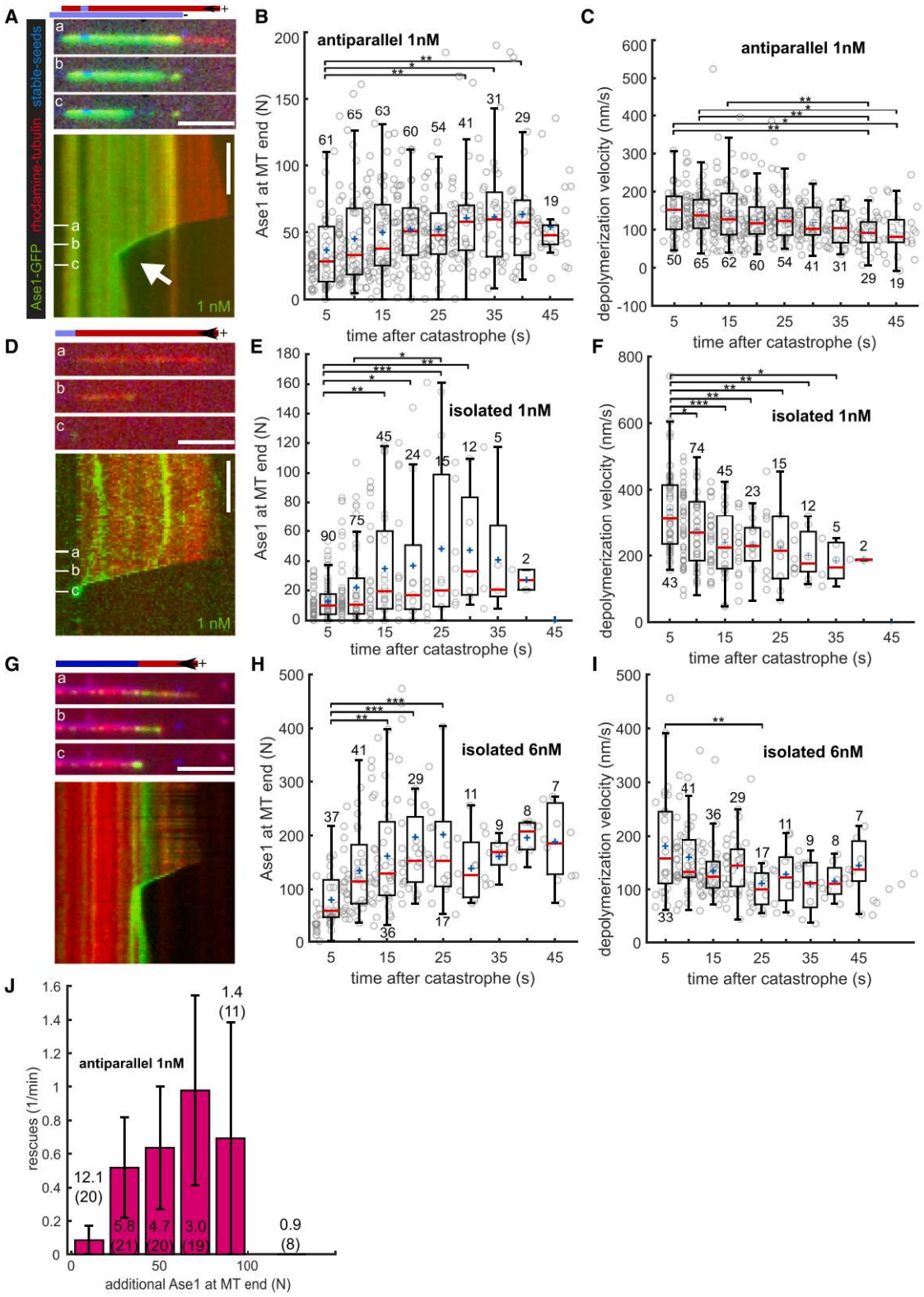

Figure 3. Slower MT depolymerization coincides with accumulation of Ase1 at depolymerizing MT

(A, D, and G) Kymographs of the plus end of depolymerizing MTs in the presence of Ase1-GFP in solution. The stabilized GMPCPP-MT seeds were labeled with 15% rhodamine and 15% Alexa 647 (or, alternatively, with 2% Alexa 647), while the free tubulin in solution was labeled with 7% rhodamine. In sketches, dynamic

(legend continued on next page)

the density of Ase1 at the depolymerizing end, creating a positive feedback that counteracts MT depolymerization. At steady state, the system can be characterized by the probability P_1 of the terminal site to be occupied and the rate of subunit loss, which is $k_d = k_d^0(1 - \Omega P_1)$. This model is sufficient to highlight the fundamental consequences of stabilizing the terminal tubulin subunits but did not fully match the experimental data. We thus generalized this model, assuming that the rate of loss of terminal tubulin subunits is reduced by the same factor $(1 - \Omega)$ if an Ase1 molecule is present in either of the N-terminal sites. Thus, this rate is $k_d = k_0^d\left[1 - \Omega\{1 - \prod_{i=1}^{i=N}(1 - P_i)\}\right]$, where P_i is the probability of site i being occupied by Ase1. Model parameters were set from experimental measurements except for Ω and N (Table S1). Models with large values of N are unlikely, since they would require Ase1 to influence the detachment of a distant tubulin subunit. We considered the previous model, model 1 ($N = 1$), where only Ase1 bound to the terminal subunits affects its unbinding, and model 2 ($N = 3$), where unbinding is also affected by the 3 terminal subunits. For these two models, we systematically varied Ω and compared the model results with the experimental data. Specifically, we aimed to reproduce the timescale of accumulation of Ase1 and the total amount of Ase1 accumulated and depolymerizing velocity reached at steady state (Table S2). We got the best match with model 2 and $\Omega = 0.9$ (Figures S4A and S4B), which could reproduce the extent and timescale of Ase1 accumulation as well as the steady-state depolymerization velocity for isolated MTs at 6 nM Ase1 (Figures 4C and S4A). With the same parameters, we could recapitulate the Ase1 accumulation timescale and steady-state accumulation for isolated MTs at 1 nM Ase1 (Figures 4D and S4B). In the case of overlaps at 1 nM of Ase1, both models predict a lower number of swept Ase1 molecules than we had measured experimentally but correctly predict that Ase1 molecules have a bigger impact on MT depolymerization in the case of overlaps (Figures S4A–S4C). In summary, built on a simple assumption of how Ase1 would affect the tubulin unbinding rate, this model explains the Ase1 sweeping at shrinking MT ends associated with the slowdown of MT disassembly and recapitulates quantitatively the behavior of the isolated MTs at 6 nM Ase1, and within an order of magnitude for 1 nM Ase1.

In this work, we show that Ase1 selectively stabilizes antiparallel overlaps without substantially affecting the dynamics of isolated MTs or MTs in parallel overlaps. In mitotic spindles and other bipolar MT arrays, this can lead to selective stabilization of the array's central regions, while keeping the rest of the array dynamic and pliable. We observed Ase1 sweeping, the accumulation of lattice-bound, diffusible Ase1 at depolymerizing MT ends, termed "protein sweeping" or "herding," which is analogous to the *in vitro* behavior of the MT-severing enzyme spastin and the kinetochore-associated Ndc80 and Dam1 complexes.[21–27] Like Ase1, Dam1 and Ndc80 complexes accumulate at depolymerizing MT ends and decrease depolymerization velocity.

We produced simple models based on the assumption that Ase1 reduces the detachment of terminal tubulin subunits when bound at the MT tip. This assumption, when allowing for diffusion of Ase1 molecules along the protofilament, leads to both a decrease of MT depolymerization velocity and accumulation of Ase1 at the tip of shrinking MTs. Sweeping occurs because subunits without Ase1 are more likely to be lost at the plus end, and their loss increases the density of Ase1 at the depolymerizing end. Our model quantitatively recapitulated the behavior of the system for 6 nM Ase1 (Figure 4C), and within an order of magnitude for 1 nM Ase1 (Figure 4D). Given the low density of Ase1 molecules at 1 nM concentration (<1% of tubulin dimers bound to Ase1), the discrepancy may be due to stochasticity of the system. Our model did not include MT rescues; however, if one assumes that each crosslink reached by a depolymerizing MT tip has a chance of inducing rescue, as proposed by Stoppin-Mellet et al.,[12] we expect a positive correlation between Ase1 density and rescue frequency, consistent with our experimental data. The quantitative disagreement with experimental data for antiparallelly crosslinked MTs might be due to the fact that Ase1 is not distributed evenly between the protofilaments of a crosslinked MT, with protofilaments involved in crosslinking containing higher densities of Ase1 (Figure 1D). A more complex model accounting for protofilament interactions would be needed for overlaps, informed by experimental measurements of such interactions. Finally, Ase1 is known to display multimerization within antiparallel MT overlaps,[28] which, as reported recently, is an important factor involved in slowdown of motor-driven MT sliding.[29] Multimerization, especially when promoted by the herding of Ase1 molecules at depolymerizing MT tips, might add another layer of complexity to the Ase1-mediated regulation of MT dynamics, possibly resulting in the addition of nonlinearities to the otherwise linear relationship between catastrophe frequency and tubulin concentration.[30] Conversely, herding of the Ase1 crosslinkers might be involved in the slowdown of MT sliding propelled by molecular motors, if the protein traffic jam at the MT tip increases the friction that motors must overcome. Though the cases of MT depolymerization and MT sliding are different in that MT depolymerization does not involve MT movement

extensions with GDP lattices are colored red and stabilized GMPCPP seeds are colored blue or light blue (in case of the weakly labeled seeds). Scale bars, 5 μm and 1 min; contrast and balance vary from panel to panel (each kymograph shows a different MT). White arrows highlight rescue events.

(B, E, and H) The number of additional Ase1 molecules at the end of depolymerizing MTs, plotted over the time passed since the catastrophe. Each data point represents data extracted from one line scan.

(C, F, and I) The frame-to-frame depolymerization velocity of MTs over time (analogous to B, E, and H). Because the exact time of catastrophe is unknown due to limits in temporal resolution, the velocity measurement right after catastrophe underestimates the actual velocity.

(J) Rescue frequency plotted over number of additional Ase1 molecules at the MT end. The duration depolymerized at a respective x value was added to the respective bin. The number of rescues observed in the same bin (N) was then divided by the sum of depolymerization durations (shown in min; the number in parentheses refers to the number of MTs) to estimate the rescue frequency. The correlation coefficient (weighted[19] by sums of depolymerization durations) is 0.67. For an example event, see (A). $^*p < 0.05$, $^{**}p < 0.01$, $^{***}p < 0.001$ (Tukey's test).

See also Figure S3 and Videos S2 and S3.

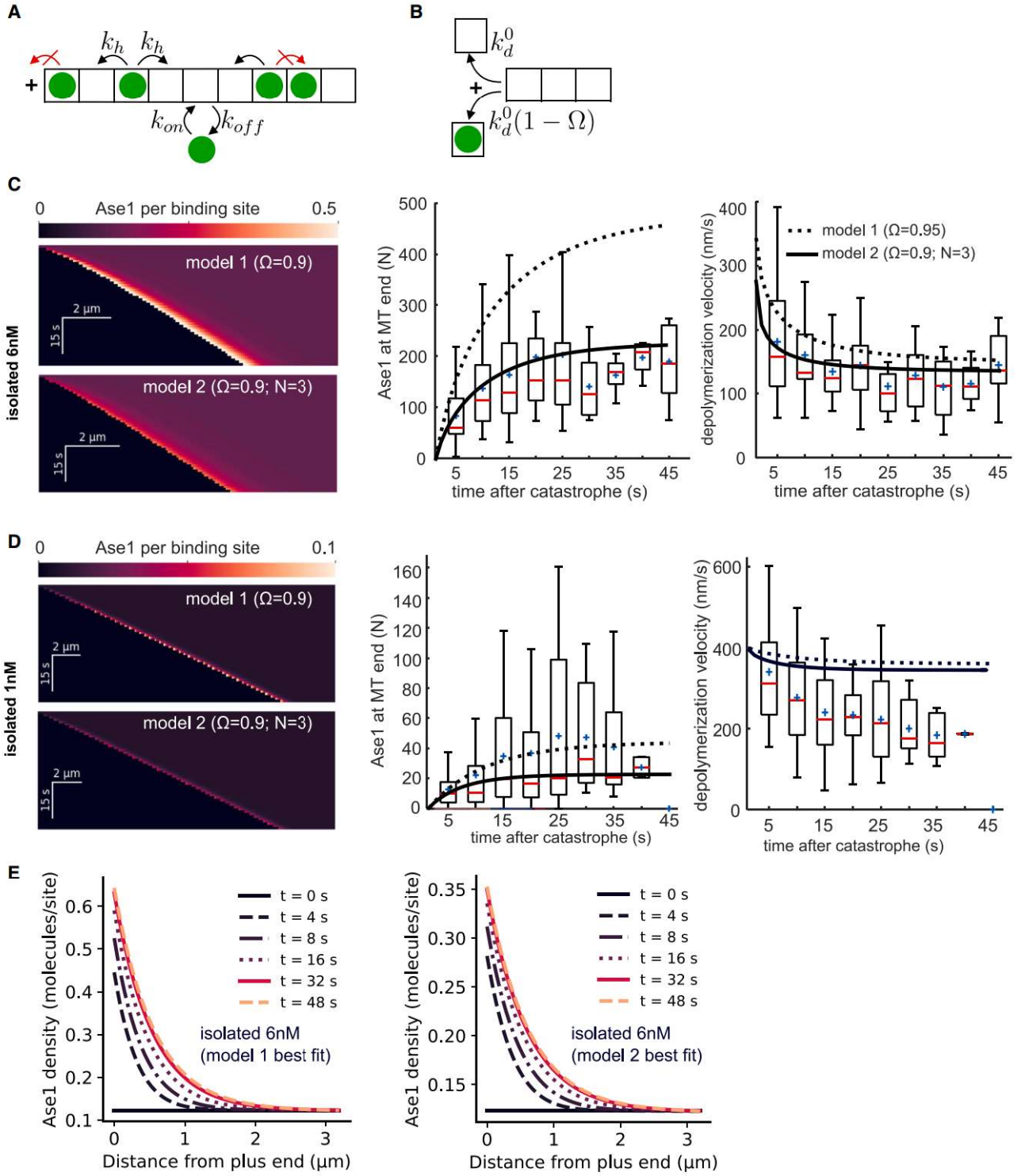

Figure 4. Stabilization of terminal tubulin subunits by Ase1 is sufficient to reproduce Ase1 sweeping and reduced MT depolymerization velocity

(A and B) Cartoons representing model assumptions (STAR Methods).

(A) Ase1 binding, unbinding, and hopping to neighboring sites are stochastic events with constant rates, k_{on} ,k_{off} ,k_h. Only one Ase1 molecule can be attached to any one tubulin heterodimer, so moving or binding to an occupied binding site is not allowed (red crossed arrow on the right). Ase1 does not fall off from the MT by hopping at its plus ends (red crossed arrow on the left).

(legend continued on next page)

and thus no movement of Ase1 binding sites, herding-driven Ase1 multimerization appears plausible by locally increasing Ase1 density. The possibility of Ase1 molecules acting cooperatively to promote rescues for antiparallel MTs specifically is intriguing and would offer the cell a lever for modulating the rescue-promoting effect of MT crosslinking. A combination of these factors could explain the stronger stabilizing effect of Ase1 on antiparallel overlaps.

Our results show that the presence of diffusible MT crosslinkers is sufficient to establish enduring antiparallel MT overlaps, such as those found in the midzone of mitotic spindles. In such context, Ase1 can work cooperatively with other MT rescue factors such as CLASP[14] or provide an alternative mechanism for selective lifetime enhancement of antiparallel overlaps. We speculate that the impact of diffusible crosslinkers on MT dynamics may be tunable by posttranslational modifications of either the crosslinkers or the MT surface. Such a tunability has recently been proposed for a seemingly related capacity of Ase1, namely the braking of MT sliding caused by molecular motors.[31,32] For actin filament overlaps, it has been observed that F-actin crosslinkers slow down actin depolymerization,[33,34] suggesting that crosslinker-dependent stabilization of filaments may be a fundamental mechanism in cytoskeletal systems.

STAR★METHODS

Detailed methods are provided in the online version of this paper and include the following:

- KEY RESOURCES TABLE
- RESOURCE AVAILABILITY
  - Lead contact
  - Materials availability
  - Data and code availability
- EXPERIMENTAL MODEL AND STUDY PARTICIPANT DETAILS
- METHOD DETAILS
  - Ase1 expression and purification
  - Microtubule seeds assembly
  - Experimental chamber preparation
  - Assay buffer
  - Imaging
  - Image analysis
  - Mathematical modelling
  - Modelling of overlaps
- QUANTIFICATION AND STATISTICAL ANALYSIS
  - Data representation
  - Comparison of experimental data and model

SUPPLEMENTAL INFORMATION

Supplemental information can be found online at https://doi.org/10.1016/j.cub.2024.07.055.

ACKNOWLEDGMENTS

We thank Veronika Vanova and Tereza Smidova for technical support. We acknowledge projects nos. 19-27477X (Z.L.), 22-11753S (M.B.), and 19-17398S (S.H.) from the Czech Science Foundation; project no. 116120 (J.K.) from the Grant Agency of Charles University; the institutional support of the Czech Academy of Sciences (RVO: 86652036); project LX22NPO5107 (MEYS) financed by European Union – Next Generation EU; CMS-Biocev (biophysical techniques) supported by MEYS CR (LM2015043); and the Centre of Imaging Methods core facility, Faculty of Science, Charles University, supported by the Czech-BioImaging through MEYS CR (LM2015062 and CZ.02.1.01/0.0/0.0/16_013/0001775). P.N. and X.L. acknowledge the financial support of 52150710541 from NSFC, P.R. China.

AUTHOR CONTRIBUTIONS

Conceptualization, S.D., M.B., and Z.L.; methodology, J.K., M.L.-R., F.N., S.D., M.B., and Z.L.; investigation, J.K. and M.L.-R.; formal analysis, J.K. and M.L.-R.; data curation, J.K.; validation, J.K.; resources, S.H., L.G., X.L., and P.N.; writing, J.K., M.L.-R., F.N., S.D., M.B., and Z.L.; visualization, J.K. and M.L.-R.; supervision, P.N., F.N., M.B., and Z.L.; funding acquisition, J.K., P.N., M.B., and Z.L.

DECLARATION OF INTERESTS

The authors declare no competing interests.

Received: August 5, 2022
Revised: April 30, 2024
Accepted: July 15, 2024
Published: August 12, 2024

REFERENCES

1. Kirschner, M., and Mitchison, T. (1986). Beyond self-assembly: from microtubules to morphogenesis. Cell *45*, 329–342. https://doi.org/10.1016/0092-8674(86)90318-1.
2. Nédélec, F., Surrey, T., and Karsenti, E. (2003). Self-organisation and forces in the microtubule cytoskeleton. Curr. Opin. Cell Biol. *15*, 118–124. https://doi.org/10.1016/S0955-0674(02)00014-5.
3. Mastronarde, D.N., McDonald, K.L., Ding, R., and McIntosh, J.R. (1993). Interpolar spindle microtubules in PTK cells. J. Cell Biol. *123*, 1475–1489. https://doi.org/10.1083/jcb.123.6.1475.
4. Löiodice, I. (2005). Ase1p organizes antiparallel microtubule arrays during interphase and mitosis in fission yeast. Mol. Biol. Cell *16*, 1756–1768. https://doi.org/10.1091/mbc.E04–10–0899.
5. Yamashita, A., Sato, M., Fujita, A., Yamamoto, M., and Toda, T. (2005). The roles of fission yeast Ase1 in mitotic cell division, meiotic nuclear oscillation, and cytokinesis checkpoint signaling. Mol. Biol. Cell *16*, 1378–1395. https://doi.org/10.1091/mbc.E04-10-0859.
6. Janson, M.E., Loughlin, R., Loïodice, I., Fu, C., Brunner, D., Nédélec, F.J., and Tran, P.T. (2007). Crosslinkers and motors organize dynamic microtubules to form stable bipolar arrays in fission yeast. Cell *128*, 357–368. https://doi.org/10.1016/j.cell.2006.12.030.

(B) In model 1, we assume that the detachment rate of the tubulin terminal subunit is k_d^0 when the first tubulin subunit is free of Ase1 and $k_d = (1 - \Omega)k_d^0$ if Ase1 is bound at the terminal site (for model 2, see main text and STAR Methods).
(C and D) Modeling results for models 1 and 2 with $N = 3$ (experimental data presented in the form of boxplots), for isolated MTs at 6 (C) and 1 nM (D). Left panels: distribution of Ase1 density in time represented as a simulated kymograph (see scale bars). Middle and right panels: values of depolymerization velocity and Ase1 accumulation at steady state derived from experiments (boxplots) or predicted by models 1 and 2 (lines). The boxplots are the same as in the corresponding plots in Figure 3.
(E) Distribution of Ase1 density on terminal sites in time for the indicated time points (see legend) as predicted by models 1 (A) and 2 (B) with model parameters as in (C).
See also Figure S4 and Tables S1 and S2.

7. Bieling, P., Telley, I.a., and Surrey, T. (2010). A minimal midzone protein module controls formation and length of antiparallel microtubule overlaps. Cell *142*, 420–432. https://doi.org/10.1016/j.cell.2010.06.033.

8. She, Z.Y., Wei, Y.L., Lin, Y., Li, Y.L., and Lu, M.H. (2019). Mechanisms of the Ase1/PRC1/MAP65 family in central spindle assembly. Biol. Rev. *94*, 2033–2048. https://doi.org/10.1111/brv.12547.

9. Subramanian, R., Wilson-Kubalek, E.M., Arthur, C.P., Bick, M.J., Campbell, E.A., Darst, S.A., Milligan, R.A., and Kapoor, T.M. (2010). Insights into antiparallel microtubule crosslinking by PRC1, a conserved nonmotor microtubule binding protein. Cell *142*, 433–443. https://doi.org/10.1016/j.cell.2010.07.012.

10. Kellogg, E.H., Howes, S., Ti, S.C., Ramírez-Aportela, E., Kapoor, T.M., Chacón, P., and Nogales, E. (2016). Near-atomic cryo-EM structure of PRC1 bound to the microtubule. Proc. Natl. Acad. Sci. USA *113*, 9430–9439. https://doi.org/10.1073/pnas.1609903113.

11. Gaillard, J., Neumann, E., Van Damme, D., Stoppin-Mellet, V., Ebel, C., Barbier, E., Geelen, D., and Vantard, M. (2008). Two microtubule-associated proteins of Arabidopsis MAP65s promote antiparallel microtubule bundling. Mol. Biol. Cell *19*, 4534–4544. https://doi.org/10.1091/mbc.e08-04-0341.

12. Stoppin-Mellet, V., Fache, V., Portran, D., Martiel, J.L., and Vantard, M. (2013). MAP65 coordinate microtubule growth during bundle formation. PLoS One *8*, e56808. https://doi.org/10.1371/journal.pone.0056808.

13. Mani, N., Wijeratne, S.S., and Subramanian, R. (2021). Micron-scale geometrical features of microtubules as regulators of microtubule organization. eLife *10*, e63880. https://doi.org/10.7554/eLife.63880.

14. Bratman, S.V., and Chang, F. (2007). Stabilization of overlapping microtubules by fission yeast CLASP. Dev. Cell *13*, 812–827. https://doi.org/10.1016/j.devcel.2007.10.015.

15. Liu, J., Wang, Z., Jiang, K., Zhang, L., Zhao, L., Hua, S., Yan, F., Yang, Y., Wang, D., Fu, C., et al. (2009). PRC1 cooperates with CLASP1 to organize central spindle plasticity in mitosis. J. Biol. Chem. *284*, 23059–23071. https://doi.org/10.1074/jbc.M109.009670.

16. Kitazawa, D., Matsuo, T., Kaizuka, K., Miyauchi, C., Hayashi, D., and Inoue, Y.H. (2014). Orbit/CLASP is required for myosin accumulation at the cleavage furrow in Drosophila male meiosis. PLoS One *9*, e93669. https://doi.org/10.1371/journal.pone.0093669.

17. Luchniak, A., Kuo, Y.W., McGuinness, C., Sutradhar, S., Orbach, R., Mahamdeh, M., and Howard, J. (2023). Dynamic microtubules slow down during their shrinkage phase. Biophys. J. *122*, 616–623. https://doi.org/10.1016/j.bpj.2023.01.020.

18. Drechsler, H., Xu, Y., Geyer, V.F., Zhang, Y., and Diez, S. (2019). Multivalent electrostatic microtubule interactions of synthetic peptides are sufficient to mimic advanced MAP-like behavior. Mol. Biol. Cell *30*, 2953–2968. https://doi.org/10.1091/mbc.E19-05-0247.

19. Pelletier, G. (2024). Weighted correlation and covariance (weightedcorrs). https://github.com/gjpelletier/weightedcorrs.

20. Braun, M., Lansky, Z., Fink, G., Ruhnow, F., Diez, S., and Janson, M.E. (2011). Adaptive braking by Ase1 prevents overlapping microtubules from sliding completely apart. Nat. Cell Biol. *13*, 1259–1264. https://doi.org/10.1038/ncb2323.

21. Powers, A.F., Franck, A.D., Gestaut, D.R., Cooper, J., Gracyzk, B., Wei, R.R., Wordeman, L., Davis, T.N., and Asbury, C.L. (2009). The Ndc80 kinetochore complex forms load-bearing attachments to dynamic microtubule tips via biased diffusion. Cell *136*, 865–875. https://doi.org/10.1016/j.cell.2008.12.045.

22. Grishchuk, E.L., Efremov, A.K., Volkov, V.A., Spiridonov, I.S., Gudimchuk, N., Westermann, S., Drubin, D., Barnes, G., McIntosh, J.R., and Ataullakhanov, F.I. (2008). The Dam1 ring binds microtubules strongly enough to be a processive as well as energy-efficient coupler for chromosome motion. Proc. Natl. Acad. Sci. USA *105*, 15423–15428. https://doi.org/10.1073/pnas.0807859105.

23. Al-Hiyasat, A., Tuna, Y., Kuo, Y., and Howard, J. (2023). Herding of proteins by the ends of shrinking polymers. Phys. Rev. E *107*, L042601. https://doi.org/10.1103/PhysRevE.107.L042601.

24. Lombillo, V.A., Stewart, R.J., and Richard McIntosh, J. (1995). Minus-end-directed motion of kinesin–coated microspheres driven by microtubule depolymerization. Nature *373*, 161–164. https://doi.org/10.1038/373161a0.

25. Franck, A.D., Powers, A.F., Gestaut, D.R., Gonen, T., Davis, T.N., and Asbury, C.L. (2007). Tension applied through the Dam1 complex promotes microtubule elongation providing a direct mechanism for length control in mitosis. Nat. Cell Biol. *9*, 832–837. https://doi.org/10.1038/ncb1609.

26. Umbreit, N.T., Gestaut, D.R., Tien, J.F., Vollmar, B.S., Gonen, T., Asbury, C.L., and Davis, T.N. (2012). The Ndc80 kinetochore complex directly modulates microtubule dynamics. Proc. Natl. Acad. Sci. USA *109*, 16113–16118. https://doi.org/10.1073/pnas.1209615109.

27. Grishchuk, E.L. (2017). Biophysics of microtubule end coupling at the kinetochore. Prog. Mol. Subcell. Biol. *56*, 397–428. https://doi.org/10.1007/978-3-319-58592-5_17.

28. Kapitein, L.C., Janson, M.E., van den Wildenberg, S.M.J.L., Hoogenraad, C.C., Schmidt, C.F., and Peterman, E.J.G. (2008). Microtubule-driven multimerization recruits ase1p onto overlapping microtubules. Curr. Biol. *18*, 1713–1717. https://doi.org/10.1016/j.cub.2008.09.046.

29. Alfieri, A., Gaska, I., and Forth, S. (2021). Two modes of PRC1-mediated mechanical resistance to kinesin-driven microtubule network disruption. Curr. Biol. *31*, 2495–2506.e4. https://doi.org/10.1016/j.cub.2021.03.034.

30. Walker, R.A., O'Brien, E.T., Pryer, N.K., Soboeiro, M.F., Voter, W.A., Erickson, H.P., and Salmon, E.D. (1988). Dynamic instability of individual microtubules analyzed by video light microscopy: rate constants and transition frequencies. J. Cell Biol. *107*, 1437–1448. https://doi.org/10.1083/jcb.107.4.1437.

31. Fu, C., Ward, J.J., Loiodice, I., Velve-Casquillas, G., Nedelec, F.J., and Tran, P.T. (2009). Phospho-regulated interaction between kinesin-6 Klp9p and microtubule bundler Ase1p promotes spindle elongation. Dev. Cell *17*, 257–267. https://doi.org/10.1016/j.devcel.2009.06.012.

32. Thomas, E.C., Ismael, A., and Moore, J.K. (2020). Ase1 domains dynamically slow anaphase spindle elongation and recruit Bim1 to the midzone. Mol. Biol. Cell *31*, 2733–2747. https://doi.org/10.1091/mbc.E20-07-0493-T.

33. Schmoller, K.M., Semmrich, C., and Bausch, A.R. (2011). Slow down of actin depolymerization by cross-linking molecules. J. Struct. Biol. *173*, 350–357. https://doi.org/10.1016/j.jsb.2010.09.003.

34. Maul, R.S., Song, Y., Amann, K.J., Gerbin, S.C., Pollard, T.D., and Chang, D.D. (2003). EPLIN regulates actin dynamics by cross-linking and stabilizing filaments. J. Cell Biol. *160*, 399–407. https://doi.org/10.1083/jcb.200212057.

35. Schindelin, J., Arganda-Carreras, I., Frise, E., Kaynig, V., Longair, M., Pietzsch, T., Preibisch, S., Rueden, C., Saalfeld, S., Schmid, B., et al. (2012). Fiji: an open-source platform for biological-image analysis. Nat. Methods *9*, 676–682. https://doi.org/10.1038/nmeth.2019.

36. Castoldi, M., and Popov, A.V. (2003). Purification of brain tubulin through two cycles of polymerization- depolymerization in a high-molarity buffer. Protein Expr. Purif. *32*, 83–88. https://doi.org/10.1016/S1046-5928(03)00218-3.

37. Gell, C., Friel, C.T., Borgonovo, B., Drechsel, D.N., Hyman, A., and Howard, J. (2011). Purification of tubulin from porcine brain. Methods Mol. Biol. *777*, 15–28. https://doi.org/10.1007/978-1-61779-252-6.

38. Zhang, H., Pekárek, J., Feng, J., Liu, X., Li, H., Zhu, H., Svatoš, V., Gablech, I., Podešva, P., Ni, S., et al. (2020). Simplifying the design complexity of microfluidic chips. J. Vac. Sci. Technol. B *38*, 063002. https://doi.org/10.1116/6.0000562.

39. Coimbatore Balram, K., Westly, D.A., Davanco, M.I., Grutter, K.E., Li, Q., Michels, T., Ray, C.H., Kasica, R.J., Wallin, C.B., Gilbert, I.J., et al.

(2016). The nanolithography toolbox. J. Res. Natl. Inst. Stand. Technol. *121*, 464–475. https://doi.org/10.6028/jres.121.024.

40. Castro, E.R., Tarn, M.D., Ginterová, P., Zhu, H., Xu, Y., and Neužil, P. (2018). Determination of dynamic contact angles within microfluidic devices. Microfluid. Nanofluidics *22*, 51. https://doi.org/10.1007/s10404-018-2066-0.

41. Mahamdeh, M., Simmert, S., Luchniak, A., Schäffer, E., and Howard, J. (2018). Label-free high-speed wide-field imaging of single microtubules using interference reflection microscopy. J. Microsc. *272*, 60–66. https://doi.org/10.1111/jmi.12744.

42. Ruhnow, F., Zwicker, D., and Diez, S. (2011). Tracking single particles and elongated filaments with nanometer precision. Biophys. J. *100*, 2820–2828. https://doi.org/10.1016/j.bpj.2011.04.023.

STAR★METHODS

KEY RESOURCES TABLE

REAGENT or RESOURCE	SOURCE	IDENTIFIER
Antibodies		
Goat Anti-Biotin	Sigma Aldrich	Cat#B3640; RRID: AB_258552
Bacterial and virus strains		
E. coli strain BL21 (DE3)	Altium International	Cat#230280
Chemicals, peptides, and recombinant proteins		
Benzonase	Novagen	Cat#70664
cOmplete Protease inhibitor cocktail EDTA-free	Roche Diagnostics GmBH	Cat#11873580001
HRV 3C protease	Merck Milipore	Cat#71493
Biotin-labeled tubulin	Cytoskeleton	Cat#T333P
GTP	Jena Bioscience	Cat#NU-1012
GMPCPP	Jena Bioscience	Cat#NU-405
Dichlorodimethylsilane (DDS)	Sigma Aldrich	Cat#440272
Pluronic F127	Sigma Aldrich	Cat#P2443
Methylcellulose	Sigma Aldrich	Cat#M0512
Recombinant DNA		
Ase1-GFP-6xHis, pET28 backbone	Janson et al.[6]	N/A
Ase1-mNeonGreen-6xHis, pET11 backbone	this manuscript	N/A
Software and algorithms		
Modelling code and code for recreating Figure 4	this manuscript	Zenodo: https://doi.org/10.5281/zenodo.12169420
Poetry (python dependency manager)	github.com/python-poetry	https://python-poetry.org/
Python	Python Software Foundation	https://www.python.org/; RRID: SCR_008394
Code for creating kymographs	this authorgroup	Zenodo: https://doi.org/10.5281/zenodo.3270572
Code for analyzing kymographs and recreating Figures 1, 2, and 3	this manuscript	Zenodo: https://doi.org/10.5281/zenodo.12517251
MATLAB (R2019a)	MathWorks	https://www.mathworks.com/products/matlab.html; RRID: SCR_001622
ImageJ 1.52 (FIJI)	Schindelin et al.[35]	https://imagej.nih.gov/ij/; RRID SCR_002285
Other		
Amicon Ultra-15	Merck	Cat#UFC910024

RESOURCE AVAILABILITY

Lead contact

Further information and requests for resources and reagents should be directed to and will be fulfilled by the lead contact, Zdenek Lansky (Zdenek.Lansky@ibt.cas.cz).

Materials availability

The plasmid Ase1-mNeonGreen-6xHis (pET11 backbone) is available from the lead contact upon request.

Data and code availability

- All original code used to generate and analyze the theoretical model simulations has been deposited at Zenodo and is publicly available as of the date of publication (Zenodo: https://doi.org/10.5281/zenodo.12169420). The DOI is listed in the key resources table (modelling code). The simulation data generated with the code as well as the experimental data used to compare with the theoretical results are deposited in the same Zenodo entry. To ensure reproducibility of the computational environment, the python library dependencies were managed using poetry (see key resources table).
- All original code used for analyzing kymographs (see "estimation of amount of Ase1 being swept" in method details) and recreating Figures 1, 2, and 3 has been deposited at Zenodo (Zenodo: https://doi.org/10.5281/zenodo.12517251). Tabular data

from which graphs in Figures 1, 2, 3, and S1–S3 can be recreated are also available there. Any additional information required to reanalyze the data reported in this paper is available from the lead contact upon request.

EXPERIMENTAL MODEL AND STUDY PARTICIPANT DETAILS

Ase1-GFP and Ase1-mNeonGreen were expressed in e.coli cells (Altium International, #230280).

METHOD DETAILS

Ase1 expression and purification

Ase1-GFP[6] and Ase1-mNeonGreen were expressed in E. coli strain BL21 (DE3) (Altium International, #230280). After harvesting the cells, the cell pellet was resuspended in 5 mL ice-cold phosphate buffered saline (PBS) and stored at - 80°C for further use. For cell lysis, the cells were homogenized in 30 mL ice-cold His-Trap buffer (50 mM Na-phosphate buffer, pH 7.5, 5% glycerol, 300 mM KCl, 1 mM MgCl2, 0.1% tween 20, 10 mM BME, 0.1 mM ATP) supplemented with 30 mM imidazole, Protease Inhibitor Cocktail (cOmplete, EDTA free, Roche, #11873580001) and benzonase (Novagen, #70664) to the final concentration of 25 units/mL, then sonicated, and finally centrifuged at 45000 x g for 60 min at 4°C in the Avanti J-26S ultracentrifuge (JA-30.50Ti rotor, Beckman Coulter). The cleared cell lysate was incubated in a lysis buffer-equilibrated Ni-NTA resin (HisPur Ni-NTA Superflow Agarose, Thermo Scientific) for 2 h at 4°C. The Ni-NTA resin was sequentially washed with wash buffer I (His-Trap buffer supplemented with 60 mM imidazole), and wash buffer II (His-Trap buffer supplemented with 60 mM imidazole and 700 mM NaCl). Ase1-GFP was eluted in His-Trap buffer supplemented with 300 mM imidazole. For Ase1-mNeonGreen, after wash buffer II, the resin was washed again in wash buffer I, now supplemented with the 3C PreScisson protease (Merck Milipore, #71493), which cut Ase1-mNeonGreen off the column, at the 3C protease cleavage site positioned in between the mNeonGreen and the 6xHis-tag. The mixture was incubated over night at 4°C. Next day the beads were removed and the cleaved protein was collected. Ase1-GFP and Ase1-mNeonGreen were concentrated by spinning the sample at 3500 RPM at 4°C using a 100kDa centrifugal filter tube (Amicon Ultra-15, Merck, #UFC910024). The second purification step for Ase1-mNeonGreen involved size exclusion chromatography, performed using a Superdex 200 10/300 column. The size exclusion buffer consisted of 100 mM Tris, 150 mM NaCl, 1 mM $MgCl_2$, 1 mM DTT, 0.05% Tween, 0.1 mM ATP, and 10% glycerol. Fractions containing the protein were collected, concentrated, The final protein concentrations were measured with a NanoDrop ND-1000 spectrophotometer (Thermo Scientific) at both 280 and 506 nm absorbance. Protein was flash-frozen in liquid nitrogen and stored at −80°C. All steps in the purification were performed at 4°C.

Microtubule seeds assembly

Porcine brains were obtained from a local abattoir and used within approx. 4 h of death. Porcine brain tubulin was isolated using the high-molarity PIPES procedure.[36,37] Biotin-labeled tubulin was purchased from Cytoskeleton Inc. (#T333P). GMPCPP-microtubule seeds were polymerized from 4 mg/mL tubulin (labelled depending on assay, as described in "experimental chamber preparation") for 2 h at 37°C in BRB80 supplemented with 1mM MgCl2 and 1mM GMPCPP (#NU-405, Jena Bioscience). The polymerized MTs were centrifuged for 30 min at 18000 x g in a Microfuge 18 Centrifuge (Beckman Coulter). After centrifugation, the pellet with MTs was resuspended, kept in BRB80 at room temperature and used within one week.

Experimental chamber preparation

For TIRF experiments, chambers were assembled by melting thin strips of parafilm in between two glass coverslips silanized with 0.05% dichlorodimethylsilane (DDS, #440272, Sigma).[20] Chambers were never re-used for additional experiments. For some experiments, flow chambers were fabricated on silicon-on-insulator substrate with a diameter of ≈100 mm and nominal value of the top silicon layer thickness of 50 μm based on a design prepared in Nanolithography toolbox software.[38,39] Two lithography steps were performed, one defining the flow chamber, the second one for through holes. We etched the top silicon and stopped it at the buried SiO_2 layer with no Si residue there, followed by anodic bonding of the silicon wafer with fabricated chambers and through holes to the corning glass type Corning 7740 with nominal thickness of 170 μm, subsequent dicing by a diamond blade dicing saw into isolated chips and coating with FAS-17 fluorosilane.[40]

Biotin antibodies were flushed into the channels for 1 min (#B3640, Sigma, 20 $\mu g\ mL^{-1}$ in PBS). The glass surface was then blocked by incubation with 1% Pluronic (F127 in PBS, #P2443, Sigma) for at least 20 min, followed by wash with TIRF assay buffer (see below). Biotinylated, GMPCPP-stabilized, fluorescence-labeled MTs in BRB80 (80 mM Pipes/KOH pH 6.9, 1 mM $MgCl_2$, 1 mM EGTA) were then flushed into the channel and bound to the biotin antibodies. Subsequently, the buffer in the flow cell was exchanged for assay buffer (see below). Then, Ase1 in assay buffer was flushed into the flow cell at the final assay concentration stated in the main text, together with tubulin. Set A experiments (Figures 1, 2, S1, and S2) were performed at room temperature and with 30μM unlabeled tubulin present in solution. Set B experiments (Figures 3, 4, and S3) were performed at 29°C and with 14μM tubulin, 7% of which was labeled with rhodamine. In the case of set B experiments, non-biotinylated GMPCPP-stabilized MTs were flushed into the flow cell and bound to the template MTs that were sparsely covered sparsely with Ase1 (these steps were performed before the assay buffer had been flushed in). These MTs were labelled with both rhodamine and Alexa 647 (represented in sketches in dark blue), while

the templates were only (very weakly) labelled with Alexa 646 (represented in sketches in light blue). To prevent evaporation in order to avoid changes in component concentrations, the channels were sealed after flushing in the assay buffer.

Assay buffer

The following buffer components common to all used buffers: 20mM PIPES pH 6.9, 10mM HEPES pH 7.2, 0.5mM EGTA, 1mM $MgCl_2$, 0.5mM Mg-ATP, 0.67mM GTP (Jena Bioscience, #NU-1012), 0.67% Tween 20, 6.7mM DTT, 0.3 mg/mL Casein, 13.5mM D-Glucose, 0.3 mg/ml glucose oxidase and 0.03 mg/ml catalase. The buffer for set A experiments, in addition to these components, contained 70mM KCl, and 0.1% methylcellulose (Sigma, #M0512), 0.1% glycerol, 1mM sodium phosphate and 1μM ATP. The buffer for set B experiments, in addition to the components common to all buffers, contained 116mM KCl and 0.065% methylcellulose (Sigma, #M0512).

Imaging

Labeled proteins were visualized sequentially by switching between the corresponding channels (Chroma filter-cubes) using Nikon-Ti E microscope equipped with a 100x Nikon TIRF objective in combination with a Hamamatsu Orca Flash 4.0 sCMOS camera (set A experiments) or 63× Zeiss oil immersion TIRF objective in combination with a Andor iXon DV 897 (Andor Technology) EMCCD camera (set B experiments). In the case of set A experiments, at Ase1 concentrations lower than 40nM, interference reflection microscopy (IRM) was used to visualize the MTs (using the same objective and camera).[41] The acquisition rate was 5 s for set A experiments and 2.5 s for set B experiments, the exposure time was 100ms for both cases. For set B experiments, the Alexa 647-labeled MT seeds were imaged before the start of the time lapse, and only the Ase1-mNeonGreen channel was imaged during the time lapse. For set B experiments, the rhodamine (tubulin) and the GFP (Ase1) channel where imaged sequentially, whereas every 40th frame the Alexa 647 channel was imaged in place of the GFP channel, in order to track the location of the GMPCPP-stabilized seeds (which we with this data determined to not move significantly during experiment time).

Image analysis

Data was analyzed using FIJI 1.52[35] and custom-written MATLAB (Mathworks) routines (https://doi.org/10.5281/zenodo.12517251).

Overlap lifetime estimation

The lifetime of regions of MT overlap was estimated for two different configurations: Antiparallel overlaps, where two dynamic extensions met and formed a dynamic "midzone", and parallel bundles of two dynamic extensions (as shown in Figure 1). For both antiparallel and parallel overlaps, lifetime was taken to start upon the bundling of the dynamic (GDP) lattices of each involved MT (for antiparallel configurations, we additionally required both plus ends to be within 3 μm to each other upon start of the event). Lifetime was taken to end upon one of the involved MTs to shrink back to its GMPCPP-stabilized region for parallel bundles, and upon the midzone ceasing to exist for antiparallel bundles. The plot is a Kaplan-Meier plot, which adequately accounts for cases where an overlapping region survived until the end of the recorded time-lapse Video (i.e., cases which were right-censored) (Figure 1C was generated by using the MATLAB function ecdf with setting "survival" and alpha = 0.05).

Estimation of parameters of MT dynamics

Parameters of MT dynamics, for set A experiments, have been estimated by generating kymographs and approximating the location of MT plus ends over time and space with straight lines (the Ase1-mNeonGreen signal was used to visually track MT ends, as MT were not imaged directly). For set B experiments, we used FIESTA to determine the locations of MTs.[42] Both methods yielded polymerization and depolymerization velocities. Rescues were identified as events where a MT switches from depolymerization to polymerization before reaching the GMPCPP-stabilized seed, and catastrophes were events where polymerization was followed by depolymerization. Rescue and catastrophe frequencies were estimated by dividing the number of rescues respectively catastrophes by the sum of the total distance depolymerized respectively polymerized by all plus ends. In the case of set A experiments, we tested the 10nM only during the revision, during a time where room temperatures were less stable. Therefore, MT velocities differed from our initial experiments across all Ase1 concentrations. To be able to pool the results from these experiments with our initial results, we multiplied the velocities of these experiments by the following factor: The mean polymerization respectively depolymerization velocity of isolated MTs at 42nM of the initial experiments divided by the mean respective velocity of isolated MTs at 42nM of the experiments performed during revision (these mean velocities were weighted by the duration of each polymerization/depolymerization event). The resulting factors were 0.4 for polymerization and 0.39 for depolymerization.

Single fluorophore quantification

Fluorescent signal of a single Ase1-mNeonGreen dimer was determined by generating intensity time-traces of Ase1-mNeonGreen molecules and estimating the height of the occurring steps in change of intensity (only small steps, i.e., steps likely to be bleaching steps). The number of steps was first estimated by eye, and this number was used as input for the *findchangepoints* function of MATLAB to determine the position of the steps (by detection of significant changes of the mean value). To yield the intensity per Ase1 dimer, the median of the heights of these steps was calculated and multiplied by two. For the estimation of single Ase1-GFP dimers, the intensity of single diffusive spots of GFP signals on MTs has been taken at very low concentration of Ase1-GFP in the buffer (no bleaching data available for these experiments). For estimation of single fluorophores for set B experiments we did not have bleaching data available, instead we measured the intensity of diffusing molecules (which may overestimate the intensity per single molecule).

Ase1 density estimation

Area selections along the MT length (only regions with at least one dynamic extension present were measured) were used to readout the mEGFP or mCherry fluorescent signal and to estimate the integrated signal intensity of GFP- or mNeonGreen-labeled Ase1 bound to the MT. The signal in regions directly adjacent to the MT was subtracted as background signal. The density of GFP- or mNeonGreen -labeled Ase1 bound to the MT was then estimated by dividing the integrated intensity by the estimated intensity per single fluorescent molecule (either GFP or mNeonGreen, see below) and the length of the region. The signal per length (S) measured on isolated MTs was used to correct for the reduced illumination intensity in outer regions of the field of view, in cases where a region of interest (ROI) was located in such a region ($S_{corrected}$(ROI) = S(ROI) *S(isolated MT in center of field of view) / S(isolated MT near ROI).

Estimation of amount of Ase1 being swept

To estimate the number of swept Ase1 molecules for corresponding panels in Figures 3, 4, and S3 (set B experiments), we first obtained density traces for each frame during a MT depolymerization period. These traces were obtained by summing the pixel intensities perpendicular to the MT, i.e., by generating a kymograph where each pixel represents such a sum (https://doi.org/10.5281/zenodo.3270572). For each frame f we analyzed the corresponding density trace D_f as follows. (1) We computed D_s by subtracting the density trace $D_{before\_catastrophe}$ of the MT before the catastrophe had occurred from D_f ($D_s = D_f - D_{before\_catastrophe}$) (2) We obtained $x = 0 = X_{Dsmax}$, the location of the local maximum of D_s in vicinity of the MT plus end. (3) We obtained $X_{Dsright}$ by finding the first local minimum of D_s to the right of $X_{Dsright}$ (to reduce the effect of noise, we smoothed D_s for this computation). "Right" of D_s, in our chosen coordinate system, means toward the MT seed ($x > 0$). (4) $X_{Dsleft} = X_{Dsmax} - 471$nm (471 nm = 3 pixels). (5) We computed D_A. D_A is equal to D_f to the left of X_{Dsmax}, and equal to $D_s + D_f(X_{Dsmax}) - D_s(X_{Dsmax})$ to the right of X_{Dsmax}. (6) We fitted a distribution Y_F (shape see below) plus an error function Y_E to D_A between X_{Dsleft} and $X_{Dsright}$. We required both Y_F and the error function to not have any x-offset: Y_F was a right-sided decaying exponential $\exp(-x/\lambda)$ ($Y_F = 0$ where $x < 0$, and with λ bounded between 1 and 1000 nm) convolved with a Gaussian $\exp(-x^2/2\sigma^2)$ (with σ bounded between 180 and 190 nm to account for the point spread function of our setup; this same σ had been used as input for Y_E). We also fixed G + E (plus a constant value) to approach the minimum of D_A to the left of the end, and the average of D_A to the right of $X_{Dsright}$ (the average of D_A within 5 μm from $X_{Dsright}$, giving more weight to values close to $X_{Dsright}$). (6) We then summed the Ase1 density below Y_F (as discretized in x by the pixel size), which we took as a proxy for the number of swept Ase1-GFP molecules after dividing by the intensity per Ase1 dimer (obtained as described above).

Fluorescence recovery after photo bleaching (FRAP)

Biotinylated GMPCPP-stabilized MTs were immobilized on the coverslip. We then flushed in the same assay buffer as for set A experiments, incubated until the Ase1 density on MTs reached a steady-state, and subsequently bleached Ase1-mNeonGreen molecules and recorded the recovering Ase1-mNeonGreen signal. We fitted the resulting recovery curve to the expression $D_s - c\exp(-bt)$, where D_s is the steady state density, and c and b are fitting parameters. Results for fitting parameter b are shown in Figure S4D.

Mathematical modelling

The scripts to reproduce the modelling, and to plot experimental and theoretical results from Figures 4 and S4 can be found in https://doi.org/10.5281/zenodo.12169420.

Assumptions

The model of Ase1 accumulation on depolymerizing MTs, and its effect on depolymerization velocity (Figure 4A) is built on the following assumptions.

(1) We neglect interactions between protofilaments and only consider a one-dimensional lattice, where lattice of size $a = 8$nm start at index $i = 1$ at the plus end, extending to $i = 400$.
(2) Only bound Ase1 molecules are considered by recording the presence or absence (0 or 1) of Ase1 in each lattice site. Bound Ase1 molecules exchange with solution with two constant rates (k_{on} ,k_{off}). Binding is only allowed if the lattice site is empty (Figure 4A). k_{off} was directly measured, and k_{on} was adjusted to match the Ase1 equilibrium density on MTs (Table S1).
(3) Ase1 particles on the lattice undergo unbiased diffusion characterized by a constant hopping rate (k_h). Hopping is only allowed to an empty site (Figure 4A). The rate k_h is calculated from the experimentally measured diffusion coefficient of Ase1 (Table S1), as $k_h = D/a^2$.
(4) The Ase1 particle in the terminal site ($i = 1$), cannot hop past the MT end (red arrow on the left of Figure 4A), but can detach with rate k_{off}.
(5) The terminal lattice site may dissociate from the MT, with rate k_d which depends on the presence of Ase1, according to each model:
   a. In Model 1, it occurs with rate k_d^0 if the terminal lattice site is not occupied (Figure 4B top), and with rate $(1 - \Omega)k_d^0$ if it is occupied (Figure 4B bottom). Ω is a parameter between zero and one. If $\Omega = 0$, the presence of Ase1 has no effect, and if $\Omega = 1$, the first tubulin subunit cannot unbind if it is bound to Ase1.
   b. In Model 2, the rate of tubulin subunits loss at the plus end is reduced by a factor $(1 - \Omega)$ if any of the N terminal sites is occupied. At steady state, this rate is $k_d = k_0^d\left[1 - \Omega\{1 - \prod_{i=1}^{i=N}(1 - P_i)\}\right]$, where P_i is the probability of site i being occupied by Ase1.

k_d^0 is derived from the depolymerization rate of MTs in the absence of Ase1 (v_0), measured experimentally (Table S1), such that $k_d^0 = v_0/a$.

(6) If the terminal lattice site dissociates when a molecule of Ase1 is bound to it, this Ase1 is lost as well (Figure 4B, bottom).

Simplification to a system of constant size

Since terminal subunits are more likely to be lost when they are without Ase1 than when they are with Ase1, any dissociation event increases the density of Ase1 remaining on the MT. This effect is only present at the MT end, and away from the end, the probability of a binding site being occupied is only determined by the binding and unbinding constants: $\alpha = k_{on}/(k_{on} + k_{off})$.

Therefore, we can restrict the model to a section of the MT with L lattice sites, as long as the probability of finding a molecule at position L is close to α. When a depolymerisation event happens, we shift the lattice indexes such that site $i+1$ becomes site i, and set $P_{i=L} = \alpha$.

Mean field theory

The system can be solved using a mean-field approximation, by just considering the ensemble of P_i, the average probability of a site i being occupied and neglecting higher-order correlations between neighbouring sites. We can then write a set of discrete differential equations to represent the dynamics of the system:

$$\frac{dP_i}{dt} = (P_{i+1} + P_{i-1} - 2P_i)k_h + (1 - P_i)k_{on} - P_i k_{off} + (P_{i+1} - P_i)k_d$$

Specific equations apply at the boundaries $i = 1$ and L:

$$\frac{dP_1}{dt} = k_h(P_2 - P_1) - P_1 k_{off} + (1 - P_1)k_{on} + k_d P_2 - k_d^0 P_1(1 - \Omega)$$

$$\frac{dP_L}{dt} = 0$$

The terms of the equation are associated with the rates of diffusion, binding, unbinding (k_h, k_{on}, k_{off}) which are constant, and the depolymerization rate (k_d), which is affected by lattice occupancy in a different way in each model (see Assumptions).

For Model 1, $k_d = k_d^0(1 - \Omega P_1)$.

For Model 2, $k_d = k_0^d[1 - \Omega + \Omega\prod_{i=1}^{i=N}(1 - P_i)]$.

This dynamical system can be evolved from any initial conditions, converging to the unique steady-state solution for a set of given parameters. Assuming that the MT is at binding equilibrium when it starts depolymerizing, we initially set $P_i = \alpha$ for all sites. From those initial conditions, we integrate the equations numerically using Python's *odeint* function (see source code).

Modelling of overlaps

To model MT overlaps (Figure 4E), we assume that the Ase1 measured in the overlaps (see Image Analysis above) is evenly distributed among 3 protofilaments that are involved in crosslinking the MTs. We neglect the other protofilaments. We had also modelled 2 protofilaments instead of 3, which did not fit the experimental data as well as 3 protofilaments.

QUANTIFICATION AND STATISTICAL ANALYSIS

All experiments were quantified by pooling data from multiple experiments performed on at least two different days. No data was excluded from the study.

Data representation

In all boxplots presented in the figures, horizontal midline indicates the median; plus symbols indicate the mean; bottom and top box edges indicate the 25th and 75th percentiles, respectively; the whiskers extend to the most extreme data points not considered as outliers (the function *Alternative boxplot* from the IoSR MATLAB Toolbox has been used); the numbers indicate the sample size. Stars indicate statistical significance as determined by applying the MATLAB *multcompare* function on test data derived from the MATLAB *anova1* (one-way ANOVA) function. One star denotes $p < 0.05$, two stars denote $p < 0.01$, and three stars denote $p < 0.001$. A line without a star denotes no statistically significant difference. For Figures 3J and S3H, the total length of a given error bar equals two times the square root of the number of the rescues in the corresponding bin divided by the sum of the time depolymerized in the corresponding bin.

Comparison of experimental data and model

To compare the predicted and observed timescale of Ase1 accumulation (τ) and Ase1 accumulation at steady state (A_{end}), the accumulated Ase1 as a function of time was fitted to $A_{end}(1 - e^{-t/\tau})$ in experiments and model predictions (e.g., Figure 4C for isolated MTs at 6nM of Ase1). In the model, the accumulation of Ase1 at any given timepoint is defined as $(\sum_{i=0}^{i=L} Pi) - \alpha L$. As a proxy of velocity of depolymerization at steady state, we used the average velocity of depolymerization observed after 20 s of depolymerization

in experiments and compared it to the depolymerization velocity at the last simulated timepoint (Figure 4C). The 95% confidence intervals of these magnitudes were estimated using the bootstrap method. For each experimental condition with N depolymerization events, a thousand sets of N depolymerization events were drawn through sample with replacement. For each of those sets, τ and A_{end} were calculated by fitting all observations in the set, and the average velocity after 20 s was calculated. Then, the distribution of each magnitude across all sets was used to calculate the 95% confidence intervals (see source code).